DEVELOPMENT OF LIDAR TECHNIQUES TO ESTIMATE ATMOSPHERIC OPTICAL PROPERTIES

by

Mariana Adam

A dissertation submitted to the Johns Hopkins University in conformity with the requirements for the degree of Doctor of Philosophy

Baltimore, Maryland

October, 2005

DEVELOPMENT OF LIDAR TECHNIQUES TO ESTIMATE ATMOSPHERIC OPTICAL PROPERTIES

by

Mariana Adam

ABSTRACT

The modified methodologies for one-directional and multiangle measurements, which were used to invert the data of the JHU elastic lidar obtained in clear and polluted atmospheres, are presented.

The vertical profiles of the backscatter lidar signals at the wavelength 1064 nm were recorded in Baltimore during PM Supersite experiment. The profiles of the aerosol extinction coefficient over a broad range of atmospheric turbidity, which includes a strong haze event which occurred due to the smoke transport from Canadian forest fires in 2002, were obtained with the near-end solution, in which the boundary condition was determined at the beginning of the complete overlap zone. This was done using an extrapolation from the ground level of the aerosol extinction coefficient, calculated with the Mie theory. For such calculations the data of the ground-based in-situ instrumentation, the nephelometer and two particle size analyzers were used. An analysis of relative errors in the retrieved extinction profiles due to the uncertainties in the established boundary conditions was performed using two methods to determine the ground-level extinction coefficient, which in turn, imply two methods to determine aerosol index of refraction (using the nephelometer data and chemical species measurements). The comparison of the three analytical methods used to solve lidar equation (near-end, far-end and optical-depth solutions) is presented.

An improved measurement methodology and modifications of a data processing technique are proposed to process the multiangle elastic-lidar data in clear atmospheres. The technique allows one to determine more accurate profiles of the optical depth and relative backscattering versus height. It is also shown that these profiles and the measured range-corrected signals can be used to determine the lidar overlap function versus range. The retrieved data allow one to analyze the influence of the local horizontal heterogeneity and measured lidar-data distortions, and thus, to estimate the retrieved data quality. The methodology and the data processing technique were tested with experimental data of two simultaneously scanning lidars operating in clear atmospheres. The experimental results obtained with the two lidars at different wavelengths are discussed. The results show that the multi-angle method is most suitable for the shortest wavelength (355 nm).

Dissertation committee:

Adviser: Dr. Marc B. Parlange

Reader: Dr. Eugene D. Shchukin

Reader: Dr. Vladimir A. Kovalev

Acknowledgments

I would like to thank my thesis adviser Prof. Marc B. Parlange for all his support and for giving me the freedom to do my own research. I appreciate his trust and his permanent and optimistic impulse: “Go for it, Mariana”.

I want to thank my colleague Markus Pahlow, who introduced me to the lidar basics, for his patience in explaining different problems and for his willingness to share and discuss various experimental and theoretical lidar issues.

I would like to express my all gratitude to Dr. Vladimir Kovalev (U.S.D.A., Fire Science Laboratory, Missoula, MT) along our collaboration for all his remarks and help. I really appreciate his patience and his willingness to help me become a lidar scientist. I am thankful for all his remarks, for all his support in overcoming my frustrations, and for trusting me.

I thank Prof. Eugene D. Shchukin for accepting to be part of my thesis committee.

I wish to thank my colleagues Jan Kleissl, Elie Bou-Zeid, Vijayant Kumar and Chad Higgins for their assistance in the field experiments and for coping together during “the best years of my life” in “the greatest city of America”.

I am thankful for the “Chemistry team” from University of Maryland at College Park, for its nice and fruitful collaboration during Baltimore PM Supersite Experiment. Special thanks to Prof. John M. Ondov and Dr. David Harrison.

I thank the lidar team from Swiss Federal Institute of Technology (EPFL), Lausanne, who helped us upgrade the lidar system. I really appreciate their efforts and I want to especially thank Dr. Valentin Simeonov, Pablo Ristori and Ioan Balin.

I want to thank Jenny Newton and Cyle Wold for their assistance during Montana experiment as well as Wei Min Hao the project manager at Fire Science Laboratory who supported this experiment.

I wish to thank all my friends along the journey, for being along my side during all good and bad times. Special thanks to my friend Anca – Monia Constantinescu.

I want to thank my family for understanding and trusting me entirely to fulfill my goals.

My gratification from everybody who reads this thesis. This gives me a sense and all my efforts were not in vain.

TABLE OF CONTENTS

List of tables……………………………………………………………….......IX

List of figures………………………………………………………………..XI

Chapter 1

1. Introduction…………………………………………………………………..1

   1.1. Research context……………………………………………...……….1

   1.2. Research presentation……………………………………….………...4

Chapter 2

2. Light propagation in atmosphere and lidar technique ………………..….…….6

   2.1. Atmosphere structure and properties……………………….………...6

      2.1.1. Overview…………………………………………………...…….6

      2.1.2. Troposphere……………………………………….……..……...11

      2.1.3. Atmospheric boundary layer ………………………..………….11

         2.1.3.1.Unstable boundary layer………..………………….…………..14

      2.1.4. Aerosols within troposphere……………………….….….……...15

         2.1.4.1.Continental aerosol…………………………………..……...16

   2.2. Light propagation in atmosphere…………………………….…………...17

      2.2.1. Overview………………………….…………………………….17

      2.2.2. Light scattering by molecules (Rayleigh theory)…………………….19

      2.2.3. Light scattering by particles (Mie theory)………………..………..20

   2.3. Lidar system………………………….……………………………...23

      2.3.1. Overview of a backscatter elastic lidar..……………………………...23

      2.3.2. JHU lidar system biaxial configuration………………..……………..25

      2.3.3. JHU lidar system coaxial configuration……………….…………..27

      2.3.4. FSL lidar system biaxial configuration…………………..……..28

2.4. Lidar equation and inversion methods……………………………..………..29

2.4.1. Lidar equation…………………………………………………….......29

2.4.2. Analytical solutions for lidar equation………………………………30

2.4.2.1.Boundary point solution (far-end and near-end solutions)……….32

2.4.2.2.Optical depth solution…………………………………………32

2.4.2.3.Multiangle methods…………………………………..……..34

Chapter 3

3. Aerosol optical characterization during Baltimore PM Supersite Experiment…..39

3.1. Baltimore PM Supersite field experiment……………………………...39

3.2. Aerosols optical properties at ground level………………………………42

3.3. Application of the near-end solution to determine vertical profile of aerosol extinction coefficient……………………………………………………...…53

3.4. Comparison of near, far and optical depth solution……………………....64

3.5. Uncertainties arising from estimation of the boundary condition in near-end solution case……………………………………………………………....68

3.6. Conclusions………………………………………………………………76

Chapter 4

4. Applications of Kano-Hamilton multi-angle method to determine vertical profile of aerosol optical properties and lidar overlap…………………………...…80

4.1. Real lidar in an ideal atmosphere: simulations……………………………...81

4.2. Methodology……………………………………………………………...…88

4.3. Determination of the lidar effective overlap……………………………...98

4.4. Instrumentation and measurement procedure……………………….......104

4.4.1. Instrumentation……………………………………………………...104

4.4.2. Measurement procedure…………………………………………….104

4.5. Results and discussion…………………………………………………...110

4.6. Procedures to determine aerosol extinction and backscatter coefficients….131

4.6.1. Determination of the aerosol extinction coefficient………………...131

4.6.2. Determination of the aerosol backscatter coefficient…………….....138

4.6.3. Application on synthetic lidar signals………………………………140

4.7. Summary…………………………………………………………………...151

Chapter 5

5. Conclusions………………………………………………………………..158

References

Appendix I: Rayleigh scattering……………………………….………….....162

Appendix II: Mie theory…………………………………………………...169

Appendix III: Derivation of the lidar equation………………………….....175

Appendix IV: Analytical solutions for lidar equation……………….…......178

Appendix V: Multianlge methods…………………………….….….......184

Appendix VI: Background subtraction and SNR estimation……….….…..…186

Appendix VII: Multiangle methods improved measurement procedure.……..............190

Appendix VIII: Notations of the main variables and parameters……………….198

Bibliography………………………………………………….…………202

Curriculum vitae…………………………………………………….……......214

LIST OF TABLES

Table 2.1. Atmospheric composition. Components are listed by mixing ratios representative in troposphere (TP) or stratosphere (ST), their vertical distribution and controlling processes

Table 2.2. JHU lidar system, biaxial configuration. Principal characteristics

Table 3.1. Correlation coefficients between measured and computed aerosol scattering and between measured aerosol scattering and mass concentration

Table 3.2. Mean, standard deviation (STD), maximum, minimum and median for measured (nephelometer) and computed (Mie theory) aerosol scattering, computed (Mie theory) aerosol extinction coefficient, derived mass and mass scattering coefficient (using measured and computed scattering coefficient)

Table 3.3. Refractive indices as calculated by indirect (I) and direct method (II)

Table 3.4. Species densities and refractive indices

Table 3.5. Errors in mass balance and density

Table 3.6. Errors in boundary condition $\kappa_p(r = 0)$ and AOD

Table 4.1. FSL and JHU Lidar systems parameters

Table 4.2. Relative errors (%) in retrieving optical depth $\tau(0, h)$, Hamilton exponent $A^*(h)$, lidar overlap $q(r)$, particles extinction coefficient $\kappa_p(h)$, particles backscatter coefficient $\beta_p(h)$ and particles lidar ratio LR

LIST OF FIGURES

Figure 2.1. Atmosphere structure and mean temperature profile versus altitude

Figure 2.2. Global mean temperature (left plot), pressure (middle plot), and mean air density (right plot) according to US Standard Atmosphere 1976

Figure 2.3. ABL structure for aerodynamically rough flow in neutrally-stratified conditions

Figure 2.4. The ABL in high pressure regions over land consists in three major parts: a turbulent mixed layer, a less turbulent residual layer containing the former mixed layer air and a nocturnal stable BL of sporadic turbulence

Figure 2.5 ABL evolution during the day (August 10, 2002, Baltimore), as revealed by JHU backscatter lidar. The main structures which can be seen are: ABL top, old and new RL, ML, entrainment zone. The color scale corresponds with the strength of the backscatter signal (a.u.), which is proportional with the number density of molecules and particles. The red correspond to strong signal and blue to weak signal.

Figure 2.6. Typical daytime profiles of mean virtual potential temperature θ_v, wind speed *v*, water vapor mixing ratio *r* and pollutant concentration *c*

Figure 2.7. Schematic representation of the major parts of a lidar system

Figure 2.8. JHU lidar system, biaxial configuration. The main components: laser, telescope, periscope, laser power supply and cooling system, computer

Figure 2.9. Details of JHU lidar system, coaxial configuration. The main components: laser, telescope, detectors box, first and second mirror

Figure 2.10. FSL biaxial (left) and JHU coaxial (right) lidar systems

Figure 3.1. Baltimore PM Supersite experiment, 2002 location in Bayview, East Baltimore, overview of the main measurements

Figure 3.2. Temporal variation of the particle size distribution (PSD); (a) particle number (NSD); (b) particle surface area (SSD); (c) particle volume (VSD)

Figure 3.3. Mean (dots) and standard deviation (crosses) of the particle size distribution over the three time periods under investigation (1, 2 and 3 are the three periods and a, b and c stand for particle number, surface area, and volume respectively)

Figure 3.4. Temporal variation of the aerosol scattering coefficient as measured by nephelometer and computed by Mie theory (a), of the derived mass (b) and of the mass scattering coefficient (c). Tick marks on the time axis correspond to midnight.

Figure 3.5. Visibility at Baltimore and BWI airport

Figure 3.6. Example of retrieving the vertical profile of the aerosol extinction coefficient by choosing the corresponding V^{2}_{max}

Figure 3.7. (a) Temporal vertical profile of the lidar RCS (the color scales represent the RCS in arbitrarily units); (b) Temporal vertical profile of the aerosol extinction coefficient (km^{-1}); on the right axis, backscatter to extinction ratio $\Pi_p(sr^{-1})$ (asterisks); (c) Vertical profile of the aerosol extinction coefficient at different time stamps for 5 July 2002 (bc = boundary condition)

Figure 3.8. Same as Figure 6.7 for 7 July 2002

Figure 3.9. Same as Figure 6.7 for 8 July 2002

Figure 3.10. Same as Figure 6.7 for 9 July 2002

Figure 3.11. Same as Figure 6.7 for12 July 2002

Figure 3.12 (a) – (e). Comparison of near-end, far-end and optical depth solutions. The data analyzed were taken under a clear sky, on 8 and 10 June 2001. AOD for each method is also shown.

Figure 3.13. Measured and computed particle scattering coefficient at 530 nm at ground level

Figure 3.14. Particle extinction coefficients as computed at 1064 nm at ground level

Figure 3.15. Particle extinction to backscatter ratio (lidar ratio) at 1064 nm at ground level

Figure 3.16. Particle extinction coefficients as computed at 1064 nm at ground level

Figure 3.17. Same as Fig. 5 but for 7 July 18:10 EST

Figure 3.18. Same as Fig. 5 but for 8 July 11:21 EST and 18.27 EST

Figure 4.1. Model dependence of the total optical depth on height (thin line) and that obtained from simulated multiangle measurements with a virtual lidar (dots) under the condition that the signals from the incomplete overlap zone are not excluded. The overlap function is shown as the bold curve.

Figure 4.2. The same model optical-depth dependence as that in Figure 4. 1 (curve 1) and the optical-depth profiles obtained from the simulated multiangle measurements with a lidar when the remaining zero-line offset is not equal to zero. Curves 2 and 3 show the retrieved optical-depth profiles with estimated background levels of 201 and 199 bins, respectively, whereas the actual value is 200 bins.

Figure 4.3. Simulated signals obtained for the same atmospheric conditions as that in Figures 4.1 and 4.2 but now corrupted with noise and systematic shifts, ΔB = -1 bin.

Figure 4.4. Optical depth retrieved from the signals in Figure 4.3 (filled circles); the thin line is the same as curve 1 in Figure 4.2.

Figure 4.5. Experimental data points of the dependence of $y_j(h)$ on x_j for the altitude range interval from 300 to 320 m.

Figure 4.6. Same as in Figure 4.5 but for the altitude interval from 580 to 600 m.

Figure 4.7. Overlap functions, $q_j(r)$, calculated with a set of simulated signals. The signal noise level is approximately the same as that for signals in Figure 4.3, but there are no systematic shifts corrupting the signals.

Figure 4.8. Same as that presented in Figure 4.7 but here the functions $q_j(r)$ are obtained when the signals, measured in the slope directions 25^o and 30^o, are corrupted by a systematic offset ΔB = -1 bin.

Figure 4.9. Mean function $q_{eff}(r)$ (bold curve) and its upper and bottom uncertainty boundaries, as estimated by its standard deviation (thin curves), obtained with an incorrect length for the complete overlap zone. Here the assumed length is 200 m, whereas the actual is ~ 450 m. The simulated lidar signals are corrupted only by random noise, the offsets $\Delta B = 0$.

Figure 4.10. FSL lidar data from the 355 nm channel, measured on April 6, 2005, Sequence 2, r_{max}=7000 m. (a) Range corrected signals $P_j(h)[h/\sin(\varphi_j)]^2$ (upper plot), $y_j(h) = \ln [P(h)[h/\sin(\varphi_j)]^2]$ (middle plot), and the functions $y_j(h)$ after removal of "bad" data points according to the criteria (1) – (4) (lower plot); (b) Total optical depth, $\tau(0, h)$ and the molecular optical depth, $\tau_m(0, h)$ shown as the solid and dotted curves, respectively (upper plot), and the intercept $A^*(h)$ (lower plot).

Figure 4.11. FSL lidar data from the 355 nm channel, measured on April 6, 2005, Sequence 2. The data presents mean values obtained from the functions of interest, calculated with the set of different maximal ranges, particularly, r_{max} = 2000 m, 2500 m, 3000 m, … 7000 m. On the first three plots from the top, the mean functions of $\tau(0, h)$, $\tau_p(0, h)$, and $\exp[A^*(h)]$ are shown. The lower plot represents the relative STD for $\exp[A^*(h)]$.

Figure 4.12. Total optical depth, $\tau(0, h)$, and the functions $\exp[A^*(h)]$ obtained with the two lidars. Their standard deviations are shown by error bars. The exponent functions are normalized by factors 10^7 and $n*10^7$ for the JHU and FSL lidars, respectively as shown in each legend. The plots represent the sets of data obtained as following: 28 February, Sequence 1 (a), February 28, Sequence 3 (b), March 4, Sequence 2 (c), March 4, Sequence 3 (d), April 5, Sequence 1 (e), April 5, 2005, Sequence 2 (f), April 5, 2005, Sequence 3 (g), April 6, 2005, Sequence 1 (h), April 6, 2005, Sequence 2 (i), April 6, 2005, Sequence 3 (j), April 6, Sequence 4 (k).

Figure 4.13. Total optical depth, $\tau(0, h)$ (upper plot), and the function $\exp[A^*(h)]$ (middle plot) obtained with the JHU lidar at the 532 nm channel on April 5, Sequence 1. The bottom plot shows the relative STD for the exponential function.

Figure 4.14. Total optical depth, $\tau(0, h)$, and the function $\exp[A^*(h)]$ obtained with the FSL lidar at the 1064 nm channel on March 4, Sequence 3 (top and middle plots, respectively). The jumps around the heights of 200 m and 470 m are due to the local heterogeneities. The bottom plot shows the relative STD for the exponential function.

Figure 4.15. (a) The overlap function $q(r)$ for the FSL lidar for the 355 nm channel; (b) the same for the 1064 nm channel; (c) the same as (a) but for the JHU lidar; (d) the overlap function $q(r)$ for the JHU lidar for the 532 nm channel; (e) the same as (d) but for the 1064 nm channel.

Figure 4.16. RCS versus range for FSL lidar, April 6, sequence 2.

Figure 4.17. Example of the overlap functions obtained from data with an inaccurate background subtraction. The overlap functions are obtained from the FSL 355 nm data on April 6, Sequence 2, $r_{max} = 7000$ m. The upper plot shows the overlaps, $q_j(r)$, for the elevation angles; one can see the underestimated overlaps obtained for the data measured in the slope directions 68° and 80°. The lower plot shows the mean overlap and its uncertainty boundaries; the increased uncertainty can be seen in the area of the 68° and 80° slope directions.

Figure 4.18. Example of a local heterogeneity (cloud) as observed in the data taken with the FSL lidar at 355 nm on March 31. (a) Function $y_j(h)$ over the range selected for the inversion (upper plot); the local heterogeneity can be seen in the 18° slant path at $h = 1500$ m. The consequences of the inhomogeneity are seen in the shape of the optical depth $\tau(0, h)$ and the intercept $A^*(h)$ (middle and lower plots). The middle and lower plots show the effect of local heterogeneity at 1500 m where $\tau(0, h)$ reaches 1.33 whereas $A^*(h)$ reaches 27.5]. (b) Overlap functions versus height and versus range (upper and bottom plots, respectively). One can see the kink at 1500 m in the overlap $q_j(h)$.

Figure 4.19. Example of heterogeneity (smoke) as observed in the data taken with the FSL lidar, at 355 nm, on April 6, 2005, sequence 1. (a) Function $y_j(h)$ over the range selected for the inversion (upper plot); the local heterogeneity can be seen over the first hundred meters. The consequences of the inhomogeneity are seen in the shape of the optical depth $\tau(0, h)$ and the intercept $A^*(h)$ (middle and lower plots). (b) The overlap functions retrieved from these data versus height and versus range (the top and bottom plots, respectively).

Figure 4.20. 2D scan taken at elevation 6^o, over 50 azimuthal angles. Two different perspectives are shown in order to emphasize the distance on different Cartesian coordinates

Figure 4.21. Picture taken from the lidar location which shows the presence of the smoke (around 1 km away).

Figure 4.22. Original and smoothed particulate optical depth (upper plot) and particulate extinction coefficient computed "classically" (black curve) and with new method (red curve)

Figure 4.23. Particulate optical depth $\tau_p(0, h)$ [original (orig) and smoothed (sm)] and particulate extinction coefficient ["classical" method (sm) and new method (sm new)] obtained with the two lidars. The plots represent the sets of data obtained as following: 28 February, Sequence 2 (a), February 28, Sequence 3 (b), March 4, Sequence 2 (c), March 4, Sequence 3 (d), April 5, Sequence 1 (e), April 5, 2005,

Sequence 2 (f), April 5, 2005, Sequence 3 (g), April 6, 2005, Sequence 1 (h), April 6, 2005, Sequence 2 (i), April 6, 2005, Sequence 3 (j), April 6, Sequence 4 (k).

Figure 4.24. Synthetic signal $Z^{*}_{90}(h)$ and its extrapolation to ground level (black curve) by polynomial fit (third order) over a range up to 1km

Figure 4.25. (a) Synthetic signal $Z^{*}_{90}(h)$ (green curve) and the RCS/q for elevation 80° (blue curve); (b) extrapolation of the synthetic signal (black curve) and of the RCS/q for elevation 80° (red curve) by polynomial fit (third order) over range up to 1 km

Figure 4.26. (a) Original profiles of the aerosol extinction coefficient $\kappa_p(h)$ and backscatter coefficient $\beta_p(h)$; also shown molecular profiles; (b) original profiles of the total optical depth $\tau(0, h)$ and intercept $A^{*}(h)$; (c) the lidar overlap function; the complete overlap starts at 1 km

Figure 4.27. (a) Functions $y_j(h)$ and their selected range. The noise level has a STD of 0.05 bin corresponding to a SNR of 18 for the last signal bins. (b) Retrieved total optical depth and intercept and their relative errors with respect to the original data. (c) Retrieved lidar overlap and its relative error. (d) Extrapolation of the retrieved vertical synthetic signal $Z_{90}(h)$ to the ground level. Also shown $Pr^{2}_{90}(h)$, original $Z_{90}(h)$ and $Pr^{2}_{90}(h)/q(h)$. (e) Retrieved aerosol extinction and backscatter coefficient, LR and their relative errors with respect to the original data.

Figure 4.28. Same as 7.27 but for the noise level with a STD of 0.10 bin corresponding to a SNR of 9 for the last signal bins.

Figure 4.29. Same as 7.27 but for the noise level with a STD of 0.20 bin corresponding to a SNR of 4.5 for the last signal bins.

Figure A1.1. Unpolarized sunlight, with equal and independent fields E_{0x} and E_{0y} induce electric dipoles p_x and $p_{y;}$ the scattering path makes an angle θ with the z direction

Figure A1.2. Phase function for Rayleigh scattering (equation A1.31). The incident light comes from the left. The maximum scattering occurs in forward (0^o) and backward (180^o) directions

Figure A2.1 Decomposition of electric vector of incident and scattered waves

Figure A5.1. Schematic of multiangle measurements

Figure A6.1. Example background subtraction, FSL lidar, channel 355 nm, April 6, sequence 2, elevation 6^o; (b) is a zoom of (a)

Figure A6.2. Background linear fit and the 99.9 % confidence intervals; FSL lidar, channel 355 nm, April 6, sequence 2, elevation 6^o; (b) is a zoom of (a)

Figure A6.3. Lidar signal after background subtraction, FSL lidar, channel 355 nm, April 6, sequence 2, elevation 6°; (b) represents a zoom of (a)

Figure A6.4. Example of background subtraction in case of heterogeneity in the lidar signal, FSL lidar, channel 355 nm, April 6, sequence 2, elevation 58°; (b) is a zoom of (a)

Figure A6.5. Background linear fit and the 99.9 % confidence intervals, FSL lidar, channel 355 nm, April 6, sequence 2, elevation 58°

Figure A6.6. Lidar signal after background subtraction, FSL lidar, channel 355 nm, April 6, sequence 2, elevation 58°; (b) represents a zoom of (a)

Figure A7.1. Lidar signal $P(r)$ (upper plot), range corrected signal $P(r)r^2$ (middle plot) and logarithm of range corrected signal $\ln[P(r)r^2]$ (lower plot) versus range for FSL lidar, 355 channel, April 6, sequence 2, $r_{max} = 7000$ m.

Figure A7.2. Same as figure A7.1 but versus height

Figure A7.3. Selected range for $y_j(h)$ after the four criteria applied to eliminate the "bad" points, FSL lidar, 355 channel, April 6, sequence 2, $r_{max} = 7000$ m.

Figure A7.4. Examples of $y_j(x_j)$ regression for $h = 316.72$ m (a) and for $h = 3139$ m (b)

Figure A7.5. Total optical depth $\tau(0, h)$, molecular optical depth $\tau_m(0, h)$ and intercept $A^*(h)$ as determined for selected range of $y_j(h)$ (figure A7.3)

Figure A7.6. Individual overlaps versus height (upper plot) and versus range (lower plot)

Figure A7.7. Mean overlap versus range (black line), standard deviation (blue lines) and relative standard deviation (red).

Figure A7.8. Individual total optical depth $\tau(0, h)$ (upper plot), particulate optical depth (second plot), intercept $A^*(h)$ (third plot) and exponential of intercept $\exp[A^*(h)]$ corresponding to each r_{max} (from 2000 m to 7000 m).

Figure A7.9. Mean total optical depth $\tau(0, h)$, particulate optical depth $\tau_p(0, h)$, intercept $A^*(h)$ and exponent of intercept $\exp[A^*(h)]$ along with their STD (blue curves), relative STD (second and lower plots). The cyan curve on upper left plot represents the molecular optical depth $\tau_m(0, h)$

Figure A7.10. Individual overlaps (upper plot) and the mean overlap (lower plot). On both plots, the relative STD are shown. On the lower plot, STD is also shown (blue curves).

1. Introduction

1.1. Research context

Light absorption and scattering by aerosols plays an important role in the atmospheric radiation balance (*Houghton et al.*, 2001) and is an important factor in climatic calculations (*Charlson at al.*, 1992, *Hobbs,* 1993). Aerosols and clouds affect the Earth's radiation budget by interacting with solar visible radiation and terrestrial infrared radiation. They determine what fraction of the solar radiation incident at the top of the atmosphere reaches the earth's surface and what fraction of long wave radiation from the earth escapes to space. Aerosols have unique optical properties that determine the amount of radiation they absorb or reflect into the atmosphere. These properties are important in radiative transfer calculations since they provide information about radiation losses through the atmosphere.

To improve radiative transfer calculations, aerosol scattering and absorption properties, need to be specified. These can be calculated when the particle size distribution (PSD), their indices of refraction and shape, are known. In addition, chemical composition is needed to calculate the refractive index of aerosols particles. Note that most aerosols are non-absorbing in the visible range. The two main atmospheric absorbing species are black carbon (the main constituent of soot) and hematite (a black iron oxide) (*Horvath*, 1998). In Mie theory (*van de Hulst,* 1981; *Bohren and Huffman,* 1983), the particle shape is assumed to be spherical. However, atmospheric aerosol particles are neither spherical nor homogeneous and therefore remain a challenge in atmospheric aerosol modeling. Today, most aerosol applications rely on an optical model that treats aerosols as a mixture of spherical homogeneous particles of different sizes with a composition characterized by the complex refractive index. These assumptions typically allow models to reproduce adequately the observed aerosol affected radiation fields (*Dubovik et al.*, 2002). Recently, progress was made in modeling light scattering by nonspherical particles (e.g., *Mishchenko*, 2000; *Mishchenko et al.*, 2000). In principle, the nonsphericity can be determined by lidars that measure the depolarization ratio, i.e. the ratio between perpendicular and parallel-polarized light components (in media where multiple scattering depolarization is negligible).

To characterize temporal and spatial distribution of the aerosol optical characteristics of the atmosphere, for use in radiative transfer applications, lidar methods have proven useful (e.g., *Collis and Russell*, 1976; *Sassen et el.,* 1989; *Sassen et al.,* 1992; *Hoff et al*., 1996; *Marenco et al.,* 1997; *Upendra et al.*, 1998; *Welton et al*., 2002; *Pahlow et al.*, 2004). Elastic backscatter lidar is a powerful remote-sensing tool that produces 1-D to 3-D qualitative maps of the relative concentration and distribution of the aerosols over a region from which optical parameters can be determined. Since lidars provide data on both high spatial and temporal resolution, air motion can also be monitored since the concentration and spatial variability of aerosols can be used as a tracer (e.g., *Mayor and Eloranta*, 2001).

In some cases airborne measurements of the aerosols are available and direct characterization is feasible. For example, aircraft data taken during TARFOX experiments were used to retrieve the particle complex index of refraction using aircraft data (*Redemann et al.*, 2003). A complete set of experiments to determine the aerosol spatial distribution and optical properties were conducted in the framework of ACE (Aerosol Characterization Experiment). ACE-2 over the Atlantic Ocean for example, measured the particle size distribution, aerosol optical depth (AOD) (using a sun photometer), aerosol extinction coefficient (using a lidar) and scattering coefficient (using a nephelometer) (*Flamant et al.*, 2000).

One of the mean challenges for lidar in applications is the indeterminacy of the lidar equation. This significantly restricts practical applications of elastic lidars for atmospheric studies, especially in clear atmospheres. To perform the inversion of the elastically scattered signal in two-component (molecular and particulate) atmospheres, measured in one-directional mode, the only practical assumption is that the particulate backscatter-to-extinction ratio is independent along the searched direction. This is a problem, but what more of a shortcoming is, that the concrete numerical value of the backscatter-to-extinction ratio must somehow be selected. The method proposed by *Kano* (1968) and *Hamilton* (1969) for the inversion of data obtained with scanning lidar is the only method that makes it possible to obtain extinction profiles from elastically scattered signals without the assumption of a backscatter-to-extinction ratio invariant with height. In our analyses (chapter 4), it is assumed that the backscatter term in the lidar equation is invariant in horizontal layers, that is, the atmosphere is assumed to be stratified horizontally. The real atmosphere is generally not homogeneous in slope or in horizontal directions. However, in most cases the atmospheric horizontal heterogeneity is much less than the vertical or slope heterogeneity. Further more, aerosol fluctuations in horizontal directions are mostly random, whereas in the vertical directions, systematic changes generally prevail, so that no averaging here will be potentially helpful. Therefore, when selecting between the two existing assumptions for the elastic signal inversion, the assumption of the horizontal homogeneity seems to be more reasonable than the assumption of the vertical (or slope) homogeneity. Another advantage of the Kano-Hamilton multiangle method is that unlike one-directional methods, there is no need to select a concrete numerical value for the backscatter-to-extinction ratio; moreover, under certain conditions, the vertical profile of this quantity can be extracted from the multiangle lidar data.

1.2. Research presentation

Within the above mentioned research context, the present work presents applications of a backscatter elastic lidar to the atmospheric optical properties and the development of improved multiangle method.

Chapter II, section 2.1, provides a brief introduction to the atmospheric structure and properties. In the context of a ground based backscatter lidar applications, we emphases the properties of the troposphere and further of the Atmospheric Boundary Layer (ABL). In section 2.2, a short discussion of light interaction with matter within atmosphere is given. Molecules and particles interactions with light (Rayleigh and Mie theories, respectively) are presented. Section 2.3 is a short description of a backscatter elastic lidar. The Johns Hopkins University (JHU) lidar system, with the two configurations used during different measurements campaigns between 2001 and 2005 is presented. A short description is also given of the Fire Science Laboratory (FSL) lidar system, which was used in parallel with JHU lidar during Montana 2005 measurement campaign. Section 2.4 is dedicated to the lidar equation and its inversion techniques. The principal analytical solutions of the lidar equation for one directional measurements are provided as well as the principles of the multiangle method.

Within Chapter III, the main results obtained during Baltimore PM Supersite experiment (2001-2003) are shown. A near-end solution of the lidar equation was used to calculate the aerosol extinction coefficient. The near-end boundary condition as well as the backscatter to extinction ratio, needed to solve lidar equation was determined at ground level from supporting instruments at the experiment site. In addition, the aerosol scattering coefficients measured by a nephelometer and computed with Mie theory are analyzed and compared, and aerosol derived mass concentrations and aerosol mass scattering coefficients are calculated for the period presented. A comparison of near-end, far-end and optical depth solutions for the lidar equation is discussed. Also, uncertainties arising from estimation of the near-end boundary condition are considered.

Chapter IV presents the results using a modified and improved Kano-Hamilton multiangle method to determine vertical profiles of the aerosol optical properties (optical depth and relative backscatter coefficient) and the lidar overlap function. The measurements campaign took place during spring 2005 in Montana, in collaboration with the Fire Science Laboratory within Rocky Mountains Research Station, belonging to the US Department of Agriculture.

In the chapter V the conclusions are discussed.

2. Light propagation in atmosphere and lidar technique

2.1. Atmosphere structure and properties

2.1.1. Overview

The atmosphere is a relatively thin layer surrounding the Earth. Atmosphere composition, physical and chemical properties varies with altitude and these features allow us to divide it in few layers.

Figure 2.1 shows the stratification of the atmosphere. The mean temperature profile is plotted and temperature inversions along the profile delimitate the different layers.

The uppermost layer of the atmosphere, the exosphere, extends from approximately 400 km to 1000 km or more. There is no clear delimitation of the upper limit as well as of the boundary to thermosphere.

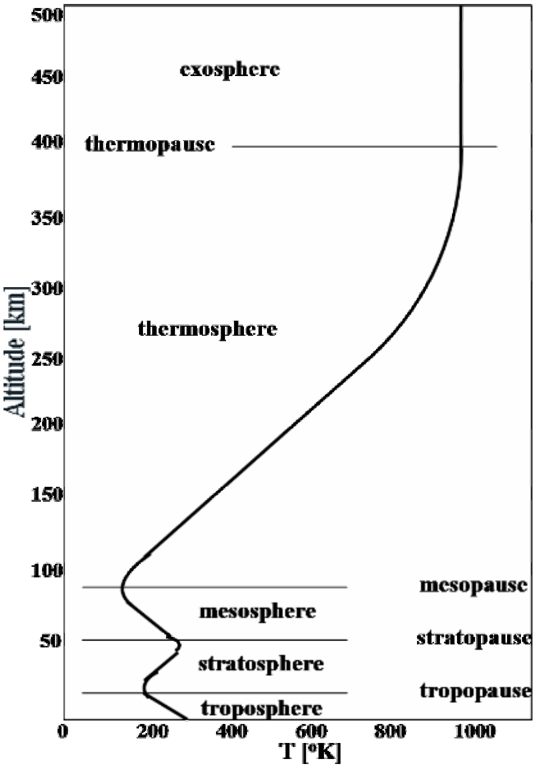

Figure 2.1 Atmosphere structure and mean temperature profile versus altitude

In this region, the particle concentration is very small, usually there is no collision between particles (they can travel great distances without hitting each other) and particles with high energy can escape to space. The temperature is around 1000 K. The thermosphere, covering the region from ~ 80 km to ~ 400 km (between mesosphere and exosphere) is a warm layer (due to N_2 and O_2 UV absorption from sun), where the molecular diffusion is the primary mixing mechanism. The mesosphere extends from ~ 50 km to ~ 80 km (between stratosphere and mesosphere) and here, the temperature decreases with altitude (little absorption of solar radiation), at mesopause the coldest temperature being reached. The ionosphere is the region from the upper mesosphere to lower thermosphere, where the ions are produced by photoionization. The stratosphere starts at 10 - 15 km and reaches 50 km (between the troposphere and the mesosphere). The temperature increases with altitude and vertical mixing is slow. It is a stratified, stable layer and contains the ozone layer (around 25 km). It is cooled by IR emission by trace gases. The main chemical components are the molecules but particles can be also found (for example particles from airplanes contrails, volcanic eruptions) and their residence time in stratosphere is long. The troposphere is the lowest layer of the atmosphere, extending from the earth's surface to 10 – 15 km (troposphere). The temperature decreases with altitude and there is a strong vertical mixing.

Note that between each layer there is an isothermal region, where the temperature inversion takes place. These regions (tropopause, stratopause, mesopause, thermopause) extend over few km to 10 km or more.

Figure 2.2 shows the global mean temperature, pressure, and mean air density as function of altitude (for the first 100 km), according to US Standard atmosphere (*NASA*, 1976). As a function of volume mixing ratio relative to the nitrogen molecule N_2, the atmosphere is well mixed over first 100 km, then it decreases with altitude as

T increases and p decreases (see for example *Goody and Young*, 1989, page 10), according to the equation of state for ideal gases:

$$pV = mRT = m\frac{R^*}{\mu}T \tag{2.1}$$

where p is the pressure, V is the volume, m is the mass, R is the specific gas constant, R^* is the universal gas constant, μ is the molar weight of the gas and T is the temperature. For a mixture of gases, according to Dalton's law:

$$pV = T\sum_i m_i R_i = m\overline{R}T \tag{2.2}$$

where $\overline{R}$ is the mean specific gas constant:

$$\overline{R} = \frac{\sum_i m_i R_i}{m} \tag{2.3}$$

and the mean molar weight is defined as:

$$\overline{M} = \frac{m}{n} \tag{2.4}$$

and n is the molar abundance.

The pressure variation with altitude is derived from the equation of state for ideal gases and the hydrostatic equation:

$$p(z) = p_s e^{-\int_{z_s}^{z} \frac{g}{RT(z')}dz'} \tag{2.5}$$

where p_s is surface pressure and g gravitational acceleration.

The main components of the atmosphere (gaseous compounds), their vertical distribution and their controlling processes are presented in Table 2.1 (after *Salby*, 1996). The atmosphere is primarily composed of Nitrogen (N_2, 78 % by volume), Oxygen (O_2, 21 % by volume), and Argon (Ar, 1 % by volume). The other components, although in small amounts play an important role in the energy balance of the earth through the radiative processes (e.g. H_2O, O_3, CO_2, which are greenhouse gases). CO_2 is tied to human activities and it became a concern for the greenhouse effect. Water vapor and ozone are highly variable, being continuously produced in some areas and destroyed in others. While ozone has a beneficial role in the stratosphere (buffer for UV radiation) it is a toxic pollutant (health, agriculture etc) and a green house gas in troposphere.

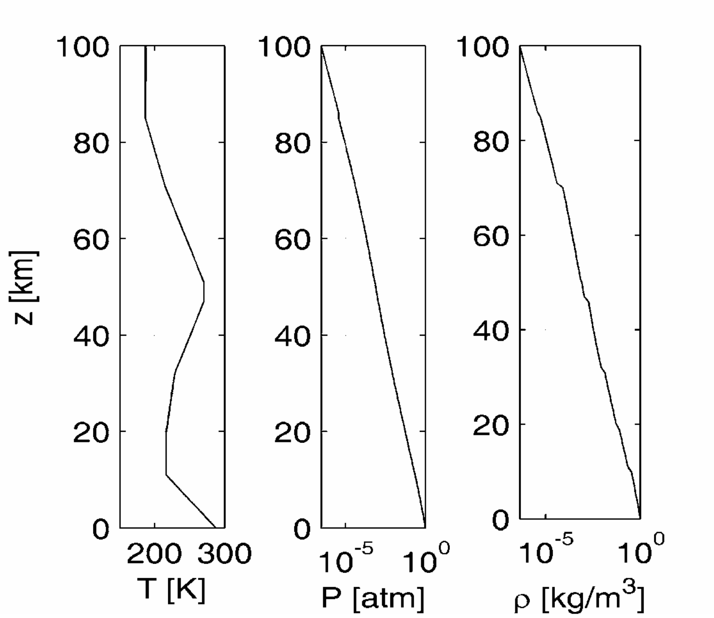

Figure 2.2. Global mean temperature (left plot), pressure (middle plot), and mean air density (right plot) according to US Standard Atmosphere 1976

O_3 is a secondary pollutant [driven by NO_x and VOCs (volatile organic compounds) by photochemistry] and it is the primary ingredient of photochemical smog (air pollution associated with sunlight driven chemical reactions). The main tropospheric sources of the ozone are stratospheric ozone, industrial emissions and biomass burning.

Other important trace gases are methane CH_4, naturally produced and chlorofluorocarbons (CFCs) as anthropogenic source. CH_4 is considered also a greenhouse gas but its effect is smaller compared with that of CO_2.

Constituent	Tropospheric mixing ratio	Vertical distribution (mixing ratio)	Controlling processes
N_2	0.7808	Homogeneous	Vertical mixing
O_2	0.2095	Homogeneous	Vertical mixing
H_2O^*	≤0.030	Decreases sharply in TP; Increases in ST; highly variable	Evaporation, condensation, Transport; production by CH_4, oxidation
Ar	0.0093	Homogeneous	Vertical mixing
CO_2^*	345 ppmv	Homogeneous	Vertical mixing; production by Surface and anthropogenic processes
O_3^*	10 ppmv	Increases sharply in ST; highly variable	Photochemical production in ST; destruction at surface transport
CH_4^*	1.6 ppmv	Homogeneous in TP; decreases in middle atmosphere	Production by surface processes; oxidation produces H_2O
N_2O^*	350 ppbv	Homogeneous in TP; decreases in middle atmosphere	Production by surface and anthropogenic processes; dissociation in middle atmosphere; produces NO transport
CO^*	70 ppbv	Decreases in TP; increases in ST	Production anthropogenically and by oxidation of CH_4 transport
NO	0.1 ppbv**	Increases vertically	Production by dissociation of N_2O catalytic destruction of O_3
CFC-11* CFC-12*	0.2 ppbv 0.3 ppbv	Homogeneous in TP; decreases in ST	Industrial production; mixing in TP; photodissociation in ST

* radiatively active ** stratospheric value

Table 2.1. Atmospheric composition. Components are listed by mixing ratios representative in troposphere (TP) or stratosphere (ST), their vertical distribution and controlling processes

CFCs are insoluble, well mixed in troposphere and have a long time residence. Nitrous oxide N_2O and nitric oxide NO are relevant for the photochemistry of ozone O_3. Relative to N_2 (which is the main constituent of the air), the volume mixing ratio for CO_2, O_2, Ar is constant over first 100 km. Other components are variable over first 100 km above the earth's surface.

2.1.2. Troposphere

In the troposphere, nearly all the weather processes takes place. Pressure and density decreases rapidly with altitude and the temperature decreases in average with a lapse rate of 6.5 ^{o}C/km. It is a well mixed layer and the rapid mixing implies weather changes. The precipitation removes particles and different gaseous compounds from atmosphere. The volume mixing ratio of the main compounds of the air, except water vapor, is pretty much constant over the troposphere. The troposphere can be divided into atmospheric boundary layer (ABL) which is also called planetary boundary layer (PBL) and the free troposphere (FT). In the FT, the kinetic energy is concentrated at periods longer than a day, where it is associated with large-scale disturbances and seasonal variations and remains over large periods of time (e.g. *Salby*, 1996). The warming and cooling of the earth due to the response to the radiation (absorption of short wavelength radiation and emission of long wavelength radiation) forces changes in ABL via transport processes.

2.1.3. Atmospheric Boundary layer

The ABL is the region where most of the humans live such that its changes and variability affect us directly. The ABL is the source of almost all of the energy, water vapor and trace constituents, which are transported higher into atmosphere. It is the layer that directly reflects close interactions with the earth's surface. The boundary layer responds to surface forcing with a time scale of about an hour or less (*Stull,* 1988). The ABL is the layer in which the effects of the surface (friction, heating and cooling) are felt directly on time scales less than a day and in which significant fluxes of momentum, heat or matter are carried by turbulent motions on a scale of the order of the depth of ABL or less (see *Stull,* 1988 and *Garratt,* 1992, for detailed discussions). The ABL height varies diurnally being related primarily with solar activity. During day, the ABL (mixing layer height) reaches 1 – 3 km, depending on time of the year and geographical location. In the ABL, large eddies are mainly generated mechanically by strong shear (due to the frictional drag with the surface) and thermally by buoyancy (thermals). Turbulent mixing transfers heat and moisture between the surface and atmosphere.

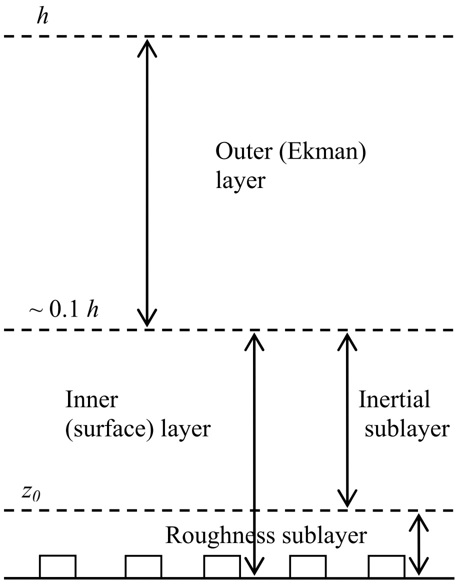

Figure 2.3. ABL structure for aerodynamically rough flow in neutrally-stratified conditions

The ABL is usually broken (Figure 2.3) into an inner or surface layer, which contains the roughness sublayer, in the vicinity of objects (e.g. trees, buildings) and where the molecular diffusion transport dominates the turbulent transport and outer sublayer (Ekman layer). The surface layer comprises the lower 10 - 20 % of the ABL and it is dominated by land surface, while the outer layer reflects the entrainment of "free-atmosphere".

During the diurnal cycle (see Figure 2.4), a number of different layers can be defined, including the surface layer, convective mixed layer, residual layer, stable (nocturnal) boundary layer, an entrainment zone and a capping inversion zone.

The mixed layer is typically convectively driven. The sources of convection are the heat transfer from a warm ground surface (rising thermals of warm air) and radiative cooling for cloud topped ABL. Wind shear across the top of mixed layer (ML) contributes to turbulence generation.

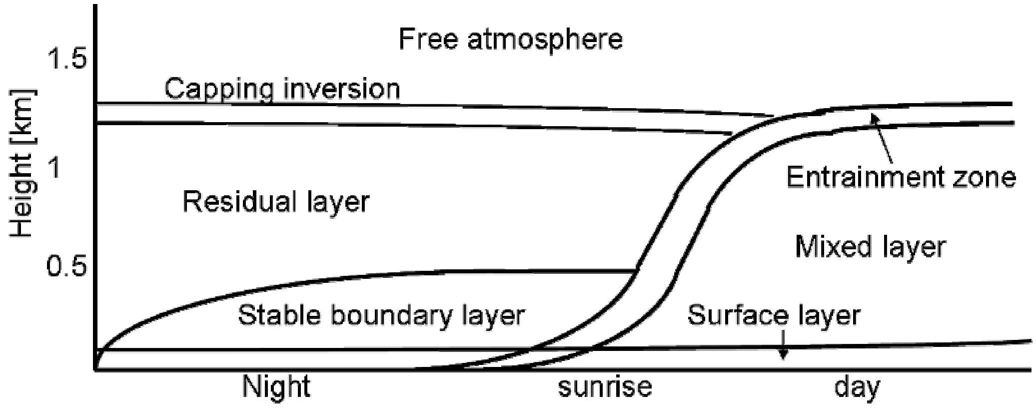

Figure 2.4. The ABL in high pressure regions over land consists in three major parts: a turbulent mixed layer, a less turbulent residual layer containing the former mixed layer air and a nocturnal stable BL of sporadic turbulence

The ML grows by entrainment of the air from above in entrainment zone (inversion layer). The remaining layer after decay of solar heating (sunset), when turbulence decays, is called the residual layer (RL). It contains many of the characteristics of the former ML. The stable boundary layer is the nocturnal boundary layer, where the air is statically stable (suppressing the turbulence).

2.1.3.1. Unstable boundary layer

The typical evolution of the ABL during day is presented in Figure 2.5, as observed with JHU backscatter lidar (1064 nm channel). After sunrise, the earth surface starts to warm and thermals arise and a turbulent ML starts to develop, reaching its maximum in the afternoon (in Figure 2.5 the maximum heights reached around 2 pm). As said before, it grows by entraining of the relatively cool air from the RL or the FT. The turbulence works to mix heat, moisture and momentum in the vertical. After sunset, ML decreases and a new RL is formed. In Figure 2.6 are shown the profiles of main characteristics as virtual potential temperature, mean wind, water vapor mixing ratio and pollutant concentration. The main characteristic for all of them is the sharp increase or decrease in the top of ABL.

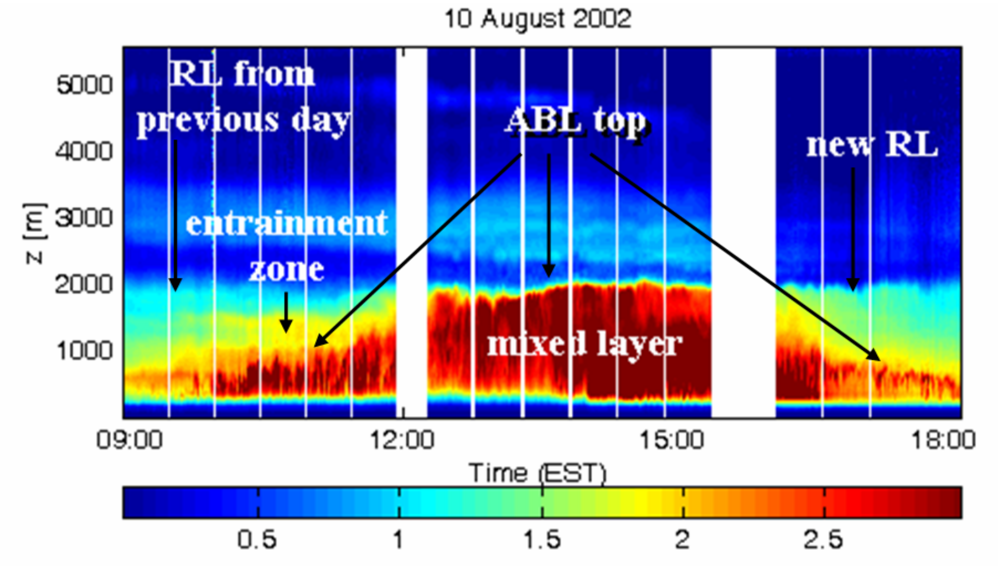

Figure 2.5. ABL evolution during the day (August 10, 2002, Baltimore), as revealed by JHU backscatter lidar. The main structures, which can be seen, are: ABL top, old and new RL, ML, entrainment zone. The color scale corresponds with the strength of the backscatter signal (a.u.), which is proportional with the number density of molecules and particles. The red correspond to strong signal and blue to weak signal.

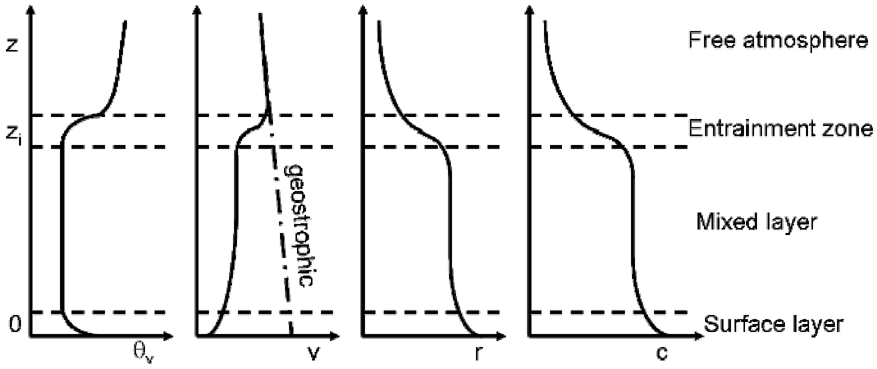

Figure 2.6. Typical daytime profiles of mean virtual potential temperature θ_v, wind speed *v*, water vapor mixing ratio *r* and pollutant concentration *c*

Virtual potential temperature is nearly adiabatic in the middle portion of ML, where mean wind, water vapor mixing ratio and pollutant concentration are almost constant (due to the uniform mixing).

2.1.4. Aerosols within the troposphere

In addition to clouds, aerosols play an important role in the atmospheric radiative transfer and further in climate change (see for example: *Hobbs and McCormick*, 1988, *Hobbs*, 1993, Horvarth, 1998). The solar radiation is scattered and absorbed by aerosols and consequently the optical depth of the atmosphere increases which means a smaller transmission of the atmosphere (and an atmospheric temperature increase). The aerosol size, distribution, composition is widely variable and depend on their different sources. The first distinction of aerosols is made between continental and maritime sources. Marine aerosols are primarily composed of sea salt, their concentration is small compared with continental aerosols and their density drops sharply above boundary layer. Primary aerosols are emitted directly as particles and secondary aerosols are formed in the atmosphere by gas to particle conversion processes. Aerosol diameters (*d*) range between nanometers to tens of micrometers. Particles smaller than 1 μm diameter have concentrations in the range from ten to several thousand per cm^3. Those larger than 1 μm diameter have usually concentrations less than 1 cm^{-3} (see *Seinfeld and Pandis*, 1998). Aerosols are removed from atmosphere by dry or wet deposition. As a function of the aerosol size, aerosols are classified into three modes: nucleation ($d < 0.1$ μm), accumulation ($0.1 < d < 1$ μm) and coarse ($d > 1$ μm). The aerosol size distribution has been fitted with various distributions, such as power low, gamma and log-normal distributions (see *Jaenicke*, 1998). For more details in atmosphere chemistry, see *Warneck* (1999).

2.1.4.1. Continental aerosols

Continental aerosols have wider variability in size and composition depending on the large number of sources. The principal aerosol compounds are sulfates, nitrates, ammonium, sodium, chloride, carbonaceous material [organic (OC) and elemental carbon (EC)], minerals and water. The main sources are erosion of the soil (minerals), combustion (carbonaceous) from industrialized regions, biomass burning (CO_2, CO, NO_x, CH_4, EC, and OC) and agriculture (nitrates, sulfates). By coagulation, individual nuclei can form larger particles (accumulation particles). The hydrophilic particles can absorb water in conditions of high relative humidity and become hygroscopic so that their optical and chemical properties change.

The typical size distribution is bimodal with a strong peak in the submicron region and a secondary, much smaller peak around 1 – 2 μm. The highest aerosol density exists within the ABL (3 – 10 times greater than in the FT) as can be seen in Figure 2.5. Different size ranges are associated with certain kind of particles even there are cases when a specific aerosol is present in all ranges (e.g. SO_4). For more details, see for example *Claes at al*. (1998).

2.2. Light propagation in atmosphere

2.2.1. Overview

According to Beer-Lambert-Bouguer's low, a collimated monochromatic beam of wavelength λ with radiant flux (radiant energy per unit time) $F_\lambda(r)$ which passes through a heterogeneous medium of length dr, will be attenuated by dF_λ. The differential element dF_λ is proportional with incident flux F_λ, element dr and a proportionality coefficient $\kappa_{t,\lambda}(r)$ such that:

$$dF_\lambda = -\kappa_{t,\lambda}(r) F_\lambda(r) dr \tag{2.6}$$

where $\kappa_{t,\lambda}(r)$ is the total extinction coefficient and is the probability per unit length of removing a photon from the beam (scattered or absorbed); it is equal with sum of molecules [$\kappa_{m,\lambda}(r)$] and particles [$\kappa_{p,\lambda}(r)$] extinction coefficients; the radiant flux F_λ is defined the rate of which the radiant energy passes a certain location per unit time and has units of J/s or W,

$$\kappa_{t,\lambda}(r) = \kappa_{m,\lambda}(r) + \kappa_{p,\lambda}(r) \tag{2.7}$$

Integrating equation (2.6) we obtain the relation for the attenuated beam:

$$F_\lambda = F_{0,\lambda} e^{-\int_0^L \kappa_{t,\lambda}(r) dr} \tag{2.8}$$

through a medium of length L; the transmittance $T(L)$ of the layer of length L is defined as the ratio of outcoming flux F_λ to the incoming flux $F_{0,\lambda}$

$$T(L) = \frac{F_\lambda}{F_{0,\lambda}} = e^{-\int_0^L \kappa_{t,\lambda}(r) dr} \tag{2.9}$$

Within this context, the optical depth of the layer of length L is defined as:

$$\tau = \int_0^L \kappa_{t,\lambda}(r)dr \qquad (2.10)$$

Further on we omit subscript λ since we only focus on discussions about monochromatic light. The extinction (attenuation) coefficient κ is the sum of the scattering coefficient σ and the absorption coefficient α by both molecules and aerosols (particles). For n_p particles of the same size, the extinction coefficient is:

$$\kappa_{t,\lambda} = n_p Q_{ext} A \qquad (2.11)$$

where A is the geometric cross section area of one particle and Q_{ext} is the extinction efficiency (which has an analytical expression for molecules and spherical particles, derived from Mie theory). Extinction efficiency is defined as the ratio of the total energy flux extinguished by a particle to the total energy flux incident on the particle.

Both scattering and absorption coefficients are expressed by so called index of refraction (which depends on wavelength):

$$m = n - \mathrm{i}k \qquad (2.12)$$

The real part of index of refraction n is related with the scattering phenomena (which determine the speed of light through different media, others than vacuum) while the imaginary part k is related with absorption phenomena. Index of refraction m is equal with square root of relative permittivity ε_r.

The irradiance (radiant flux per unit projected area, in W/m^2) of light entering a receiver obeys Allard's law, which tells us that the light intensity decreases along the range r as $1/r^2$:

$$E(r) = \frac{IT}{r^2} = \frac{I}{r^2} e^{-\int_0^r \kappa_t(r')dr'} \qquad (2.13)$$

where $E(r)$ is the irradiance, and I is the radiant flux (power) of light energy source (W).

The interaction of electromagnetic radiation (light) with molecules and particles (aerosol) is described in the context of relationship between the size (or diameter) of the molecules and particles and the wavelength of the radiation. Different mechanisms are involved when light interacts with molecules and particles. Molecules are of order of Ångstroms, much smaller than the wavelength of light, while particles are comparable sizes to wavelength of light (on order of nanometers to microns). Because our discussion is focused on interaction of electromagnetic radiation with molecules and particles at wavelengths of 355 nm, 532 nm and 1064 nm (our lidar channels), no treatment of radiation absorption by molecules is discussed since such phenomena are negligible at these wavelengths. The scattering of light by molecules is described using Rayleigh theory. The interaction of light with particles (scattering and absorption) is given by Mie theory. The detailed description of these two theories is given in *van de Hulst* (1957) and *Bohren and Huffman* (1983).

2.2.2. Light scattering by molecules (Rayleigh theory)

Since molecules are much smaller than the radiation wavelength they can act as point scatterers and as oscillating dipoles (Rayleigh scattering regime). The efficiency to scatter light is found analytically to be in the case of spherical molecules:

$$Q_{sca} = Q_{ext} = \frac{8}{3}\left(\frac{\pi d}{\lambda}\right)^4 \left(\frac{m^2-1}{m^2+2}\right)^2 \qquad (2.14)$$

where Q_{sca} is the scattering efficiency. The ratio $\pi d/\lambda$ is called the size parameter, m is index of refraction, d the diameter of the molecule and λ the wavelength. In the limits of $m \cong 1$, it becomes:

$$Q_{sca} = Q_{ext} = \frac{32}{27}\left(\frac{\pi d}{\lambda}\right)^4 (m-1)^2 \qquad (2.15)$$

The scattering coefficient due to n_m spherical molecules will be

$$\sigma_m = n_m \pi r^2 Q_{ext} \tag{2.16}$$

$$\sigma_m = n_m \pi r^2 Q_{ext} = \frac{32\pi^3 (m-1)^2}{3\lambda^4} \frac{KT}{P} \frac{6+3\delta}{6-7\delta} \tag{2.17}$$

where K is the Boltzmann's constant, T is the temperature and P is the pressure; δ is a correction factor (depolarization factor) which accounts for the anisotropy of the molecules. The details of these derivations as well as the pressure and temperature dependence of the refractive index are given in Appendix I.

The molecular scattering is proportional to λ^{-4}, so the light at short wavelengths (e.g. blue) will scatter better than light at long wavelengths (e.g. red); thus, the molecular scattering is efficient in UV region and is negligible in IR region and the molecular phase function is symmetric (has $3/8\pi$ at 0^o and 180^o).

2.2.3. Light scattering by particles (Mie theory)

The assumptions made in Mie theory are: the particle is a sphere; the particle is homogeneous such that it can be characterized by a single index of refraction for a given wavelength. In the case of a particles mixture, an average index of refraction is specified. The Mie theory uses the relative index of refraction, which is the ratio of particle index of refraction to the air index of refraction. As air index of refraction is about 1, the relative index of refraction is about the same as the particle index of refraction. Mie theory is used to calculate the scattered electromagnetic field at all points in the particle (internal field) and at all points in the homogeneous medium in which the particle is embedded. For all applications in the atmosphere, light scattering observations are carried in the far-field of the particle so that the solutions of the Maxwell equations for the electromagnetic field have the specific form of the far-field zone. The efficiencies of the particles are calculated for scattering (Q_{sca}), backscattering (Q_{back}), extinction (Q_{ext}) and absorption (Q_{abs}) of electromagnetic radiation.

The relationships for extinction, scattering, backscattering and absorption efficiencies (which are functions of r, λ and m) respectively, are:

$$Q_{ext} = \frac{2}{x^2} \sum_{n=1}^{\infty} (2n+1) \mathrm{Re}(a_n + b_n) \tag{2.18}$$

$$Q_{sca} = \frac{2}{x^2} \sum_{n=1}^{\infty} (2n+1) \left\{ |a_n|^2 + |b_n|^2 \right\} \tag{2.19}$$

$$Q_{back} = \frac{1}{x^2} \left| \sum_{n=1}^{\infty} (2n+1)(-1)^n (a_n + b_n) \right|^2 \tag{2.20}$$

$$Q_{abs} = Q_{ext} - Q_{sca} \tag{2.21}$$

where a_n and b_n are coefficients of the amplitude functions of the scattered waves, x is the ratio $2\pi r/\lambda$ (size parameter) and r is the particle radius; more details about efficiencies can be found in Appendix II.

Once the efficiencies are calculated, the extinction (κ), scattering (σ), backscattering (β) and absorption (α) coefficients are computed as:

$$\begin{aligned} \kappa &= n_p \pi r^2 Q_{ext} \\ \sigma &= n_p \pi r^2 Q_{sca} \\ \beta &= n_p \pi r^2 Q_{back} \\ \alpha &= n_p \pi r^2 Q_{abs} \end{aligned} \tag{2.22}$$

where n_p is the number of particles. If the particles have different radii within a radii range [r_1, r_2], then the relations become:

$$\begin{aligned}
\kappa &= \int_{r_1}^{r_2} n_p(r)\pi r^2 Q_{ext}(r,\lambda,m)dr \\
\sigma &= \int_{r_1}^{r_2} n_p(r)\pi r^2 Q_{sca}(r,\lambda,m)dr \\
\beta &= \int_{r_1}^{r_2} n_p(r)\pi r^2 Q_{back}(r,\lambda,m)dr \\
\alpha &= \int_{r_1}^{r_2} n_p(r)\pi r^2 Q_{abs}(r,\lambda,m)dr
\end{aligned} \tag{2.23}$$

For a mixture of particles, with different indices of refraction, different methods are used to determine an average refractive index. One of the most popular formulas is that of volume weighted method (e.g. *Ouimette and Flagan,* 1982; *Hasan and Dzubay*, 1983):

$$\overline{m} = \sum_j m_j f_j \tag{2.24}$$

where m_j and f_j are individual refractive index and volume fraction. The volume fraction f_j is

$$f_j = \frac{V_j}{V} = \frac{m_j \overline{\rho}}{\rho_j m} = X_j \frac{\overline{\rho}}{\rho_j} \tag{2.25}$$

where X_j is the mass fraction, m_j and ρ_j are the individual mass and density, and $\overline{\rho}$ is the mean density, defined as:

$$\overline{\rho} = \sum_j \frac{X_j}{\rho_j} \tag{2.26}$$

2.3. Lidar system

2.3.1. Overview of a backscatter elastic lidar

A lidar system is an active remote sensing system, which uses a laser as an artificial source of energy. Passive remote sensing systems use natural sources of energy (as the sun, moon or stellar light). Mainly, the two components of a lidar system are the transmitter and the receiver. The transmitter is a laser which sends a beam (intense, collimated, monochromatic, short light pulses) at one or more wavelengths into atmosphere. The beam is scattered and absorbed by molecules and particles. The backscatter signal is recorded with a receiver. The receiver itself consists of a telescope, which collects the backscattered signal and focuses it on the photodetector. The photodetector measures the amount of backscattered light and transforms it to an electrical signal. Figure 2.7 shows a schematic representation of the main parts of a lidar system. Additional parts include the computer/recording system (which contains a digitizer for analog to digital conversion of the signal and records it as a function of distance from the lidar and a computer for data acquisition), power supply and cooling system for the laser.

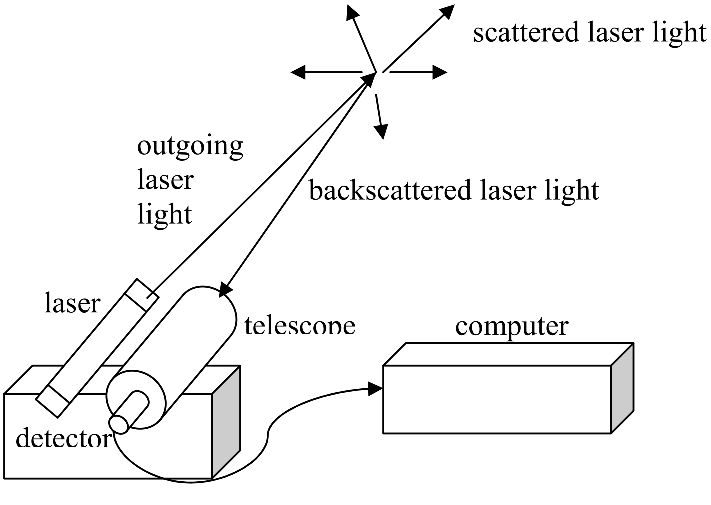

Figure 2.7. Schematic representation of the major parts of a lidar system

A backscatter elastic lidar records signals at the outgoing laser wavelengths (elastic scattering). Usually, a laser has a fundamental frequency (fundamental harmonic) and few higher order harmonics. Using a few crystals within the laser, the fundamental harmonic can be doubled, tripled or quadrupled, thus obtaining the second, third and forth harmonics. For each outgoing frequency, a photodetector is needed. There are two different systems to record the backscattered signal: analog (current mode) and photocounting (photon counting mode). The analog mode uses direct, high speed digitization of the signal from photodetector. The use of a current mode maximizes the near-field spatial resolution (and it is useful in ABL observations) but minimizes the far-field, as the signal decreases with range squared and the signal to noise ratio (SNR) decreases. On the other hand, the photon counting mode is required for long range soundings (troposphere or stratosphere). The returning photons are recorded over long periods of time compared with analog mode periods. For more details, see for example *Kovalev and Eichinger* (2004). The common photodetectors used for acquiring light in UV, VIS and NIR are: avalanche photodiode (APD) for near infrared (NIR) (1064 nm) and sometimes for visible (VIS) (532 nm) and photo multiplier tube (PMT) for VIS (532 nm) and ultraviolet (UV) (355 nm). An APD is a p-n junction photodetector (a common material is silicon Si). The optical input is multiplied (avalanche multiplication) such that the electric output is 10 - 50 times larger. A PMT is a kind of vacuum tube, which transforms light into electrical signal by photoelectric effect. See for more details, *Measures* (1980), *Zuev* (1982), *Kovalev and Eichinger* (2004). A lidar system can have a biaxial or coaxial configuration. In the case of the biaxial configuration, the transmitter and the receiver are spaced at some distance. In the coaxial configuration, the transmitter and receiver axis coincides. For the last one, the zone of the incomplete overlap begins earlier, i.e. it is closer to the system.

2.3.2. JHU lidar system, biaxial configuration

The JHU lidar system was built in collaboration with Professor William Eichinger from University of Iowa. See more details in *Pahlow* (2002). It was primarily designed for ABL studies. It is a mobile, compact and light lidar system, which allows us to deploy it fast in various locations.

The JHU lidar system, biaxial configuration, consists of a Q - switched Nd-YAG laser (BigSkyLaser, model CFR 400) operated at 1.064 μm (maximum repetition rate 30 Hz, maximum output 324 mJ/pulse, 10 ns pulse duration, 1.8 mrad divergence), a Cassegrain telescope (Meade LX 50, f/10, diameter 25.4 cm, 5 mrad divergence), a periscope, a photodetector (IR-enhanced Si APD), laser power supply and cooling system, rotary table and a computer for data acquisition. The higher spatial resolution was 1.875 m (corresponding to 12.5 ns detector sampling duration). The zone of incomplete overlap in the case of this biaxial configuration is estimated to be ~ 300 m. The output laser pulses are sent parallel with the axis of the telescope axis at 45 cm apart by means of a periscope (41 cm long) which has two mirrors inside to deflect the beam. The mirrors are adjustable and the realignment is done whenever is necessary. Figure 2.8 presents the JHU lidar system in its biaxial configuration. The main characteristics of the biaxial configuration lidar are synthesized in Table 2.2.

laser	Q-switched Nd-YAG with 320 mJ/pulse at 1064nm (additional wavelengths: 532 nm and 355 nm); 30 Hz repetition rate; ~10ns pulse; 1.8 mrad beam divergence; BigSky laser model CFR 400
telescope	25.4 cm (10 in) diameter, Cassegrain f/10, 5mrad FOV (Meade LX50)
detector	IR-enhanced Si avalanche photodiode (APD Analog Modules)
digitizer	12-bit 100MHz, dual channel (Signatec PDA12)
maximum range resolution	1.5 m (3.75 m was used in our measurements)
time resolution used	5 s (corresponding to 150 shots averaged at 30 Hz)
scanning system	Azimuthally 0-180, Elevation 0-90 (AT6400 controller)
data acquisition	Pentium 133 MHz laptop; 2GB HD

Table 2.2. JHU lidar system, biaxial configuration. Principal characteristics

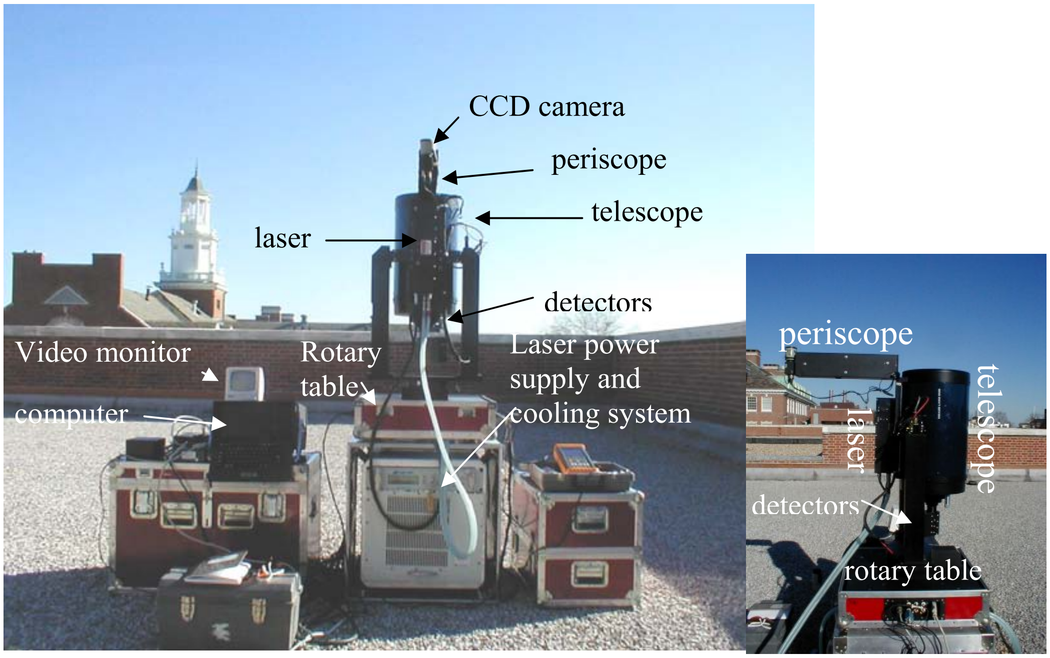

Figure 2.8. JHU lidar system, biaxial configuration. The main components: laser, telescope, periscope, detectors, laser power supply and cooling system, rotary table, computer

2.3.3. JHU lidar system, coaxial configuration

Some improvements were done to the JHU lidar system in collaboration with the lidar team (lead by Valentin Simeonov) from the Swiss Federal Institute of Technology (Ecole Polytechnique Fédérale de Lausanne - EPFL) at Lausanne, Switzerland. The biaxial configuration was changed to a coaxial one.

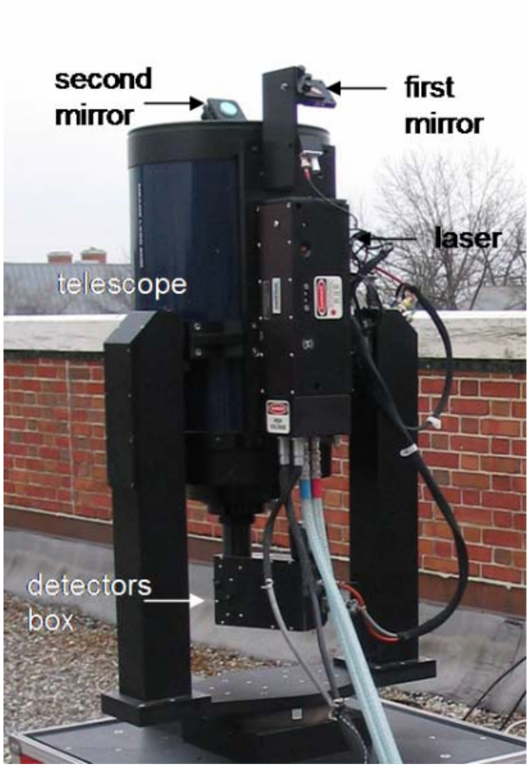

Figure 2.9. Details of JHU lidar system, coaxial configuration. The main components: laser, telescope, detectors box, first and second mirror

The laser beam is deflected by two mirrors such that it is sent from the middle of the telescope, coaxial with telescope axis. Figure 2.9 shows a detail of the lidar system with the new configuration. An important upgrade was made with regard to the other two wavelengths available from the laser (532 nm and 355 nm). The old and improper APDs used for collecting 532 nm and 355 nm were replaced by two PMTs (Hamamatsu). The software was changed, improved and configured to acquire three wavelengths simultaneously in either TD (time domain), 2D or 3D option. The maximum energy per pulse at λ = 532 nm is ~ 200 mJ whereas at λ = 355 nm it is ~ 100 mJ. Due to high amount of data in the case of three wavelengths recording option and lower processor speed on the quite old computer, the optimal frequency for laser is 15 Hz. For higher frequencies, the computer is not able to record all the data provided by the digitizers.

2.3.4. FSL lidar system, biaxial configuration

The outgoing laser beam is deflected by the periscope (41 cm long) to 45 cm away from the telescope axis. The FSL lidar is operative at 355 nm and 1064 nm. The 1064 nm backscatter signal is recorded by means of an IR-enhanced Si APD whereas the 532 nm backscatter signal is recorded with a PMT (Figure 2.10).

Figure 2.10. FSL biaxial (left) and JHU coaxial (right) lidar systems

The FSL lidar system has the same scanning capability as JHU lidar. It was also built by Professor William Eichinger. The JHU lidar in coaxial configuration and FSL lidar have the highest spatial resolution of 1.5 m. The differences between the systems, apart from their configuration and number of operating channels are laser energy per pulse and the different optical configurations at the receiver.

2.4. Lidar equation and inversion methods

2.4.1. Lidar equation

The lidar equation can be written as

$$P(r) = \frac{C}{r^2}\beta(r)e^{-2\int_0^r \kappa(r')dr'} \qquad (2.27)$$

where *P(r)* is the received backscattered energy by the photoreceiver [J] as a function of range *r*; C is the lidar constant (C ~ $\xi A_t c t_d q P_0$) which accounts for effective area of the receiving telescope A_t [m^2], speed of light *c* [ms^{-1}], detector sampling duration t_d [s], lidar overlap function *q*, outgoing laser energy per pulse P_0 [J], receiver's spectral transmission (accounts for lenses, filters, mirrors) and photodetector quantum efficiency ξ; β(*r*) is the backscatter coefficient [m^{-1}sr^{-1}] and κ(*r*) is the extinction coefficient [m^{-1}] for two atmospheric components (molecular and particulate). See details of the lidar equation derivation in Appendix III.

A more complete expression of the lidar equation has two additional terms that account for the multiple scattering (MS) and for background signal. In the present work, the background signal has been subtracted from the total received energy and we assume that MS does not occur. *Ackermann et al.* (1999) studied numerically the influence of MS on the retrieval of the extinction coefficient of tropospheric aerosols. In their simulations the extinction coefficient was assumed to be a constant within the ABL (the values chosen were 15.65, 3.91, 1.96, 0.783 and 0.078 km^{-1}) and with an exponential decay above the ABL. They found that the contribution of MS on the lidar signal in such situations is typically less than 10 % and never exceeds 20 %. Note, the relative error of the MS on the retrieved aerosol extinction profile in the atmospheric boundary layer (ABL) is found to be less than 3 % for all aerosols types, including urban environments. Thus, in the lidar equation, we have one equation and three unknowns, C, $\beta(r)$ and $\kappa(r)$. There are several approaches to solve the underdetermined lidar equation, which take into account additional information from either supporting instruments or theoretical estimates. Additional measurements of the aerosols may include determination of the reference values of the extinction coefficient, optical depth, PSD, etc. (see, *Klett*, 1985*; Weinman,* 1988; *Hoff et al.,* 1996; *Redemann et al.,* 1996; *Marenco et al.,* 1997; *Flamant,* 2000; *Barnaba et Gobbi,* 2001; *Gobbi et al.,* 2002; *Gobbi et al.,* 2003; *Kovalev*, 2003).

When determining the extinction coefficient in a two-component atmosphere, it is generally assumed that molecular backscattering and extinction coefficients are known (e.g. computed from the Standard Atmosphere 1976 (*NASA*, 1976) or in-situ measurements, such as from meteorological balloons).

2.4.2. Analytical solutions for lidar equation

Based on a variety of studies (*Fernald,* 1984; *Klett,* 1985; *Weinman,* 1988; *Sassen,* 1989; *Kovalev and Moosmüller*, 1994; *Flamant,* 2000; *Gobbi et al.,* 2002; *Kovalev,* 2003), the particulate extinction [$\kappa_p(r)$] can be found from:

$$\kappa_p(r) = \frac{P(r)r^2 e^{2\int_0^r (1-a)\kappa_m(r')dr'}}{C\Pi_p - 2\int_0^r P(r')r'^2 e^{2\int_0^{r'} (1-a)\kappa_m(r'')dr''} dr'} - a\kappa_m(r) \qquad (2.28)$$

where $a = \Pi_m/\Pi_p$, Π_m $(3/8\pi)$ is the molecular backscatter to extinction ratio [$\beta_m(r)/\kappa_m(r)$] and Π_p is the particulate backscatter to extinction ratio or inverse of lidar ratio 1/LR [$\beta_p(r)/\kappa_p(r)$] (see Appendix IV for complete derivation). Note that the assumption of a = const [Π_p = const] is the most common assumption when inverting the elastic-lidar signals and it is used in our first set of analysis (chapter 3).

To determine $\kappa_p(r)$ with equation (2.28), the value of Π_p and the lidar constant C must be determined. Generally, the solution for $\kappa_p(r)$ is found by using reference values of $\kappa_p(r)$ rather than through direct determination of the constants Π_p and C. In other words, $\kappa_p(\mathrm{r})$ can be found if the boundary conditions (κ_p at some specified r_m) are known either at a local point or over some range.

The most stable solution, and most commonly used, was proposed by *Fernald* (1984) and *Klett* (1985) and it was derived for aerosol backscatter coefficient. In our study however we focus in the derivation of the aerosol extinction coefficient. To apply this solution (in terms of κ_p), the boundary value of $\kappa_p(r_m)$ at some distant range, r_m ($0 < r_0 < r_m < r$) should be known. In this case, equation (2.28) can be rewritten in the general form

$$\kappa_p(r) = \frac{P(r)r^2 e^{2(1-a)\int_{r_m}^{r} \kappa_m(r')dr'}}{\dfrac{P(r_\mathrm{m})r_\mathrm{m}^2}{\kappa_p(r_\mathrm{m}) + a\kappa_m(r_\mathrm{m})} - 2\int_{r_m}^{r} P(r')r'^2 e^{2(1-a)\int_{r_m}^{r'} \kappa_m(r'')dr''} dr'} - a\kappa_m(r) \qquad (2.29)$$

One way to determine the boundary condition $\kappa_p(r_m)$ is to assume a homogeneous atmosphere over some restricted zone close to r_m and to determine the boundary condition $\kappa_p(r_m)$ using the slope method for this zone (*Collis*, 1966). In clear atmospheres, the solution in Equation (2.29) is practical only when the molecular contribution at distance r_m alone has to be considered, i.e., some distant aerosol-free area exists where $\kappa_p(r_m) = 0$.

2.4.2.1. Boundary point (far-end and near-end solutions)

When $r_m = r_{max}$ ($r_0 < r < r_{max}$) we obtain the stable far-end solution:

$$\kappa_p(r) = \frac{P(r) r^2 e^{-2(1-a)\int_r^{r_{max}} \kappa_m(r')dr'}}{\dfrac{P(r_{max}) r_{max}^2}{\kappa_p(r_{max}) + a\kappa_m(r_{max})} + 2\int_r^{r_{max}} P(r') r'^2 e^{-2(1-a)\int_{r'}^{r_{max}} \kappa_m(r'')dr''} dr'} - a\kappa_m(r)$$

(2.30)

Typically then one treats r_{max} in the far-field at a location where $\kappa_p(r_{max}) = 0$. In polluted atmospheres r_{max} is the distance where signal becomes indiscernible from noise.

When $r_m = r_0$ such that $r_0 < r < r_{max}$,, we obtain the near-end solution

$$\kappa_p(r) = \frac{P(r) r^2 e^{2(1-a)\int_{r_0}^{r} \kappa_m(r')dr'}}{\dfrac{P(r_0) r_0^2}{\kappa_p(r_0) + a\kappa_m(r_0)} - 2\int_{r_0}^{r} P(r') r'^2 e^{2(1-a)\int_{r_0}^{r'} \kappa_m(r'')dr''} dr'} - a\kappa_m(r) \qquad (2.31)$$

Note that this solution is unstable because of the singularity in the denominator.

2.4.2.2. Optical depth solution

The alternative method known as the optical depth solution uses the total optical depth or the related transmittance over the total lidar measurement range as the boundary value when determining $\kappa_p(r)$ (*Weinman*, 1988; *Kovalev*, 1995; *Marenco et al.,* 1997). The most general form of the solution can be written (see Appendix III for complete derivation):

$$\kappa_p(r) = \frac{0.5P(r)r^2 e^{2(1-a)\int_{r_0}^{r}\kappa_m(r')dr'}}{\dfrac{\int_{r_0}^{r_{max}} P(r')r'^2 e^{2(1-a)\int_{r_0}^{r'}\kappa_m(r'')dr''}dr'}{1-\mathrm{V}_{max}^2} - \int_{r_0}^{r} P(r')r'^2 e^{2(1-a)\int_{r_0}^{r'}\kappa_m(r'')dr''}dr'} - a\kappa_m(r) \tag{2.32}$$

where, r_0 is the minimum lidar measurement range, and r_{max} is the maximum lidar measurement range (*Kovalev* ,1995)

$$\mathrm{V}_{\max}^2 = e^{-2\int_{r_0}^{r_{max}}[\kappa_p(r)+a\kappa_m(r)]dr} \tag{2.33}$$

and V^2_{max} is defined as the effective transmittance (the conventional transmittance being defined when $a = 1$) as it is computed for the effective extinction coefficient $\kappa_p(r) + a\kappa_m(r)$. The first term in the denominator specifies the constant (C/2) in the lidar equation. For a vertically staring lidar with an extended measurement range (> 10 km), V^2_{max} can be determined using a sun photometer (see *Weinman,* 1988; *Kovalev*, 1995; *Marenco et al.,* 1997; *Flamant,* 2000). However, such a method is largely inappropriate for lidars with relatively small measurement range (5 - 7 km). In this case *in-situ* measurements of the aerosol scattering made by a nephelometer can provide useful information when applying the optical depth solution (e.g., *Flamant,* 2000). Since initially the total atmospheric AOD is used (provided by a ground based or satellite based sun photometer), the next step is a normalization of the extinction coefficient and then a second iterative solution for extinction coefficient is applied. The iterative process goes on until convergence is reached.

A combination of the near-end and optical-depth methods, known as the One Angle Method (OAM) was developed for clear atmospheres by *Kovalev* (2003) using a combination of the optical depth solution and a near-end constraint for the lidar equation. The solution relies on aerosol scattering measured at the lidar location at ground level using a nephelometer. It was also assumed in that study that no particulate absorption occurred. The scattering coefficient as measured by the nephelometer at 0.530 μm is converted to 1.064 μm with the Ångstrom formula. The lidar scattering profile at the lowest end is extrapolated to the ground level scattering coefficient by linear regression. The numerical value of V^2_{max} is varied until the extrapolated lidar near-end signal and the scattering coefficient from the nephelometer match. It should also be mentioned that there also exist combinations of far-end and optical depth solutions (e.g., *Marenco et al.,* 1997). Different numerical methods for the optical depth solution were developed (iterative procedures). See for example *Kovalev* (1993).

2.4.2.3. Multiangle methods

The indeterminacy of the lidar equation significantly restricts practical applications of elastic lidars for atmospheric studies, especially in clear atmospheres (where the sensitivity to the small particles load is high). To perform the inversion of the elastically scattered signal in two-component (molecular and particulate) atmospheres, measured in one-directional mode, the only practical assumption is that the particulate backscatter-to-extinction ratio is independent along the searched direction. What is even worse, the concrete numerical value of the backscatter-to-extinction ratio must somehow be selected. The method proposed by *Kano* (1968) and *Hamilton* (1969) for the inversion of data obtained with scanning lidar is the only method that makes it possible to obtain extinction profiles from elastically scattered signals without the assumption of a backscatter-to-extinction ratio invariant with height. Here, it is assumed that the backscatter term in the lidar equation is invariant in horizontal layers, that is, the atmosphere is assumed to be stratified horizontally.

The real atmosphere is generally homogeneous neither in slope nor in horizontal directions. However, in most cases the atmospheric horizontal heterogeneity is less (and often significantly less) than the vertical or slope heterogeneity. Note that aerosol matter fluctuations in horizontal directions are mostly random, whereas in the vertical directions, systematic changes generally prevail, so that no averaging here will be potentially helpful. Therefore, when selecting between the two existing assumptions for the elastic signal inversion, the assumption of the horizontal homogeneity seems to be more reasonable than the assumption of the vertical (or slope) homogeneity. Another advantage of the Kano-Hamilton multiangle method is that unlike one-directional methods, there is no need to select a concrete numerical value for the backscatter-to-extinction ratio even when working in clear atmospheres; moreover, under certain conditions, the vertical profile of this quantity can be extracted from the multiangle lidar data.

In spite of the obvious fact that the assumption of the atmospheric horizontal homogeneity is, at least, more reasonable than the assumption of the vertical homogeneity, the latter assumption is used in the most one-directional (mostly vertical) measurements. This is due to the one-directional method appearing deceptively robust, especially when using stable solutions. However, the "plausible" looking inversion results obtained with such methods can be quite inaccurate. Meanwhile the multiangle methods based on the assumption of atmospheric horizontal homogeneity are rarely used in practice for lidar searching of the atmosphere (*Spinhirne et al*, 1980; *Russel and Livingston*, 1984; *Rothermal and Jones*, 1985; *Takamura at al.*, 1994; *Sasano*, 1996; *Sicard et al.*, 2002) this is mainly due to poor inversion results often obtained with such methods (*Spinhirne et al*, 1980; *Russel and Livingston*, 1984; *Kovalev and Eichinger*, 2004). The use of additional assumptions in the multiangle measurements, such as a presence of an aerosol-free area at height altitudes (*Takamura at al.*, 1994; *Sasano*, 1996) severely restricts their application in a lower troposphere.

Under the conditions of a horizontally stratified atmosphere, the optical depth of the atmosphere can be found directly from lidar multiangle measurements (see *Kovalev and Eichinger*, 2004). The two principal conditions are: the backscattering coefficient in any horizontal homogeneous slice is constant and it does not change in time during the period over which the lidar is scanning all the region of interest (over an elevation range). In other words, the backscatter measured at a certain height h under *N* elevation angles is the same.

$$\beta\left(h,\varphi_1\right)=\beta\left(h,\varphi_2\right)=\ldots=\beta\left(h,\varphi_N\right)=const. \tag{2.34}$$

The second condition is that, the optical depth of a layer from ground to some height *h* along different slant paths is inverse proportional to the sine of the elevation angle. For *N* elevation angles we have (see Appendix V for details):

$$\tau\left(h,\varphi_1\right)\sin\varphi_1=\tau\left(h,\varphi_2\right)\sin\varphi_2=\ldots=\tau\left(h,\varphi_N\right)\sin\varphi_N=const. \tag{2.35}$$

Consequently, the mean extinction coefficient of a layer [0, *h*] is constant and we can write:

$$\overline{\kappa_t}\left(h,\varphi_1\right)=\overline{\kappa_t}\left(h,\varphi_2\right)=\ldots=\overline{\kappa_t}\left(h,\varphi_N\right)=\overline{\kappa_t}\left(h\right)=const. \tag{2.36}$$

So, in a horizontally homogeneous atmosphere, the mean extinction coefficient of a layer [0, *h*] does not change when it is measured at different angles φ_1, $\varphi_{2,}\ldots\varphi_N$.

The minimum number of angles required to extract optics parameters is 2, from which the two-angle method is derived. Consider two lidar measurements in the slant paths under elevation angles φ_1 and φ_2. The mean extinction coefficient is (see Appendix V for complete derivation):

$$\overline{\kappa_t}(h)=\frac{1}{2h}\frac{\ln\left(\dfrac{P(h,\varphi_2)\sin^2\varphi_1}{P(h,\varphi_1)\sin^2\varphi_2}\right)}{\left(\dfrac{1}{\sin\varphi_1}-\dfrac{1}{\sin\varphi_2}\right)} \tag{2.37}$$

One should pay attention at the angular separation of the two angles such that the related uncertainty is in some error limits. See more details in *Kovalev and Eichinger* (2004).

With increasing number of elevation angles, the uncertainty due to the random errors can be reduced by the use of a least-square method is used. The initial variant of the multiple angle method was used by Hamilton in 1969. With condition (2.35) true, the lidar equation for any elevation angle is written as:

$$P\left(h,\varphi_j\right)=C\beta_t\left(h\right)\frac{\sin^2\varphi_j}{h^2}e^{-\frac{2h}{\sin\varphi_j}\overline{\kappa_t}(h)} \tag{2.38}$$

Taking the logarithm of the range corrected signal $Z\left(r_j\right)=P\left(r_j\right)r_j^2$, written as a function of h and φ_j

$$Z\left(h,\varphi_j\right)=P\left(h,\varphi_j\right)\frac{h^2}{\sin^2\varphi_j} \tag{2.39}$$

equation (2.38) can be written

$$\ln Z\left(h,\varphi_j\right)=\ln\left[C\beta_t\left(h\right)\right]-2\overline{\kappa_t}(h)\frac{h}{\sin\varphi_j} \tag{2.40}$$

Defining the independent variable x

$$x=\frac{h}{\sin\varphi_j} \tag{2.41}$$

and the dependent variable y

$$y=\ln Z\left(h,\varphi_j\right) \tag{2.42}$$

one obtains a set of linear equations

$$y = B - 2Ax \tag{2.43}$$

where the intercept is $B=\ln[C\beta(h)]$ and the slope is $-2A=\kappa_t(h)$. Using a set of range corrected signals $Z(h,\varphi_j)$ for $j = 1{:}N$ at the same height h, the constants A and B are determined through linear regression. With the Hamilton method, the backscatter to extinction ratio is not needed when determining the extinction coefficient. If the lidar constant C can be determined somehow, the backscatter coefficient is determined from B. For further information in some other variants of multi-angle method, see *Kovalev and Eichinger* (2004).

3. Aerosol optical characterization by nephelometer and lidar during Baltimore PM Supersite Experiment

3.1. Baltimore PM Supersite experiment

Cities are a large source of primary soot particles due to the high number of motor vehicles. In addition, cities tend to be dustier, because cars and trucks enhance the dispersion of road dust into the air. Soot has a long residence time and impacts light scattering and absorption in the atmosphere and the clouds for substantial distances downwind. Particle concentration and composition in cities vary widely by season and under different meteorological conditions. In this respect, the optical characterization of aerosols over cities is important for the radiative balance calculations.

The Baltimore PM Supersite project, supported by the US Environmental Agency (EPA 99-NCERQA_X1), provided an excellent opportunity to study urban aerosols and their optical properties. Surface level scattering and vertical profiles of extinction are discussed for the intensive observing period of 4 - 12 July 2002, which includes a major haze event due to Canadian forest fires (7 - 8 July 2002) which was transported to the Baltimore region. During this period, aerosol size distribution, surface aerosol scattering, lidar, aerosol composition and meteorological parameters were measured at temporal resolutions ranging from 5 minutes to 1 hour. This presented an excellent opportunity to characterize atmospheric optical properties under typical urban atmospheric conditions existing prior to the smoke episode and compare them with those of the forest-fire period where soot dominated the atmospheric aerosols.

The visual range is first computed since it is directly related to the aerosol content. The key parameter that determines the influence of aerosols on visibility is the aerosol light extinction coefficient. *Elterman* (1970) conducted classical work on the meteorological range (or visual range) related to molecular and aerosol extinction and ozone absorption for different wavelengths (ranging from 0.27 μm to 2.17 μm) and different altitudes (ranging from 0 km to 50 km). This study is a useful reference for work that relates to the effect of aerosols on visibility.

In this chapter the vertical profiles of the aerosol extinction coefficient are determined by employing a near-end approach (specifically OAM) to solve the lidar equation using ground based measurements for the near end boundary value in the lidar equation. In addition, the aerosol scattering coefficients measured by a nephelometer and computed with Mie theory are analyzed and compared, and aerosol derived mass concentrations and aerosol mass scattering coefficients are calculated for the period (*Adam et al.*, 2004a). In subchapter 3.4, a comparison of the three methods to invert lidar equation is presented whereas the next subchapter presents an analysis of the uncertainty arising from estimates of the near-end boundary condition (*Adam et al.*, 2004b).

The 2002 summer field campaign took place in an urban area in East Baltimore. A general view of the filed experiment is shown in Figure 3.1.

The aerosol scattering coefficient was measured with an integrating nephelometer (Radiance Research model M903), the particle number size distribution was obtained with a combination of Scanning Mobility Particle Sizer (SMPS) (model TSI, Differential electrical mobility particle analyzer DMA 3081, Sheath Air Flow 6 l pm and Aerosol Flow 0.6 l pm) with 53 channels and a 52 channel Aerodynamic Particle Sizer (APS).

Figure 3.1. Baltimore PM Supersite experiment, 2002 location in Bayview, East Baltimore, overview of the main measurements

The SMPS covers a range of particle sizes from 9.31 μm to 0.437 μm and the APS, 0.490 μm to 20.535 μm, hence spanning a total range from 0.00931 μm to 20.535 μm. The integrating nephelometer was operated at 0.530μm and provided the aerosol scattering coefficient with a detection limit of 0.001 km^{-1}. The procedure for computing the aerosol scattering takes into account Rayleigh scattering by molecules. The nephelometer has sensors for pressure p, temperature T and relative humidity RH, such that the Rayleigh scattering coefficient is corrected for the actual p and T. The JHU lidar system operated at 1.064 μm (repetition rate 30 Hz, maximum output 324 mJ/pulse, 10 ns pulse duration, 1.8 mrad divergence). During this measurement campaign, we chose a 3.75 m spatial resolution (corresponding to 25 ns detector sampling duration). The lidar was pointing straight up during the entire measurement period. The zone of incomplete overlap in the case of the actual biaxial configuration was estimated at ~ 300 m. We gratefully acknowledge the loan of the nephelometer by Prof. Phil Hopke from Clarkson University.

3.2. Aerosol optical properties at ground level

In figure 3.2 (a), (b), and (c) the particle number, the particle surface area, and the particle volume, are presented, respectively. Particle number peaks usually below 0.1 μm (nucleation region: nucleation and fresh combustion particles).

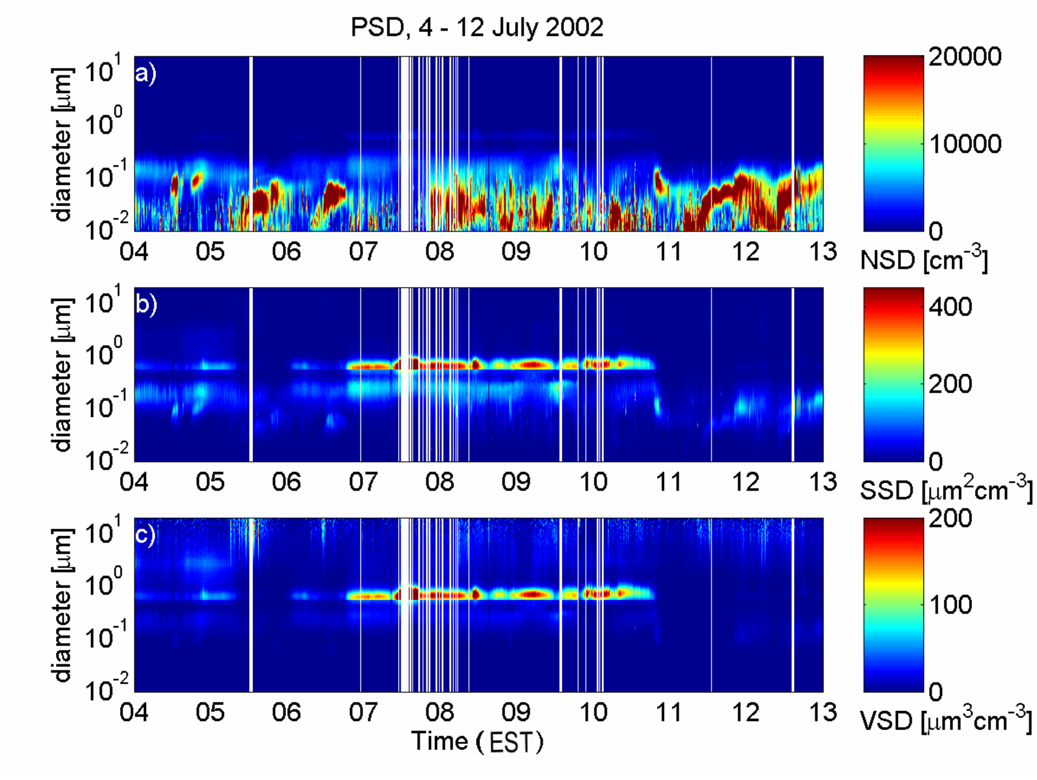

Figure 3.2. Temporal variation of the particle size distribution (PSD); (a) particle number (NSD); (b) particle surface area (SSD); (c) particle volume (VSD)

During the haze event (July 7, 8), the particle surface area peaks between 0.6 and 0.7 μm (which corresponds to an increase in aerosol scattering) and particle volume peaks at 0.7 μm (which corresponds to derived mass increase). The scattering coefficient is proportional with particle surface area $\sigma_p(r) \sim$ (particle surface area) $*$ $(1/\ln(10))(\Delta r/r)$ where the particle surface area = (particle number) $*(\pi d^2/4)$ and $(\Delta r/r) \sim 0.07$.

In Figure 3.3 the average and the standard deviation of particle number (a), particle surface area (b) and particle volume (c) for the time period separated into 'before', 'during' and 'after' the haze event. The large standard deviation reflects the strong variations during each period. In the first period, particle number is predominantly within the range [0.01 - 0.2] μm and peaks at ~ 0.04 μm. The maximum of the daily mean occurs on July 5 (15000 cm^{-3}). During the second period (haze event) the particle number increases and the peak shifts towards ~ 0.015 μm. The maximum daily mean occurs during July 8 (20000 cm^{-3}). During the last period the particle number remains high but the peak shifts to 0.04 μm. The maximum of the daily mean occurs on July 11 (17000 cm^{-3}). The surface area peaks at 0.2 μm in the first period (a second peak occurred at ~ 0.7 μm), the maximum of the daily mean being on July 6 (~ 110 μm^2 cm^{-3}). Surface area increases during the second period (smoke period) and peaks at 0.6 - 0.7 μm (with a second peaks at 0.1 - 0.2 μm). The maximum of the daily mean occurs on July 7 (450 μm^2 cm^{-3}). During the third period, surface area decreases and peaks at 0.1 μm (the maximum of the daily mean, on July 12 is 100 μm^2 cm^{-3}). The particle volume includes many peaks during the first period with a maximum at 0.6 μm (maximum of the daily mean on July 6 of 47 μm^3 cm^{-3} at 0.6 μm). During the second period, particle volume increases and has a peak at 0.7 μm (maximum of the daily mean on July 7 is 200 μm^3 cm^{-3} at ~ 0.7 μm). During the third period particle volume decreases and peaks at 10 μm (maximum daily mean ~ 20 $\mu m^3\ cm^{-3}$ on both 11 and 12 July).

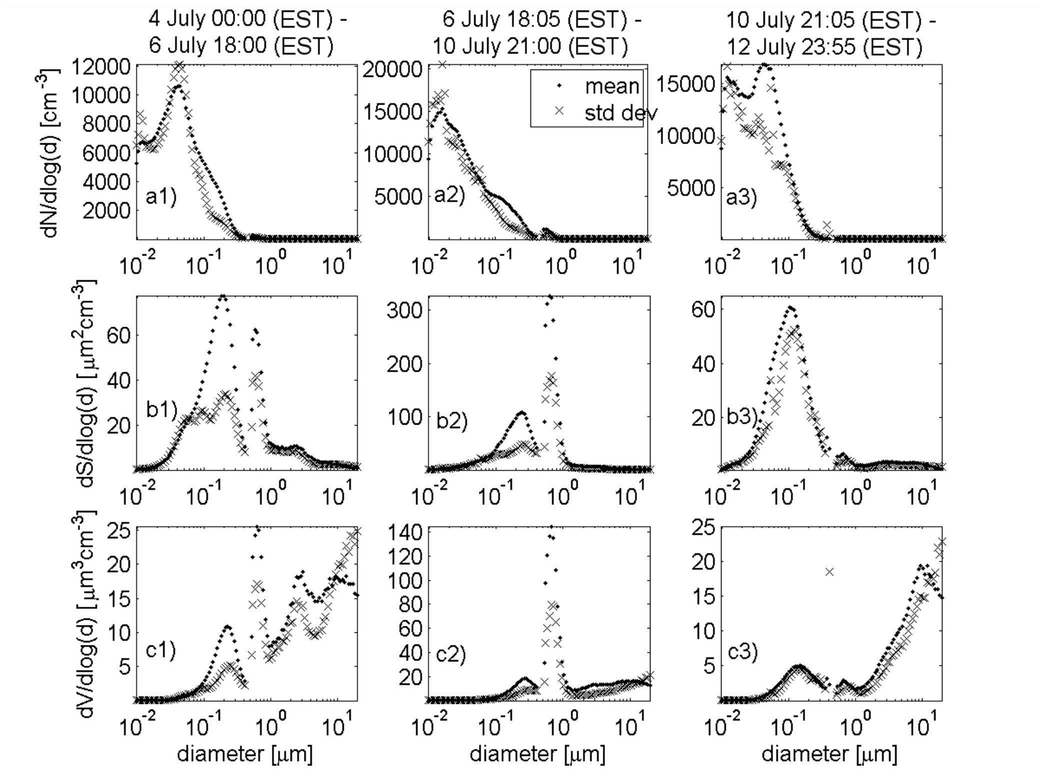

Figure 3.3. Mean (dots) and standard deviation (crosses) of the particle size distribution over the three time periods under investigation (1, 2 and 3 are the three periods and a, b and c stand for particle number, surface area, and volume respectively)

The aerosol scattering coefficients for July 4 - 12 measured and computed at $\lambda = 0.530\ \mu m$ (equation 3.1) are shown in Figure 3.4 (a).

We choose the index of refraction $m = n - ik$ such that the computed aerosol scattering coefficient using Mie theory (equation 2.23 and 3.1) matches the measured one by nephelometer [Figure 3.4 (a)]. This is an indirect method to determine the refractive index.

$$\sigma_p = \int_{r_1}^{r_2} \pi r^2 n(r) Q_{sca}(m,r,\lambda)dr = \frac{\pi}{\ln(10)} \sum_i \left(\frac{\Delta N}{\Delta \log(d)} \right)_i \bar{r}\, Q_{sca}(m,\bar{r},\lambda)\Delta r \quad (3.1)$$

where r_1 and r_2 are the minimum and the maximum of the aerosol particle radius r, $n(r)$ is the number density (differential number size distribution, in $\mathrm{cm^{-3}cm^{-1}}$), Q_{sca} is the scattering efficiency computed according to Mie theory (see *Hulst*, 1981; *Bohren and Huffman*, 1983, $\bar{r}$ is the mean radius of the i^{th} aerosol sampling channel, Δr is the channel width, m is the index of refraction, λ is the wavelength (0.530 μm), ΔN is the number density in the particle diameter range $\Delta\log(d)$ [$\mathrm{cm^{-3}}$]. Once m is determined,

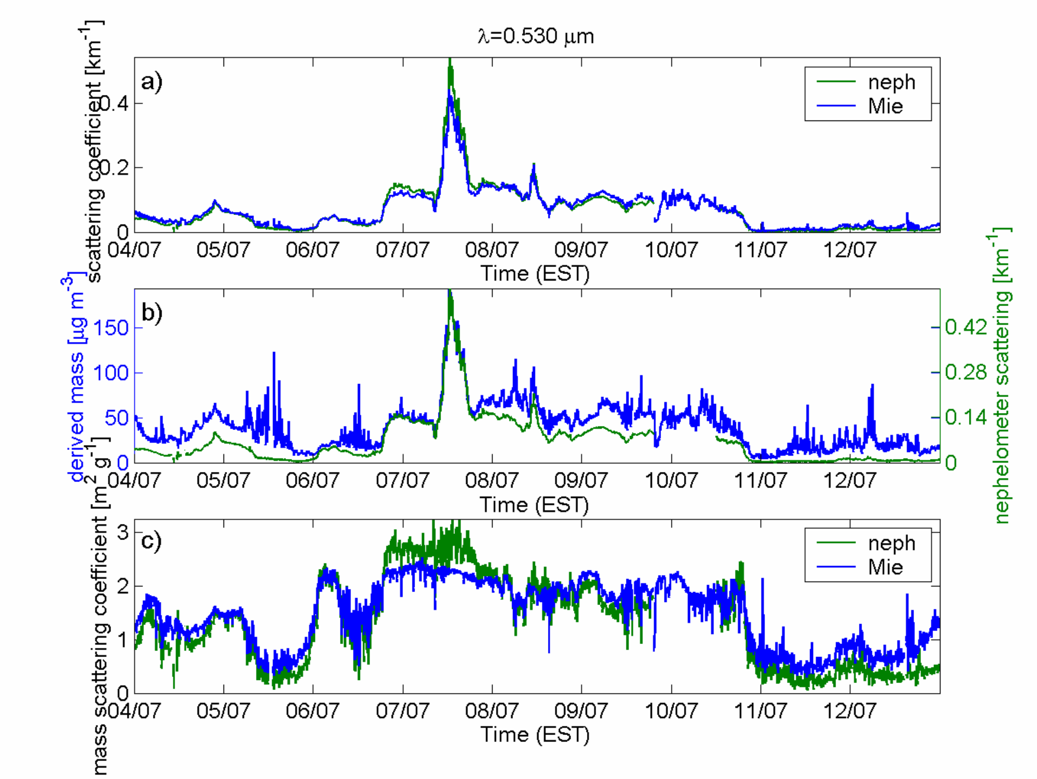

Figure 3.4. Temporal variation of the aerosol scattering coefficient as measured by nephelometer and computed by Mie theory (a), of the derived mass (b) and of the mass scattering coefficient (c). Tick marks on the time axis correspond to midnight.

we calculate scattering, extinction and backscattering coefficients at λ = 1.064 μm as well as the aerosol backscatter-to-extinction ratio. The computed aerosol extinction coefficient at ground level is used as the boundary value in the lidar equation [$\kappa_p(r = 0)$]. We assume that there is no dispersion between 0.530 μm and 1.064 μm (i.e. index of refraction does not vary with wavelength).

The retrieved value of the index of refraction is that of soot (i.e., for λ = 0.550 μm, m = 1.5 - 0.47i (*Horvath*, 1998) which is consistent with the proximity of the field site next to major highways and urban traffic. A commonly used value for the refractive index for aerosols in a polluted area is $m = 1.5 - 0.1i$ (at 550 nm, corresponding to mixed absorbing particles, e.g., *Horvath,* 1998). Under these conditions, considering m = 1.5 - 0.47i, λ = 0.530 μm and particle size distribution (measured) ranging from 10 nm to 20 μm, the scattering efficiency Q_{sca} increases from 0 to ~ 1.2 for particle diameters ≥ 0.5 μm. It is 1 for particles with diameters ~ 0.35 μm, 0.5 for particles with diameter of ~ 0.2 μm and decreases sharply for smaller particles. In other words the contribution to the scattering coefficient comes from particles with large surface area or large scattering efficiency (both are large during the second period July 6 - 10). The maximum extinction efficiency (~ 2.6) occurs for particles with a diameter of 0.5 μm, an efficiency of 1 corresponds to particles of 0.15 μm and an efficiency of 0.5 to particles of 0.08 μm. The overall correlation coefficient for the entire period between measured and computed scattering coefficient is 0.98 (see Table 3.1). A high correlation coefficient is of course expected because the refractive index was chosen such that the agreement between measured and computed aerosol scattering coefficient was the greatest. The correlation coefficients for each individual day are also presented in Table 3.1. A weak correlation was found for 12 July, when the computed aerosol scattering coefficient shows large fluctuations, which correspond to large variations in PSD. Note that a first peak in the scattering coefficient was observed during the night of July 4 due to fireworks that locally increased the aerosol concentrations.

	July 4	July 5	July 6	July 7	July 8	July 9	July 10	July 11	July 12	July 4-12
R σ_{pm} - σ_{pc} *	0.96	0.98	0.99	0.99	0.95	0.92	0.98	0.82	0.57	0.98
R σ_{pm} – M **	0.86	0.51	0.84	0.98	0.82	0.42	0.91	0.49	0.54	0.91

* R σ_{pm} - σ_{pc} = correlation coefficient between measured and computed aerosol scattering

** R σ_{pm} - M = correlation coefficient between measured aerosol scattering and mass concentration

Table 3.1. Correlation coefficients between measured and computed aerosol scattering and between measured aerosol scattering and mass concentration

The scattering coefficient increased again during the evening of July 6, the onset of the haze event (due to the forest fires). The largest scattering coefficient was recorded on July 7, around noon (12:35 EST), with $\sigma_p = 0.540$ km^{-1}. A second peak with $\sigma_p = 0.215$ km^{-1} was recorded on July 8 again around noon (11:25 EST). The scattering coefficient remains high (> 0.1 km^{-1}) until the beginning of a rainstorm on July 9 (~ 19.30 EST). Due to the storm, no data were recorded until the afternoon of July 10. The values recorded at that time were still high but they decreased during the night of 10 July. The extinction coefficient κ_p maximum value of 1.05 km^{-1} was obtained on July 7 12:35 EST.

Statistics for the measured and computed aerosol scattering coefficients as well as computed aerosol extinction coefficients are presented in Table 3.2. The total period analyzed here was divided into three intervals as follows.

		4 July 00:00 EST – 6 July 18:00 EST	6 July 18:05 EST – 10 July 21:00 EST	10 July 21:05 EST– 12 July 23:55 EST
Measured aerosol scattering σ_p [km^{-1}] (nephelometer)	Mean	0.032	0.126	0.006
	STD	0.019	0.080	0.003
	Minimum	0.002	0.007	0.002
	Maximum	0.095	0.541	0.018
	Median	0.032	0.107	0.005
Computed aerosol scattering σ_p [km^{-1}] (Mie theory)	Mean	0.039	0.126	0.013
	STD	0.020	0.066	0.007
	Minimum	0.006	0.010	0.003
	Maximum	0.104	0.467	0.060
	Median	0.037	0.113	0.012
Computed aerosol extinction κ_p [km^{-1}] (Mie theory)	Mean	0.107	0.306	0.047
	STD	0.049	0.146	0.027
	Minimum	0.024	0.045	0.010
	Maximum	0.267	1.05	0.206
	Median	0.103	0.282	0.042
Derived mass M [μg m^{-3}]	Mean	30.1	59.6	17.3
	STD	14.5	27.0	9.83
	Minimum	7.69	10.3	3.96
	Maximum	123	194	86.9
	Median	26.5	53.4	15.5
Mass scattering σ_p/M [m^{2}g^{-1}] – nephelometer	Mean	1.1	2.05	0.365
	STD	0.533	0.495	0.147
	Minimum	0.071	0.469	0.058
	Maximum	2.42	3.26	0.921
	Median	1.10	2	0.348
Mass scattering σ_p/M [m^{2}g^{-1}] – Mie	Mean	1.34	2.08	0.762
	STD	0.470	0.270	0.248

theory	Minimum	0.354	0.794	0.315
	Maximum	2.41	2.61	2.16
	Median	1.38	2.1	0.715

Table 3.2. Mean, standard deviation (STD), maximum, minimum and median for measured (nephelometer) and computed (Mie theory) aerosol scattering, computed (Mie theory) aerosol extinction coefficient, derived mass and mass scattering coefficient (using measured and computed scattering coefficient)

The intervals 4 July at 00:00 EST to 6 July at 18:00 EST, 6 July at 18:05 EST to 10 July at 21:00 EST and 10 July at 21:05 EST to 12 July at 23:55 EST corresponds to pre-smoke, smoke, and post-smoke periods. The influence of the smoke as a result of mixing into the ABL can be seen in Figure 3.4 and Table 3.2, especially during the peak period on 7 July. The average value of the scattering coefficient during the haze event (second interval) was four times larger than for the first period and 21 times larger than for the third period (see Table 3.2). The ratio of aerosol absorption (κ_p - σ_p) to aerosol scattering (σ_p) coefficient varies during the three periods due to different elemental carbon fraction in the aerosol. Smaller absorption coefficients can occur when other chemical components dominate over elemental carbon. For example, during the haze event a large contribution to the aerosol loading came from the smoke layer, mainly as organic carbon.

It is interesting to compare these measurements taken during the Baltimore PM Supersite experiment with results from other Supersite studies. For instance, the Atlanta Supersite Experiment (*Carrico*, 2003) shows an average and standard deviation for measured (integrating nephelometer M903, Radiance Research) aerosol scattering of $\sigma_p = 0.121 \pm 0.048$ km^{-1} (average over entire period of study, 30 July to 3

September 1999). They measured absorption (Particle Soot Absorption Photometer, Radiance Research) and obtained $\alpha_p = 0.016 \pm 0.012$ km^{-1}. This gives an extinction coefficient of $\kappa_p = 0.137 \pm 0.06$ km^{-1}. The absorption coefficient found in the present study is large compared with that found during the Atlanta Supersite (*Carrico,* 2003), which could be related to the proximity of the Baltimore site to highways.

Figure 3.4 (b) represents the temporal variation of the particle mass concentration [termed 'derived mass' by *Hoff et al*. (1996)] and the temporal variation of the aerosol scattering coefficient measured by the nephelometer. The mass concentration is defined

$$M(V,\rho) = V\rho \tag{3.2}$$

where M is in [μg cm^{-3}], V represents the particle volume in [μm^{3}cm^{-3}] (derived from particle number) and ρ is the particle density in [g cm^{-3}]. The corresponding value for ρ is chosen to be equal to 1.0 g cm^{-3}, representative for soot (*Horvath*, 1998). The correlation between mass concentration and the measured aerosol scattering is given in Table 3.1. The overall correlation coefficient was R = 0.91. A small correlation coefficient was found on days where the mass concentration showed large variation (due to the variation recorded in PSD). On the last two days, the low correlation might be related to the nephelometer, which recorded values close to the detection limit. As expected, the derived mass concentration increased during the smoke event (see Table 3.2). The maximum of 194 μg m^{-3} occurred at 12:30 EST on July 7th. This is in broad agreement with the values of 162.65 μg m^{-3} and 197.94 μg m^{-3} measured with the TEOM (Tapered Element Oscillating Microbalance) PM2.5 as the average from 12:00 to 12:30 and from 12:30 to 13:00 EST (see the paper by *Pahlow et al.*, 2003).

Figure 3.4 (c) represents the temporal variation of the mass scattering coefficient [m^2 g^{-1}] [or 'specific scattering coefficient' (*Horvath*, 1998) or 'light scattering efficiency' (*Sloane*, 1986)]. The mass scattering coefficient is defined as the ratio between scattering coefficient and mass concentration of the aerosol (*Charlson*, 1969) or change in particle scattering per unit aerosol mass (*Hoff*, 1996). Hence, this parameter is a measure of the effectiveness with which aerosol particles interact with light. The mass scattering coefficient also varies with particle diameter. The mass extinction remains constant if the PSD always has the same shape (other pertinent aerosol characteristics being fixed). This is called 'self-preserving size distribution' (*Charlson*, 1969). As the PSD changes, the mass extinction will not remain constant. In our study, the mass scattering coefficient ranges from 0.06 to 3.26 m^2g^{-1} [see Figure 3.4 (c) and Table 3.2]. The statistics for each interval are shown in Table 3.2. Tremendous changes in ambient aerosol characteristics, mostly due to the forest fire smoke, are reflected in the large change in the mass scattering coefficient, which strongly increases during the second period 6 July 18:00 EST to 10 July 21:00 EST.

Hoff et al. (1996), describe an experiment carried out in Ontario, Canada, where a haze event was observed and they measured an average mass scattering of 3.2 m^2g^{-1} (the observed range was 1 - 10 m^2g^{-1}) assuming a mean particle density of 2.0 gcm^{-3}. During the Atlanta Supersite Experiment (*Carrico at al.*, 2003), a range between 3.5 and 4.4 m^2g^{-1} was found (a mean particle density of 1.5 gcm^{-3} was used). The different ranges for these two previous studies and the present one arise in part from the different particle density assumptions. These assumptions are based on the particle chemical composition. Furthermore, derived mass depends also on the particle volume distribution, which may be quite different from one location to another.

A first characterization of the aerosol extinction is made considering the visibility criteria (e.g., *Elterman,* 1970). The clear-haze regime delimitation is defined at 15 km (*Hulbert*, 1941) which corresponds to aerosol extinction $\kappa_p \sim 0.26$ km^{-1} at $\lambda = 0.550$ µm. Figure 3.5 shows the result for the visibility calculations, determined as a function of molecular and aerosol extinction at 0.530 µm. The procedure used was based on the Koschmieder formula (see *Elterman,* 1970) which relates the aerosol extinction at $\lambda = 0.550$ µm to the visual range. Herein we use the aerosol extinction coefficient computed with Mie theory at $\lambda = 0.530$ µm. On the same graph the visibility determined at BWI airport is shown, located 15 km south of Baltimore (based on measurements of the aerosol forward scattering).

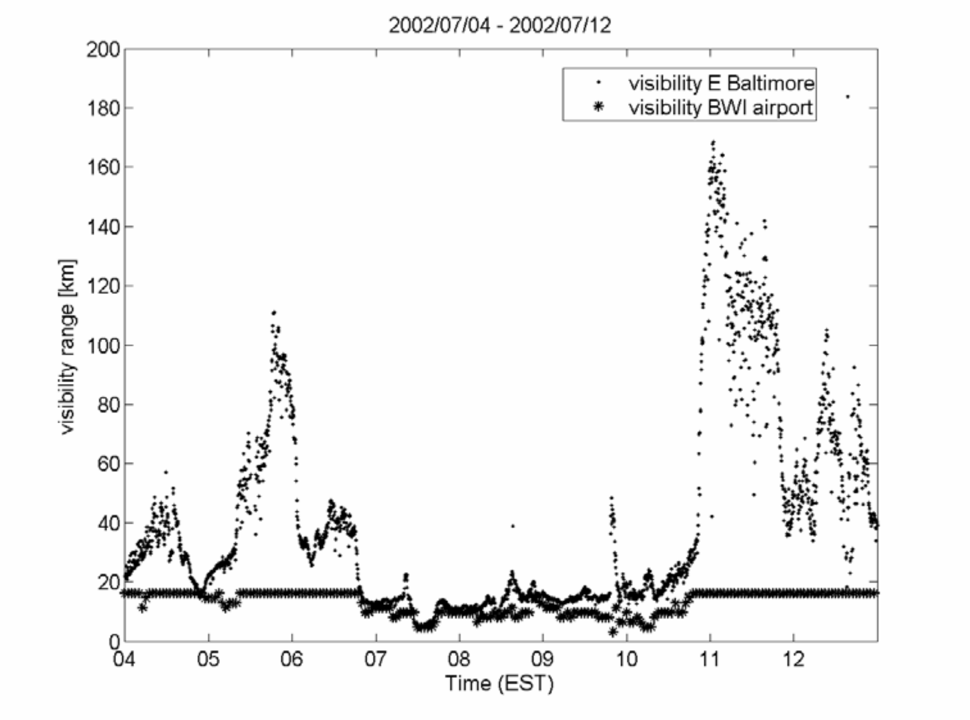

Figure 3.5. Visibility at Baltimore and BWI airport

Note that at BWI airport, as at all civil airports, only poor visibility events are actually recorded. High visibilities are simply reported as equal to 16 kilometers. Based on our computations, the atmosphere was clear on 4, 5, 6, 11 and 12 July (visibility > 15 km) and hazy on 7, 8, 9 July. July 10 was characterized by visual ranges between clear and hazy regime limits.

3.3. Application of the near-end solution to determine vertical profile of aerosol extinction coefficient

As mentioned before, in the application from this chapter, a constant backscatter to extinction ratio was used. It should be mentioned that at 1.064 µm the molecular backscatter in lower atmospheric layers generally is much smaller than aerosol backscatter, and an incorrect aerosol backscatter to extinction ratio Π_p does not produce significant errors, at least in the zones where the approximation Π_p = const. is valid. In the zones where this assumption is not valid, a +/- 20 % change of the ratio produces approximately the same order of change (15 – 25 %) in the retrieved extinction coefficients. It is straightforward to show that the use of a constant Π_p over an extended vertical profile, where the actual Π_p varies from 0.04 sr^{-1} to 0.05 sr^{-1}, induces errors in the retrieved extinction-coefficient profile of approximately 10 %. The use of a constant Π_p over a region where the actual Π_p varies as much as twice, from 0.02 sr^{-1} to 0.04 sr^{-1}, induces the error of approximately, 30 %, etc. Various experimental studies were carried out concerning the vertical variability of the Π_p. It has been shown (e.g., *Ferrare et al.,* 1998a; *Ferrare et al.,* 1998b) that a significant change in the lidar ratio (or Π_p) mostly occurs above ABL. *Sasano and Browell* (1989) showed that backscatter profiles at 1.064 µm are relatively insensitive to the value of the lidar ratio for continental aerosols. In summation, generally one can expect moderate changes of Π_p, and, accordingly, moderate distortions in the retrieved extinction coefficient profiles, when using a constant Π_p for the signal inversion in the lower atmosphere. In summary, for 1.064 μm, the extinction coefficient is much more sensitive to the boundary condition than to the lidar ratio (e.g., *Althausen et al.*, 2000).

Equation 2.32 can be written

$$\kappa_p(r) = \frac{0.5P(r)r^2 e^{2(1-a)\int_{r_0}^{r} \kappa_m(r')dr'}}{\frac{I_{max}}{1-\mathrm{V}_{max}^2} - \int_{r_0}^{r} P(r')r'^2 e^{2(1-a)\int_{r_0}^{r'} \kappa_m(r'')dr''} dr'} - a\kappa_m(r) \qquad (3.3)$$

where

$$I_{max} = \int_{r_0}^{r_{max}} P(r')r'^2 e^{2(1-a)\int_{r_0}^{r'} \kappa_m(r'')dr''} dr$$

and V^2_{max} as defined by equation 2.33, r_0 is the minimum lidar measurement range, r_{max} is the maximum lidar measurement range.

Here we develop a modified OAM procedure to invert the lidar equation using the optical-depth solution and a near-end boundary condition. Recall that OAM is a combination of optical depth and near-end methods. It uses the optical-depth solution to invert lidar equation (equation 3.3) but the boundary condition is determined in the near-end field (at r_0) such that it can be catalogued as a near-end method. A near-end solution (equation 2.31) can be used as well with the near-end boundary condition determined as described below. The differences from the study by *Kovalev* (2003) are: (i) we take into account aerosol absorption; (ii) the ground level aerosol extinction coefficient at 1064 nm, $\kappa_p(0)$, is determined with Mie theory. The near-end boundary condition $\kappa_p(r_0)$ is determined by using an extrapolation from the ground level aerosol extinction coefficient $\kappa_p(0)$, calculated with the Mie theory (it is the same procedure as in OAM and it is described below). The ground level boundary value, $\kappa_p(0)$, is determined (Mie theory) using measurements the particle size distribution (measured by SMPS and APS instruments) and an indirect method to determine the aerosol refractive index (needed in efficiency computation; see Appendix II). The operation steps are as following. The indirect method to determine the aerosol refractive index is an inversion problem of the equation 3.1. Once m is determined, the Mie theory is applied for $\lambda = 1064$ nm to compute aerosol extinction coefficient as well as aerosol backscatter coefficient to determine LR.

Once the boundary value $\kappa_p(0)$ and the aerosol backscatter to extinction ratio at ground level are obtained, we invert the lidar equation using equation (3.3). The integral is found over the range from r_0 to r. The main assumption is that the aerosol backscatter to extinction ratio (or lidar ratio) is range-independent for the vertical profile. For the molecular extinction coefficient we use *Edlen*'s formula (1966) for the refractive index and a vertical decay function of pressure and temperature from the Standard Atmosphere 1976 (*NASA*, 1976) to account m variation with p and T.

We select an apparent linear range of the aerosol extinction profile in the lidar near field and then extrapolate to the ground level ($r = 0$) such that

$$\kappa_p(r_0) = \kappa_p(r = 0) + br_0 \tag{3.4}$$

where b is the slope of the linear fit. The effective transmittance V^2_{max} is chosen such that the value of the extinction coefficient obtained from the lidar signal and extrapolated to the ground level matches the value determined by Mie theory. An initial guess of V^2_{max} ($0 < V^2_{max} < 1$) in equation (2.33) is determined from

$$V^2_{max,\ init} = 1 - \frac{2\left[a\kappa_m\left(r_0\right)+\kappa_p\left(r=0\right)\right]}{S\left(r_0\right)}\int_{r_0}^{r_{max}} S\left(r'\right)dr' \qquad (3.5)$$

by assuming $\kappa_p(r_0) = \kappa_p(0)$. $S(r)$ represents the range corrected signal $[P(r)r^2]$. The procedure is illustrated in Figure 3.6.

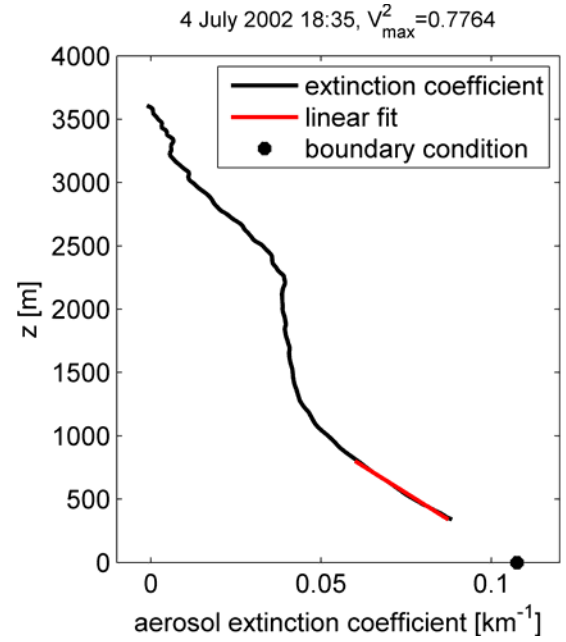

Figure 3.6. Example of retrieving the vertical profile of the aerosol extinction coefficient by choosing the corresponding V^2_{max}

The vertical aerosol extinction coefficient profiles retrieved from the lidar data are given in Figures 3.7 - 3.11 for July 5, 7, 8, 9, 12, respectively. Panels (a) and (b) represent the time series of the lidar range corrected signal, RCS, (color scale in arbitrary units) and the corresponding aerosol extinction coefficients (color scale represents the aerosol extinction coefficient in km^{-1}). Panel (c) shows vertical profiles of the aerosol extinction coefficient at different times of the day. Note that the vertical profiles of the extinction coefficient are averages over periods of ~ 30 min. In panel (b), values of the backscatter to extinction ratio Π_p are shown (right y-scale in sr^{-1}). With one exception (on 12 July 17:00 EST), Π_p ranges between 0.043 and 0.073 sr^{-1}

with a mean and standard deviation of 0.055 ± 0.007 sr^{-1}. This corresponds to a mean lidar ratio of 18 sr.

Vertical extinction profile computations, in general, were made for selected lidar profiles taken in cloud free conditions. Cloud free conditions prevail on 5, 7, 8 and 12 July. We present profile results for just 5 of the measurement days.

The profiles obtained on July 5 are shown in Figure 3.7. The maxima of the particle extinction coefficient occurred at the beginning of the day and at noon, when thermals mix aerosols into the ABL, which can be seen in the lidar range corrected signals [panel (a)]. A large extinction is recorded at noon (12:13 EST) which correspond to the thermal seen in the range corrected signal [panel (a)]. During this period the ABL height was between 1500 and 1700 m from 11:00 to 18:00 EST.

On July 7 just a few profiles could be determined, which correspond to times before and after the smoke was entrained into the ABL [see Figure 3.8, panel (a)]. It must be noted that the method used here to retrieve the extinction coefficient profiles does not work for particularly high turbid atmosphere observed on July 7. We presume that for this situation, multiple scattering cannot be ignored. The maxima in the extinction profiles correspond to the smoke layer. The extinction values at ground level [marked by asterisks in panel (c)] were large (0.13 – 0.24 km^{-1}) whereas those in the region of smoke layers were higher with a maximum of 0.45 km^{-1} at 9:00 EST around 1.5 km. Higher values are expected during the mixing of the smoke layer with the ABL (10:00 - 18:00 EST).

For 8 July (Figure 3.9) the aerosol extinction is still high, especially in the aerosol layer and in the region of a plume arising from the ground during the first part of the day (from 8:00 to 11:00 EST). At ground level, the values were still high ranging from 0.12 to 0.34 km^{-1} whereas in the region of the plume intrusion and of the smoke layer the values are larger (maximum 0.7 km^{-1} around 8:00 around 400m).

On 9 July (Figure 3.10), slightly cloud cover was predominant [~ 2 – 3 km as indicated by panel (a)]. The plots of the extinction profiles are shown in panel (b) where only the first 1800 m are displayed to emphasize the ABL. The extinction coefficient is lower than in previous days but it can be considered still large (with a maximum around 0.21 km^{-1}). Panel (c) displays the few vertical profiles at different time stamps also in the range up to 1800m. It should be mentioned that the presence of a cloud layer at the far end of the measurement range does not have an impact on the aerosol extinction coefficient retrieval below the cloud since we use a near-end solution approach. However, the retrieval may be less accurate within the cloud layer due to possible MS within the cloud and a sharp change in LR on the cloud boundary. Hence we chose to plot the aerosol extinction profiles beneath clouds only. July 12 (Figure 3.12) was a clear day characterized by small aerosol extinction coefficients (smaller than 0.12 km^{-1}). The profiles and temporal variation of the extinction coefficient are shown in panels (b) and (c). Relatively large values can be seen during the plume present in first part of the period (~ 13:00 - 15:00 EST).

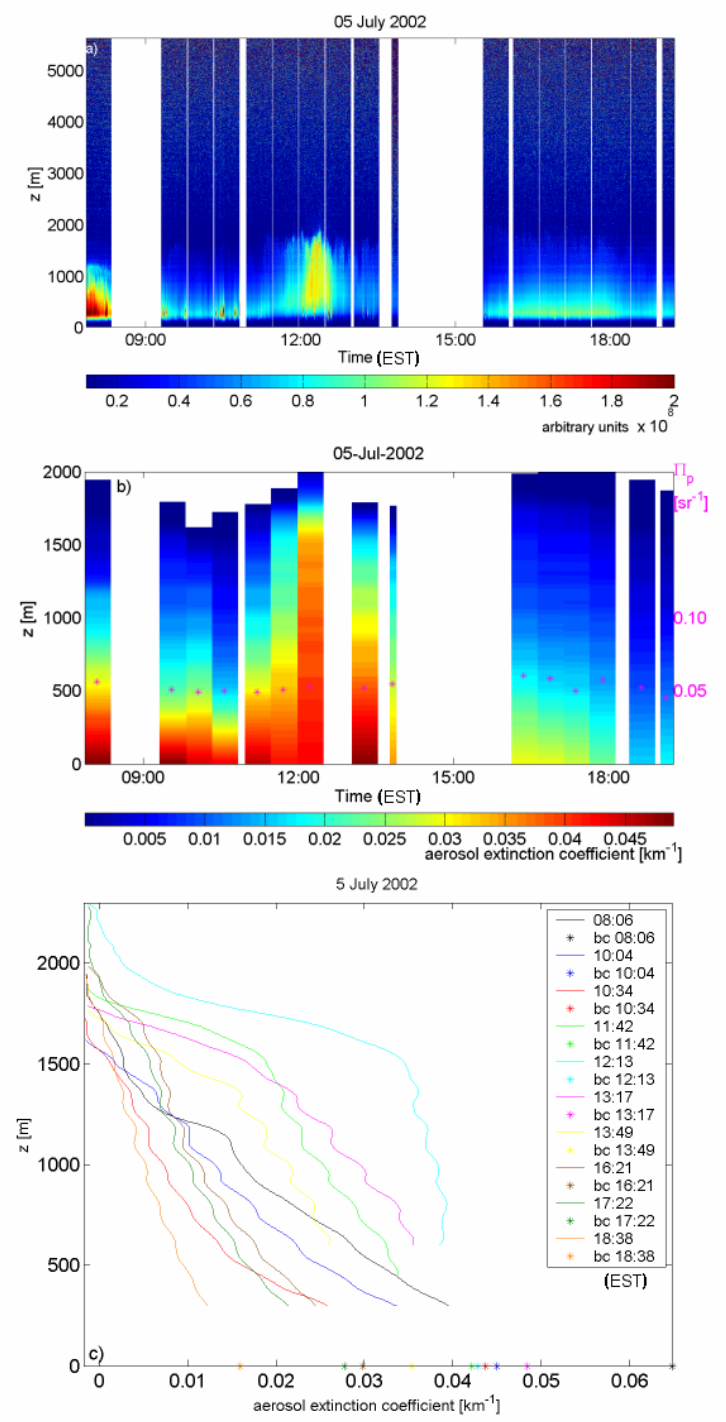

Figure 3.7. (a) Temporal vertical profile of the lidar RCS (the color scales represent the RCS in arbitrarily units); (b) Temporal vertical profile of the aerosol extinction coefficient (km^{-1}); on the right axis, backscatter to extinction ratio Π_p (sr^{-1}) (asterisks); (c) Vertical profile of the aerosol extinction coefficient at different time stamps for 5 July 2002 (bc = boundary condition)

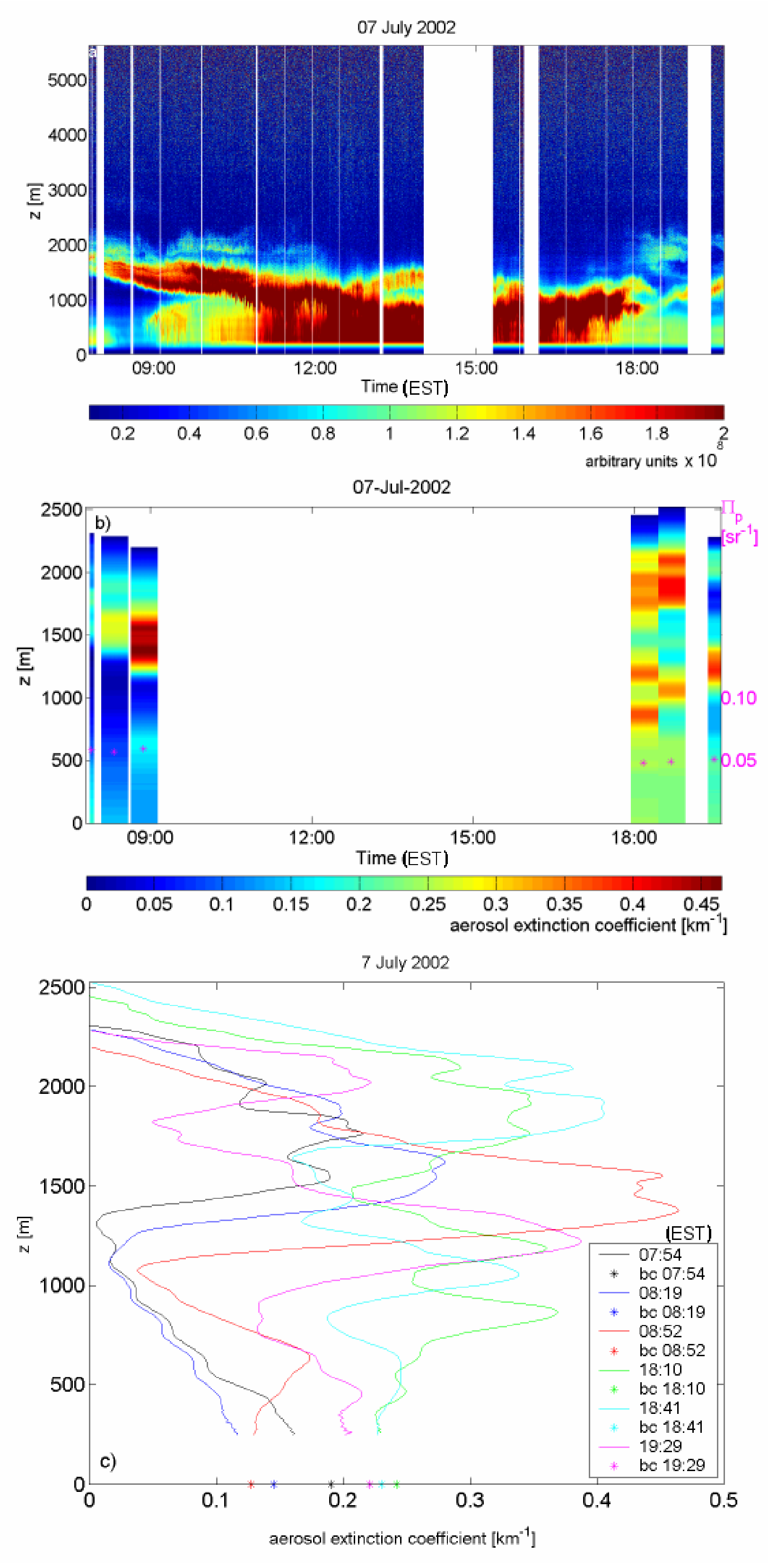

Figure 3.8. Same as Figure 3.7 for 7 July 2002

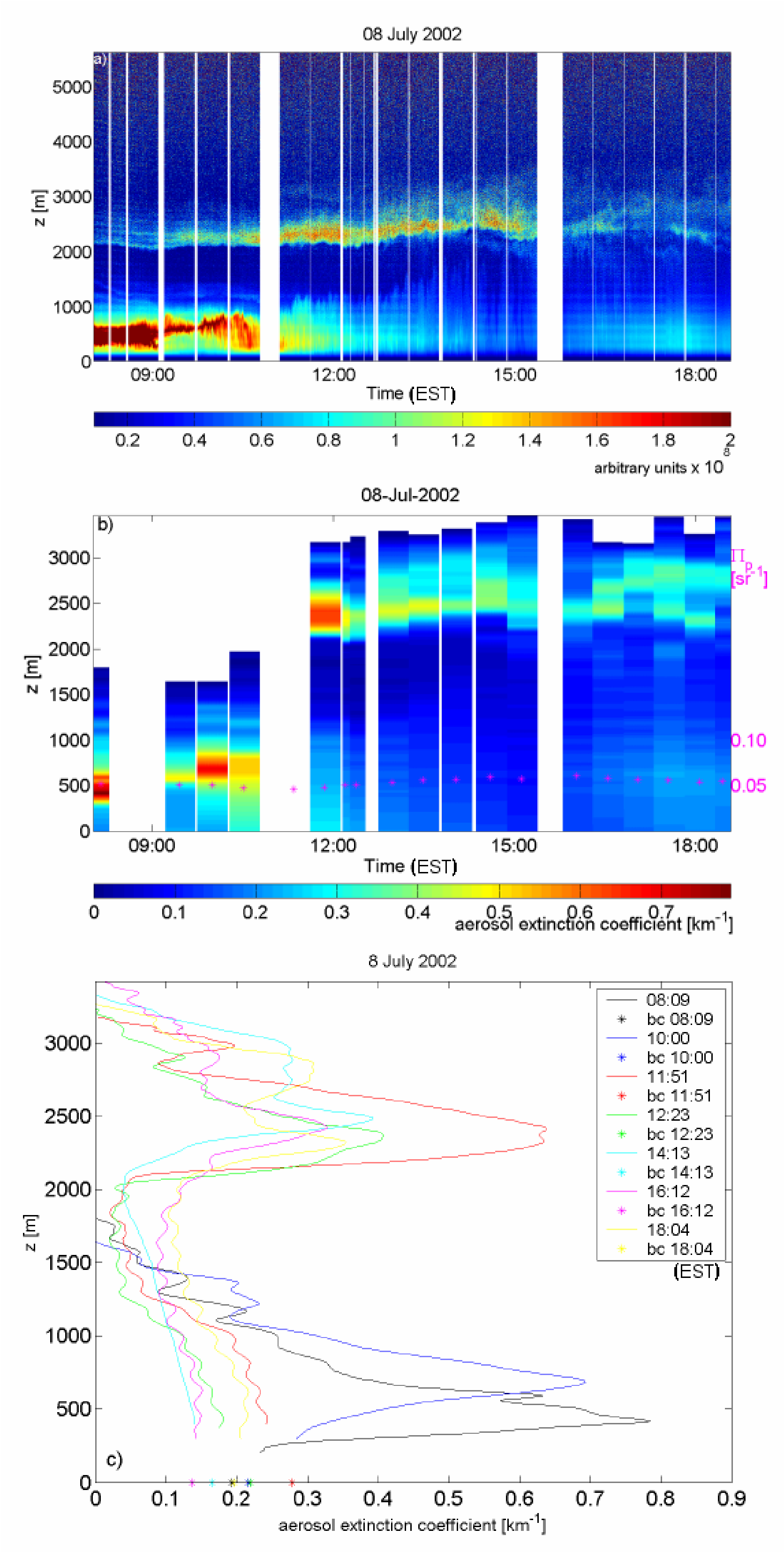

Figure 3.9. Same as Figure 3.7 for 8 July 2002

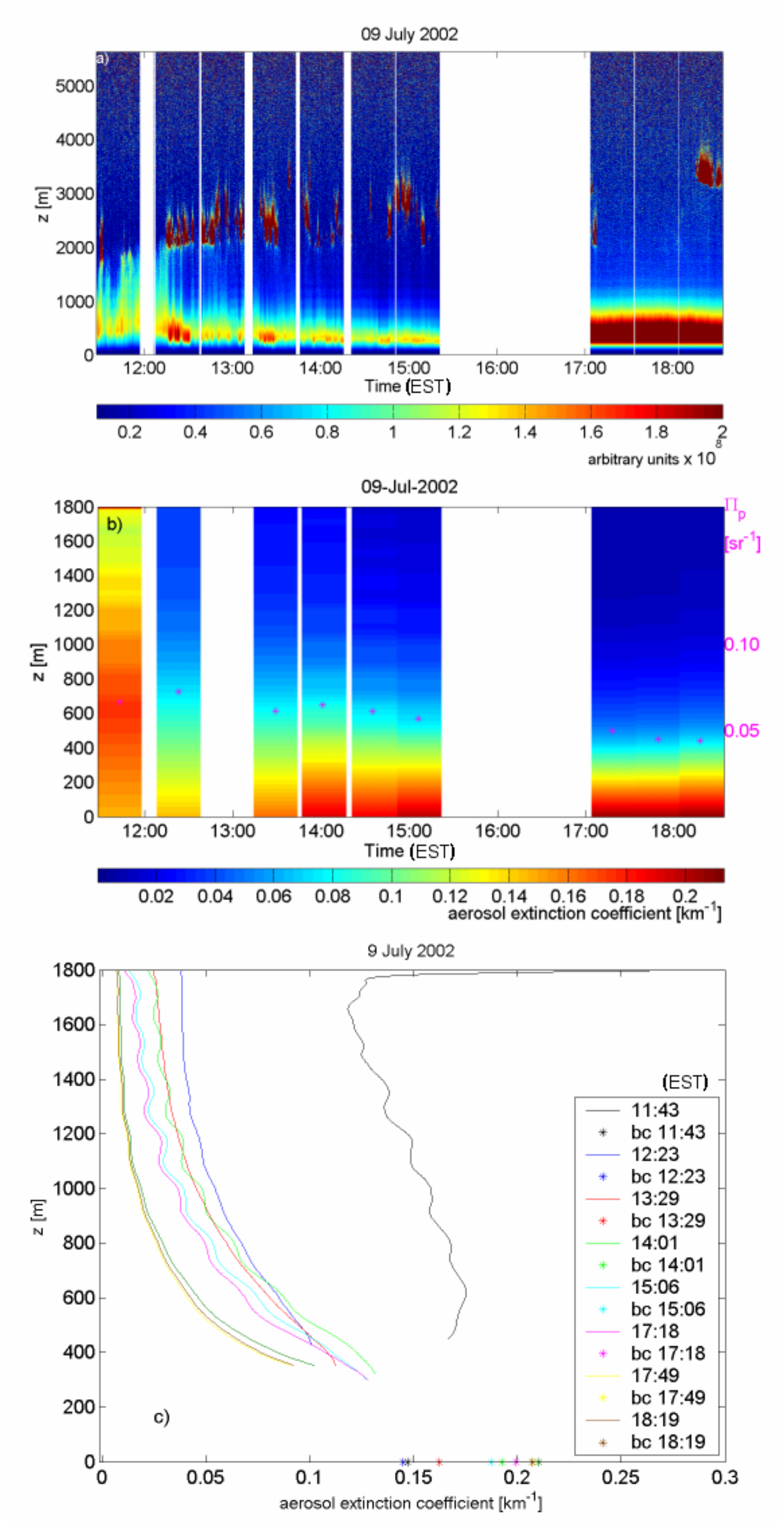

Figure 3.10. Same as Figure 3.7 for 9 July 2002

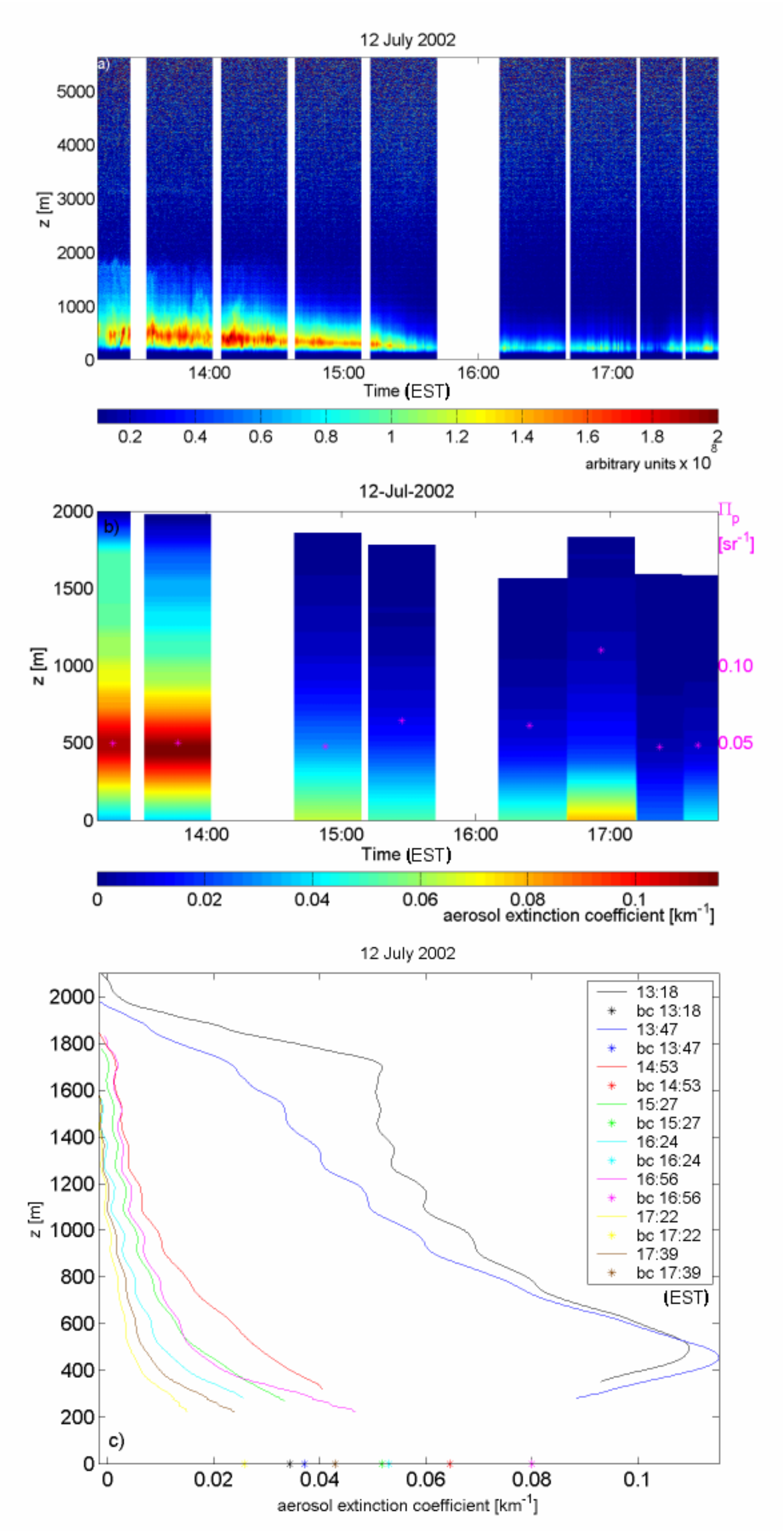

Figure 3.11. Same as Figure 3.7 for12 July 2002

3.4. Comparison of near, far and optical depth solution

A comparison of the three analytical methods (as described in 2.4.2.1 and 2.4.2.2), i.e. near-end, far-end and optical depth (OD) solutions was done for some periods during Baltimore PM Supersite Experiment. The method used for the near-end solution is described in section 3.3 (equation 3.3). For the optical depth method, we use the AOD measured with a ground based sun photometer to specify the boundary condition. The reference far field value for the far end method (equation 2.30) was chosen assuming that no particle contribution to extinction occurs at the maximal range r_{max}, i.e. $\kappa_p(r_{max}) = 0$. The particles backscatter to extinction ratio is computed with Mie theory, as described in the procedure for near-end solution (section 3.3). Its value, considered range independent, is used in all the three methods involved in the comparison.

For the near-end solution, we used the equation 3.3, which uses a specific $\mathrm{V}_{\max}^2\ \kappa_p(r_0)$. As described in section 3.3, the near-end boundary condition $\kappa_p(r_0)$ is extrapolated from $\kappa_p(0)$ and this extrapolation corresponds to a certain $\mathrm{V}_{\max}^2$. Let us write again equation 3.3:

$$\kappa_p(r) = \frac{0.5P(r)r^2 e^{2(1-a)\int_{r_0}^{r} \kappa_m(r')dr'}}{\dfrac{I_{max}}{1-\mathrm{V}_{max}^2} - \int_{r_0}^{r} P(r')r'^2 e^{2(1-a)\int_{r_0}^{r'} \kappa_m(r'')dr''} dr'} - a\kappa_m(r) \qquad (3.3)$$

with

$$I_{max} = \int_{r_0}^{r_{max}} P(r')r'^2 e^{2(1-a)\int_{r_0}^{r'} \kappa_m(r'')dr''} dr .$$

For far-end solution, we use equation 2.30 for which the boundary condition assume $\kappa_p(r_{max}) = 0$. Thus, equation 2.30 becomes:

$$\kappa_p(r) = \frac{P(r) r^2 e^{-2(1-a)\int_r^{r_{\max}} \kappa_m(r')dr'}}{\dfrac{P(r_{max}) r_{max}^2}{a\kappa_m(r_{max})} + 2\int_r^{r_{max}} P(r') r'^2 e^{-2(1-a)\int_{r'}^{r_{max}} \kappa_m(r'')dr''} dr'} - a\kappa_m(r) \qquad (3.6)$$

The optical depth solution uses the equation 3.3 where the boundary condition is given by the AOD measured by a ground based sun photometer. Equation for V_{max}^2 2.33) can be written explicitly as

$$V_{max}^2 = e^{-2\int_{r_0}^{r_{max}} a\kappa_m(r)dr} e^{-2\tau_p} \qquad (3.7)$$

where τ_p is the particle optical depth over range $[r_0, r_{max}]$.

The boundary value AOD was provided by a sun photometer located at Maryland Science Center, a few miles away from our sites (courtesy to Brett Holben, http://aeronet.gsfc.nasa.gov/). A sun photometer measures the AOD over the entire atmosphere. As in the case of far-end approach, we assume that there are not particles above r_{max}. The procedure to compute particle extinction starts assuming that τ_p represents a fraction of the AOD measured with the sun photometer. An iterative procedure is used such that τ_p is updated after each step, until the computed AOD converge to the measured AOD. In other words, in the first step, assuming an initial τ_p, we compute $\kappa_p(r)$. A linear extrapolation for $\kappa_p(r)$ from r_0 to the ground is used (the same procedure as used in OAM). Then we compute the AOD over the range $[0, r_{max}]$ and compare with AOD given by the sun photometer. The τ_p is updated {computing the integral of $\kappa_p(r)$ over $[r_0, r_{max}]$} and a new $\kappa_p(r)$ is determined. Then the comparison of computed AOD with measured AOD follows. The iterations follow until the convergence of the computed AOD toward measured AOD. Few examples (*Adam et al.*, 2003) are given in the Figure 3.12 for two days in 2001. In 2001, the experimental setup was located in south Baltimore, in an industrial area.

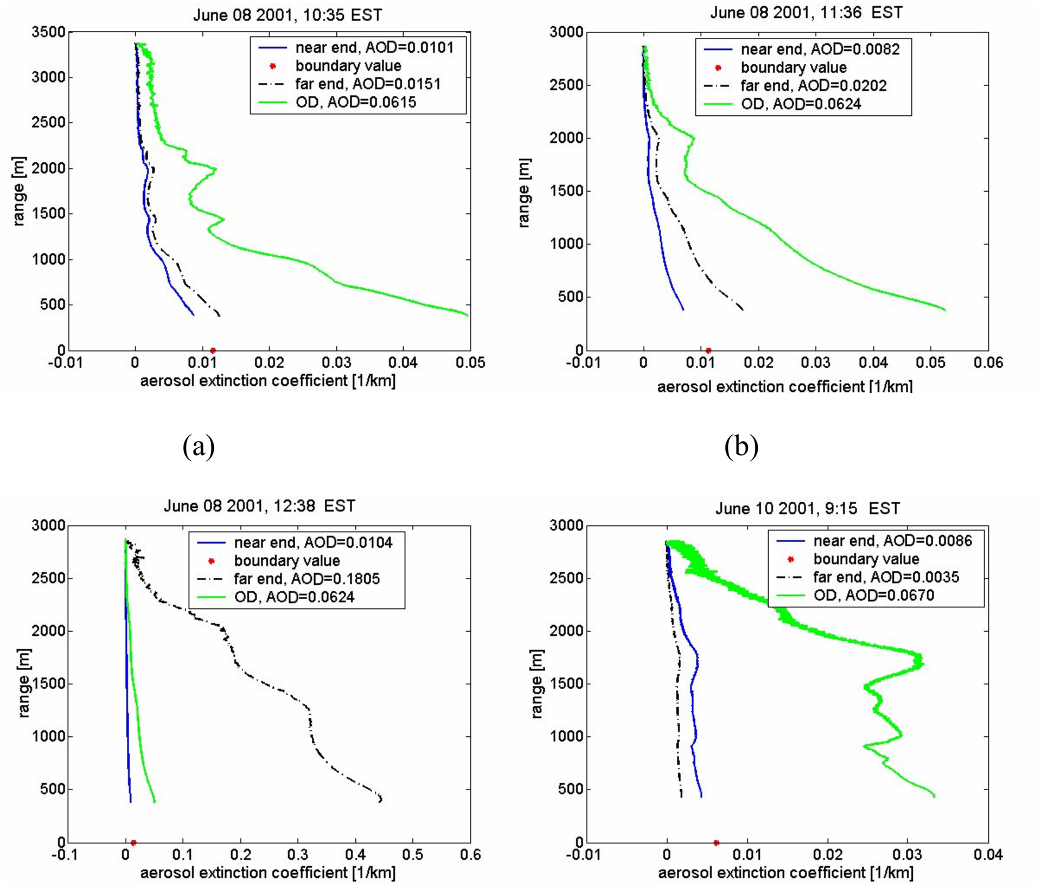

(a) (b)

(c) (d)

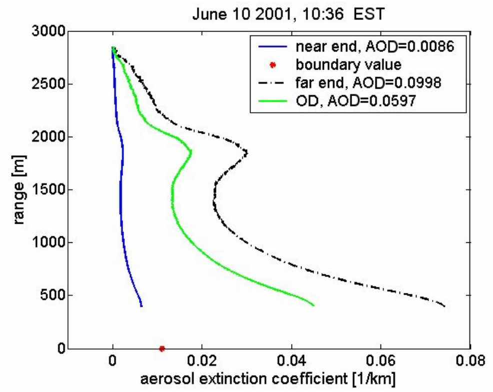

(e)

Figure 3.12 (a) - (e). Comparison of near-end, far-end and optical depth solutions. The data analyzed were taken under a clear sky, on 8 and 10 June 2001. AOD for each method is also shown.

The comparison between the three methods (OAM, optical depth method and far-end method) under clear sky conditions does not allow one to determine the suitability of the far end solution or optical depth solution. From the ten cases analyzed, in four of them the optical depth method profile is closer to the near end profile (three of them corresponding to a measured aerosol optical depth AOD > 0.1). With one exception, for a measured AOD < 0.1, the far end solution is closer to the near end profile. Possible distortions can occur for each method because of the uncertainty inherent to the boundary value used. In case of the near end solution, we can have errors due to an inaccurate determination of the refractive index whereas the particles were considered spherical in accordance with Mie theory. Furthermore, we considered the refractive index equal for the lidar wavelength (1064 nm) and the nephelometer wavelength (530 nm), i.e. no dispersion occurred. Another cause can be a non-appropriate assumption for the linear fit in the near field. In the case of the optical depth and far-end solutions, we have considered that the aerosols are concentrated within the lidar measurement range (assumed purely molecular scattering at the end of the interval). It must also be noted that the boundary value AOD was obtained some 5 km away from the lidar measurement site. Further analyses have to be done in order to determine the impact of the errors due to all these assumptions. First, we will do a direct computation of the refractive index using the chemical composition of the aerosols. Other assumptions will be considered for the near field in order to extrapolate from r_0 to ground level (e.g. exponential fit).

For the case of JHU lidar, biaxial configuration, where the good measurement range covered only 2 - 3 km the optical-depth and far-end solutions are not appropriate since we might have aerosols lasting over more kilometers. It follows that, in these conditions, the near-end solution is more suitable for computing aerosol extinction coefficient. Of course, in this case, an acceptable boundary condition has to be determined.

3.5. Uncertainties arising from estimation of the boundary condition in near-end solution case

The far-end solution and the optical-depth solution assume a purely molecular atmosphere at the end of the interval and they are of limited use under certain atmospheric conditions to solve for the lidar equation, especially for backscatter lidar systems with a limited maximum range of 5 - 8 kilometers. To circumvent this problem we have used a near-end solution using the boundary condition and the backscatter to extinction ratio at ground level using measurements of supporting instruments and Mie theory (see section 3.3).

The period investigated was 5 - 9 July 2002 during the Baltimore PM Supersite project. The characteristics of the JHU lidar system were described in section 3.1. The lidar equation was inverted using near-end method (equation 2.31). The determination of the boundary condition follows the procedure described in section 3.3. So, the aerosol extinction coefficient at ground level $\kappa_p(r = 0)$ at the lidar wavelength 1064 nm is computed using Mie theory, which in turn uses the measured particle number and the refractive index that was determined using to two independent methods (*Adam et al.*, 2004b).

In the first method, the refractive index is computed as described in section 3.2 ("indirect determination"). For a given time interval, the computed aerosol scattering was simulated for different refractive indices within the range 1.3 - 1.7 (step 0.01) for the real part and from 0 - 0.6 (step 0.001) for the imaginary part. The "best" refractive index was the one for which the relative error between measured and computed scattering was minimum. Once the best match is found and refractive index is determined, Mie theory is applied at 1064 nm to compute the aerosol extinction coefficient and the backscatter to extinction ratio. Dispersion is not considered. The second method ("direct determination") accounts for particle chemical composition in order to determine the refractive index. The approach uses the volume-weighted method (*Hassan and Dzubay*, 1983), with the mean density and mean refractive index given by equations 2.26 and 2.24.

$$\bar{\rho} = \sum_j \frac{X_j}{\rho_j} \tag{2.26}$$

$$\bar{m} = \sum_j m_j f_j = \bar{\rho} \sum_j \frac{X_j m_{r,j}}{\rho_j} - \bar{\rho} \sum_j \frac{X_j m_{i,j}}{\rho_j} \tag{2.24}$$

where X_j and ρ_j are mass fraction (%) and density (g cm^{-3}), $m_{r,j}$ and $m_{i,j}$ are the real and imaginary parts of the refractive index for species j.

The entire period was divided into 6 time intervals according to similar behavior of the species concentrations. The time intervals are: I: 5 Jul 8:00 - 6 Jul 1:00 EST, II: 6 Jul 1:00 - 6 Jul 19:00 EST, III: 6 Jul 19:00 - 7 Jul 9:00 EST, IV: 7 Jul 9:00 - 7 Jul 19:00 EST, V: 7 Jul 19:00 - 8 Jul 9:00 EST, VI: 8 Jul 9:00 - 9 Jul 13:00 EST.

The refractive indices determined with the first method for each interval are shown in Table 3.3, denoted as m_rI (real part) and m_iI (imaginary part). The computed aerosol scattering coefficients using these refractive indices are shown in Figure 3.13 by the blue line whereas the black line represents the measured aerosol scattering, with very close agreement. For the second method, in order to apply equations 2.24 and 2.26, we assume that sulfates originate from $(NH_4)_2SO_4$, nitrates originate from NH_4NO_3 as NH_4^+, NO_3^- and SO_4^{2-} are major components in the region (*Chen et al.,* 2003). Organic matter is estimated as 1.6 times OC (intervals I - II) for urban aerosols and 2.1 times OC for non-urban aerosols (intervals III - VI) (*Turpin and Lin*, 2001).

	I 5 Jul 8:00 6 Jul 1:00 EST	II 6 Jul 1:00 6 Jul 9:00 EST	III 6 Jul 19:00 7 Jul 9:00 EST	IV 7 Jul 9:00 7 Jul 19:00 EST	V 7 Jul 19:00 8 Jul 9:00 EST	VI 8 Jul 9:00 9 Jul 3:00 EST
m_rI	1.3	1.37	1.68	1.52	1.3	1.39
m_iI	0.170	0.116	0.565	0.236	0.077	0.498
m_rIIa	1.453	1.432	1.420	1.413	1.432	1.442
m_iIIa	0.0113	0.0027	0.0080	0.0053	0.0159	0.0108
m_rIIb	1.539	1.552	1.570	1.551	1.556	1.548
m_iIIb	0.011	0.0029	0.0077	0.0054	0.0150	0.0104

Table 3.3. Refractive indices as calculated by indirect (I) and direct method (II)

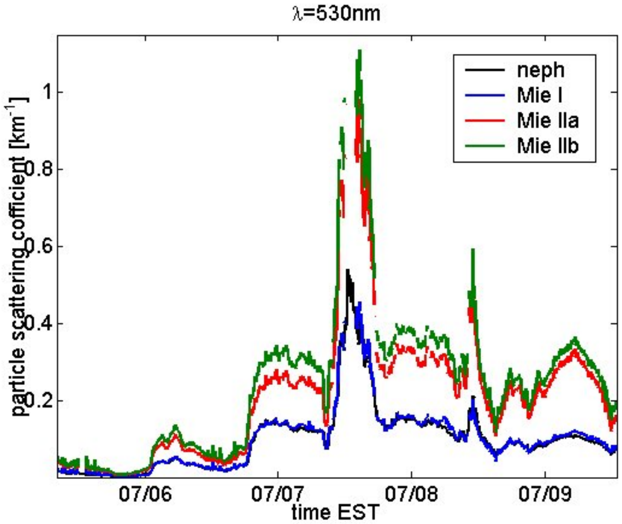

Figure 3.13. Measured and computed particle scattering coefficient at 530 nm at ground level

The refractive indices determined using the four components [$(NH_4)_2SO_4$, NH_4NO_3, EC and OM] are shown in Table 3.3 (IIa). The corresponding scattering coefficients for 530 nm are shown in Figure 3.13 by the red line (Mie IIa). Densities and refractive indices used for those components are given in Table 3.4 (*Hand and Kreidenweis*, 2002).

	$(NH_4)_2SO_4$	NH_4NO_3	EC	OM	Fe_2O_3
ρ	1.769	1.725	2	1	5.24
m	1.53	1.56	1.96 - 0.66i	1.4	3.011

Table 3.4. Species densities and refractive indices

A first test to check these assumptions was to evaluate the mass balance and to compare the sum of all 4 concentrations (M_{sum}) with the total PM2.5 measured using TEOM (M_{TEOM}). A second test compares the mean density as given by equation 2.26 (ρ_2) with the mean density obtained as $\rho_1 = M_{TEOM} / volume$ where the volume is determined from particle number assuming spherical particles. These comparisons are given in Table 3.5.

	I 5 Jul 8:00 6 Jul 1:00 EST	II 6 Jul 1:00 6 Jul 9:00 EST	III 6 Jul 19:00 7 Jul 9:00 EST	IV 7 Jul 9:00 7 Jul 19:00 EST	V 7 Jul 19:00 8 Jul 9:00 EST	VI 8 Jul 9:00 9 Jul 3:00 EST
err_{mb}	20.86	26.86	33.80	31.98	29.22	24.29
ρ_1	1.844	1.612	1.544	1.19	1.258	1.302
ρ_2	1.59	1.612	1.639	1.555	1.583	1.594
err_ρ	13.8	0.02	6.13	30.7	25.8	22.5

Table 3.5. Errors in mass balance and density

The error in the mass balance err_{mb} is the relative error between M_{TEOM} and M_{sum} (%) and err_{ρ} is the relative error between ρ_1 and ρ_2 (%). As the mass balance is not closed (error of 20 – 30 %), according to equation 2.26 the mean density is overestimated. According to equation 2.24, the refractive index increases with overestimated density but also decreases with the missing part (err_{mb}).

Next, we investigated the effect of the missing part (err_{mb}) in the mass balance, considering that it represents different mineral soil components. The largest influence on the refractive index is found when we consider that the soil is composed only of Fe_2O_3 (its density and refractive index is given in Table 3.4). The mean refractive indices obtained in this case are given in Table 3.3 (IIb). The computed scattering coefficient at 530 nm is shown in Figure 3.13 (green line). Using other compounds for mineral dust such as SiO_2 does not result in large changes in m and ρ_2 compared with case IIa. With the three cases selected (I, IIa and IIb) the particle extinction coefficient and the lidar ratio were computed for 1064 nm (Figures 3.14 - 3.15). For the vertical profiles of the particle extinction coefficient as determined with equation 2.31, we compare the profiles computing AOD from ground level to the end of lidar range.

Illustrative examples are given for different intervals in Figures 3.16 - 3.18. Errors arising in the AOD due to errors in $\kappa_p(r = 0)$ are given in Table 3.6, where for each interval (containing several averaged vertical profiles) we list the minimum (first row) and maximum (second row) errors.

The errors in $\kappa_p(r = 0)$ and AOD represent the relative errors with respect to method I. The errors in $\kappa_p(r = 0)$ and AOD represent the relative errors with respect to method I. For the first two intervals, the errors in $\kappa_p(r = 0)$ are less than 30 % whereas the errors in AOD are less than 48 %.

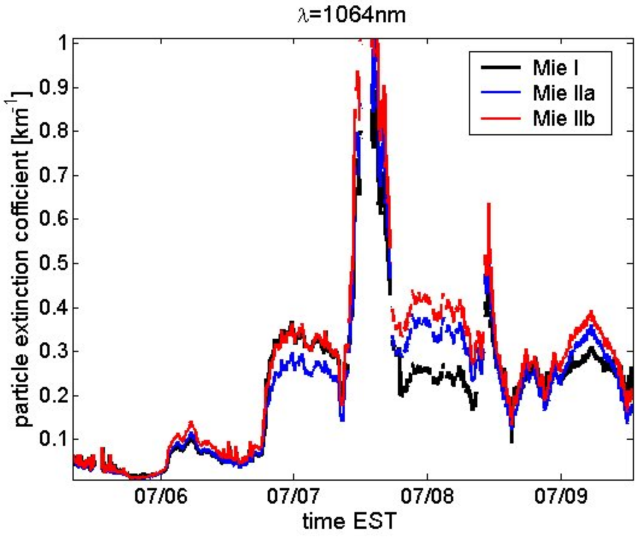

Figure 3.14. Particle extinction coefficients as computed at 1064 nm at ground level

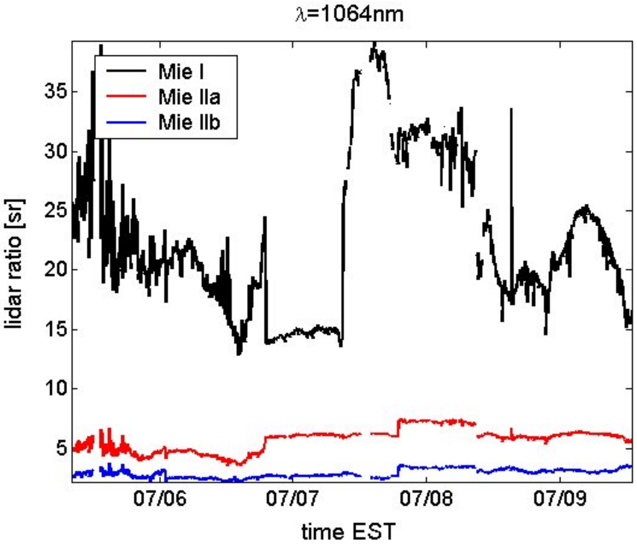

Figure 3.15. Particle extinction to backscatter ratio (lidar ratio) at 1064 nm at ground level

For the first interval, we determined 15 vertical profiles of the aerosol extinction coefficient (averaged over 30 min). The errors in $\kappa_p(r = 0)$ and AOD are quite similar for the 2 comparisons (I - IIa and I - IIb) (Table 3.6). Figure 3.16 presents two profiles taken on 5 July at 2 different times. For the first profile (13:06 EST) the errors in $\kappa_p(r = 0)$ are 5.5 % (I - IIa) and 2.5 % (I - IIb). The error in AOD is 2 % in both cases. For the second profile (19:06 EST) the errors in $\kappa_p(r = 0)$ are 28.3 % (I - IIa) and 24 % (I - IIb) whereas the errors in AOD are 35.7 % and 48.8 %. For the second period, (6 profiles determined), on average, the errors are larger than for first interval. Overall, during the first two intervals, with a few exceptions, the errors in $\kappa_p(r = 0)$ are less than 20 %. The errors in $\kappa_p(r = 0)$ become larger at the beginning of the haze event (6 July) (Figure 3.14).

	5 Jul 8:00 6 Jul 1:00 EST (I)	6 Jul 1:00 6 Jul 9:00 EST (II)	6 Jul 19:00 7 Jul 9:00 EST (III)	7 Jul 9:00 7 Jul 19:00 EST (IV)	7 Jul 19:00 8 Jul 9:00 EST (V)	8 Jul 9:00 9 Jul 3:00 EST (VI)
$err\kappa_p$ *I-IIa*	5.6 28.3	18.5 21.3	61.9 63.5	45.8 49.5	19.4 26.3	40.5 58.8
err_{OD} *I-IIa*	0.5 35.7	15.7 21.8	69.2 73.1	57.1 74.1	23.1 31.9	53.8 70.3
$err\kappa_p$ *I-IIb*	0.3 24.8	4.9 13.7	37.7 39.9	12.6 18.3	70 87.7	16.2 45.8
err_{OD} *I-IIb*	0.2 48.8	6.3 16.5	45.5 51	18.8 43.6	93.5 116.3	28 58.7

Table 3.6. Errors in boundary condition $\kappa_p(r = 0)$ and AOD

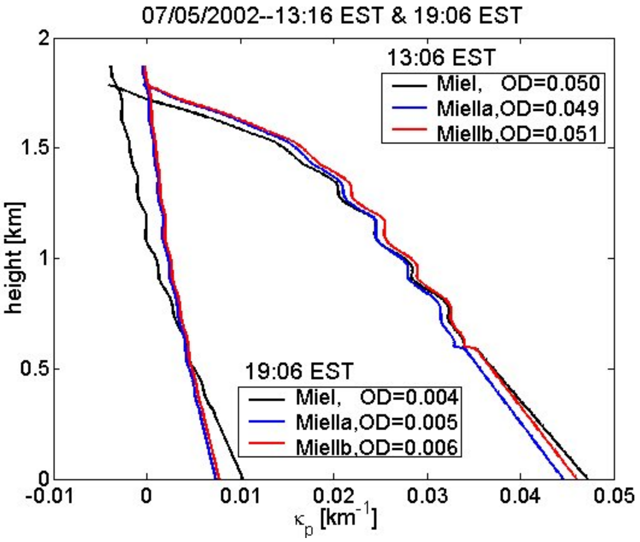

Figure 3.16.

Particle extinction coefficients as computed at 1064 nm at ground level

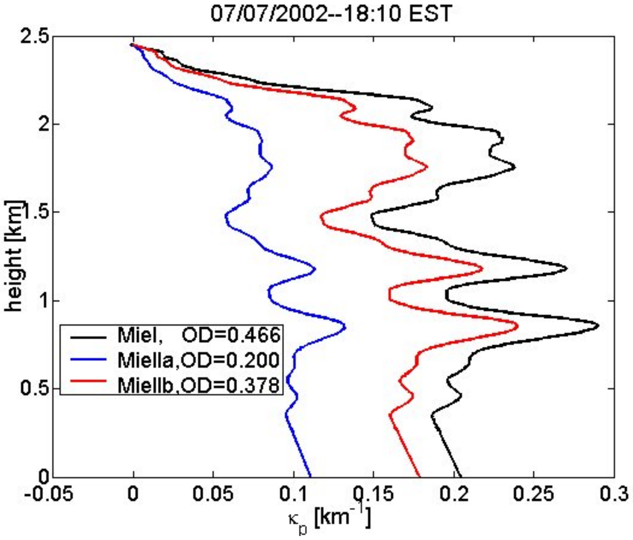

Figure 3.17.

Same as Figure 3.16 but for 7 July 18:10 EST

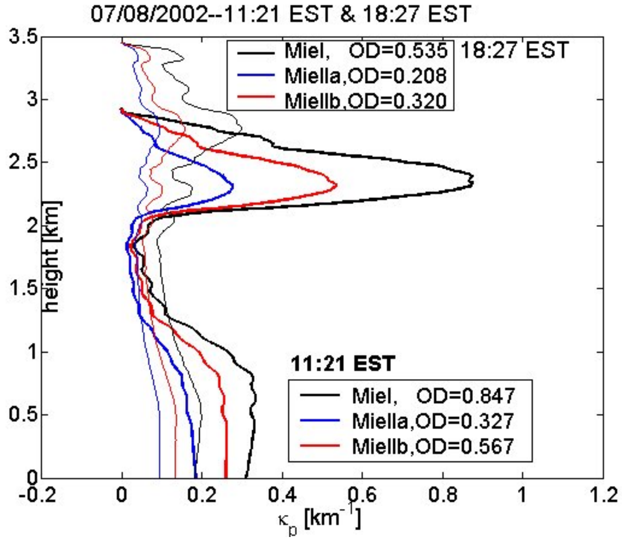

Figure 3.18.

Same as Figure 3.16 but for 8 July 11:21 EST and 18.27 EST

Figure 3.17 shows an example during 7 July (haze event). The errors in $\kappa_p(r = 0)$ are 45.8 % (I - IIa) and 12.6 % (I - IIb) whereas the errors in AOD are 57.1 % (I - IIa) and 19% (I - IIb). The last interval contains 20 profiles. The errors are larger in the case I - IIa. Figure 3.18 shows two profiles taken on 8 July at 11:21 EST (thick lines) and 18:27 EST. During the day (8-18 EST), a haze layer was present at 2 - 2.5 km. The layer diminished towards sunset (as can be seen in the second profile). The errors for both profiles are larger for the case I - IIa.

Overall, except the fifth interval, the results obtained in the case IIb are closer to those obtained in case of the method I. The results using method I and II differ significantly and possible reasons are: improper calibration of the nephelometer; the mass balance is not closed and assumptions made with regard to the components might not be accurate; the assumptions for the missing part considered just the extremes in order to set limits for the refractive indices. We mention that the near-end method does not work in the case of heavy pollution (as during haze peak, on 7 July 12 EST). In those cases, the multiple scattering cannot be ignored.

3.6. Conclusions

Aerosol optical properties were investigated at the Baltimore PM Supersite experiment in East Baltimore and a modified OAM method was used to invert the lidar equation. The method incorporates additional measurements to compute the lidar ratio and the boundary condition at ground level. Nevertheless, this remains an ill-posed problem since one might obtain several refractive indices that match the scattering profile. The value found for the refractive index (*m* = 1.5 - 0.47i) is consistent with ambient air that is strongly influenced by heavy traffic. In comparison, *Dalzell and Sarofim*, (1969) using the Kramers-Krönig dispersion formula obtained for soot the refractive indices of 1.59 - 0.58i and 1.63 - 0.70i for 0.532 μm and 1.064 μm respectively. *LaRocca and Turner* (1975) report refractive indices of 1.83 - 0.74i and 1.95 - 0.68i for the same wavelengths while *Müller et al.* (2001) estimated a value for soot like particles of 1.75 - 0.45i for both wavelengths. *Smyth and Shaddex* (1996) provide a detailed discussion about the refractive index of soot. The scattering coefficients calculated using the three refractive indices above are well correlated with the measured scattering in each case (~ 0.98). However, the computed extinction coefficient boundary value at 1.064 μm differs from those obtained with our estimated refractive index. Comparisons were made for three extinction profiles using ground boundary conditions of 0.0429, 0.1075 and 0.2072 km^{-1}. For instance, using the refractive index 1.63 - 0.7i at 1.064 μm resulted in boundary conditions which differed by about 17 % in each case. The AOD of the new profiles differed by about 20 % from the AOD of our profiles. The second refractive index (1.85 - 0.68i) gave similar results while the third refractive index (1.75 - 0.45i) gave a somewhat closer (~ 7 %) match of the extinction coefficient profiles with the ones we determined and a difference in the AOD about 9 %. Future work should include the development of a dispersion relation between 0.530 μm and 1.064 μm. Incorporating the chemical composition will improve the analysis, as the range of refractive indices can be restricted. A direct calculation of the refractive index (as well as of the mean density) will follow from the species analysis (using the volume-weighted method). The indirect method to estimate the refractive index using Mie theory has to be compared with the direct method using species analysis. The derived mass concentration has to be compared with the measured TEOM PM2.5. Finally, the density inferred to compute the derived mass would be compared with the density given by the species analysis.

In this chapter, the lidar ratio has been assumed constant with height. No other supporting measurements within the boundary layer were available. Because of real changes in aerosol properties with height (size distribution, chemical composition, and humidity), the lidar ratio estimates are inaccurate and thus prohibit a proper estimation of the vertical extinction profile and the aerosol optical depth. As we mentioned earlier, using a constant lidar ratio over the vertical range will result in errors in extinction coefficient in and above the ABL but they are not particularly high for 1.064 μm as we discussed earlier.

The measured aerosol scattering from the nephelometer at 0.530 μm ranged from $\sigma_p = 0.002$ km^{-1} to $\sigma_p = 0.541$ km^{-1}, whereas the computed aerosol extinction coefficient with Mie theory at 0.530 μm ranged from $\kappa_p = 0.010$ km^{-1} to $\kappa_p = 1.05$ km^{-1}. In the present study, the aerosol optical properties were dominated by light absorption. The single scattering albedo, determined using the computed scattering and extinction (at $\lambda = 0.530$ μm) was found to be 0.358 ± 0.063, with minimum and maximum values of 0.179 and 0.511, respectively. The small values of the albedo are directly related to strong absorption by the soot. Future studies should include a direct measurement of the aerosol absorption coefficient.

A good correlation was found between derived mass and measured aerosol scattering coefficient ($R = 0.91$). The derived mass ranged between 4 and 194 μg m^{-3}. The maximum was reached on July 7th at 12:30 EST, which agreed favorably with the TEOM PM2.5, which measured a mean value of 197.94 between 12:30 and 13:00 EST. The mass scattering coefficient (or mass scattering efficiency) ranged between 0.2 and 3.3 m^2 g^{-1}.

The comparison of the results obtained with the three analytical methods to determine aerosol extinction coefficient brought less encouraging results, which showed in general large disagreement. Nevertheless, we consider that a near-end method is preferable for our lidar data, for which a good measurement range ranged between 2 and 4 km. In this context, synergetic measurements are necessary.

Other work, related to the Baltimore PM Supersite, is built upon these results (e.g. *Adam et al.*, 2004). The results of the study over the uncertainty of the boundary condition (actually of the ground level aerosol extinction coefficient) revealed poor agreement of the two methods involved in determination of the aerosol index of refraction. In general, better matches were obtained between the two methods when the mineral compound was included in the direct method. Ideally, more precise measurements of the main chemical species in PM2.5 have to be done. Further investigations have to be done to understand the divergence of the two methods. The extensive monitoring with both in situ and remote sensing instruments during the Baltimore PM Supersite experiment provided valuable data on aerosol optical properties.

4. Applications of Kano-Hamilton multiangle method to determine vertical profile of aerosol optical properties and lidar overlap

As mentioned in the introduction and described in chapter 2, section 2.4.2.3, the multiangle methods are the only option for an elastic backscatter lidar to determine the aerosol extinction coefficient without a priori assumptions (estimation of lidar ratio and of a boundary condition). When lidar constant is somehow determined, the aerosol backscatter coefficient can be also determined. The only assumption used in multiangle method is the horizontal homogeneity, which implies constant backscatter and extinction coefficients in a certain horizontal layer. The multiangle methods based on the assumption of the horizontal homogeneity of the lower atmosphere often yield unphysical results, such as negative extinction coefficients over extended ranges. In spite of the almost total absence of thorough and comprehensive analyses of the various multiangle methods, the common belief is that the major reason for their poor accuracy is atmospheric heterogeneity. However, our theoretical and experimental work reveals that the actual problem of the multiangle measurement is much deeper than just atmospheric heterogeneity. To obtain a comprehensive understanding of the specifics of the multiangle measurements, we have performed some simulations and analysis, the results of which are discussed in this chapter. Numerical experiments are undertaken to study the sensitivity of the Kano-Hamilton method to the noise and systematic errors (section 4.1). A methodology for practical application of this method is described in section 4.2. The experimental results of the particle optical depth and relative backscatter coefficient are discussed in section 4.5. The estimation of the lidar overlap is described in section 4.3 and experimental results are shown in section 4.5.

4.1. Real lidar in an ideal atmosphere: simulations

In our numerical experiments we investigated an imaginary case, when a real scanning lidar (that is, the lidar that signals are corrupted by random noise and may have some non-zero offset) operates in an ideal horizontally homogeneous atmosphere. In Figures 4.1 – 4.3 we present some results of our simulations, obtained from such a lidar operating in the multiangle mode at 532 nm in a clear atmosphere. For simplicity we assume that the atmospheric particulate extinction coefficient at this wavelength decreases linearly from 0.1 km^{-1} at the ground level to 0.04 km^{-1} at the height of 6000 m. The incomplete overlap zone of the assumed lidar extends up to approximately 450 m, and the lidar operates along discrete slope directions of 10, 15, 20, 25, 30, 40, 50, and 60 degrees. The procedure to construct lidar synthetic signals is described in details in section 4.6.3. Briefly, in order to build lidar signals one needs to describe a vertical profile of the aerosols extinction and backscatter coefficients (assume that molecular ones are known), chose a lidar constant C_1 and the lidar overlap $q(r)$. Then the signals are derived using lidar equation (equation 2.27), where $C = C_1 q(r)$. The height dependence of the lidar signals is transformed as described with equation 2.38 or equation 4.1.

In Figure 4.1 we show the actual dependence of the total optical depth on height for our artificial atmosphere (thin line) and that obtained with our virtual lidar (filled squares) under the conditions that the lidar signal is measured without any random noise or systematic distortions. None of the lidar data points is excluded from consideration. The divergence between the two profiles close to the lidar, up to a range of ~ 300 m, is completely due to the influence of the incomplete overlap zone; the overlap function is shown as the bottom bold curve. In Figure 4.2 we present similar optical-depth dependences but now obtained with the lidar data when the zero-line offset, remaining after the background subtraction, is not equal to zero. It is assumed that for these measurements a 12 - bit digitizer is used, and the maximal signal for these measurements is about 4000 bins; the actual background component in the lidar signals is 200 bins. The maximal range for the inverted lidar signals was selected to be 6000 m for all slope directions, therefore the number of points that are available for regression decreases with height.

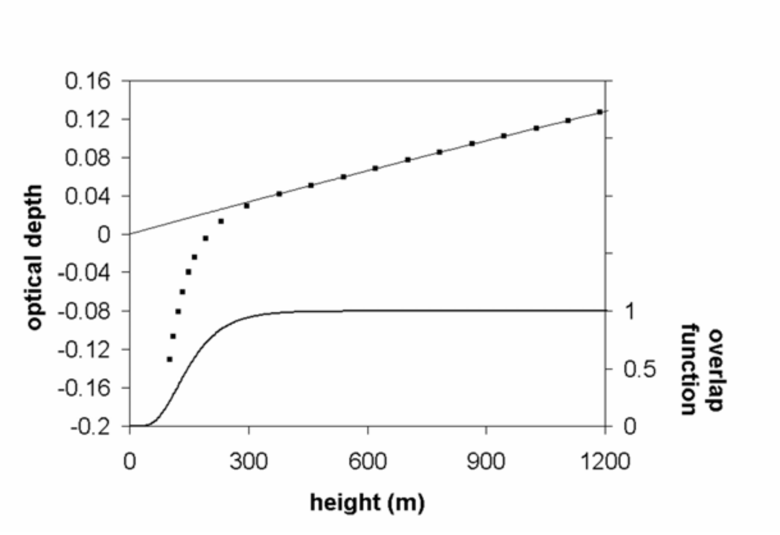

Figure 4.1. Model dependence of the total optical depth on height (thin line) and that obtained from simulated multiangle measurements with a virtual lidar (dots) under the condition that the signals from the incomplete overlap zone are not excluded. The overlap function is shown as the bold curve.

In Figure 4.2, curve 1 shows the actual (model) dependence of the optical depth versus height; curves 2 and 3 show the retrieved optical-depth profiles obtained with incorrectly estimated background levels, of 201 and 199 bins, respectively, in the all signals; no signal noise is assumed to corrupt the data. One can see that even such an insignificant offset, plus or minus 1 bin, can dramatically distort the derived profiles. Periodic jumps on the curves are another specific of the derived optical-depth profiles. The jumps are related with the change in the number of points used in regression and not accurate background subtraction, a jump occurs when the number of points in regression changes.

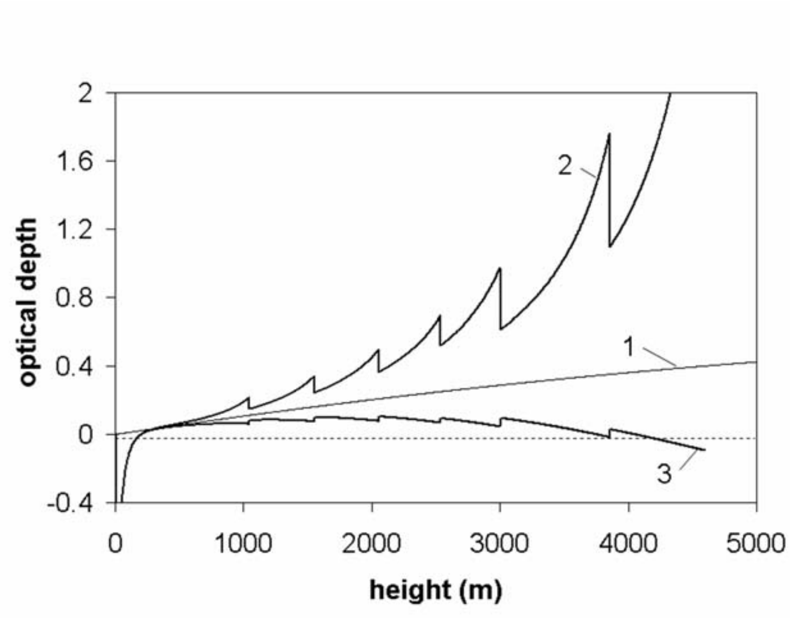

Figure 4.2. The same model optical-depth dependence as that in Figure 4. 1 (curve 1) and the optical-depth profiles obtained from the simulated multiangle measurements with a lidar when the remaining zero-line offset is not equal to zero. Curves 2 and 3 show the retrieved optical-depth profiles with estimated background levels of 201 and 199 bins, respectively, whereas the actual value is 200 bins.

In Figure 4.2 the number of points decreases towards the larger height range because of the condition r_{max} = const. for any slope direction. If the data points of the incomplete overlap zone are excluded from consideration, similar jumps occur at the beginning of range interval; it takes place when the number of points used in the regression increases. A more realistic situation, when both the random noise and systematic shifts present in the lidar signals, is shown in Figures 4.3 and 4.4. The simulated signals corrupted by noise and the systematic shifts are shown in Figure 4.3, and the optical depth retrieved from these signals is shown as the filled circles of curve 2 in Figure 4.4. Curve 1 in that figure is the same as that in Figure 4.2. Note that over the nearest range ~ 1000 – 2500 m the influence of the systematic distortions is more destructive than the influence of the moderate random noise. The increased data-point scattering at the high altitudes (3000 – 4500 m) is due to both signal noise and the decrease of number of points available for regression.

The results of this investigation revealed that even minor systematic distortions, the same as the relatively moderate signal noise of lidar data might significantly impede the use of the Kano-Hamilton method even in such an ideal horizontally homogeneous atmosphere.

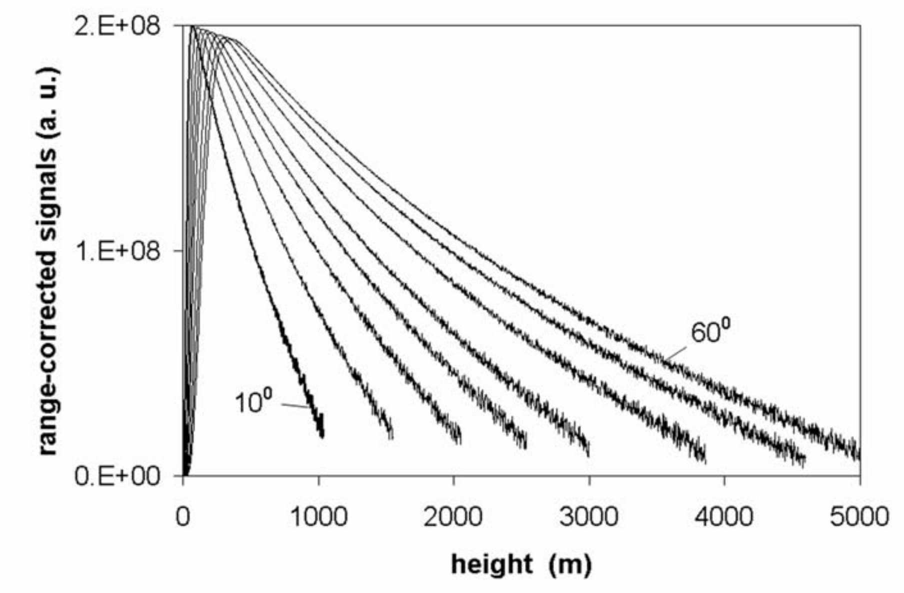

Figure 4.3. Simulated signals obtained for the same atmospheric conditions as that in Figures 4.1 and 4.2 but now corrupted with noise and systematic shifts, ΔB = -1 bin.

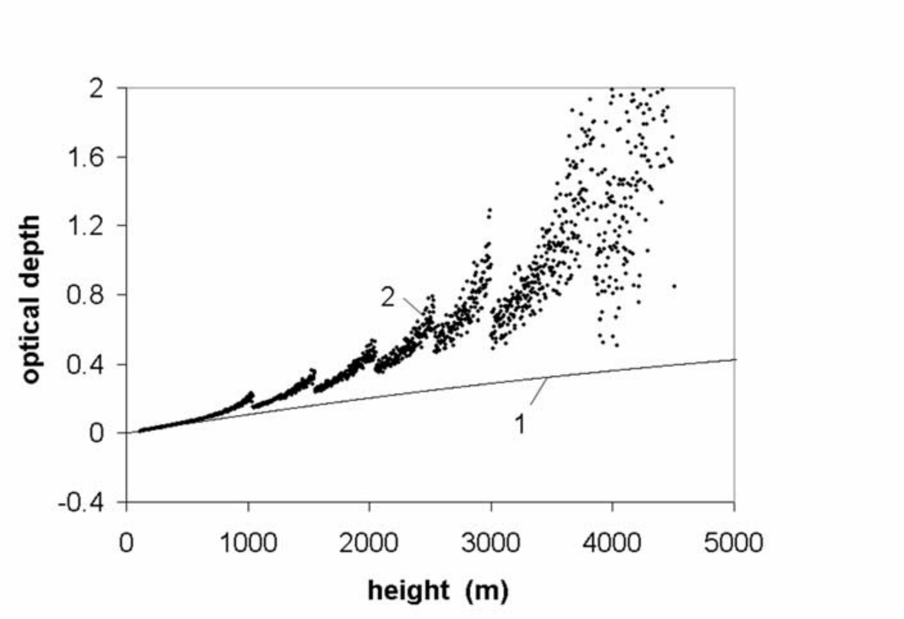

Figure 4.4. Optical depth retrieved from the signals in Figure 3 (filled circles); the thin line is the same as curve 1 in Figure 4.2.

Our analysis revealed that there exist at least three major sources of measurement uncertainty, not related with the atmospheric heterogeneity, which severely impede the multiangle measurements. These sources are related with specifics of the measured lidar data rather than with atmospheric heterogeneity. The first source, which has already been widely discussed in literature, is related to the general problem of the determination of slope in lidar data. Similar to DIAL (differential absorption lidar), high spectral resolution and Raman lidar measurements, the quantity that is regressed in the multiangle measurements is not normally distributed (*Whiteman*, 1999). Different ways have been proposed to improve the accuracy of the slope determination in lidar data (*Whiteman*, 1999; *Kunz and Leeuw*, 1993; *Rocadenbosch et al.*, 2000; *Rocadenbosch et al.*, 1998; *Rocadenbosch et al.*, 2004; *Volkov et al.*, 2002; *Kovalev*, 2002 a). However, they are more or less practical only under certain restrictions and conditions. The most common assumption being that random errors obey Gaussian (or Poisson) distribution and no systematic distortions in the inverted data are present. There is a big question as to how close the real lidar data follow the assumed distributions. In addition, systematic distortions in experimental data always exist, and these distortions might be a significant source of large multiangle measurement uncertainties. Moreover, different sources of the systematic distortions are responsible for the corruption of the lidar data over the near and distant ranges. The near-end distortions may be due to inaccuracies in determining the incomplete overlap zone, signal low-frequency noise components, distortions due to the restricted frequency range of the photoreceiver, and receiving optics aberrations. The second type of systematic distortions is distortions in lidar data, due to the signal offset (invariant or range dependant) that remains after subtraction of the signal background component. Note that the latter distortions in the inversed lidar data may occur even if the lidar signal is precisely measured. These distortions are extremely influential over the distant ranges, where the useful signal is found as a small difference of two large quantities. Finally, the imperfect measurement technologies and multiangle inversion methods, related with ignoring the above error sources, aggravate the problem.

Our analysis lead us to the strong conclusion that before lidar measurements in clear atmospheres are performed (either in one-directional or multiangle mode), the lidar should be properly tested, the possible signal and data distortions revealed, and lidar parameters, including the length of the incomplete overlap zone reliably determined (*Kovalev*, 2004 a). The conventional methods of determining the overlap function, based on the lidar horizontal measurements in a homogeneous atmosphere (*Sasano et al*. 1979; *Sassen and Dodd*, 1982; *Tomine et al*., 1989; *Dho et al*., 1997) have significant drawbacks; moreover, some of them are just impractical if the lidar is assigned for measurements (especially, multiangle measurements) in clear atmospheres. The first problem is that the accuracy of the overlap determination at distant ranges strongly depends on the accuracy of the determination of the signal zero line, especially in presence of signal distortions such as signal-induced noise or distortions due to low-frequency noise components. Any non-zero offset remaining in the lidar signal after the background component subtraction may significantly worsen the accuracy of determining the overlap function, even over relatively moderate distances from the lidar. In practice, it might also be an issue to find an appropriate lidar test site with flat terrain, open space in a horizontal direction, and with an extended zone of homogeneous atmosphere. Moreover, the estimate of the actual level of the atmospheric homogeneity during the overlap determination may be a challenge. The only practical criterion of the atmospheric homogeneity level is the linearity of the logarithm of the square range corrected signal over an extended range; however, the linearity of this function does not necessarily mean atmospheric homogeneity, especially in clear atmospheres. The determination of the overlap function in a moderately turbid atmosphere, as proposed in study (*Tomine et al.*, 1989) is not reliable if the lidar is designated for searching in clear atmospheres. Finally, for the scanning lidar, an additional requirement is that its overlap should not change with the change of the slope. This test cannot be performed using data from horizontal lidar measurements only.

Because the multiangle methods are extremely sensitive to any instrumental distortions in lidar data, it is quite tempting to use these methods not only for atmospheric measurements, but also for lidar tests and calibrations, including the determination of the effective lidar overlap (we will clarify this term later) and the lidar minimal and maximal measurement ranges, where the acceptable measurement accuracy can be achieved. We will show that such lidar tests may be performed using data of routine multiangle measurements. The data of multiangle measurements should always be properly analyzed to estimate the real level of atmospheric homogeneity, and actual quality of the performed atmospheric measurements. One should always make sure that the level of the atmospheric heterogeneity and measurement data distortions does not prevent obtaining acceptable measurement accuracy. Such a measurement technology is considered in the following sections.

4.2. Methodology

After theoretical analysis and numerical simulations, and based on thorough analyses of experimental data, we concluded that the existing multiangle measurement methodology for determining profiles of the extinction coefficient is not an accurate way to invert lidar measurement data. It is well known that the determination of slope in lidar data is an issue. Meanwhile, the existing multiangle methods, including the Kano-Hamilton method, require two consecutive slope-determination procedures. In the first, the discrete vertical optical depths, $\tau(0, h)$ from the ground level to height h are found by determining the slopes of the range-corrected signal logarithms. In the second step, the extinction coefficient profile is found with the numerical differentiation of the obtained optical depth of $\tau(0, h)$ versus height h. The both functions, the optical depth and the extinction coefficient, are extracted by determining the slopes of the noise-corrupted functions with unknown systematic shifts, so that the retrieved particulate extinction coefficient profiles are aggravated by large measurement errors. These errors are found as the product of the square root of the sum of squared uncertainties of the involved quantities, multiplied by a magnification factor. When extracting the extinction coefficient in clear atmospheres, the factor depends dramatically on the optical depth of the length of the range resolution used for the differentiation (*Russel and Livingstone*, 1984). Accordingly, the large, often unacceptable measurement uncertainty is the price for the resolved vertical extinction-coefficient profile.

There are three specifics in our modification of the conventional multiangle method. First, as it was proposed in the recent study in *Kovalev et al*. (2004 b), lidar scanning for each slope direction is made over an extended (wide) azimuthal range, and the signal, averaged over this azimuthal range, is used for the inversion. This allows us to reduce significantly the influence of the local atmospheric horizontal heterogeneity, especially close to the ground surface. Moreover, the standard deviation of the azimuthally averaged signal provides an estimate of the existing horizontal heterogeneity. The lidar signals from the azimuthal sectors, where significant inhomogeneity is found, should be excluded from the inversion. Second, no extinction coefficient profile should be derived until a sensible particulate optical-depth profile is obtained (the corresponding criteria will be discussed below). Third, we concluded that the determination of the particulate extinction profile through numerical differentiation of the derived optical depth profile is generally not practical in clear atmospheres, especially when measurements are made in the infrared region of spectra. It is worth mentioning that the latter is not unique to multiangle measurements only; the inversion of Raman and high spectral resolution lidar data has the same issue. There is a strong need to develop alternative processing methods for extracting the extinction-coefficient profiles in clear atmospheres from the transmission term. As a preliminary solution for multiangle measurements, we recently proposed a combination of the multiangle and optical depth solutions to solve the issue (*Kovalev et al*., 2004 b). This methodology is not discussed in this paper;

here we consider only the technology for obtaining the optical-depth profiles versus height, vertical profiles of the relative backscatter, and profiles of the effective lidar overlap which allows an estimation of lidar data quality and measurement conditions. In other words, our measurement technology is focused on determining the constants in the Kano-Hamilton equation.

With the assumption of a horizontally stratified atmosphere, the lidar signal $P_j(h)$ measured along the elevation angle φ_j can be written as

$$P_j(h) = \frac{Cq_j(h)\beta(h)}{\left(\frac{h}{\sin\varphi_j}\right)^2} e^{-\frac{2\tau(0,h)}{\sin\varphi_j}} \tag{4.1}$$

where C is a lidar system constant and $q_j(h)$ is the overlap function, normalized to one; in general case, $q_j(h = const.)$ is different for different slope angles, φ_j. $\beta(h)$ is the total (molecular and particulate) backscatter coefficient at the height h, that is $\beta(h) = \beta_m(h) + \beta_p(h)$; $\tau(0, h)$ is the total optical depth from the ground level to the height h, which also includes the molecular and particulate components, $\tau(0, h) = \tau_m(0, h) + \tau_p(0, h)$.

The dependence of the Kano-Hamilton function $y_j(h)$, defined as

$$y_j(h) = \ln\left[P_j(h)\left(\frac{h}{\sin\varphi_j}\right)^2\right] \tag{4.2}$$

taken versus independent $x_j = [\sin\varphi_j]^{-1}$ can be written as

$$y_j(h) = A(h) - 2\tau(0,h)x_j \tag{4.3}$$

here $P_j(h)(h/\sin\varphi_j)^2$ is the range-corrected lidar signals measured at the elevation angle φ_j and

$$A(h) = \ln\left[Cq_j(h)\beta(h)\right] \qquad (4.4)$$

In this method, the vertical optical depth, $\tau(0, h)$ from the ground level to the stepped heights, h_{min}, $h_{min}+\Delta h$, $h_{min}+2\Delta h$,… h_{max} is found, where Δh is a selected height resolution. For each height h, the least-square technique is applied using data points from the signals measured along different slope angles relatively to horizon, φ_j ($j = 1, 2, \ldots N$). However, the constants $A(h)$ and $\tau(0, h)$ in equation (4.3) may only be found if the overlap function at the heights h in equation (4.4) does not depend on the searching angle, φ_j. To achieve this, only the lidar signals over the complete overlap zone, where $q_j(h) = 1$, should be used. Accordingly, the minimal height for each slope direction, at which the lidar data can be used for the inversion, is restricted by formula $h_{min} = r_{min} \sin \varphi_j$, where r_{min} is the minimum measurement range defined by the length of the lidar incomplete overlap zone. Only after the removal the data points from incomplete overlap zone, one can determine an accurate linear fit for each dependence of $y_j(h)$ versus x_j and obtain quantities $\tau(0, h)$ and the intersect, $A^*(h)$. Note that now we denote the intercept of the linear fit as $A^*(h)$, whereas in equation (4.2) this function was denoted as $A(h)$. The difference between $A(h)$ and $A^*(h)$ is that the latter is determined from the data obtained after excluding "bad" data points from the assumed incomplete overlap zone. This allows us to define the function $A^*(h)$ as being independent on $q_j(h)$, that is, $A^*(h) = \ln [C\beta(h)]$. Note that the maximal lidar range, r_{max}, at which the lidar data are still acceptable for inversions should also be established, and all data at $r > r_{max}$ should be excluded from the inversion. Determining the best values of r_{max} in multiangle measurements is separate issue, which will be discussed later (section 4.4.2).

To clarify the selection of signal range intervals in the Kano-Hamilton inversion method, in Figures 4.5 and 4.6, experimental data points of the dependence of $y_j(h)$ on x_j are shown, calculated for the restricted altitude range intervals of 300 – 320 m and 580 – 600 m, respectively; here the height resolution is $\Delta h = 0.63$ m. The dependences were obtained with the Missoula Fire Sciences Laboratory (FSL) lidar, which operated at the wavelength 355 nm along the slope directions 6°, 7.5°, 9°, 12°, 15°, 25°, 35°, 45°, 60°, and 75°. For each elevation angle, a wide-range azimuthal scanning was made, and an azimuthal averaging of the range-corrected lidar signals was done. Such signal averages were obtained for all slope directions, recalculated as the functions of height, and then used for determining the data points of $y_j(h)$ for the discrete quantities of x_j in equation (4.3). Then an additional averaging of all data points was made by performing height-stepped averaging of $y_j(h)$ for each consecutive height h with the height step equal to 6 m (11 points). These averages were analyzed, and the "bad" sets of the data points were excluded from the consideration; only remaining "good" data points were used to determine the linear fit and calculate the constants in equation (4.3). To clarify the principle of removing the "bad" points, consider Figure 4.5. One can see that for the small values of x_j ($x_j < 2$), the independent $y_j(h)$ versus x_j increases rather than decreases with the increase of x_j. Such an increase can be, in principle, caused by two reasons: (a) the overlap function $q(r)$ is not range invariant in this range, or (b) the assumption of the horizontally homogeneous atmosphere is not valid in this area. The analysis of the data made for nearest heights shows that such a systematic increase of the dependence of $y_j(h)$ for the small x_j is typical for the small heights h; for increased heights the unphysical increase of $y_j(h)$ in this zone vanishes (Figure 4.6). This allows us to draw the conclusion that the change of the overlap with the range causes this systematic effect over low heights for large elevation angles. Obviously, these data points, where $q(r)$ = var., should be excluded from processing before the next inversion procedure, the determination of the slope of $y_j(h)$, is done. Note that in principle, the atmospheric inhomogeneity can also be a reason for the "incorrect" behavior of $y_j(h)$, but generally such distortions of $y_j(h)$ are significantly different. For every individual dependence of $y_j(h)$ on x_j, shown in these figures, the location of the maximum value of $y_j(h)$ may be found. In Figure 4.5, the maximal value of $y_j(h)$ for all individual profiles is located at $x_j = 2.37$, which correspond to the elevation angle 25°.

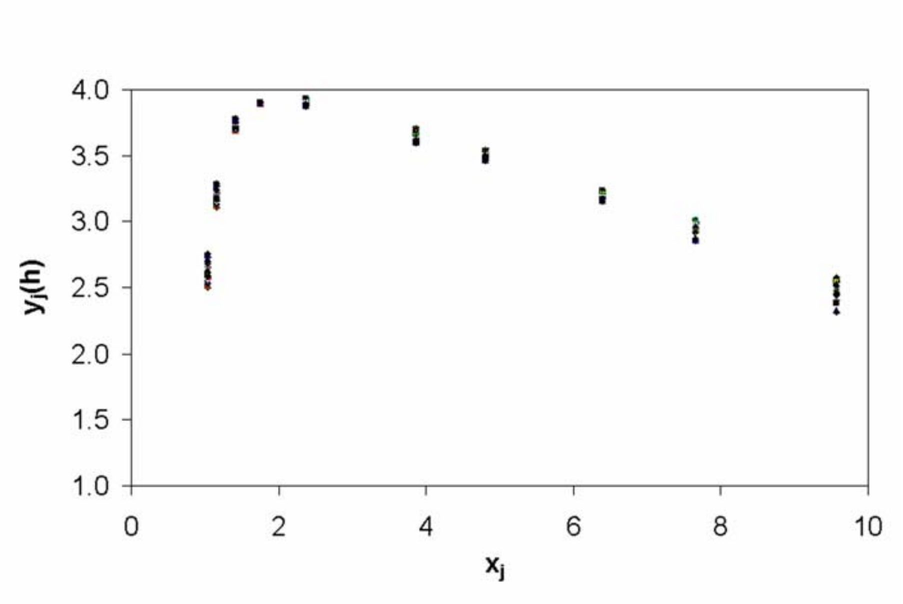

Figure 4.5. Experimental data points of the dependence of $y_j(h)$ on x_j for the altitude range interval from 300 to 320 m.

For the data shown in Figure 4.6, the maximum of all profiles of $y_j(h)$ is at x_j = 1.41 (the corresponding elevation angle is 45°). After determining the location of these maxima, all data-points located on the left side from these maxima should be excluded from further consideration, particularly, all data-points from the signals measured along slopes 35° – 75° in Figure 4.5 and along slopes 60° and 75° in Figure 4.6.

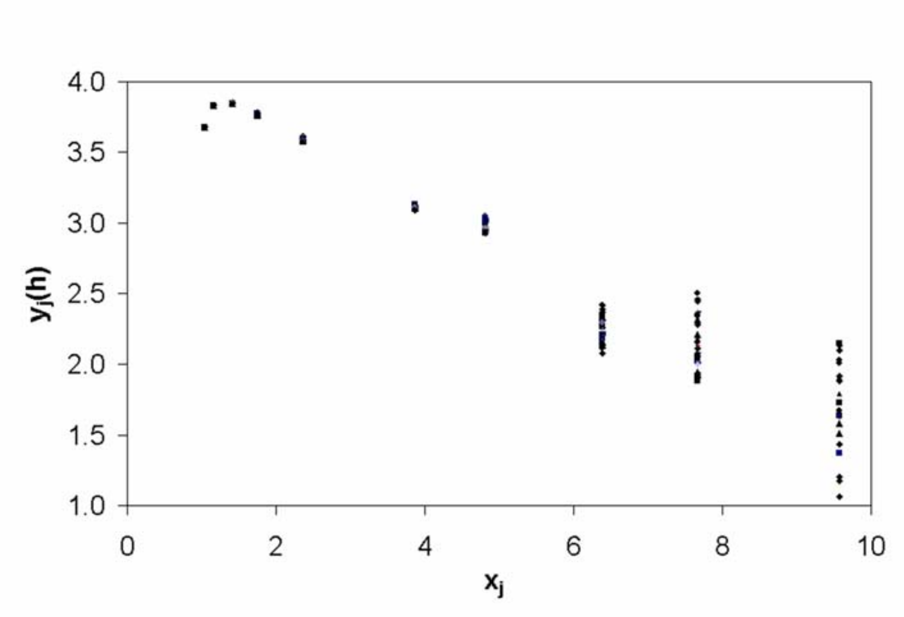

Figure 4.6. Same as in Figure 4.5 but for the altitude interval from 580 to 600 m.

After determining the location of these maxima, all data-points located on the left side from these maxima should be excluded from further consideration, particularly, all data-points from the signals measured along slopes 35° – 75° in Figure 4.5 and along slopes 60° and 75° in Figure 4.6.

The lidar incomplete overlap zone data points should not be used for inversion, particularly the data obtained over the large elevation angles at small heights. This restricts the use of the data points obtained in the lidar near zone. On the other hand, the useful maximum altitude range, up to which the data can be used for the inversion, is also restricted. As one can see in Figure 4.6, the data points $y_j(h)$ obtained under small elevation angles, 6°, 7.5°, and 9° within the altitude range 580 – 600 m (the corresponding x_j are equal 9.57, 7.66, and 6.39, respectively) are significantly scattered as compared with larger angles. For example, for the slope direction 6° ($x_j = 9.57$), the function $y_j(h)$ changes from 1.06 to 2.15. Meanwhile, in clear atmospheres, the scattering, which is proportional $2\tau(0,\ h)/\sin\ \varphi_j$ [equation (4.1)], should be insignificant. There could be two major sources of such a large data-point scattering, the random error, which dramatically increases after the signal square-range correction, and a non-zero systematic offset, ΔB, which at distant ranges becomes compatible with the backscatter signal of interest. Unfortunately, it is a common principle to ignore the latter factor in multiangle measurement analysis. Meanwhile, as is shown in the study (*Rocadenbosch et al.*, 2000), even for one-directional measurements, a relatively small offset, ΔB, destructively influences measurement accuracy over distant ranges; however, here this effect is masked, especially when using so-called "stable" solutions. In multiangle measurements, highly scattered data-points over the distant ranges just do not allow sensible measurement results, similar to the one-directional measurements in which the near-end solution is used.

Thus, the bad data points should be excluded both over the near incomplete overlap zone and from the distant ranges. Our analysis showed that the slope of the inversion results strongly depends on the selected maximum range, r_{max}. There is always some restricted range of acceptable maximum ranges from $(r_{max})_{min}$ to $(r_{max})_{max}$, which provides the best possible inversion results. The selection of the maximum range outside this range, that is, either less than $(r_{max})_{min}$, or larger than $(r_{max})_{max}$, results in increased distortions in the retrieved profiles of $A^*(h)$ and in $\tau(0,\ h)$. The principles and criteria for the selection of optimal values of r_{max}, are analyzed in detail in the experimental part of this chapter (subchapter 4.4.2).

A maximal altitude, h_{max}, up to which the profiles of $A^*(h)$ and in $\tau(0,\ h)$ can be determined should also be established, and its value is an additional restraint for the multiangle data processing. At this maximal height, the signals obtained under small elevation angles cannot be used for the inversion, otherwise, these had be taken from the distances larger than established r_{max}, that is, over ranges where the signal-to-noise ratio is poor. Meanwhile, to determine the values of $A^*(h)$ and in $\tau(0, h)$ at the heights close to and equal to h_{max}, there should be some minimal number of the data points, n_{min} for the regression. Moreover, to provide acceptable measurement accuracy, these data-points should be obtained over an angular sector, from φ_k to the maximal angle, φ_{max}, so that some established minimal sinus ratio $g = \sin \varphi_{max}/\sin \varphi_k$ is achieved. It follows from these considerations that the maximal height is found as

$$h_{\max} = r_{\max} \sin \varphi_k = r_{\max} \frac{\sin \varphi_{\max}}{g} \tag{4.5}$$

One should stress that the above established maximal height, h_{max}, is the maximum height for determining the quantities $A^*(h)$ and $\tau(0, h)$ only, and not for the retrieval of the extinction coefficient profile whose range is generally more restricted.

Our analysis showed that in some cases one can improve the inversion accuracy when determining the set of profiles $\tau_j(0, h)$ by using individual functions $y_j(h)$ and a smoothed $A^*(h)$ rather than by determining $\tau(0, h)$ directly through the slope of the linear fit for the dependence $y_j(h)$ versus x_j. Particularly, with the smoothed $A^*(h)$, the set of the vertical profiles $\tau_j(0, h)$ can be found with formula

$$\tau_j(0,h) = 0.5 \sin \varphi_j \left[A^*(h) - y_j(h)\right] \tag{4.6}$$

Using the set of the functions $y_j(h)$ one can obtain with equation (4.6) the corresponding set of $\tau_j(0, h)$, its mean value, $\tau(0, h)$, and the standard deviation of the mean. With an assumed (or balloon measured) vertical profile of the molecular extinction coefficient, the vertical molecular optical depth, $\tau_{mol}(0, h)$ and the particulate component, $\tau_{part}(0, h) = \tau(0, h) - \tau_{mol}(0, h)$, can be then calculated.

The two quantities, $A^*(h)$ and $\tau(0, h)$ are assumed to be used as boundary values when extracting the profiles of the backscatter and extinction coefficients. Then the corresponding extinction coefficient can be found using, for example, the method proposed in the study by *Kovalev et al.* (2004). However, an optimal methodology of deriving the extinction coefficient profiles still should be developed. This requires an additional investigation, which is beyond of this study. This study is confined to the methodology of obtaining the profiles of the optical depths $\tau(0, h)$ and the intercept $A^*(h)$ only. The analysis of both functions allows one to make grounded conclusions on the quality of the lidar data, and particularly, on whether the atmospheric conditions are favorable for applying the multiangle inversion algorithms. There are, at least, three criteria for the obtained optical depth dependence versus height, $\tau(0, h)$, that allows the determination of the quality of lidar data, the level of the horizontal atmospheric homogeneity, and the correct selection of $x_{i,min}$, $x_{i,max}$, r_{min}, and r_{max}. The criteria are as follows: (a) the retrieved total optical-depth, $\tau(0, h)$ has to be a positive function that increases monotonically within the measurement range from r_{min} to r_{max}. The presence of extended zones, where the optical depth monotonically decreases with the height, or zones where strong jumps of the retrieved function occur, means the poor quality of the data. If such zones are revealed over the far areas, the maximum measurement range should be reduced to exclude such data from further consideration. (b) In areas close to the minimum height, h_{min}, the function $\tau(0, h)$ should tend to zero when the height tends to zero; the presence of negative values of $\tau_p(0, h)$ in the near zone (Figure 4.1) means incorrect selection of r_{min}(c). The particulate optical depth dependence versus height, $\tau_p(0, h)$, obtained after subtracting the molecular component, $\tau_m(0, h)$ from $\tau(0, h)$ should meet the requirements cited in the items (a) and (b). If the optical depth profiles do not meet these requirements, a thorough analysis has to be made to determine the responsible factors, such as inhomogeneous layers, the remaining zero-line offset, extensive noise, etc.; if these factors cannot be compensated, the data-points at the corresponding ranges should be excluded before new values of $\tau(0, h)$ and $A^*(h)$ are recalculated. Additional analysis of the inversion data, obtained with different ranges of r_{max} can also be very helpful for estimating the quality of the retrieved data. As mentioned in the introduction, the quantity that is regressed in the multiangle measurements is not normally distributed. Because of this some systematic shifts in the profiles of $\tau(0, h)$ and $A^*(h)$ occur when noise corrupted data are regressed. The calculations and analysis of the set of such profiles, obtained with different r_{max}, allows one to determine an acceptable range from $(r_{max})_{min}$ to $(r_{max})_{max}$ where the revealed shifts are not destructive to the inverted data. Using such profiles, the mean functions $A^*(h)$, the vertical particulate optical depths, $\tau_{part}(0, h)$, and their standard deviations can be calculated to yield realistic estimates of the inverted data quality. Note that in clear atmospheres, the backscatter coefficient [and accordingly, $A^*(h)$] mostly gradually decreases with the height, and this might be an additional criterion of quality of the obtained data. For example, a systematic increase of the retrieved function $A^*(h)$ with the height over an extended altitude range might mean that something is wrong in the obtained results.

4.3. Determination of the lidar effective overlap

The procedures described in the previous section yield profiles of $A^*(h)$ and $\tau(0, h)$. These functions make it possible to calculate a synthetic range-corrected vertical signal, $Z^*_{90}(h)$, with compensated overlap changes down to a minimal height, which depends on minimal and maximal slopes used for the searching. The signal can be found as

$$Z_{90}^{*}(h) = \exp\left[A^{*}(h)\right] e^{-2\tau(0,h)} \tag{4.7}$$

and the corresponding range-corrected synthetic signals along the slope directions φ_j can be found as

$$Z_j^{*}(h) = e^{A^{*}(h)} e^{-\frac{2\tau(0,h)}{\sin\varphi_j}} \tag{4.8}$$

Now using both synthetic and the real signals for the slope direction φ_j [equations (4.8) and (4.1), respectively], one can calculate the lidar overlap function along this direction as

$$q_j(h) = \frac{P_j(h)\left(\dfrac{h}{\sin\varphi_j}\right)^2}{Z_j^{*}(h)} \tag{4.9}$$

The height-dependant functions $q_j(h)$, determined for different φ_j, may then be recalculated as the functions of the slope range, $q_j(r)$, and then averaged. This average will yield the best possible estimate of the lidar overlap function. Comparing the averaged overlap function with the individual functions $q_j(r)$, one can also determine whether the overlap function remains unchanged, without systematic shifts, while changing the lidar elevation angles during the scanning. In Figure 4.7 we present such overlap functions, $q_j(r)$, calculated with a set of simulated signals similar to that shown in Figure 4.3, but with no systematic shifts; the noise level is approximately the same as that for the signals in Figure 4.3. The minimal height at which the overlap function can be found with the data obtained along the smallest angles used for the simulation (10^{o} and 15^{o}), is h_{min} = 117 m; the minimal $q_j(r)$, found from the data from the maximal slope angle (60^o) measurements is $q_j(r)$ = 0.33. The corresponding minimal range at which the overlap function can be found is 135 m. One can see that in the assumed ideal atmosphere, the presence of the signal random noise does not significantly influence the overlap functions; on the not colored plot in this figure, they cannot even be discriminated from each other.

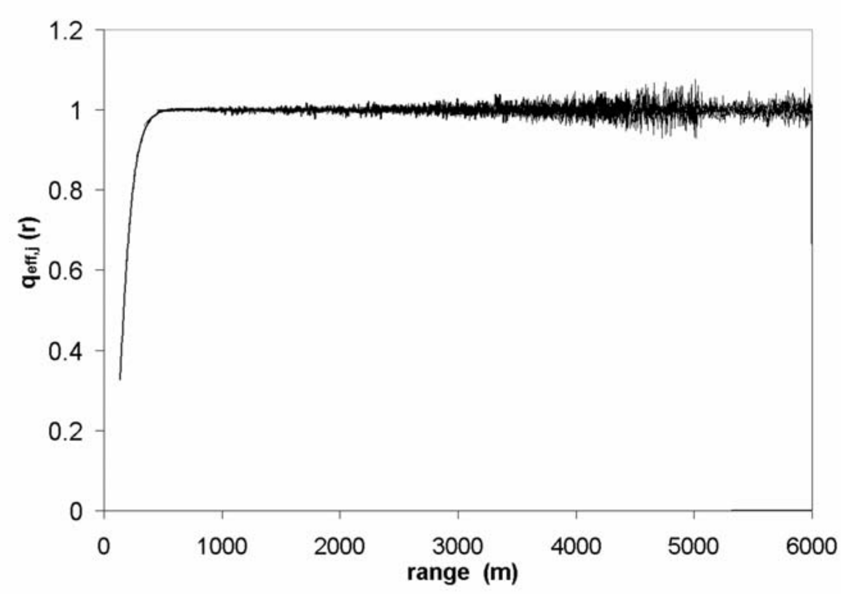

Figure 4.7. Overlap functions, $q_j(r)$, calculated with a set of simulated signals. The signal noise level is approximately the same as that for signals in Figure 4.3, but there are no systematic shifts corrupting the signals.

Equation (4.9) is valid under the condition that the signal $P_j(h)$ is not spoiled by a local inhomogeneity. Another assumed condition is that the signal has no systematic distortions. However, as we pointed out earlier, in real situations neither condition is necessarily true. It is unrealistic to expect that the standard deviation of the estimated component B is zero, so the background component, B, always has some non-zero uncertainty. In other words, the real lidar signal may contain some zero-line offset ΔB that remains after subtracting the estimated signal background component. Therefore, in more general form, Equation (4.9) should be written as

$$q_{j,eff}(h) = \frac{\left[P_j(h) + \Delta B\right]\left(\frac{h}{\sin\varphi_j}\right)^2}{\langle Z_j^*(h)\rangle} \tag{4.10}$$

where the shift ΔB can be either positive, negative or even range-dependent. Note that any shift also corrupts the functions $A^*(h)$ and $\tau(0, h)$, and accordingly, the synthetic signal, $Z^*_j(h)$. The corruption is generally minor, and does not influence the overlap $q_{j,eff}(h)$ significantly at distances close to lidar, where the initial uncorrected backscattered signal is large as compared to ΔB. However, at the distant ranges where the backscatter signal is found as the difference of the total signal $[P_j(h) + B]$ and the estimated component B_{est}, the weight of ΔB dramatically increases. Actually, when estimating the overlap function, even using conventional methods (*Rocadenbosch et al.*, 1998; *Volkov et al.*, 2002; *Kovalev*, 2002; *Rocadenbosch et al.*, 2004) we always determine some "effective" overlap function, $q_{eff}(r)$. The effective overlap is a function influenced by all signal distortions, including the non-zero offset, rather than the assumed theoretical function $q(r)$. Note also that the shape of $q_{j,eff}(r)$ at the distant ranges depends on whether the shift ΔB is positive or negative, and the calculated $q_{j,eff}(r)$ may have either a systematic increase or a systematic decrease from the unit with range. Because ΔB for different slopes will generally be different, and due to the presence of possible jumps in the functions $\tau(0, h)$ (Figure 4.4) and in $A^*(h)$, the shape of the averaged function, $q_{eff}(r)$ in the complete overlap zone may differ unpredictably from the unity. In Figure 4.8, a set of overlap functions $q_{j,eff}(r)$ similar to that presented in Figure 4.7 is shown.

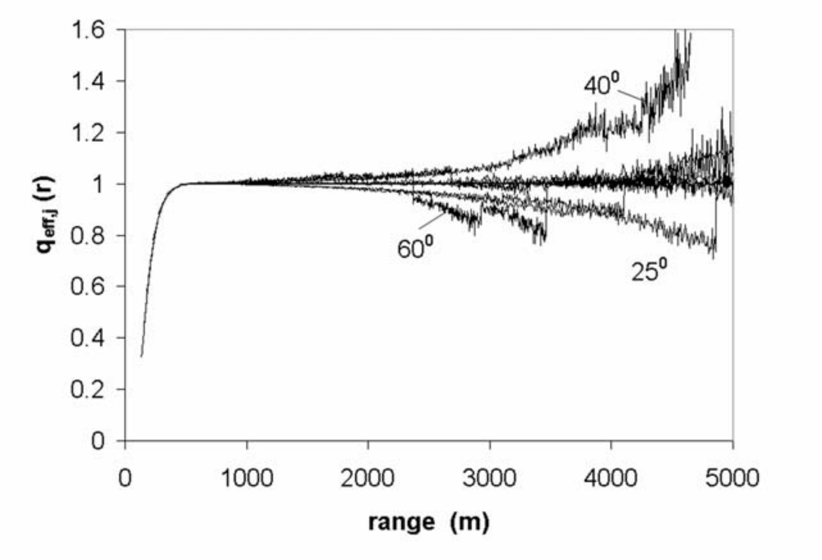

Figure 4.8. Same as that presented in Figure 4.7 but here the functions $q_j(r)$ are obtained when the signals, measured in the slope directions 25° and 30°, are corrupted by a systematic offset ΔB = -1 bin.

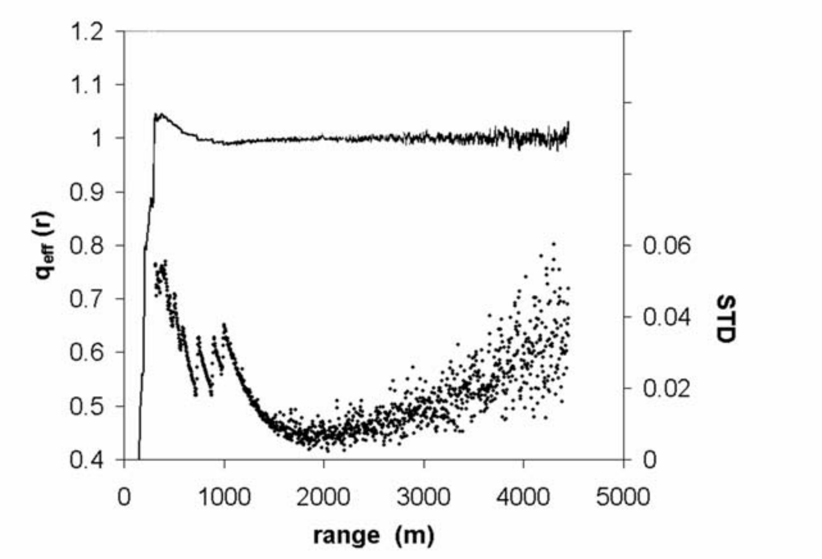

Figure 4.9. Mean function $q_{eff}(r)$ (bold curve) and its upper and bottom uncertainty boundaries, as estimated by its standard deviation (thin curves), obtained with an incorrect length for the complete overlap zone. Here the assumed length is 200 m, whereas the actual is ~ 450 m. The simulated lidar signals are corrupted only by random noise, the offsets ΔB = 0.

The signal noise level in both figures is the same; the only difference is that the curves in Figure 4.8 are obtained when signals are corrupted by both systematic distortions and random noise. Specifically, the two signals measured in the slope directions 25° and 30° were corrupted; the assumed background component for these signals was chosen to be 201 bins instead the actual value of 200 bins, or ΔB = -1 bin. One can see that the corruption of two signals may significantly distort the function $q_{j,eff}(r)$ found under other slope directions. In Figure 4.9, the mean function $q_{eff}(r)$ (thin curve) and its standard deviation (dots) versus range are shown assuming an incorrect length of 200 m for complete overlap zone used for the inversion (the actual length ~ 450 m). In this case, the signal data points from the part of the incomplete overlap zone, over the range 200 – 450 m, are not excluded from the inversion. The simulated lidar signals are corrupted only by random noise; no systematic shifts exists, so that $\Delta B = 0$. One can see that in this case systematic wave-like deviations of $q_{eff}(r)$ from the unit may occur in the near field areas close to r_{min}. This figure shows that to yield good inversion results, the accurate determination of the length of the incomplete overlap zone is required in order to avoid the use of the bad data points when determining the linear fit for the dependence of $y_j(h)$ on x_j. Concrete criteria that were used to exclude such bad points in our experimental data are considered in subchapters 4.4 and 4.5 (see *Adam et al*., 2005). Note that there might be also other types of systematic signal distortions, caused for example, by a restricted receiver frequency band, effects of inhomogeneous photomultiplier sensitivity (*Simeonov et al.,* 1999*)* etc. that can cause similar distortions in the retrieved effective overlap.

4.4. Instrumentation and measurement procedures

In the next sections we analyze the experimental data obtained from the lidar signals measured in clear atmospheres with the methodology described above (*Adam et al.*, 2005). The experiments were performed at the Fire Science Laboratory (FSL) test site located in mountainous terrain, approximately 20 miles to the west of the city of Missoula (Montana, USA) at an altitude of ~ 1000 m. The measurements were made in clear atmospheres, in conditions with small optical depths over the measurement range, when extremely accurate determination of the slope of the logarithm of the square range-corrected signal is required to get acceptable measurement results.

4.4.1. Instrumentation

Two scanning lidars were used in the test experiments: the FSL lidar and the Johns Hopkins University (JHU) lidar (Figure 2.10). The lidar systems have the following technical characteristics (Table 4.1):

4.4.2. Measurement procedures

The main steps in the measurement procedures, which allow the determination of the multiangle solution constants (the Kano-Hamilton constants) and the lidar overlaps function (section 4.2) are the following:

- Lidar measurements at the number of selected elevations are made. At each single slant path, 30 shots were averaged. To reduce the influence of atmospheric horizontal heterogeneity, the mean of 50 azimuth angle scans taken at 1^{o} steps was calculated and used for the inversion.
- Once the mean of the 50 azimuth angle scans for each elevation is determined, the signal background component is subtracted from the mean, and the

logarithm of the square-range corrected signal [that is, the function $y_j(h)$ as defined in equation (4.3)] is calculated.

	FSL Lidar	**JHU Lidar**
Laser	Q-switch Nd-YAG	Q-switch Nd-YAG
Wavelengths	1064 nm, 355 nm	1064 nm, 532 nm, 355 nm
Receiver	25.4 cm Cassegrain Telescope	25.4 cm Cassegrain Telescope
Detectors	1064 nm - Chilled, IR-enhanced Si Avalanche Photodiode 355 nm - Photomultiplier	1064 nm - IR-enhanced Si Avalanche Photodiode 355 nm and 532 - Photomultiplier
Light pulse duration	~10 ns	~10 ns
Configuration	Biaxial	Coaxial
Resolution	6 meters	6 meters
Scanning capability	Azimuth 0º - 180º Elevation 0º -90º	Azimuth 0º - 180º Elevation 0º - 90º
Maximum range	12288 meters (2048 bins)	12288 meters (2048 bins)
Digitizers	Dual 12-bit, 125 MHz	Dual 12-bit, 100 MHz

Table 4.1. FSL and JHU Lidar systems parameters

- For each height h, the function $y_j(h)$ is plotted versus x_j, where $x_j = 1/\sin \varphi_j$. Next, all "bad" data points of the function $y_j(h)$ are determined and excluded. These bad points are determined according to the principles discussed in sections 4.1 - 4.2; the concrete criteria will be discussed below.

- The linear fit for the function $y_j(h)$ versus x_j is found which gives us the regression constants, the intercept $A^*(h)$, defined as $A^*(h) = \ln [C\beta(h)]$, and the total optical depth [$\tau(0, h) = -$ slope/2]. [In some cases a more accurate profile of $\tau(0, h)$ can be obtained when using individual functions $y_j(h)$ and smoothed $A^*(h)$ in equation (4.6)].
- The set of synthetic lidar signals $Z_j^*(h)$ is computed [equation (4.8)] using unsmoothed $A^*(h)$ and $\tau(0, h)$ obtained from the linear fit. The corresponding set of the effective overlap functions $q_{j,eff}(h)$ is determined as the ratio of the corresponding range-corrected signals to $Z_j^*(h)$ [equation (4.9)]. These height-dependant functions are then recalculated as functions of the slope range r and averaged to obtain a mean value of the overlap function $q(r)$ (for simplicity, the subscript '*eff*' in the overlap function from here on is omitted).

In order to provide the best inversion results and to estimate the data quality, the calculations of $A^*(h)$ and $\tau(0, h)$ are made using a set of discrete maximal ranges, from $(r_{max})_{min}$ to $(r_{max})_{max}$ (sections 4.1 - 4.2); their means and standard deviations provides us with practical estimates of the measurement uncertainty and its dependence on height. We should stress that in this subchapter, tasks are restricted to those related with the practical application of the Kano-Hamilton method, particularly, the determination of the functions $\tau(0, h)$ and $A^*(h)$. We do not consider the determination of the extinction coefficient profile, the backscatter coefficient profile, or the lidar constant. This is the subject of section 4.6.

Let us consider some details of our measurement methodology and data processing procedures. The first problem that arises in the lidar measurements is the subtraction of the signal background component. It is well known that accurate background subtraction is a serious issue, especially when measurement is performed in a clear atmosphere. When conventional commercial digitizers are used, even a few bins of uncertainty in the estimated background component can dramatically affect the measurement accuracy (*Zhao*, 1999). In multiangle measurements, the small systematic offset remaining after background subtraction can either significantly overestimate the measured optical depth (and accordingly, the particulate loading), or yield erroneous negative values of the extinction coefficients over distant ranges. Generally, the determination of the background level is made by determining a minimum averaged signal, $P(r)$, somewhere over a far-end range region, where the backscatter component is assumed to be indiscernible from zero, that is, where the measured signal is completely due to the background component. The problem is that the actual background component level can be masked by low frequency noise, so that the signal varies slightly but permanently over the entire far-end range. This problem, which has been widely discussed in literature (see, for example, *Zhao*, 1999, *Bristow*, 2002, *Lee et al*., 1990, *Kovalev*, 2004), has no general solution, so we tried different methods to solve it. Our best results were obtained when we determined a linear fit of the signal over the far-end range, computed the slope of the fit, and then extrapolated it to $r = 0$. To determine the linear fit of the background subtraction, 300 bins (1800 m) over the far-end range was used for FSL data and 600 bins (3600 m range) for JHU data (due to more noise). Since we recorded data out to ~ 12 km, there were many chances to get signals from clouds. We visually checked the results since the above background subtraction algorithm gives erroneous results in the case of the clouds. In those cases, a range interval for the linear background was manually chosen. Details are given in Appendix VI. The effect of a bad background subtraction can clearly be seen, especially when determining the effective lidar overlap.

The selection of the optimum number of the elevation angles requires special attention. Initially we selected 10 angles (6, 7.5, 9, 12, 15, 25, 35, 45, 60 and 75 degrees); later we used 14 angles (6, 7.5, 9, 12, 15, 18, 22, 26, 32, 40, 49, 58, 68 and 80 degrees), that is, we increased the number of slant paths for the large slopes, using 9 slope searching directions instead the initial 5 slope angles for angles greater than 15^{o}. The total time required for obtaining an entire set of lidar data was, approximately, 22 and 30 minutes, respectively. The change towards a larger number of elevations was done after the analysis of the measurement results obtained with the 10 angles. The main requirement when choosing the searching slope directions is that the number of angles selected within the range of x_j close to unit ($x_j \sim 1 - 1.4$) should be high enough to get acceptable measurement accuracy when determining the linear fit of $y_j(h)$ versus x_j at high altitudes.

General criteria to determine the operative range for the dependence $y_j(h)$ versus x_j are considered in section 4.2. Because of restricted measurement ranges of lidar, only the signals measured over the range $r \leq r_{max}$ may be used for the inversion. There are different criteria for determining the maximum range, r_{max}; the simplest (and most sensible) is the selection of the initial maximal range where the signal-to-noise ratio, SNR = 1 (see Appendix VI for more details about estimation of SNR = 1). For the case of multiangle measurements, it corresponds to the limitation of the height for each slope range such that $h_{max,j} = r_{max}\sin\,\varphi_j$ (criterion 1). The beginning of the selected range for $y_j\,(h)$ was chosen as following. First, we exclude all nearest data points at the ranges up to 100 $\sin(\varphi_j)$ m from the maximum of $y_j(h)$ versus height (criterion 2) or 100 m when reporting to range. Then we determine the location of the maximum of $y_j(h)$ for the dependence of $y_j(h)$ versus x_j and exclude all points that are located on the left side of that maximum (criterion 3). The next step is to compute constants (the slope and intercept) of the linear fit of the dependence $y_j(h)$ versus x_j through linear regression. To perform accurate regression of $y_j(h)$ versus x_j at heights close to h_{max}, the additional restrictions are implemented: at the maximal height, h_{max}, at which the linear fit constants are determined, one should have at least n_{min} points for the regression (as referred in section 4.2) (criterion 4). Initially we chose $n_{min} = 4$ points (case of 10 angles), and later $n_{min} = 6$ points (the case of 14 angles). With these criteria, the functions $\tau(0, h)$ and $A^*(h)$ are calculated from Equation 4.2. Note that these criteria 2 and 3 (similarly to local atmospheric heterogeneity) can induce gaps for the derived functions $\tau(0, h)$ and $A^*(h)$ within the initially selected altitude range $[h_{min}, h_{max}]$, where these functions cannot be determined. Accordingly, it is possible to have situations when at certain heights, a linear fit for the dependence $y_j(h)$ versus x_j cannot be determined. This situation generally occurs when the data are not good enough, and in the most cases, this is due to the atmospheric heterogeneity and inaccuracies in the background subtraction.

After the functions $\tau(0, h)$ and $A^*(h)$ are found, the synthetic signal and the overlap function can be calculated [equations (4.7) and (4.9)]. To obtain statistically significant results, we determine ranges of r_{max} over which no large systematic shifts in the derived functions occur, and repeat the above-described procedures using discrete values of r_{max} within the established range from $(r_{max})_{min}$ to $(r_{max})_{max}$. Next, we compute the mean values for the unknown functions $\tau(0, h)$, $A^*(h)$, and the overlap, $q(h)$. For the wavelength 355 nm, the best results during the first days of measurements (10 angles) were obtained for the ranges up to $(r_{max})_{max} = 4000$ m, and for the last days $(r_{max})_{max} = 7000$ m (14 angles and different set up for the FSL lidar). Note that values of $(r_{max})_{min}$ that are too small also yield increased measurement errors because of the decrease in number of data points that remain available for regression.

The minimal acceptable range for the FSL and JHU lidars at 355 nm is $(r_{max})_{min}$ = 2000 m. Obviously, the optimal measurement range for each lidar differs from wavelength to wavelength. Discussion on this issue with the corresponding measurement results will follow below. A detailed example of the measurement procedure is given in Appendix VII.

Backscatter signals of the JHU lidar had an increased level of electronic noise, which we were not able to remove completely during the experiment. To denoise these signals, we used the wavelet technique (see *Strang and Nguyen*, 1996; *Matlab*). Denoising by wavelets impose a threshold over the wavelet coefficients such that the reconstructed signal is a low pass version of the original signal. In other words, the wavelet is related to a low pass filter and a high pass filter. The low pass filter applied to the original signal gives a series of approximation coefficients whereas a high pass filter gives a series of detail coefficients. Denoising implies reconstruction of the signal using only the approximation coefficients. Since strong wavelet smoothing of the initial lidar data can implement undesirable systematic shifts in the inverted data, we used a wavelet (db10) with a minimum amount of denoising (level 2). Because of the small level of denoising, some high-frequency noise still remained and it can be seen in the inverted JHU lidar data.

4.5. Results and discussion

The experiment was performed during six days between 28 February and 6 April 2005, and several sets (sequences) of data (from 1 to 4) per each day were recorded. The increase of the number of elevation angles from 10 to 14 significantly improved the quality of data obtained during the final two days. During the experiment, the electronic noise in the FSL lidar data was generally much less than in the JHU lidar;

therefore, here the results of the former will mainly be discussed. A few examples will be given to demonstrate the agreement between the FSL and JHU lidar data at 355 nm and show the differences in overlaps for different wavelength channels.

When starting our experiments, we anticipated that in clear atmospheres, where the particulate loading is comparable with the molecular loading, the basic condition of the Kano-Hamilton method, that is, the requirement of the horizontally stratified atmosphere, would be better met with the shorter wavelengths. The experiment showed that in all cases the backscatter signal at 355 nm, where the molecular component is larger, yielded the best inversion results as compared to the signals at 532 and 1064 nm. Therefore, we will first focus on the inversion results obtained from the lidar signals at 355 nm.

A typical example of experimental data obtained with the FSL lidar on April 6, 2005 with the use of 14 elevation angles is shown in Figure 4.10. In Figure 4.10 (a), the range corrected signals $P(h)[h/\sin(\varphi)]^2$ are shown on the top plot, and their logarithms, the functions $y_j(h)$, on the middle plot. The function $P(h)$ shows the selected signal over the range where SNR ≥ 1. The lower plot presents a selected range of the function $y_j(h)$ after implementing restrictions established by the four criteria. The forth "drastic" criterion, related with the minimal value of n_{min}, reduces the height interval from the initial h = 6894 m (corresponding to r_{max} = 7000 m) to h = 3700 m. Figure 4.10 (b) represents the total optical depth $\tau(0, h)$, which increases with the height, and the intercept $A^*(h)$, which decreases with height (the upper and lower plot, respectively). The dotted curve on the upper plot represents the molecular optical depth at 355 nm. Both optical depths are accumulated from the ground level to the height h. Note the jumps in $\tau(0, h)$ and $A^*(h)$ in Figure 4.10 (b), especially noticeable over the distant ranges. As explained in section 4.2, these jumps are related with the change in the number of points used in regression. More precisely, a jump occurs when the number of points used in regression increases (at the beginning of the height interval) or decreases (towards the end of height interval); however, according to the analysis in the sections 4.1 - 4.3, this can occur only if atmospheric inhomogeneity exists in this area, or signal distortions are not completely removed. In Figure 4.10 (b) one can clearly see the discontinuities in $A^*(h)$ around 3100 m, 2600 m, etc., which corresponds to the exact location where $y_j(h)$ ends for the slope directions 26^o and 22^o, respectively. Accordingly, the number of points available for regression changes from 8 to 7 and then from 7 to 6 [see Figure 4.10 (a), lower plot]. In Figure 4.10 the inversion results obtained with the fixed maximal range, r_{max} = 7000 m, are shown. The best way to examine the robustness of the inversion results and estimate the solution uncertainty is the determination of the set of the functions $\tau(0, h)$ and $A^*(h)$ with different r_{max}, and then estimate their mean values and STD. Such mean functions obtained from the same set of data as the functions shown in Figure 4.10, but now with different r_{max}, are presented in Figure 4.11. The first three plots show the mean functions of $\tau(0, h)$, $\tau_p(0, h)$, $\exp[A^*(h)]$, and their uncertainty boundaries, as determined by their standard deviations. In the bottom plot, the relative STD of the exponent function is shown, which does not exceed ~ 10 % up to a height of ~ 3000 m. Here and further we present the exponent function of the intercept, that is, $\exp[A^*(h)] = C[\beta_p(h) + \beta_m(h)]$, because the exponential function will be used in our future investigations to determine the vertical profile of the particulate backscatter coefficient when the constant C is someway determined (this may be achieved, for example, by using the assumption of an aerosol-free atmosphere at high altitudes). The relative STD of the exponential will equal the relative STD of the aerosol backscatter coefficient when the lidar constant is accurately determined.

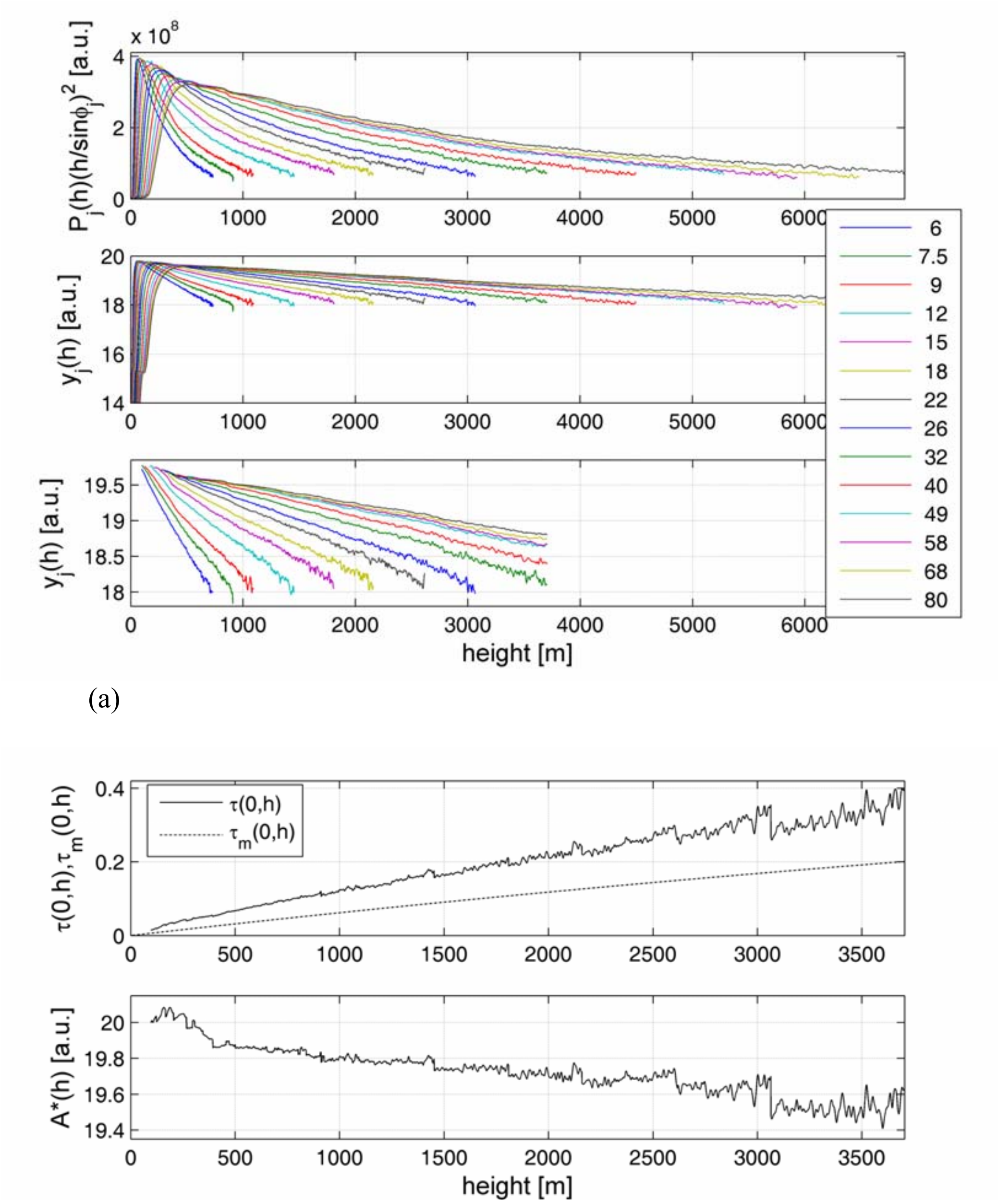

(a)

(b)

Figure 4.10. FSL lidar data from the 355 nm channel, measured on April 6, 2005, Sequence 2, r_{max}=7000 m. (a) Range corrected signals $P_j(h)[h/\sin(\varphi_j)]^2$ (upper plot), $y_j(h) = \ln [P(h)[h/\sin(\varphi_j)]^2]$ (middle plot), and the functions $y_j(h)$ after removal of "bad" data points according to the criteria (1) – (4) (lower plot); (b) Total optical depth, $\tau(0, h)$ and the molecular optical depth, $\tau_m(0, h)$ shown as the solid and dotted curves, respectively (upper plot), and the intercept $A^*(h)$ (lower plot).

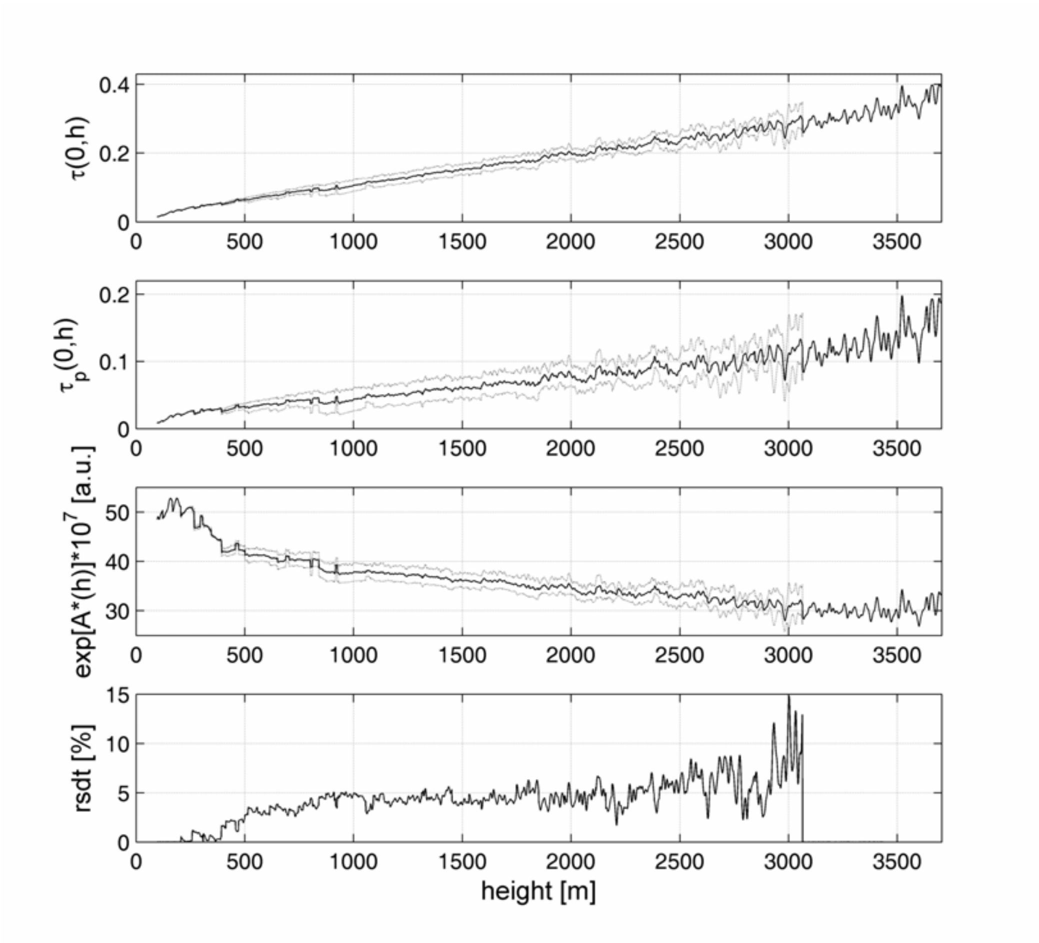

Figure 4.11. FSL lidar data from the 355 nm channel, measured on April 6, 2005, Sequence 2. The data presents mean values obtained from the functions of interest, calculated with the set of different maximal ranges, particularly, $r_{\max}$ = 2000 m, 2500 m, 3000 m, … 7000 m. On the first three plots from the top, the mean functions of $\tau(0, h)$, $\tau_p(0, h)$, and $\exp[A^*(h)]$ are shown. The lower plot represents the relative STD for $\exp[A^*(h)]$.

In Figure 4.12 the results for the optical depths and the corresponding exponential functions, $\exp[A^*(h)]$, retrieved from the data of the two lidars at the wavelength 355 nm, are shown. In Figures 4.12 (a) - (d) the initial measurement results for two lidars are shown, obtained in the beginning of our investigation when 10 slope directions were used. For February 28, both sequences, the JHU lidar data were not very good and the results were not trusty [(a) and (b)]. On March 4, the FSL data were noisier as usual. Even so, the two lidar results are comparable for 1400 m. For sequence 2 (c) FSL data presents a kink between 300 m and 400 m due to a non homogeneity (probably a cloud) which for some reasons was not recorded with JHU lidar. Similar behavior was seen in the last two days of measurements where either JHU lidar [(g)] or FSL lidar [(h), (j), and (k)] revealed the presence of a nonhomogeneity. The inversion results obtained during the last days, when the measurements were made along 14 slope directions, are shown in Figures 4.12 (e) – 4.12 (k). Our analysis of the 355 nm data obtained during the last two days showed that over ranges of up to 1600 m (the longest range for the JHU lidar), the optical depth for FSL lidar ranged largely between 0.15 and 0.2, while the optical depth for JHU lidar over the same range was between 0.16 and 0.25. The relative error between them ranged from 0 % to 23 % except one case when the relative error was about 66 %.

Now let us briefly discuss general results obtained with our lidars for other wavelengths. Figure 4.13 presents an example of the results from JHU lidar data, taken with the 532 nm channel. One can see that the retrieved profiles of $\tau(0, h)$ and $\exp[A^*(h)]$ meet the established criteria for the heights from a few hundred meters up to ~ 1 km. Note that the height interval over which the optical depth profiles extracted from the 532 nm data obey criteria (a) and (b) is significantly less than that of the 355 nm case.

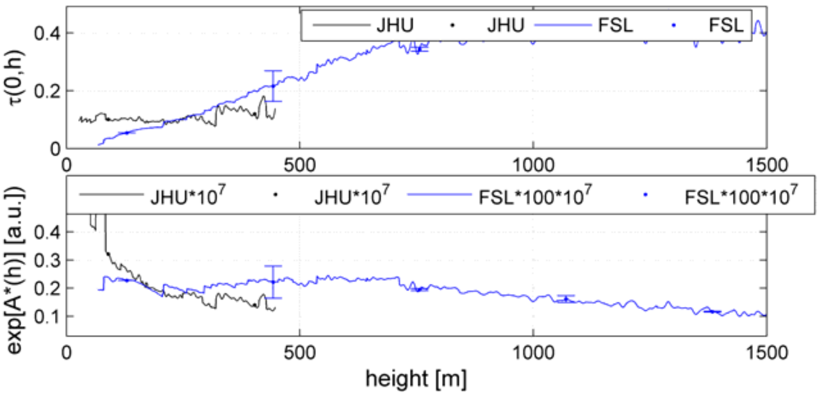
τ(0,h)
JHU
JHU
FSL
FSL
0
0.2
0.4
0
500
1000
1500
exp[A*(h)] [a.u.])
JHU*10^7
JHU*10^7
FSL*100*10^7
FSL*100*10^7
0.1
0.2
0.3
0.4
height [m]

(a)

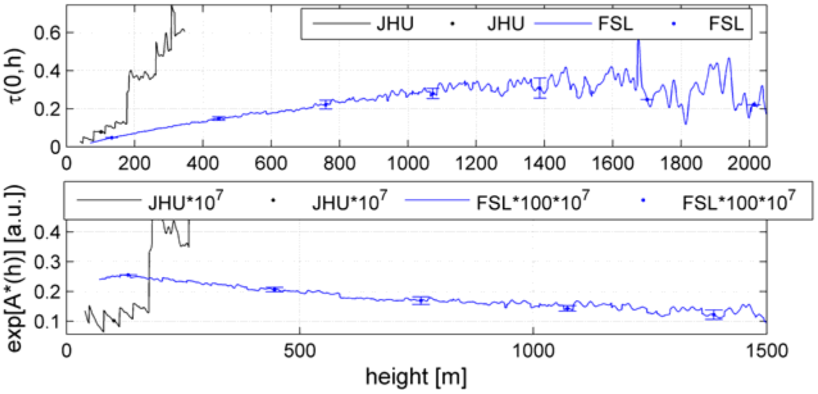
τ(0,h)
JHU
JHU
FSL
FSL
0
0.2
0.4
0.6
0
200
400
600
800
1000
1200
1400
1600
1800
2000
exp[A*(h)] [a.u.])
JHU*10^7
JHU*10^7
FSL*100*10^7
FSL*100*10^7
0.1
0.2
0.3
0.4
0
500
1000
1500
height [m]

(b)

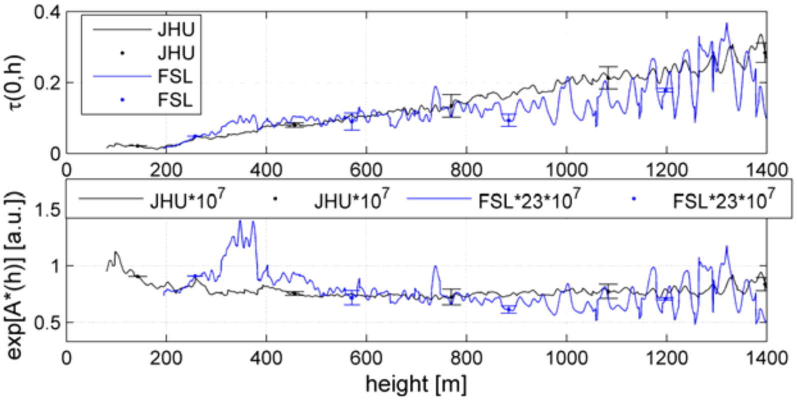
τ(0,h)
JHU
JHU
FSL
FSL
0
0.2
0.4
0
200
400
600
800
1000
1200
1400
exp[A*(h)] [a.u.])
JHU*10^7
JHU*10^7
FSL*23*10^7
FSL*23*10^7
0.5
1
1.5
height [m]

(c)

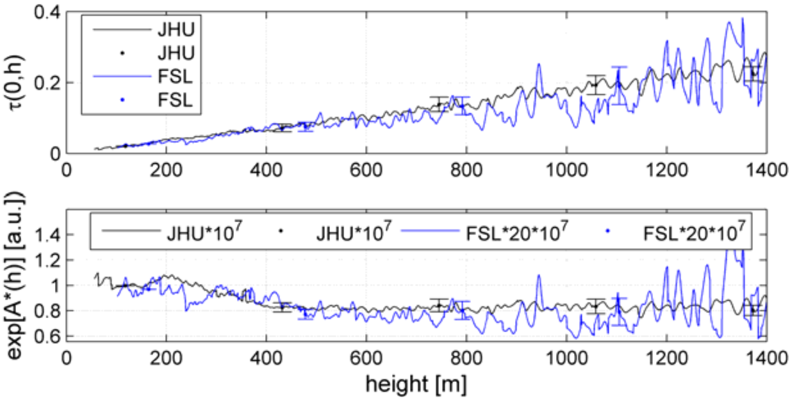
τ(0,h)
JHU
JHU
FSL
FSL
0
0.2
0.4
0
200
400
600
800
1000
1200
1400
exp[A*(h)] [a.u.])
JHU*10^7
JHU*10^7
FSL*20*10^7
FSL*20*10^7
0.6
0.8
1
1.2
1.4
height [m]

(d)

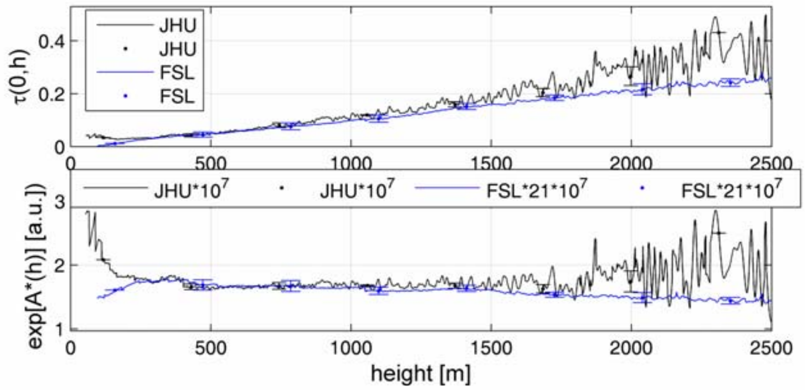

JHU
JHU
FSL
FSL
τ(0,h)
0
0.2
0.4
0
500
1000
1500
2000
2500
JHU*10^7
JHU*10^7
FSL*21*10^7
FSL*21*10^7
exp[A*(h)] [a.u.])
1
2
3
height [m]

(e)

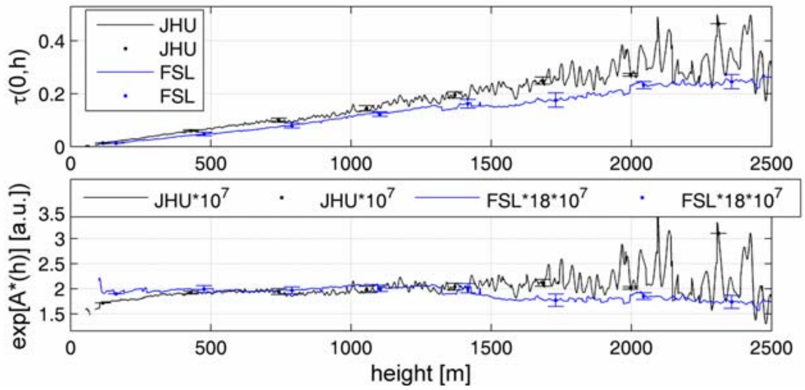

JHU
JHU
FSL
FSL
τ(0,h)
0
0.2
0.4
0
500
1000
1500
2000
2500
JHU*10^7
JHU*10^7
FSL*18*10^7
FSL*18*10^7
exp[A*(h)] [a.u.])
1.5
2
2.5
3
3.5
height [m]

(f)

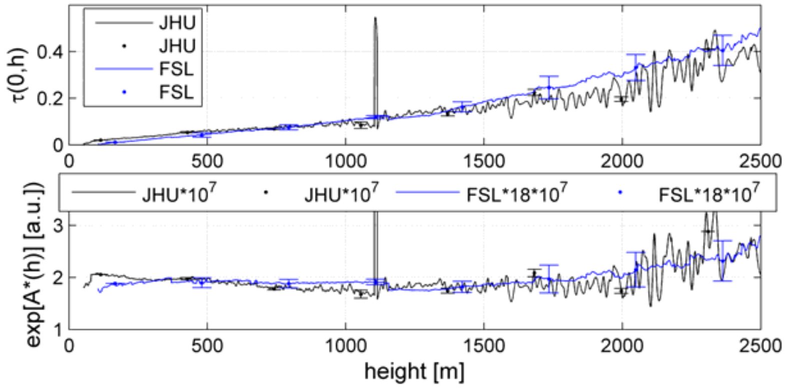

JHU
JHU
FSL
FSL
τ(0,h)
0
0.2
0.4
0
500
1000
1500
2000
2500
JHU*10^7
JHU*10^7
FSL*18*10^7
FSL*18*10^7
exp[A*(h)] [a.u.])
1
2
3
height [m]

(g)

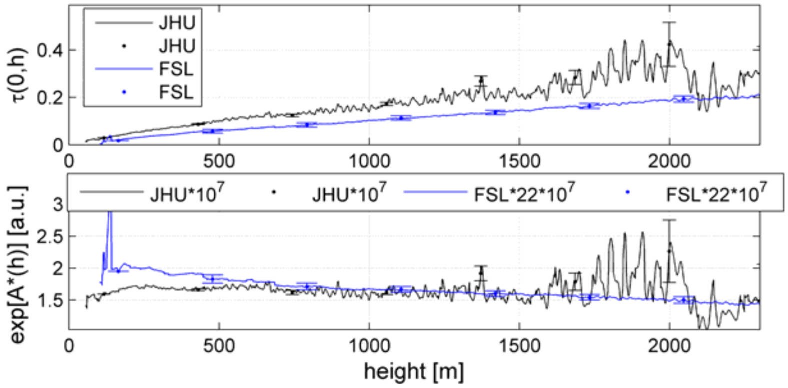

JHU
JHU
FSL
FSL
τ(0,h)
0
0.2
0.4
0
500
1000
1500
2000
JHU*10^7
JHU*10^7
FSL*22*10^7
FSL*22*10^7
exp[A*(h)] [a.u.]
1.5
2
2.5
3
height [m]

(h)

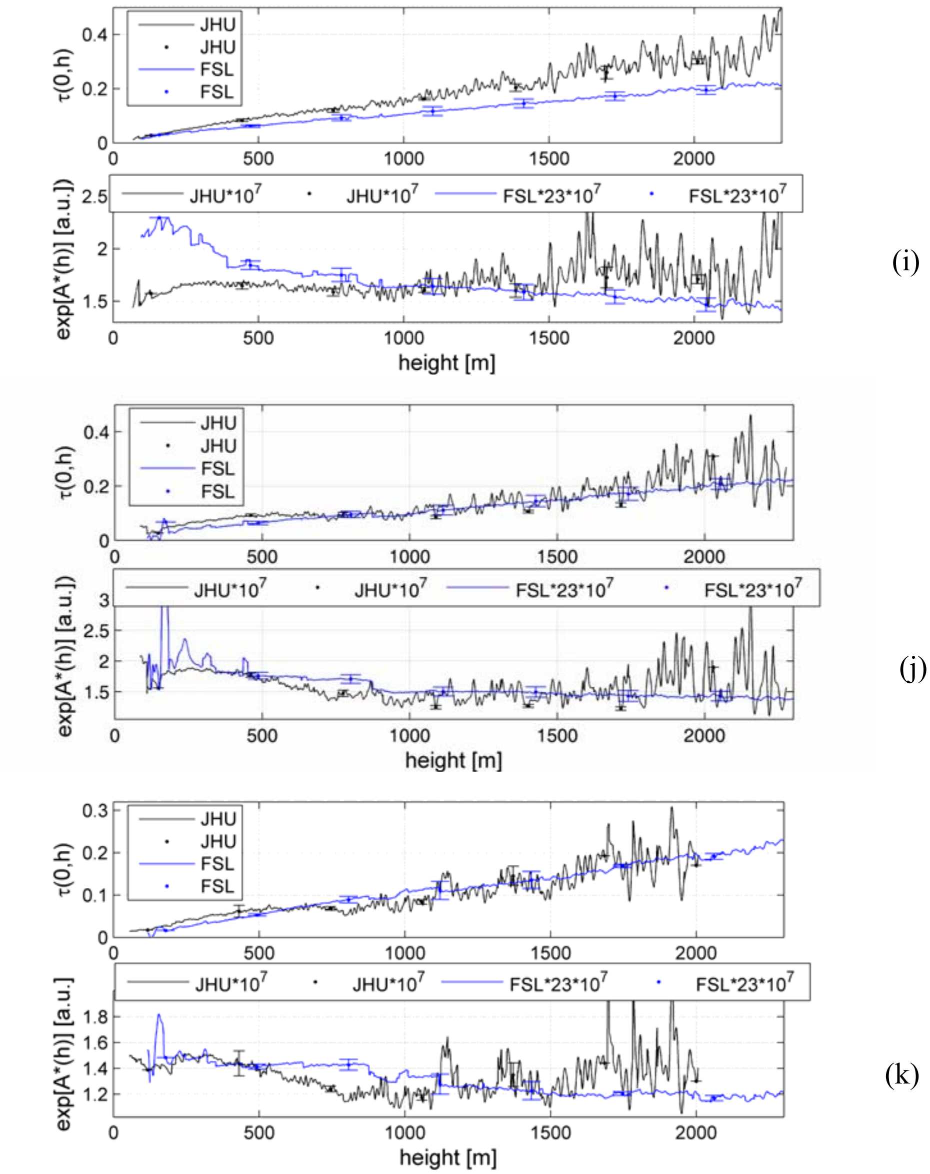

Figure 4.12. Total optical depth, τ(0, *h*), and the functions exp[A^*(*h*)] obtained with the two lidars. Their standard deviations are shown by error bars. The exponent functions are normalized by factors 10^7 and n*10^7 for the JHU and FSL lidars, respectively as shown in each legend. The plots represent the sets of data obtained as following: 28 February, Sequence 1 (a), February 28, Sequence 3 (b), March 4, Sequence 2 (c), March 4, Sequence 3 (d), April 5, Sequence 1 (e), April 5, 2005, Sequence 2 (f), April 5, 2005, Sequence 3 (g), April 6, 2005, Sequence 1 (h), April 6, 2005, Sequence 2 (i), April 6, 2005, Sequence 3 (j), April 6, Sequence 4 (k).

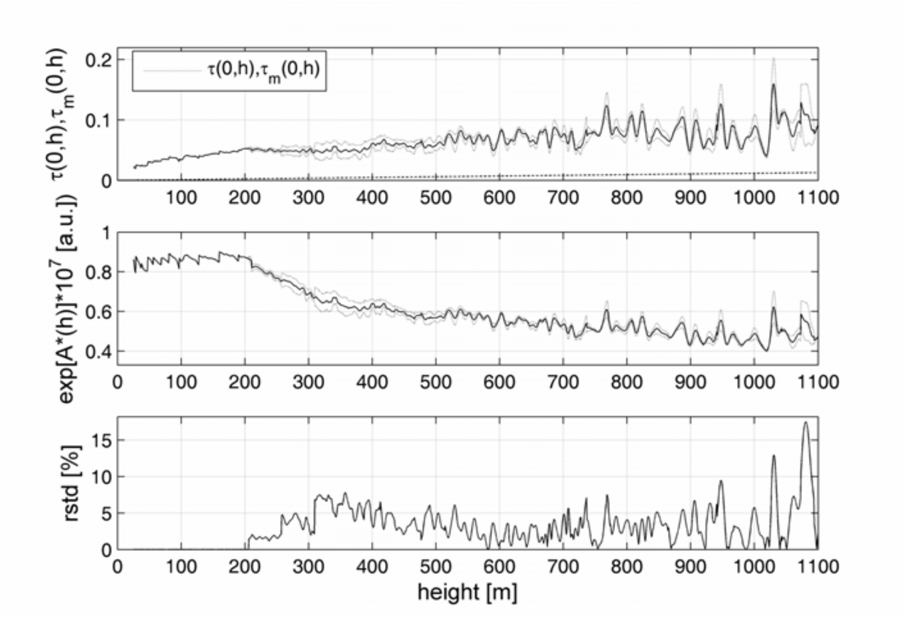

Figure 4.13. Total optical depth, τ(0, *h*) (upper plot), and the function exp[A^*(*h*)] (middle plot) obtained with the JHU lidar at the 532 nm channel on April 5, Sequence 1. The bottom plot shows the relative STD for the exponential function.

In Figure 4.14, an example of the FSL lidar data obtained from the 1064 nm channel is shown. The spikes observed in the near field (at the heights of around 200 m and 470 m) correspond to local layers; these layers could also be seen in 355 nm data. However, for the 355 nm channel inversion results, the intensity of the signal spikes, and accordingly, the corresponding distortions in the retrieved τ(0, *h*) and exp[*A**(*h*)] are significantly less than that for the 1064 nm channel. In other words, in such atmospheres, the signals measured at 1064 nm are significantly more sensitive to inhomogeneous layering (and accordingly, less appropriate for the multiangle measurements) than signals at 355 nm. The optical depth values for 1064 nm (Figure 4.14, upper plot) up to the height of ~ 1000 m are quite small, and the function τ(0, *h*) does not meet our criteria and thus can hardly be used for the extraction of the extinction coefficient profile. The increase of the slope of τ(0, *h*) with height, starting at the heights of ~ 900 – 1000 m, (Figure 4.14) is presumably due to background subtraction inaccuracies rather than an actual increase in aerosol loading. As the backscatter coefficient extracted from the exponential function exp[*A**(*h*)] does not require numerical differentiation, the exponential function, shown in the middle plot of Figure 4.14 can be used, at least up to heights of ~ 500 m. It follows from our experimental results that the uncertainty of the profile of the exponent, exp[*A**(*h*)], is normally less than that for the optical depth; accordingly, this function can generally be used for analyses over a more extended height interval.

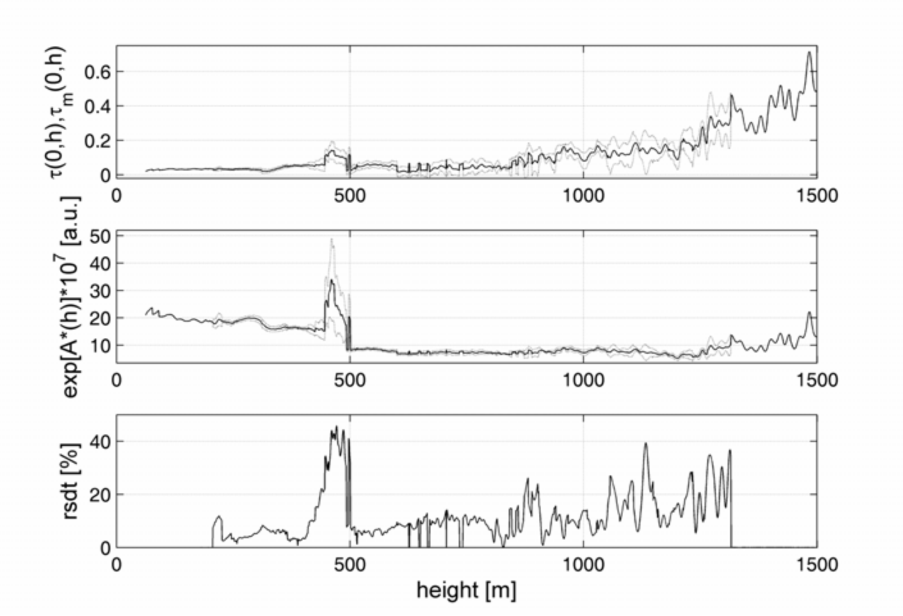

Figure 4.14. Total optical depth, τ(0, *h*), and the function exp[A^*(*h*)] obtained with the FSL lidar at the 1064 nm channel on March 4, Sequence 3 (top and middle plots, respectively). The jumps around the heights of 200 m and 470 m are due to the local heterogeneities. The bottom plot shows the relative STD for the exponential function.

Comparing the general behavior for $\tau(0, h)$ and $A^*(h)$ for different wavelengths, we come to the following conclusions. In an optimal lidar setting, choosing proper angles and a good SNR, we can determine $\tau(0, h)$ from the FSL lidar data at 355 nm with an accuracy between 3 % and 20 % for maximum heights of 2 - 3 km. The corresponding values of $A^*(h)$ have small uncertainty, ~ 0.6 %, but its exponential reaches errors up to 1 – 10 %. For the JHU lidar, the measurement range is generally less than that for the FSL lidar due to increased noise. This is true for all data measured at the wavelength of 355 nm except for the case that took place in the very beginning of our measurements [Figure 4.12 (a)]. For the 532 channel of the JHU lidar, useful $\tau(0, h)$ information was extracted over altitude ranges up to ~ 500 m and useful $A^*(h)$ information up to ~ 1000 m. In clear atmospheres we worked, the optical depth at 1064 nm was always very small and its uncertainty extremely large; therefore only little information about the relative behavior of the total backscatter versus height is available from $A^*(h)$. Thus, the general conclusion from our experimental data is that for the investigated clear atmospheres, the multiangle method is most suitable for 355 nm. Longer wavelengths are more sensitive to heterogeneities of aerosol loading. We should again point out that for such clear atmospheres, the influence of the local heterogeneity on the function $A^*(h)$ is generally significantly less than on the function $\tau(0, h)$. It follows from this observation that in most cases, the altitude backscatter profile can potentially be extracted with better accuracy than the altitude extinction coefficient profile.

The lidar effective overlap function, $q(r)$, is another parameter that can be extracted from the multiangle data. Typical overlap functions for the different wavelength channels of the FSL and JHU lidars are shown in Figures 4.15. These plots represent mean overlap profiles and their uncertainty boundaries. Here the mean overlap and its STD are determined using whole sets of the individual functions obtained under 14 slope angles and using 11 different values for r_{max} for each slope direction. Figure 4.15 (a**)** represents the mean overlap function, $q(r)$ for the 355 nm channel of the FSL lidar. This overlap was obtained from the lidar data taken on April 6, sequence 2. The profiles of $\tau(0, h)$, $\tau_p(0, h)$, and $A^*(h)$ are shown in Figure 4.11. The overlap for the 1064 nm channel of this lidar is given in Figure 4.15 (b). The overlap functions for the three channels of the JHU lidar are shown in Figures 4.15 (c, d, and e). In the favorable conditions which took place during the last days of measurements, the FSL lidar overlap could be accurately determined up to 7000 m for the 355 nm channel and up to 4000 m for the 1064 channel; for the JHU lidar the overlap could be determined up to ~ 4000 m for the 355 nm channel, up to ~ 3500 m for the 532 nm channel, and up to ~ 1000 - 1200 m for the 1064 nm channel. One can see that for the FSL lidar, the complete overlap zone starts around 1000 m for the 355 nm channel and around 300 m for the 1064 nm channel. For the JHU lidar, the complete overlap starts around 600 m for 355 nm channel, and around 100 m for the 532 nm and 1064 channels. Note also that during the experiment, an optics readjustment (realignment) was periodically made, therefore the near-end overlap could be slightly different during different measurements days. One can notice that in some cases wave-like deviations of $q_{eff}(r)$ from the unit may occur in a boundary area between the complete and incomplete overlap zones (recall Figure 4.9 and the comments). This effect is most noticeable for the 1064 nm channel of the JHU lidar [Figure 4.13 (e)]. Our analysis revealed that this effect is generally stronger for the lidar channels with shorter incomplete overlap zones. Presumably it is related to the systematic signal distortions in the zones where the steepest decrease of the lidar signal occurs (rather than to the incorrect selection of r_{min}); however, the validity of this presumption should still be examined.

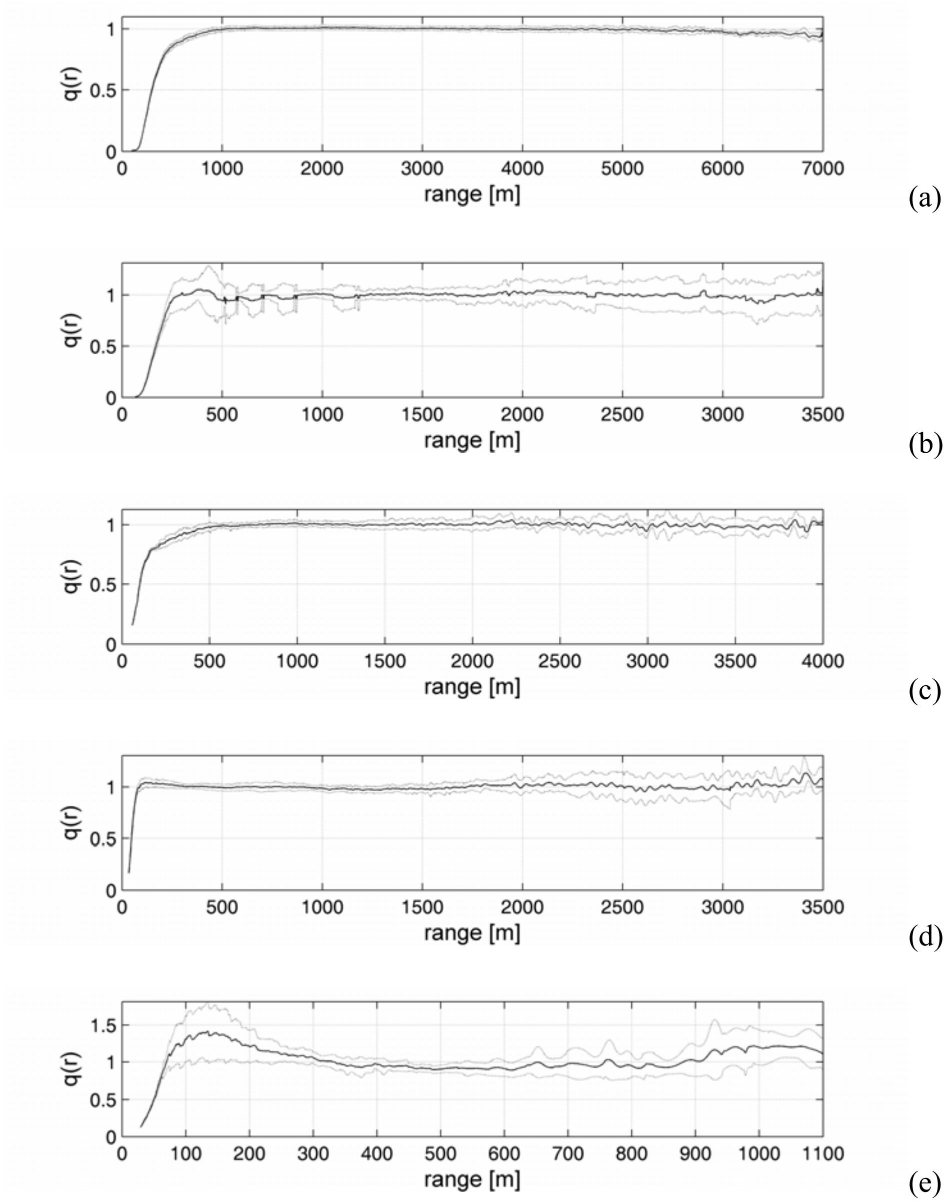

Figure 4.15. (a) The overlap function *q*(*r*) for the FSL lidar for the 355 nm channel; (b) the same for the 1064 nm channel; (c) the same as (a) but for the JHU lidar; (d) the overlap function *q*(*r*) for the JHU lidar for the 532 nm channel; (e) the same as (d) but for the 1064 nm channel.

The behavior of the retrieved overlap function $q(r)$ in the more distant zones of the complete overlap, particularly, its deflection from unity is strongly related with quality of measured data, that is, on both the presence of heterogeneous zones and lidar data distortions, particularly distortions related with inaccurate background subtraction.

Remember that usually, the beginning of complete overlap function is determined from one LOS, in a horizontally homogeneous atmosphere, from the linearity of logarithm of RCS versus range. However, the selection of the linearity region is not trivial. Below (Figure 4.16) is an example of RCS versus range (FSL lidar, April 6, sequence 2). Let us consider the signal of 6° (upper most curve) as a horizontal measurement. A first guess for the beginning of complete overlap function is ~ 600 m. Comparing with our result of ~ 1 km [Figure 4.15 (a)] we find a difference of 400 m.

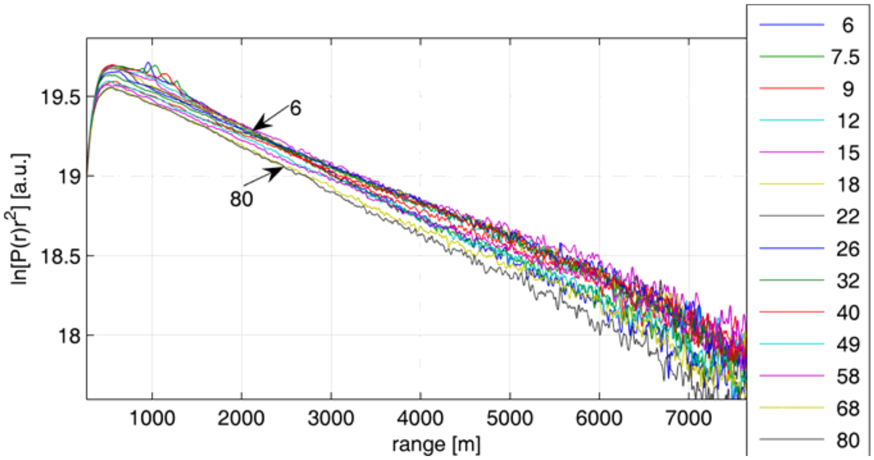

Figure 4.16. RCS versus range for FSL lidar, April 6, sequence 2.

To summarize, let us specify three typical situations, which were met during our tests:

1. The atmospheric situation is favorable for the multiangle measurements on the selected lidar wavelength, mostly at the wavelength of 355 nm. In this case, the profiles of the particulate optical depth, $\tau_p(0, h)$, can be retrieved which basically meet criteria (a) - (c) listed in the section 4.2. Generally in these cases, the determination of the profile of $A^*(h)$ also does not meet significant difficulties. As stated above, the comparison of these two functions, obtained in very clear atmospheres, showed that as compared to the retrieved optical depth profiles, the intercepts $A^*(h)$ are much less sensitive to signal noise and lidar data distortions, and accordingly, to the selected r_{max}. In addition, the overlap may be accurately determined over extended ranges.
2. The atmospheric situation is not favorable enough for the multiangle measurements on the selected lidar wavelength, so that the derived profiles of the particulate optical depth, $\tau_p(0, h)$, either do not meet the above mentioned criteria, or meet them only over a short altitude range. For the wavelength 355 nm such a situation is met only when the particulate loading is small relative to molecular or the atmosphere is not stable enough while scanning is performed. The STD in the set of obtained profiles of $A^*(h)$ often remains small, generally much less than that for $\tau_p(0, h)$, so that the extraction of the backscattering coefficient profile is potentially possible (if the lidar constant is someway determined). The accuracy of the retrieved overlap function generally remains acceptable.
3. The atmospheric situation is not favorable for multiangle measurements. This situation occurs when the optical depth is small or strong inhomogeneous layering is present in the searched area. This situation is most typical for the 1064 nm channel.

Now let us briefly consider the influence of an inaccurate background subtraction and local atmospheric heterogeneities on multiangle inversion results. The consequences of an incorrect background subtraction are shown in Figure 4.17. Here the overlap functions found for the last two angles (68° and 80°) are underestimated due to an overestimated background level (upper plot).

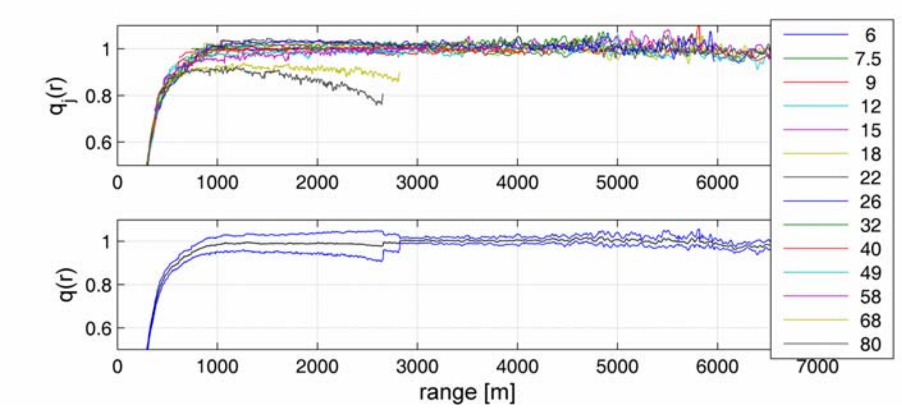

Figure 4.17. Example of the overlap functions obtained from data with an inaccurate background subtraction. The overlap functions are obtained from the FSL 355 nm data on April 6, Sequence 2, r_{max} = 7000 m. The upper plot shows the overlaps, $q_j(r)$, for the elevation angles; one can see the underestimated overlaps obtained for the data measured in the slope directions 68° and 80°. The lower plot shows the mean overlap and its uncertainty boundaries; the increased uncertainty can be seen in the area of the 68° and 80° slope directions.

The lower plot shows the mean overlap with slight deflections from the unity and increased uncertainty boundaries over the region where two functions $q_j(r)$ are much smaller than unity. It is necessary to point out that in this specific case, the inaccurate background subtraction for the signals measured along largest slope directions does not significantly influence the mean overlap function. Moreover, our analysis showed that in such cases, the inaccurate determination of the signal background only locally affects the retrieved profiles of $\tau(0, h)$ and $A^*(h)$. This is because the background offsets take place at the maximal angles (68^o and 80^o), which does not influence inversion results at the lower heights. As follows from the simulations given in section 4.2, the influence of the zero-line offsets for the smaller slopes is much more destructive.

Figures 4.18 and 4.19 illustrate the influence of local heterogeneities on the retrieved functions $\tau(0, h)$, $A^*(h)$, and $q(h)$. Here two kinds of distortions are presented. The first one, shown in Figure 4.18, presents a case of a relatively thin cloud seen at an 18^o slant path. The data were taken with the FSL lidar, at $\lambda = 355$ nm, on 31 March 2005 ($r_{max} = 7000$ m). The result of the presence of the cloud is a strong kink at $h = 1500$ m in the functions $\tau(h)$, $A^*(h)$, and in the overlap functions $q_j(h)$. One can see that when the searched area is free from other strong heterogeneity, such a local heterogeneity does not destroy the data inversion as a whole. However, such heterogeneity strongly influences the shape of the overlap $q_j(r)$, as can be seen in the bottom plot in Figure 4.18 (b).

The plots in Figure 4.19 illustrate the influence of another type of local atmospheric heterogeneity, which violates the Kano-Hamilton method condition of the atmospheric horizontal homogeneity, now for a greater number of slope directions. The data were taken with FSL lidar, at $\lambda = 355$ nm on 6 April 2005. Small heterogeneities, which can be seen in the upper plot, where the function $y_j(h)$ versus height is shown, were originated by a small smoke plume a few hundred meters away from our test site. One can see strong spikes in $\tau(h)$ and $A^*(h)$ at the height ~ 150 m. The consequences of these spikes on the overlap are shown in Figure 4.19 (b). The effect on overlap is seen as small undulations of the function up to ranges of ~ 1100m.

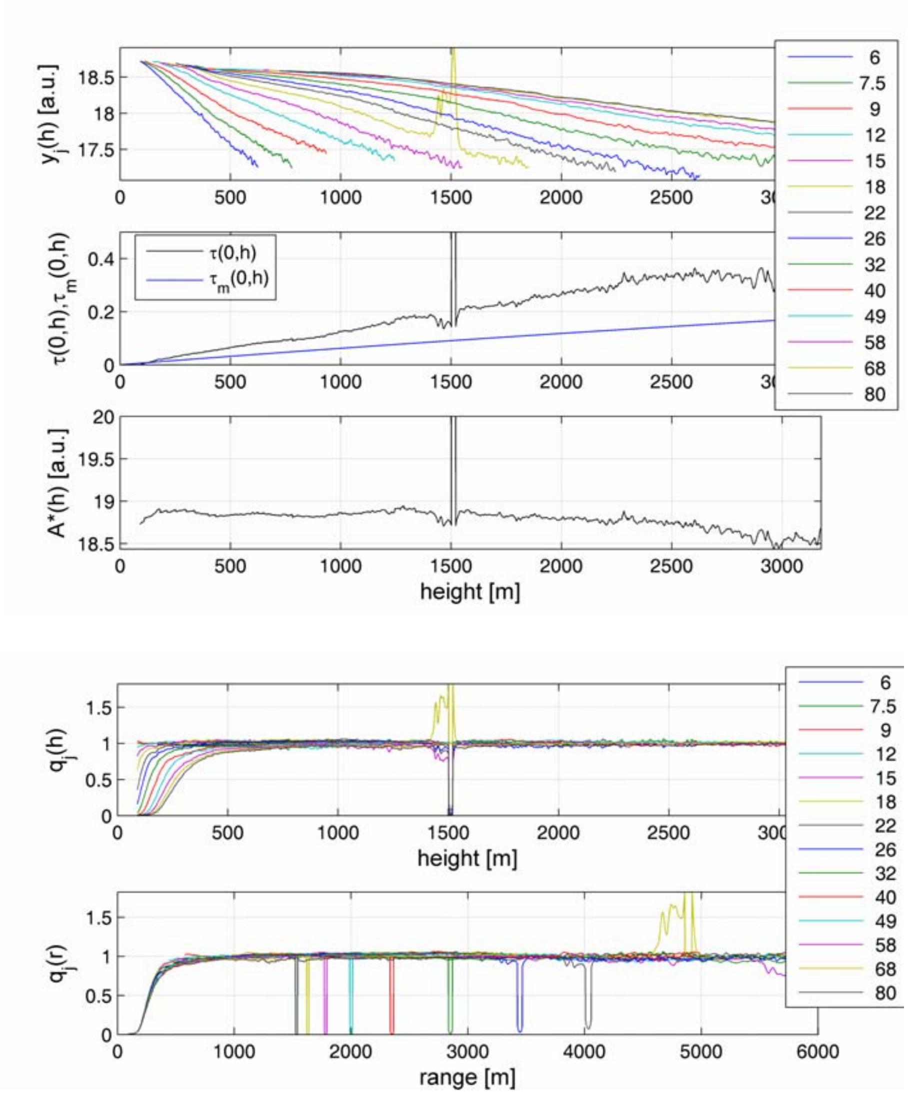

Figure 4.18. Example of a local heterogeneity (cloud) as observed in the data taken with the FSL lidar at 355 nm on March 31. (a) Function $y_j(h)$ over the range selected for the inversion (upper plot); the local heterogeneity can be seen in the 18^o slant path at h = 1500 m. The consequences of the inhomogeneity are seen in the shape of the optical depth $\tau(0, h)$ and the intercept $A^*(h)$ (middle and lower plots). The middle and lower plots show the effect of local heterogeneity at 1500 m where $\tau(0, h)$ reaches 1.33 whereas $A^*(h)$ reaches 27.5]. (b) Overlap functions versus height and versus range (upper and bottom plots, respectively). One can see the kink at 1500 m in the overlap $q_j(h)$.

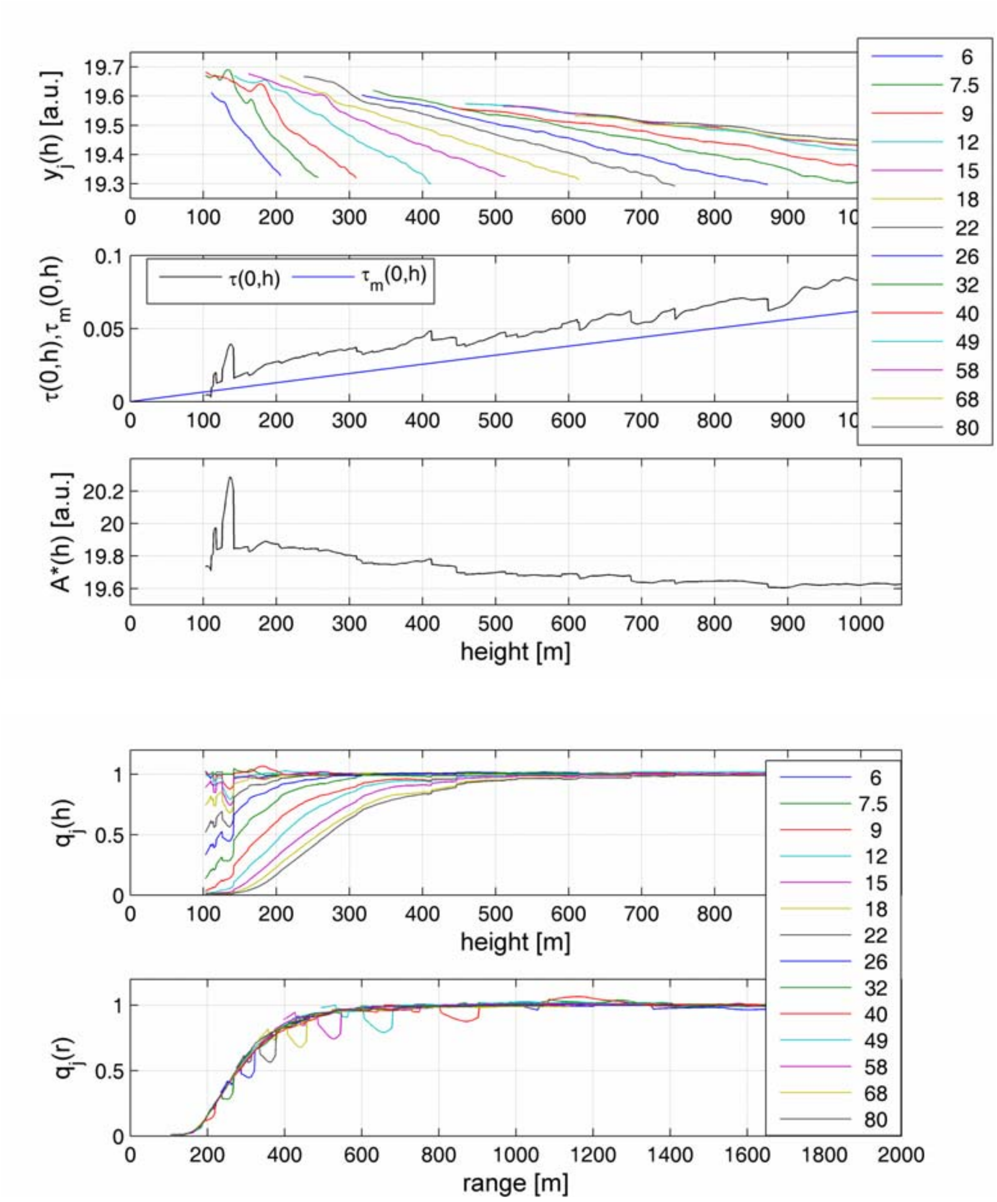

Figure 4.19. Example of heterogeneity (smoke) as observed in the data taken with the FSL lidar, at 355 nm, on April 6, 2005, sequence 1. (a) Function $y_j(h)$ over the range selected for the inversion (upper plot); the local heterogeneity can be seen over the first hundred meters. The consequences of the inhomogeneity are seen in the shape of the optical depth $\tau(0, h)$ and the intercept $A^*(h)$ (middle and lower plots). (b) The overlap functions retrieved from these data versus height and versus range (the top and bottom plots, respectively).

Since the heterogeneities are located in the near field, no changes in r_{max} can improve the inversion results. However, one can avoid a small heterogeneity if its size is relatively small and does not cover the entire azimuthal range. In the present case, the smoke at small altitudes prevailed only over a restricted azimuthal range of 10^o - 15^o, so that these data can be excluded from the horizontal averaging before the inversion is made. When small height heterogeneity is observed over the whole azimuthal range, one can avoid using the distorted signals from the range where the heterogeneity is observed by choosing a higher r_{min}. A visual check of such data is highly recommended when the calculated uncertainties in the retrieved data have unacceptably high values.

Figure 4.20 shows the 2D scan taken at elevation 6^o. We can observe the presence of the smoke around 1 km [(a)] away from the site and at an altitude around 100 m [(b)].

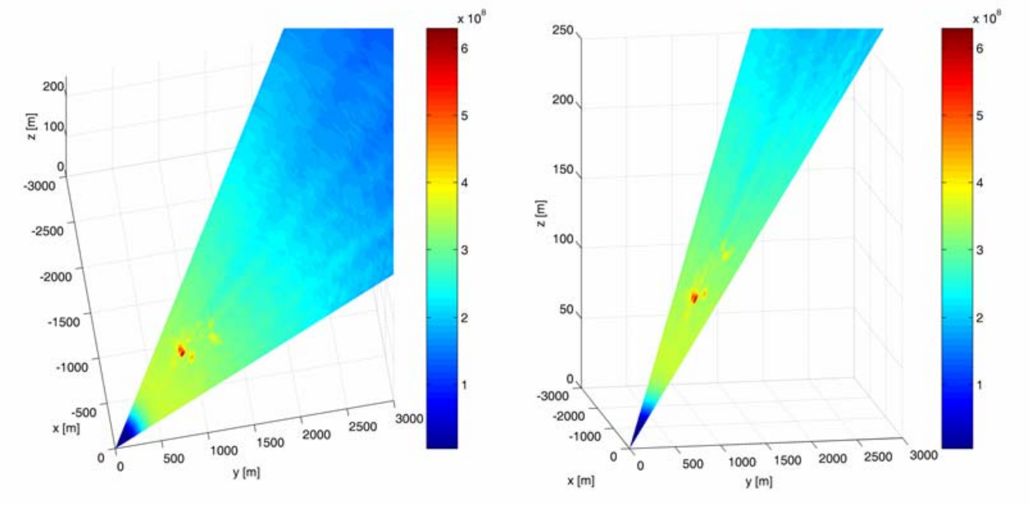

(a) (b)

Figure 4.20. 2D scan taken at elevation 6^o, over 50 azimuthal angles. Two different perspectives are shown in order to emphasize the distance on different Cartesian coordinates

Figure 4.21 is a picture taken at the site that clearly shows the smoke, especially in the few meters above the ground level.

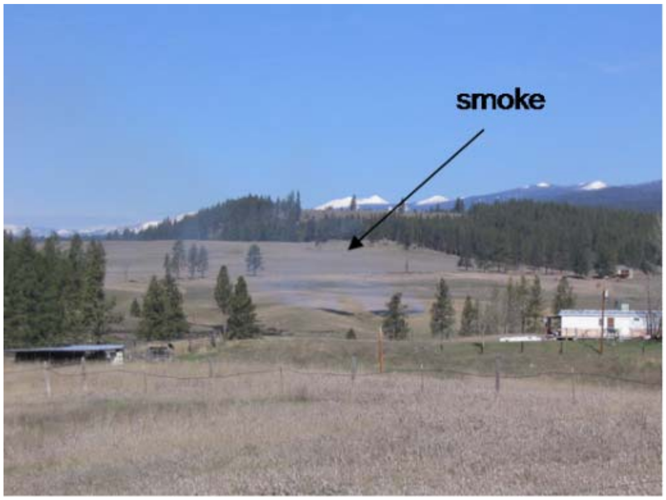

Figure 4.21. Picture taken from the lidar location, which shows the presence of the smoke (around 1 km away).

The general conclusion, which follows from our data analysis, is that the presence of high clouds may not influence the inversion results dramatically, whereas local low–altitude nonhomogeneities and remaining zero-line offsets in signals measured along small angles will strongly affect the inversion results.

4.6. Procedures to determine aerosol extinction and backscatter coefficients

4.6.1. Determination of the aerosol extinction coefficient

The aerosol extinction coefficient is determined from the profiles of the aerosol optical depths. The profiles of the total optical depths are presented in Figures 4.12, upper plots. The aerosol optical depths profiles are obtained by subtracting the molecular optical depths. Due to the noise and systematic errors, the particle optical depth profiles are not smooth and monotonically increasing such that a smoothing technique is needed. Our procedure used to determine the particles extinction coefficient (applied for 355 nm channel) consisted of the following:

a) We determine more accurately $h_{\min}$ for $y_j(h)$ once we have determined the beginning of the complete overlap (1000 m and 600 m for FSL and JHU lidar respectively); the second criterion involved in determining $h_{\min}$ for $y_j(h)$ along the forth criterion (which implies at least two points for regression, excepting $h_{\max}$) gives us $h_{\min} = 1000\sin(7.5^{\circ}) = 130.5$ m and $h_{\min} = 600\sin(7.5^{\circ}) = 78.3$ m for FSL and JHU lidar respectively; accordingly, $h_{\min}$ are adjusted to these values.

b) Smooth the particles optical depth profile and obtain a monotonically increasing signal, using a moving average over 500 points (313.6 m).

c) Since the smoothness of the optical depth profile is not good enough and the moving average can not be done over too many points to not loose the trend of the profiles, we also apply following procedure to calculate the extinction coefficient: the first set of optical depth gradient was determined considering the 1st, 81st, 161st… points, the second set was determined considering 2nd, 82nd, 162nd… points, the last set being determined considering the 80th, 160th, 240th… points. The height resolution corresponding to 80 points is 50 m. In other words, the gradient was computed over a high resolution of 50 m.

Figure 4.22 presents an example of extinction coefficient estimation for data from FSL lidar, April 6, sequence 2. The upper plot shows the particulate optical depth (original and smoothed) while the lower plot presents the particulate extinction coefficient as determined by this procedure (red curve). To emphasize the difference between this method and the “conventional” method of the gradient (which accounts for three adjacent points of the red curve above, corresponding to a height resolution of 0.63 m), the later is also shown on the lower plot. The particle extinction coefficient extinction was computed for both lidars. The next plots (Figures 4.23) show the results. For comparison, both lidar results are shown on the same plot. For February 28, the JHU data were not reliable such that no computations were performed [see JHU optical depth profile on Figure 4.12 (a)]. For the optical depth profiles (Figure 7.23, upper plots), the original profiles for FSL data are in black (FSL orig) and for JHU data in blue (JHU orig) while the smoothed profiles for FSL data are in red (FSL sm) and for JHU data in magenta (JHU sm). The aerosol extinction coefficients obtained applying the "conventional" method for the gradient to the smoothed optical depth are shown in black for FSL data (FSL sm) and in blue for JHU data (JHU sm) while the extinction coefficients obtained applying the new method are shown in red for FSL data (FSL sm new) and in magenta for JHU data (JHU sm new).

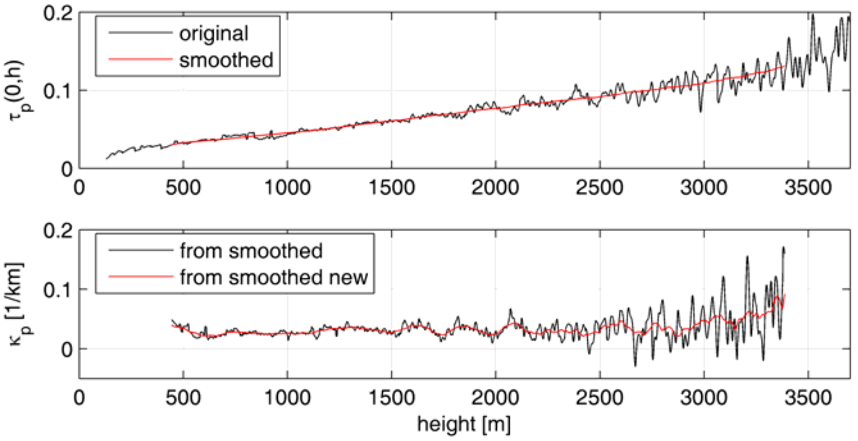

Figure 4.22. Original and smoothed particulate optical depth (upper plot) and particulate extinction coefficient computed "classically" (black curve) and with new method (red curve)

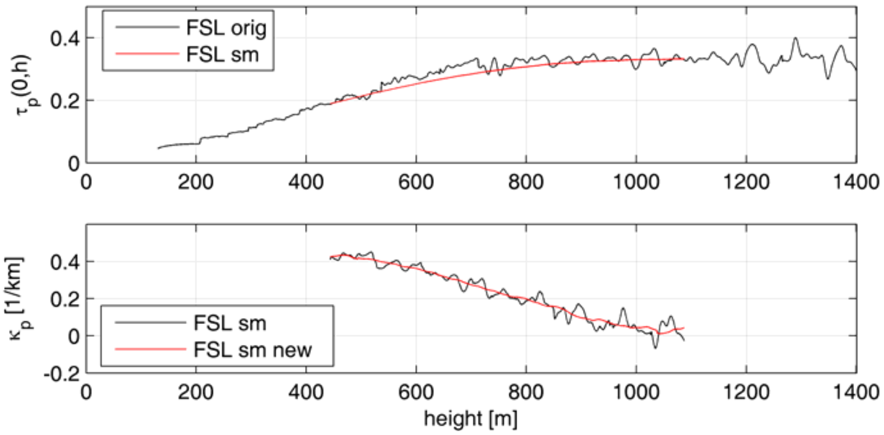
FSL orig
FSL sm
$\tau_p(0,h)$
0.4
0.2
0
0
200
400
600
800
1000
1200
1400
FSL sm
FSL sm new
κ_p [1/km]
0.4
0.2
0
-0.2
height [m]

(a)

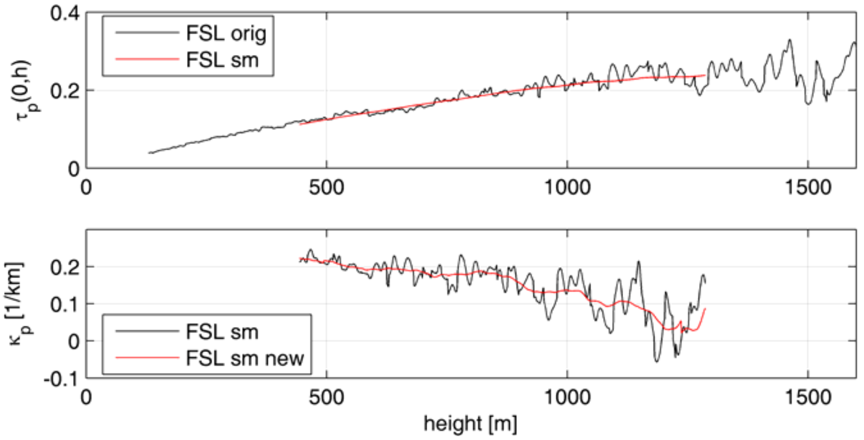
FSL orig
FSL sm
$\tau_p(0,h)$
0.4
0.2
0
0
500
1000
1500
FSL sm
FSL sm new
κ_p [1/km]
0.2
0.1
0
-0.1
height [m]

(b)

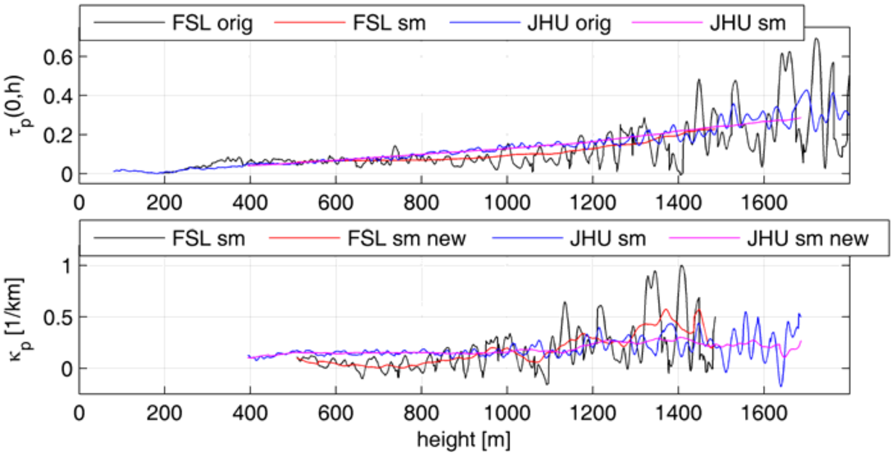
FSL orig
FSL sm
JHU orig
JHU sm
$\tau_p(0,h)$
0.6
0.4
0.2
0
0
200
400
600
800
1000
1200
1400
1600
FSL sm
FSL sm new
JHU sm
JHU sm new
κ_p [1/km]
1
0.5
0
height [m]

(c)

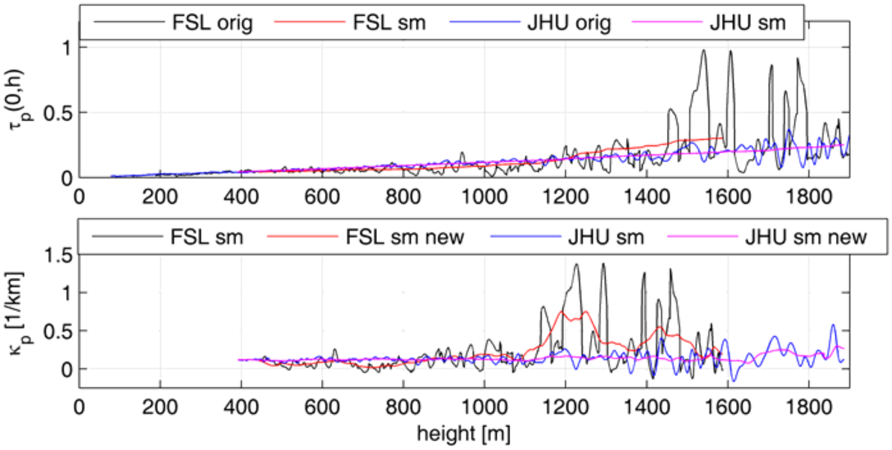
FSL orig
FSL sm
JHU orig
JHU sm
$\tau_p(0,h)$
0
0.5
1
0
200
400
600
800
1000
1200
1400
1600
1800
FSL sm
FSL sm new
JHU sm
JHU sm new
κ_p [1/km]
0
0.5
1
1.5
0
200
400
600
800
1000
1200
1400
1600
1800
height [m]

(d)

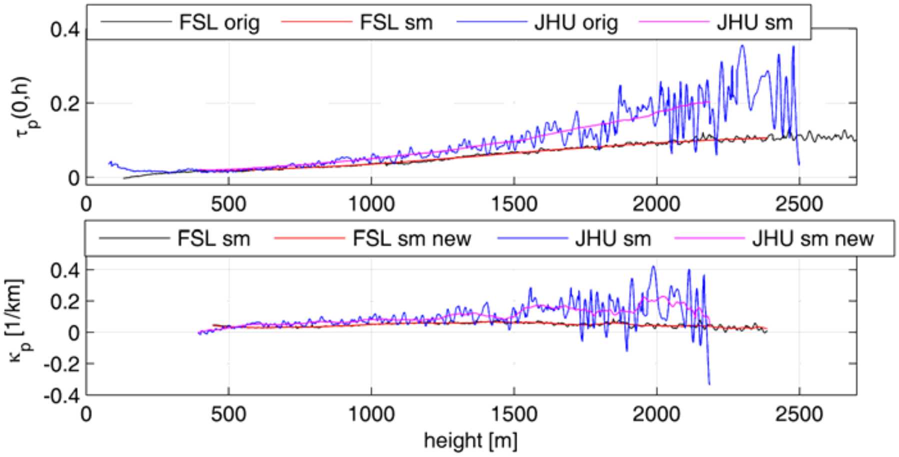
FSL orig
FSL sm
JHU orig
JHU sm
$\tau_p(0,h)$
0
0.2
0.4
0
500
1000
1500
2000
2500
FSL sm
FSL sm new
JHU sm
JHU sm new
κ_p [1/km]
-0.4
-0.2
0
0.2
0.4
0
500
1000
1500
2000
2500
height [m]

(e)

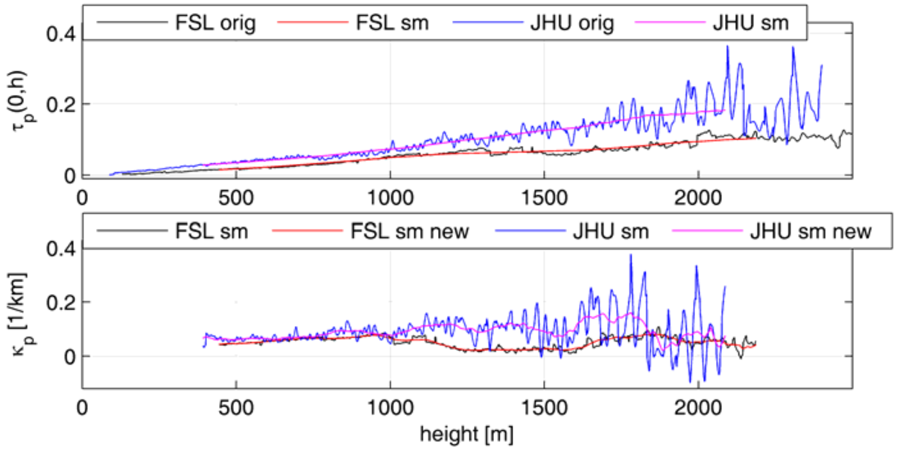
FSL orig
FSL sm
JHU orig
JHU sm
$\tau_p(0,h)$
0
0.2
0.4
0
500
1000
1500
2000
FSL sm
FSL sm new
JHU sm
JHU sm new
κ_p [1/km]
0
0.2
0.4
0
500
1000
1500
2000
height [m]

(f)

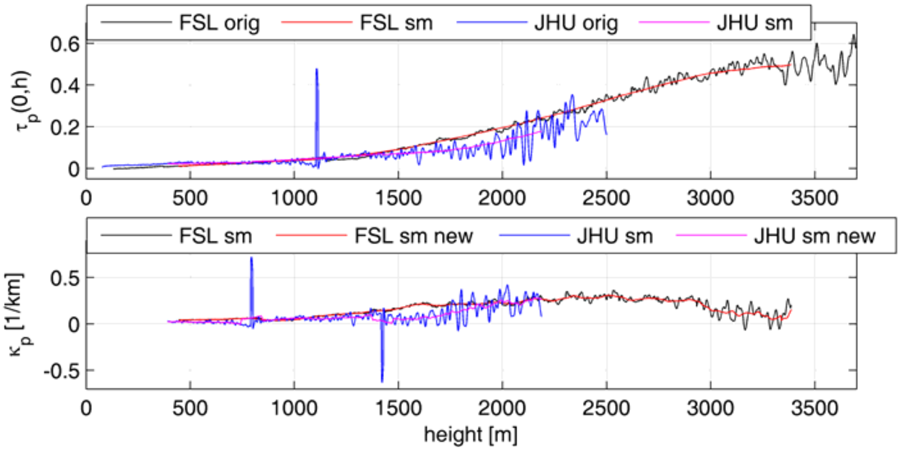
FSL orig
FSL sm
JHU orig
JHU sm
$\tau_p(0,h)$
0.6
0.4
0.2
0
0
500
1000
1500
2000
2500
3000
3500
FSL sm
FSL sm new
JHU sm
JHU sm new
κ_p [1/km]
0.5
0
-0.5
0
500
1000
1500
2000
2500
3000
3500
height [m]

(g)

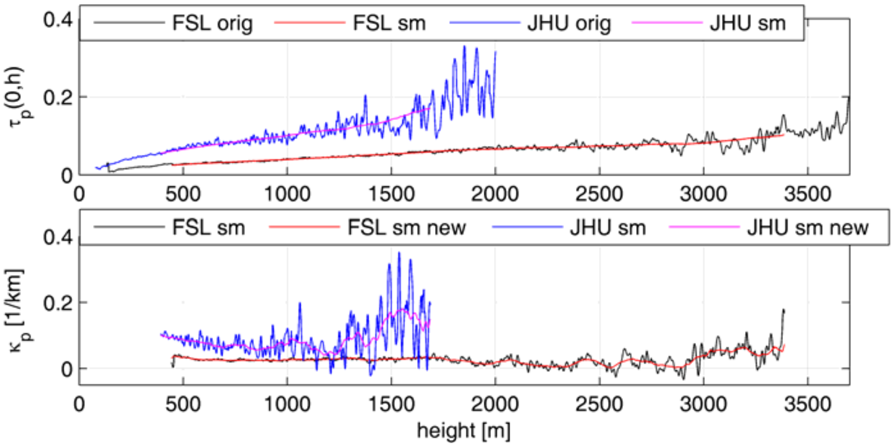
FSL orig
FSL sm
JHU orig
JHU sm
$\tau_p(0,h)$
0.4
0.2
0
0
500
1000
1500
2000
2500
3000
3500
FSL sm
FSL sm new
JHU sm
JHU sm new
κ_p [1/km]
0.4
0.2
0
0
500
1000
1500
2000
2500
3000
3500
height [m]

(h)

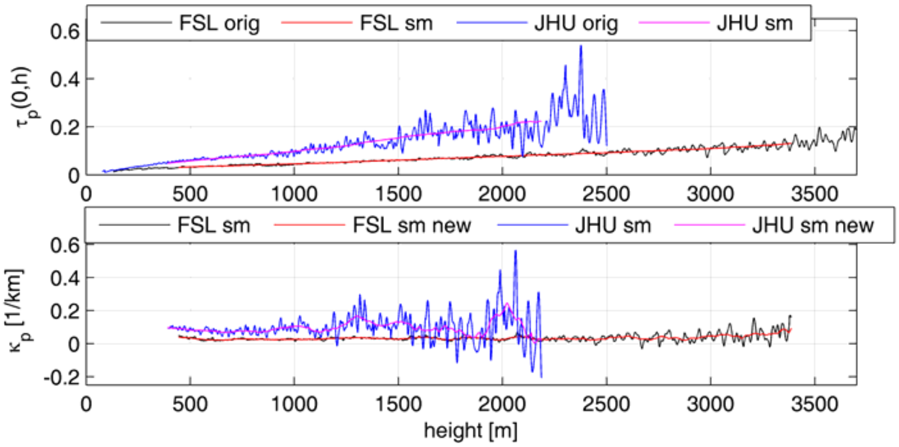
FSL orig
FSL sm
JHU orig
JHU sm
$\tau_p(0,h)$
0.6
0.4
0.2
0
0
500
1000
1500
2000
2500
3000
3500
FSL sm
FSL sm new
JHU sm
JHU sm new
κ_p [1/km]
0.6
0.4
0.2
0
-0.2
0
500
1000
1500
2000
2500
3000
3500
height [m]

(i)

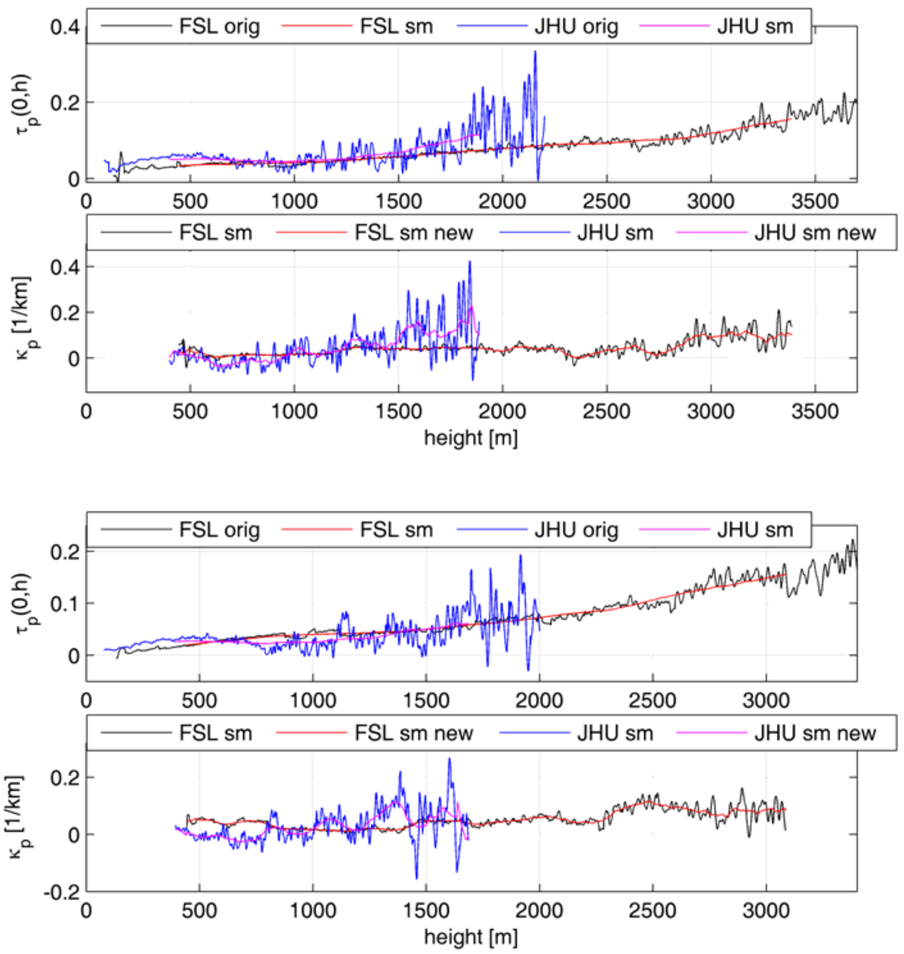

(j)

(k)

Figure 4.23. Particulate optical depth $\tau_p(0, h)$ [original (orig) and smoothed (sm)] and particulate extinction coefficient ["classical" method (sm) and new method (sm new)] obtained with the two lidars. The plots represent the sets of data obtained as following: 28 February, Sequence 2 (a), February 28, Sequence 3 (b), March 4, Sequence 2 (c), March 4, Sequence 3 (d), April 5, Sequence 1 (e), April 5, 2005, Sequence 2 (f), April 5, 2005, Sequence 3 (g), April 6, 2005, Sequence 1 (h), April 6, 2005, Sequence 2 (i), April 6, 2005, Sequence 3 (j), April 6, Sequence 4 (k).

As previously discussed, there are some discrepancies between the optical depths profiles determined with both lidars [e.g. April 6, sequences 1 and 2; see Figure 4.12 and 4.23, plots (h) and (i)]. Accordingly, there are some differences between the aerosol extinction profiles [Figure 4.23, plots (h) and (i)]. Overall, the profiles determined by the two lidar data are similar, but the JHU lidar profiles have more fluctuations. Note that above method applied to determine the extinction profiles gives more reasonable and less fluctuating profiles. Another remark is that this method can not overcome the systematic distortions in the profiles of the optical depths due to various heterogeneities [see Figure 4.23 (h) and (j), JHU profiles]. We know that there were heterogeneities due to a smoke fire close to our site. The effect is a kink in the optical depth profile (~ 500 m) and as a consequence, we obtained a negative extinction coefficient.

4.6.2. Determination of the aerosol backscatter coefficient

As mentioned before, in order to determine the particulate backscattering coefficient from the exponent of intercept [$\exp(A^*) = C(\beta p + \beta_m)$] we should determine the lidar constant C. Here we describe a simple procedure to determine C from the ground based measurement of the particulate backscatter coefficient [$\beta_p(h = 0)$]. The steps are the following:

- Extrapolate the synthetic signal $Z^*_{90}(h)$ (determined with equation 4.7) down to the ground level; when vertical signal is also measured, then its RCS/q can also be extrapolated down to the ground; the extrapolation is performed using a polynomial fit (second or third order) over a range ending at 1 km
- At the ground level, we have

$$Z^*_{90}(h=0) = C\left[\beta_m(h=0) + \beta_p(h=0)\right] \tag{4.11}$$

and the lidar constant C is

$$\mathrm{C}=\frac{Z_{90}^{*}\left(h=0\right)}{\beta_{m}\left(h=0\right)+\beta_{p}\left(h=0\right)} \tag{4.12}$$

- Then, from equation A7.2 we have

$$e^{A^{*}(h)}=\mathrm{C}\left[\beta_{m}\left(h\right)+\beta_{p}\left(h\right)\right] \tag{4.13}$$

from which the aerosol backscattering coefficient is determined

$$\beta_{p}\left(h\right)=\frac{e^{A^{*}(h)}}{\mathrm{C}}-\beta_{m}\left(h\right) \tag{4.14}$$

Figure 4.24 shows an example of such an extrapolation of $Z^{*}_{90}(h)$ (the original - blue line and the smoothed - green line).

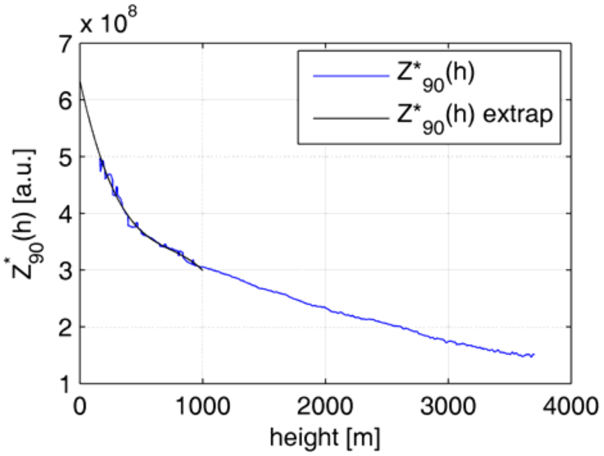

Figure 4.24. Synthetic signal $Z^{*}_{90}(h)$ and its extrapolation to ground level (black curve) by polynomial fit (third order) over a range up to 1 km

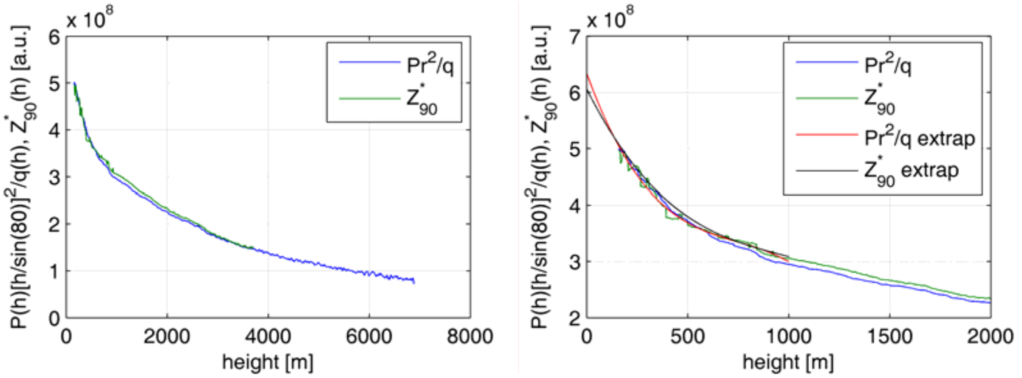

Figure 4.25. (a) Synthetic signal $Z^{*}_{90}(h)$ (green curve) and the RCS/*q* for elevation 80° (blue curve); (b) extrapolation of the synthetic signal (black curve) and of the RCS/*q* for elevation 80° (red curve) by polynomial fit (third order) over range up to 1 km

When vertical signal is available then its RCS/*q* can also be extrapolated. Below is an example (Figure 4.25) with the signal taken at the elevation 80^o (which is very close to the vertical one).

4.6.3. Application on synthetic lidar signals

The methodology to calculate aerosol extinction and backscatter coefficients (described in previous two sections) is tested with synthetic lidar signals. The following cases are analyzed: the noise-free lidar signals and the noisy lidar signals. In the case of the noisy signals, the noise level has a STD of 0.05, 0.10 and 0.20 bin. The simulated lidar signals have no background added such that no background subtraction is necessary and consequently, there is no systematic error due to an accurate background subtraction. If we define the minimum SNR as the ratio of the signal $P(r)$ to the noise STD over the last bins used in the computations (in this particular case at 7 km), then we have for the three cases (STD = 0.5, 0.10 and 0.20 bins) the minimum SNR of ~ 18, 9 and 4.5 respectively.

The entire procedure consists of the following steps:

a) The vertical profiles of the aerosol extinction and backscatter are defined over ~ 10 km; the extinction profile decreases linearly, from a ground level value of 0.1 km^{-1}, with the slope 0.001 km^{-2}; the backscatter coefficient is considered 1/20 extinction coefficient (LR = 20, constant over the vertical profile); the profiles are shown in Figure 4.26 (a)
b) The lidar constant C is set as $4*10^{10}$ [J km sr]
c) For the above conditions, the total optical depth profile and intercept A^* are computed [Figure 4.26 (b)]; the molecular extinction and backscatter profiles follows the US Standard Atmosphere; the synthetic signals $Z_\varphi(h)$ for the 14

angles (the same as those used in our experiment) as well as the vertical synthetic signal $Z_{90}(h)$ are computed (equation 4.8)

d) The lidar overlap function $q(r)$ is modeled as shown in Figure 4.26 (c) from the ground to the height ~ 8 km; the complete overlap starts at 1 km; all the functions and parameters defined in the items (a) - (d) will be further referred as "original" [e.g. original $Z_{90}(h)$, $q(r)$, LR, $\kappa_p(h)$, $\beta(h)$, $\tau(0, h)$, $A^*(h)$, C; within the plots the shortcut "orig" is used]

e) The RCS for the 14 angles as well as for the vertical one are determined as $\mathrm{RCS}(r) = Z_\varphi(r)q(r)$

f) The lidar signals $P(r)$ are determined as $P(r) = \mathrm{RCS}(r)/r^2$

g) The noise are added to the lidar signals as:

   $P(r) = P(r) + x\mathrm{N}$

   where x=0; 0.05; 0.10; 020; N is the noise, normally distributed, with mean 0 and STD = 1 (defined by the function randn in Matlab)

h) RCS are recalculated (to account for noise) and then their logarithms determined

i) The MA procedure is used to determine the total (and particulate) optical depth and the intercept as well as the overlap; a maximum range of $r_{\max} = 7$ km was considered; all the functions defined from now on will be referred as calculated or retrieved [e.g. calculated $Z_{90}(h)$, $q(r)$, LR, $\kappa_p(h)$, $\beta(h)$, $\tau(0, h)$, $A^*(h)$, C; within plots the shortcut "calc" is used]

j) The aerosol extinction coefficient is calculated as described in section 4.6.1

k) The aerosol backscatter coefficient is calculated as described in section 4.6.2; the lidar constant C is determined using extrapolation to the ground level (the second order polynomial fit) of the calculated vertical synthetic signal [$Z_{90}(h)$ calc];

l) The relative errors with regard to the original profiles are computed and shown for the total optical depth (same as for the particulate optical depth), the intercept, the mean overlap, the aerosol extinction and the backscatter coefficient.

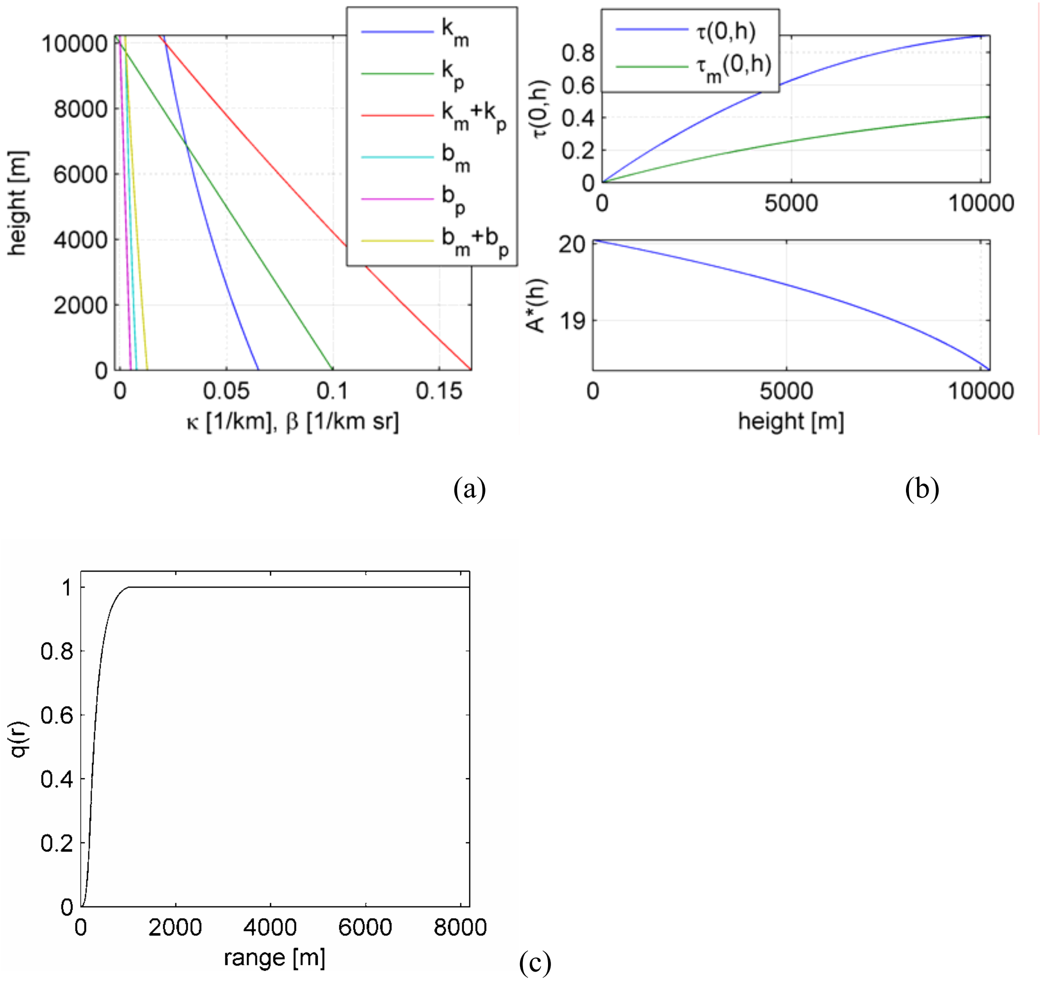

(a) (b)

(c)

Figure 4.26. (a) Original profiles of the aerosol extinction coefficient $\kappa_p(h)$ and backscatter coefficient $\beta_p(h)$; also shown molecular profiles; (b) original profiles of the total optical depth $\tau(0, h)$ and intercept $A^*(h)$; (c) the lidar overlap function; the complete overlap starts at 1 km

Figures 4.27 – 4.29 show the results over the simulated (synthetic) lidar signals for three cases of different noise level. The results of the case of noise free are not shown. The retrieved functions are almost the same as the original data. Note that some small relative errors could exist and they are due to the numerical methods involved in the computations. For example, the extinction coefficient is retrieved within relative errors smaller than 10^{-4} % ("new method"), the backscatter coefficient and LR within 0.81 %. The relative error of the lidar constant is 0.3 %. Note that in the case of the clean data, the application of the "conventional" gradient method is also possible, within the error limits of 0.05 %. For the noisy data, this is not possible, the relative errors reach huge values (thousands %). Note also that new simulations of lidar signals will give slightly different relative errors since we use random numbers to generate the noise.

In the case of 0.05 bin noise (minimum SNR = 18), the calculated total optical depth are retrieved with the error smaller than 3 % while the intercept is recovered with an error of 0.15 % [Figure 4.27 (b)]. The errors slightly increase towards high heights. The overlap is recovered within 1 % relative error [Figure 4.27 (c)]. The extrapolation of the calculated vertical synthetic signal [$Z_{90}(h)$ calc in Figure 4.27 (d)] gives a lidar constant with an error of 0.37 %. The aerosol extinction is recovered generally within the errors less than 20 % (30 % towards higher heights), the backscatter coefficient within the errors less than 8 % and the LR generally within errors less than 20 % (30 % towards higher heights). For the height range less than 2.2 km, the errors are smaller [Figure 4.27 (e)].

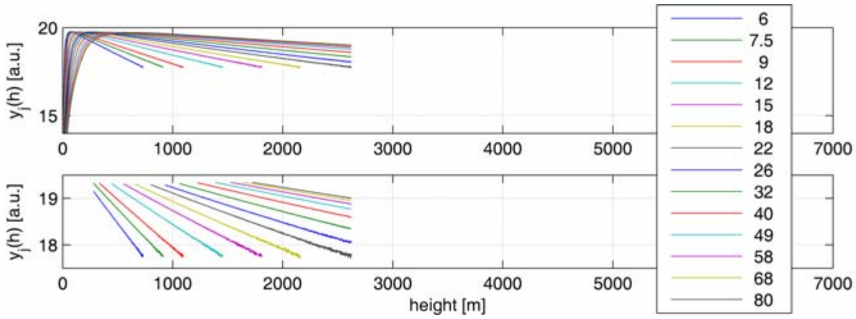

y_j(h) [a.u.]
20
15
19
18
0
1000
2000
3000
4000
5000
7000
height [m]
6
7.5
9
12
15
18
22
26
32
40
49
58
68
80

(a)

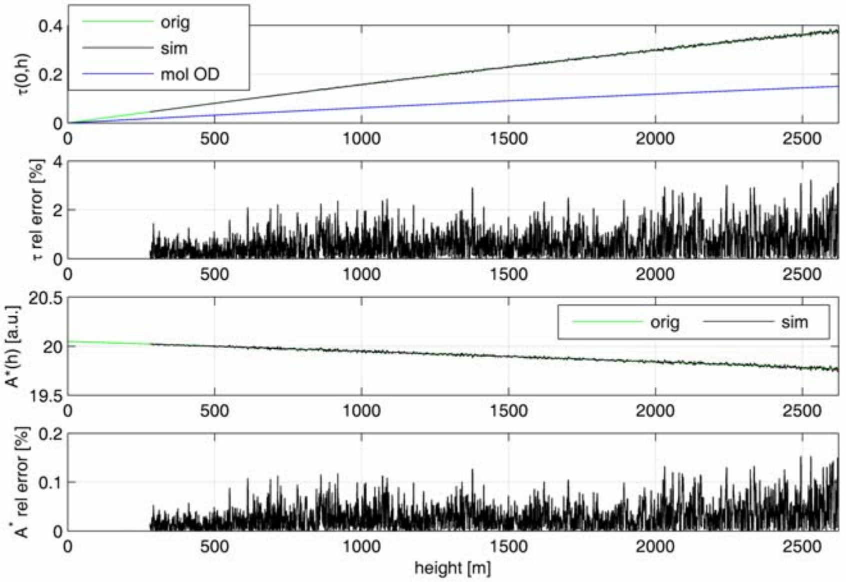

τ(0,h)
0.4
0.2
0
orig
sim
mol OD
τ rel error [%]
4
2
A*(h) [a.u.]
20.5
20
19.5
A* rel error [%]
0.2
0.1
0
500
1000
1500
2000
2500
height [m]

(b)

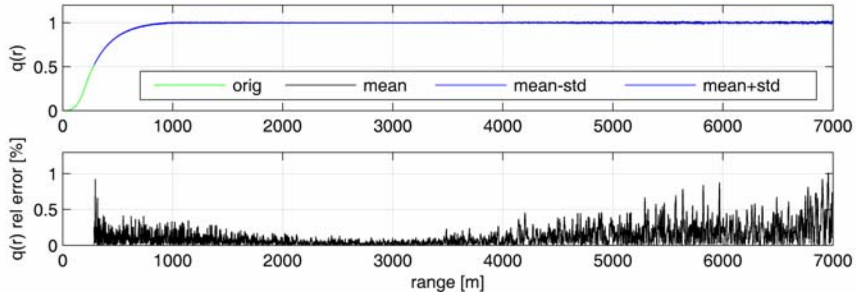

q(r)
1
0.5
0
orig
mean
mean-std
mean+std
q(r) rel error [%]
0
1000
2000
3000
4000
5000
6000
7000
range [m]

(c)

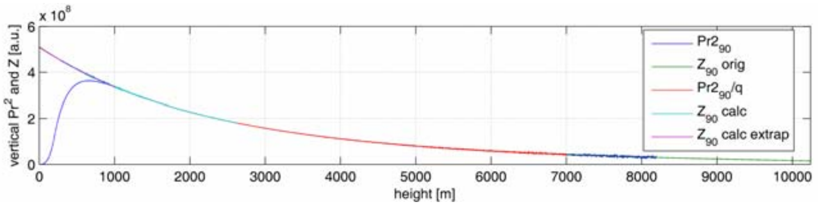

x 10^8
vertical Pr^2 and Z [a.u.]
6
4
2
0
Pr2_90
Z_90 orig
Pr2_90/q
Z_90 calc
Z_90 calc extrap
0
1000
2000
3000
4000
5000
6000
7000
8000
9000
10000
height [m]

(d)

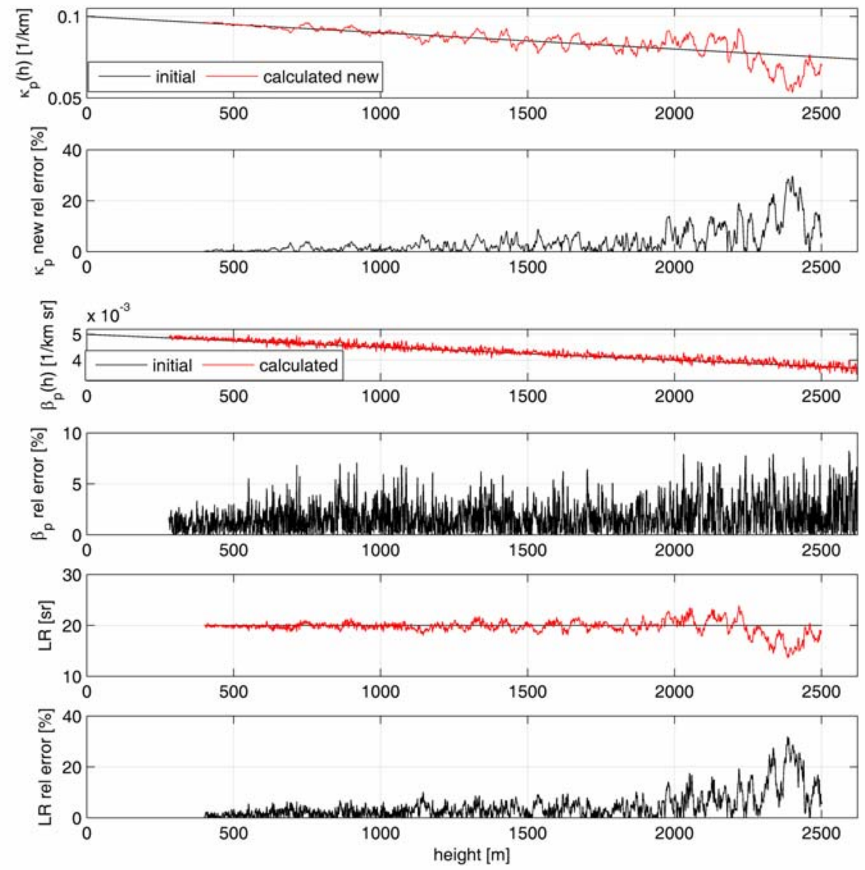

(e)

Figure 4.27. (a) Functions $y_j(h)$ and their selected range. The noise level has a STD of 0.05 bin corresponding to a SNR of 18 for the last signal bins. (b) Retrieved total optical depth and intercept and their relative errors with respect to the original data. (c) Retrieved lidar overlap and its relative error. (d) Extrapolation of the retrieved vertical synthetic signal $Z_{90}(h)$ to the ground level. Also shown $Pr^2_{90}(h)$, original $Z_{90}(h)$ and $Pr^2_{90}(h)/q(h)$. (e) Retrieved aerosol extinction and backscatter coefficient, LR and their relative errors with respect to the original data.

For the case of 0.10 bin case noise (minimum SNR = 9), the calculated total optical depth are recovered with the error smaller than 5 % while the intercept is recovered with an error of 0.3 % [Figure 4.28 (b)]. The errors slightly increase toward the highest heights. The overlap is recovered within 2 % relative error [Figure 4.28 (c)]. The extrapolation of the calculated vertical synthetic signal [$Z_{90}(h)$ calc in Figure 4.28 (d)] gives the lidar constant with an error of 1.09 %. The aerosol extinction is recovered generally within the errors less than 30 % (40 % at higher heights), the backscatter coefficient within the errors less than 20 % and the LR generally within the errors less than 30 % (50 % towards higher heights). For heights smaller than 2 km, the errors are smaller [Figure 4.28 (e)].

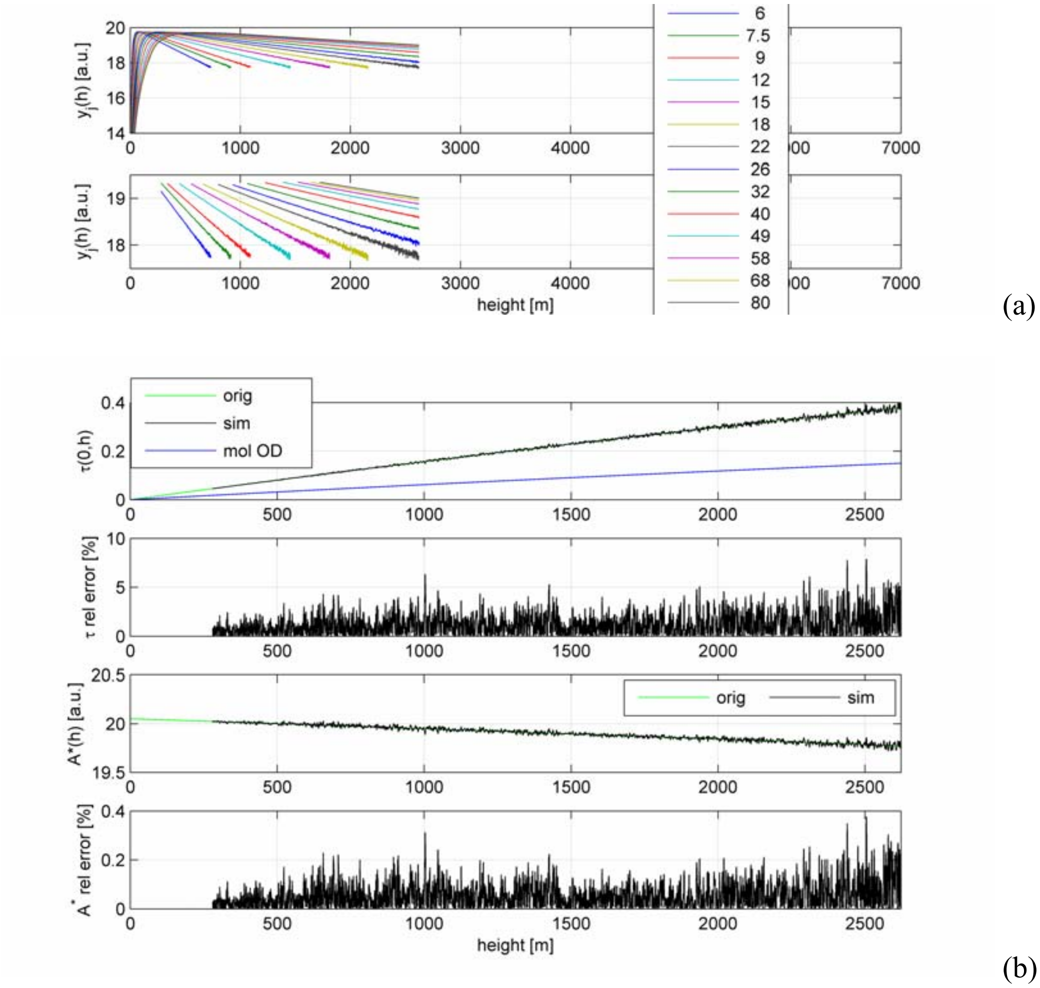

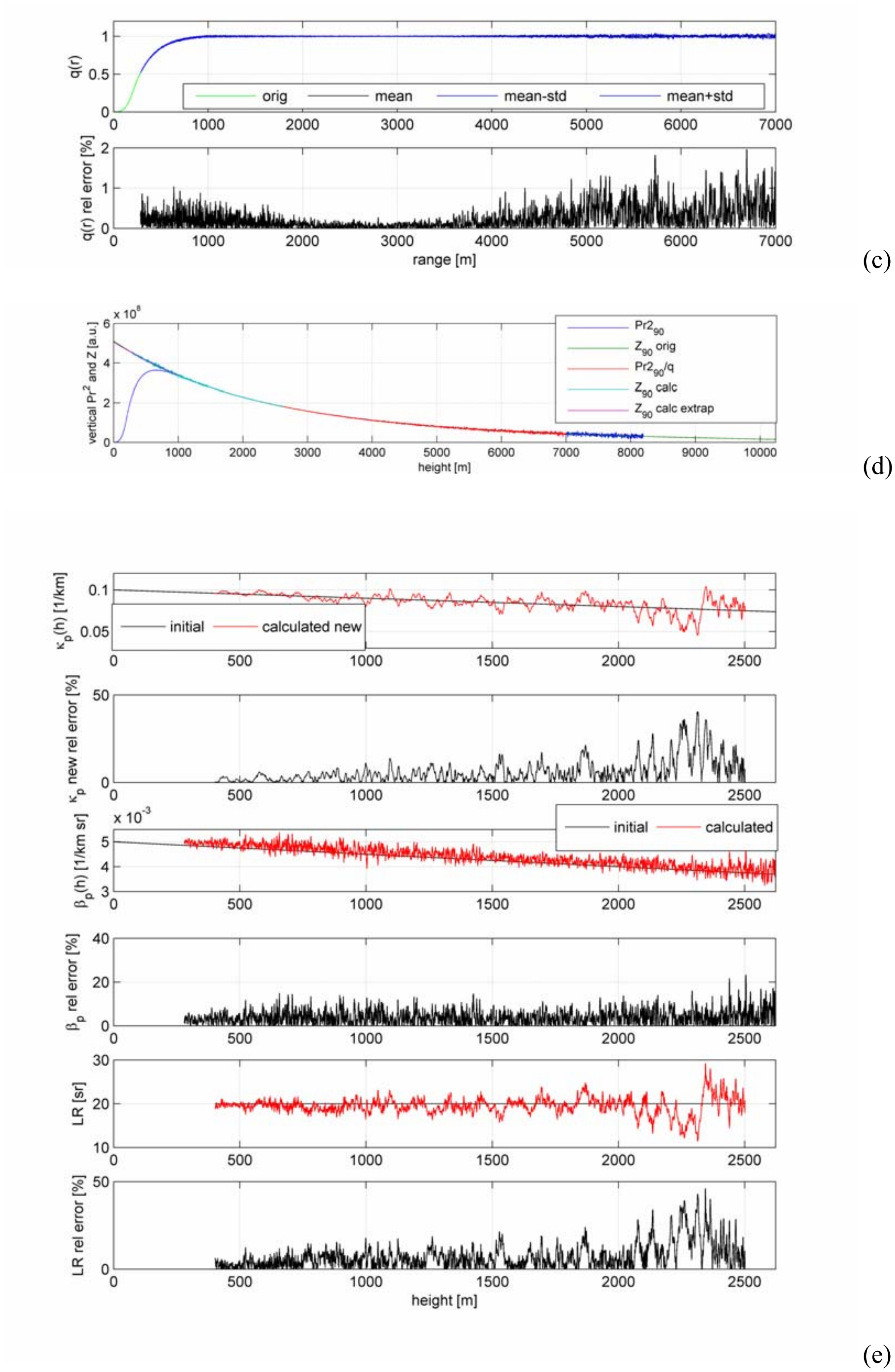

Figure 4.28. Same as 4.27 but for the noise level with a STD of 0.10 bin corresponding to a SNR of 9 for the last signal bins.

For the 0.20 bin case noise (minimum SNR = 4.5), the calculated total optical depth are recovered with an error smaller than 12 % while the intercept is recovered with an error of 0.7 % [Figure 4.29 (b)]. Again, the errors slightly increase at the highest heights. The overlap is recovered within 4 % relative error [Figure 4.29 (c)]. The extrapolation of the calculated vertical synthetic signal [$Z_{90}(h)$ calc in Figure 4.29 (d)] gives a lidar constant with an error of 2.12 %. The aerosol extinction is recovered generally within 50 % errors (100 % over higher heights), the backscatter coefficient within errors 40 % errors, and the LR generally within 40 % errors (110 % over higher heights). For the height range less than 1.9 km, the errors are smaller [Figure 4.29 (e)].

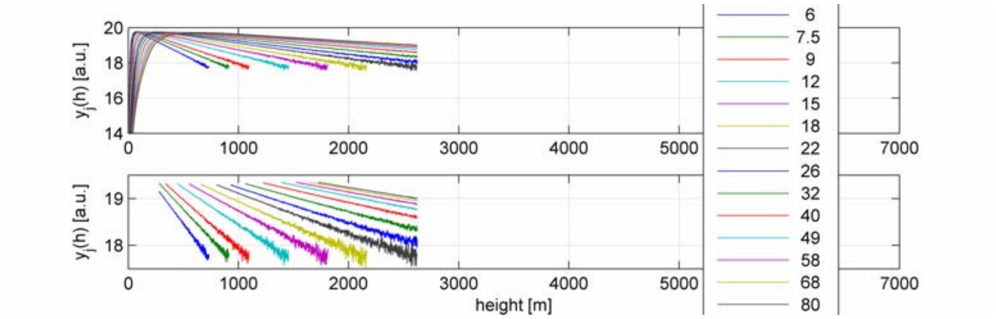

(a)

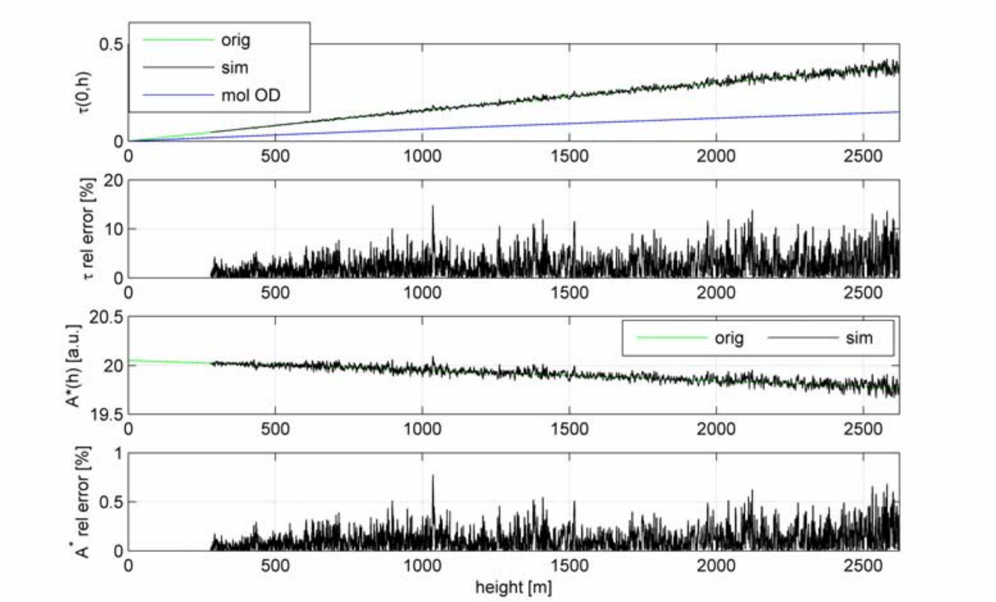

(b)

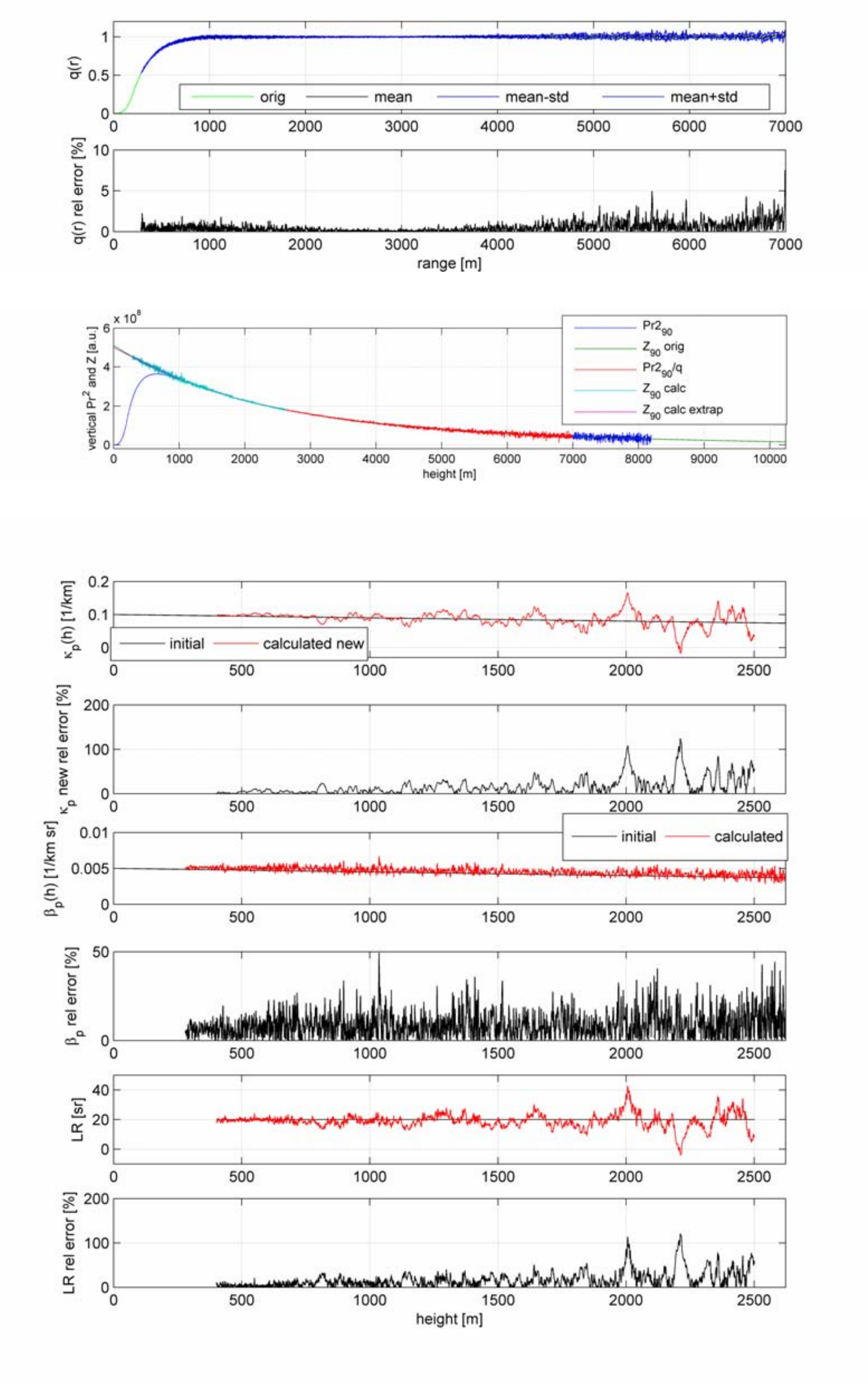

(c)

(d)

(e)

Figure 4.29. Same as 4.27 but for the noise level with a STD of 0.20 bin corresponding to a SNR of 4.5 for the last signal bins.

The table 4.2 summarizes the relative errors obtained in retrieving the total (particles) optical depth, Hamilton exponent, overlap, lidar constant, particles extinction and backscatter coefficients, and lidar ratio for the three cases of the noise level.

	STD_{noise} = 0.05 bin SNR =18 at 7 km	STD_{noise} = 0.10 bin SNR = 9 at 7 km	STD_{noise} = 0.20 bin SNR = 4.5 at 7 km
Relative error (%) $\tau(0, h)$	3	5	12
Relative error (%) $A^*(h)$	0.15	0.3	0.7
Relative error (%) $q(r)$	1	2	4
Relative error (%) C	0.37	1.09	2.12
Relative error (%) $\kappa_p(h)$	20 (30*)	30 (40*)	50 (100*)
Relative error (%) $\beta_p(h)$	8	20	40
Relative error (%) LR	20 (30*)	30 (50*)	40 (110*)
Observations	Good results over first 2.2 km	Good results over first 2 km	Good results over first 1.9 km
* represents errors over large heights (higher than 2.2 km, 2 km and 1.9 km for the three noise cases analyzed)			

Table 4.2. Relative errors (%) in retrieving optical depth $\tau(0, h)$, Hamilton exponent $A^*(h)$, lidar overlap $q(r)$, particles extinction coefficient $\kappa_p(h)$, particles backscatter coefficient $\beta_p(h)$ and particles lidar ratio LR

As expected, the increase of the noise level (the decrease of SNR) in the lidar signals reduces the height range over which the calculated optical properties are retrieved within reasonable errors (e.g. < 20 %). For high values of the noise level (e.g. when minimum SNR < 10) the range of acceptable calculated properties is reduced from 2.5 km to ~ 1.9 km. These results can be used as an estimate of the accuracy of the retrieved optical properties and the lidar ratio once one knows estimates of the SNR of the lidar signals. More sophisticated correlations can be developed between SNR over range interval [$r_{\min}$, $r_{\max}$] and relative errors of the lidar overlap over the same range interval on one hand and between SNR over range interval [$r_{\min}$, $r_{\max}$] and the relative errors over the height interval [$h_{\min}$, $h_{\max}$] of the retrieved optical properties.

4.7. Summary

The principal purpose of the study presented in this paper is to analyze and improve practical methods that would allow better inversion of multiangle searching data obtained with an elastic lidar in a clear atmosphere. In most related publications, it is generally assumed that the basic problem of such multiangle measurements is atmospheric heterogeneity. Our analysis revealed that the problem is much deeper. We established that even minor instrumental uncertainties, that are inherent to real lidar data, are extremely destructive for the conventional Kano-Hamilton method (*Kano*, 1968; *Hamilton*, 1969), and this significantly would impede the use of this method even in an ideally homogeneous atmosphere. We drew the conclusion that the method needed to be improved in order to be applied to real experimental data. In previous study (*Kovalev*, 2004) the authors proposed the use of a two-step procedure for the multiangle data inversion. In the first step, the vertical optical depth is derived and the retrieved data quality is analyzed; in the second step, a combination of the one-directional and multiangle methods was proposed to extract the particulate extinction coefficient from the optical-depth profile. In this chapter we propose ways of improving the measurement accuracy while performing the first-step procedure, that is when determining and analyzing both constants in equation (4.3) and the behavior of the effective overlap functions, retrieved from the functions $A^*(h)$ and $\tau(0,$

h). The basic principle of our approach is to establish and remove all "bad" data points that distort the dependence of the function $y_j(h)$ versus the independent x_j. Additionally, we implement a thorough analysis of the uncertainty in the retrieved data, which allows one to take into consideration both signal random errors and systematic distortions. Our current study also includes a new principle in the determination of effective overlap for scanning lidar operating in clear atmospheres. With this procedure not only the actual behavior of the overlap function in the incomplete overlap zone can be established, but also useful information on quality of derived atmospheric parameters can be obtained. Particularly, this procedure allows the determination of whether a significant offset remains in the inverted data after background subtraction, and whether the atmosphere is appropriate for multiangle measurements.

Some results of initial tests of the above methodology obtained with the experimental data of two simultaneously operating scanning lidars were given in the section 4.5 (*Adam et al*., 2005).

The use of the modified Kano-Hamilton method, which is based on the assumption of horizontally stratified atmosphere, might be practical only if all-important issues are taken into consideration. This includes issues related to different relative weights of the molecular component in the total scattering for different wavelengths, real technical characteristics of the lidar instrumentation, and the imperfectness of the conventional methodology and algorithms, used for the multiangle lidar-data inversion.

Let us consider some of these issues. The application of the modified Kano-Hamilton method to the experimental data obtained in clear atmospheres at different wavelengths showed that the lidar signals measured at 355 nm yield much more accurate inversion results than signals measured at longer wavelengths. Our results show that (1) the retrieved profiles of $\tau(0, h)$ and $\tau_p(0, h)$ better meet criteria (a) - (c) (section 4.2, page 97) than the signals at longer wavelengths; (2) in most situations the exponential function, $\exp[A^*(h)]$, and accordingly, the total backscattering profile, systematically decreases with height; (3) the profiles of the vertical optical depths at 355 nm measured by two lidars agrees significantly better then the profiles measured at the wavelength 1064 nm; and (4) the lidar incomplete overlap determined through multiangle measurements at 355 nm agrees well with rough estimates made through analysis of the shape of the range corrected signal.

As expected, the application of the multiangle method to the data from the 532 nm channel, and especially the 1064 nm channel, brought less encouraging results. The first reason is that the total optical depth for these wavelengths over the same altitude range is significantly less than that for 355 nm, and accordingly, the signals are much more sensitive to the heterogeneity of particulate loading. Another reason is that the molecular backscatter component, which stabilizes the solution at 355 nm, at 1064 nm is almost hundred times less as compared to that at 355 nm. The major requirement for successful application of the Kano-Hamilton method is that the total backscatter coefficient $\beta(h)$, which is the sum of the molecular and particulate components, $\beta_m(h) + \beta_p(h)$, does not depend on searching angle φ_j. In such clear atmospheres, the component $\beta_p(h)$ is generally comparable (or even less) than $\beta_m(h)$; obviously the Kano-Hamilton condition $\beta_m(h) + \beta_p(h) = \text{const.}$ holds better when the molecular component, $\beta_m(h)$, which generally meets the condition of the horizontal homogeneity, is large as compared to the particulate component. The other issue related to this specific is that the backscatter signals at 1064 nm are much weaker than the signals at 355 nm, the signal-to-noise ratio is worse, and accordingly, the total measurement range at this wavelength is much shorter than at 355 nm. This is why the 355 nm channel is much more appropriate for the application of the multiangle method than the 1064 nm channel. As for the lidar measurements at 532 nm, our feelings are that the capabilities lie somewhere between the above two cases, and potentially this wavelength can be used successfully in multiangle measurements in clear atmospheres. However, because we had the 532 nm channel only in the JHU lidar where signals generally had an increased noise level, the discussion of this topic should be postponed until more experimental data at 532 nm are available.

For most of our experimental data at 532 and 1064 nm, accurate optical depth profiles that meet the conditions (a) - (c) cannot be obtained, or in the best case, may be obtained over a significantly reduced altitude range. Because of extremely small attenuation and the poor signal-to-noise ratio of the signals at 532 nm and 1064 nm, the extraction of the vertical optical depth at these wavelengths was an issue. However, even in these cases, one can often obtain relatively stable profiles of $\exp[A^*(h)]$. Because of small values of the optical depths, the attenuation term ~ 1, and the vertical synthetic signal depends primarily on the accuracy of determining $\exp[A^*(h)]$; the large relative uncertainty in the retrieved optical depth does not significantly affect the shape of the synthetic signals $Z_j^*(h)$, and accordingly, the shape of the retrieved overlap function, $q(r)$. However, the shape of these functions, especially extracted from the signals at 1064 nm, is sensitive to atmospheric heterogeneity and signal distortions. This may prevent obtaining accurate estimates of the lidar overlap, but makes it possible to discriminate even weak atmospheric layering and reveal lidar hardware problems.

When performing the multiangle data inversion, the level of atmospheric heterogeneity should first be estimated. In other words, instead of general wording about atmospheric heterogeneity, concrete criteria of the atmospheric homogeneity levels in conformity with a concrete multiangle measurement methodology and lidar parameters should be developed. As shown above, the level of the horizontal homogeneity in a clear atmosphere (as defined in conformity with Kano-Hamilton algorithms) depends on the wavelength used for the measurements. Second, the level of the horizontal homogeneity will be different when using the data from a lidar that scans vertically under a fixed azimuthal direction and that of a lidar that gathers data over a wide azimuthal sector for any slope direction. The latter method allows a direct check of the atmospheric horizontal homogeneity (that is, how the signals coincide with each other when taken at the same slope elevation in different azimuthal directions); azimuthal signals distorted by a local heterogeneity can easily be detected and excluded from the data processing. The issue that appears when using such a method lies in the selection of an optimal number of the slope directions and optimum angular separation between these. To get the best results, one should use an appropriate number of searching angles to obtain enough data points in the dependence $y_j(h)$ versus x_j for the regression. A greater number of elevation angles reduces the intensity of jumps in the functions $\tau(0, h)$, $\exp[A^*(h)]$, and $q(h)$ but increases the total scanning time. After we analyzed the above functions with regards to their jumps, we decided to increase the number of slope directions from 10 to 14 angles. However, we realize that such a selection of the number of slope directions and the angular separation between these is still not optimal, and should possibly be reconsidered to increase the number of measurements at large angles and avoid large jumps at high altitudes. Further investigation will be done concerning this issue. It might also be beneficial to combine this method (using it for lower slope elevations) with the conventional vertical scanning (using that for large slope elevations). This might improve the quality of the data inversion at the high altitudes. We also plan to investigate such an approach in turbid atmospheres, including atmospheres in vicinities of wildfires.

The selection of an optimal measurement range (r_{min}, r_{max}) of the lidar signals for the inversion is another issue of the multiangle measurements. The accurate selection of the minimum range, r_{min}, is directly related to the accurate determination of the length of the incomplete overlap zone. In clear atmospheres, the incomplete overlap zone can be achieved using the searching data. Our analysis showed that more accurate data (that is the functions of interests with smaller STD) were generally obtained when r_{min} was at least 100 m greater than the maximal function $y_j(h)$. In other words, the determination of the length of the incomplete overlap zone, $r_{min,}$ as the distance from $r = 0$ to the range of the maximal $y_j(h)$ may yield underestimated r_{min}. The increase of STD due to the underestimated minimal range might also be aggravated by distortions of the electric signal in the areas of its sharp decrease, where the term $q(r)/r^2$ has the largest negative gradient. In the future we plan to improve the determination of r_{min}. A simple way is the following: after first estimate of the overlap {considering r_{min} 100 m away from $\max[\ln(P(r)r^2]$} we determine the new r_{min} corresponding to the beginning of the complete overlap and we redo the calculations [for a complete overlap beginning at 1 km, the corresponding $r_{\min} = 1000*\sin(7.5^{\circ}) = 130.5$ m]. The selection of the maximum range, r_{max}, for the inversion is of the same importance as the selection of the minimal range. The signal random noise at the far end of the measurement range, which dramatically increases with range may result in large systematic shifts in the linear fit of the dependence $y_j(h)$ versus x_j, from which parameters of interests, $\tau(0, h)$ and $\exp[A^*(h)]$, are then determined. This occurs because after the lidar signal square-range correction and its transformation into $y_j(h)$, the noise fluctuations do not obey normal distribution. One should also keep in mind that small systematic shifts in the inverted lidar data at the far end of the measurement range are unavoidable even if the total signal is precisely measured. Over distant ranges, the backscatter signal is always found as a small difference of two large quantities, and eventually, the signal becomes comparable with the standard deviation of the determined background level.

The main points are:

- In the clear atmospheres under investigation, the Kano-Hamilton multiangle method is most applicable for short wavelength lidars.
- It follows from our experimental data that the multiangle method may work properly when the total vertical optical depth over the measured altitude range is not less than ~ 0.1. In this case, the derived vertical profiles of the optical depth at 355 nm mostly meet conditions (a) - (c). In certain cases, potentially good values for optical depth can be found for the 532 nm channel for ranges of few hundred meters. Due to the noise, the retrieved profiles are not exactly monotonically increasing and therefore further smoothing is necessary to obtain acceptable measurement accuracy. The optical depth extracted from the signals at the wavelength 1064 nm was smaller than 0.1 and generally did not satisfy the conditions (a) - (c).
- The a posteriori analysis of the functions $\tau(0, h)$, $\exp[A^*(h)]$, and $q(h)$ allows one to estimate the atmospheric conditions and decide if the existing atmospheric conditions are relevant enough to apply the multiangle approach and extract both vertical profiles of $\tau(0, h)$ and $\exp[A^*(h)]$, or if only the profile of $\exp[A^*(h)]$ might be used as the source of information on the searched atmosphere.

The methods described in section 4.6 to determine the aerosol extinction and backscatter coefficients showed promising results.

5. Conclusions

The research was largely focused on the development and testing of new generation lidar inversion techniques. The main theoretical findings concerning these techniques were treated at two field campaigns: the Baltimore PM Supersite Experiment (2001 - 2003) and the Montana Experiment (2005).

High spatial and temporal resolution elastic backscatter lidar data from the Baltimore PM Supersite experiment were analyzed with a near-end approach to estimate vertical profiles of the aerosol extinction coefficient. The near-end approach makes use of a boundary condition in the near field of the lidar measurement range. The established boundary values are extrapolated from the ground level where the aerosol extinction coefficient is determined making use of the measured aerosol scattering coefficient (at 0.530 μm), particle size distribution, and computed refractive index (Mie theory). The lidar ratio was assumed constant over the vertical profile; its value was determined at ground level with Mie theory. In addition to the vertical profiles of aerosol extinction coefficient, various ground level optical parameters that were measured and computed were analyzed. The average index of refraction was determined by matching the computed and measured aerosol scattering coefficient at 0.530 μm (indirect method). Finally, the uncertainty in determining the boundary condition and how this is ultimately reflected in the vertical profiles of the aerosol extinction coefficient is discussed. In addition to the inherent errors due to the assumptions in Mie theory, the most uncertain factor in determining the boundary condition is the aerosol index of refraction. Two methods were employed to determine ground level extinction coefficient, which in turn means that two methods (indirect and direct) to determine aerosol refractive index were studied. The first method is referred to as the indirect method and the second method (the direct method) computes the average refractive index accounting for the chemical composition of the aerosols. The analyses show that there is not a good agreement between the estimates of the refractive index by the two methods, which in turn reflect different profiles for aerosol extinction coefficient. Possible causes are: ill-posedness of the inversion problems in Mie theory, incompleteness of the chemical measurements (radicals), as parts of PM2.5, as well as assumptions made to relate the radicals with chemical species.

The Montana experiment was undertaken to develop and test an improved multi-angle method for processing multiangle data obtained with an elastic scanning lidar in clear atmospheres. The selected Kano-Hamilton multiangle method is the only method that allows one to avoid the assumption of a height-invariant backscatter-to-extinction ratio (or the lidar ratio) when inverting the elastic-lidar data. The method is based on the regression of the logarithm of the range-corrected signal versus inverse of the sine of the elevation angle. The technique allows one to determine profiles of the optical depth and relative backscattering versus height. The intercept gives the relative backscatter coefficient {$\ln[C\beta(h)]$ where C is the lidar constant and $\beta(h)$ the total backscatter coefficient}; the slope gives the total optical depth [optical depth $\tau(0, h)$=-slope/2]. These profiles and the range-corrected signals obtained in the process of the multiangle measurements are also used to determine the lidar overlap function versus range. The retrieved data allows one to analyze the influence of the local horizontal heterogeneity and measured lidar-data distortions, and thus, to estimate the retrieved data quality.

The methodology and the data processing technique were tested with experimental data obtained from two simultaneously scanning lidars when operating in clear atmospheres. The methodology focuses primarily in finding the optimal range for the logarithm of RCS used for inversion. The application of the modified Kano-Hamilton method to the experimental data obtained in clear atmospheres at different wavelengths showed that the lidar signals measured at 355 nm yield much more accurate inversion results than signals measured at longer wavelengths. As expected, the application of the multiangle method to the data from the 532 nm channel, and especially the 1064 nm channel, brought less encouraging results. The first reason is that the total optical depth for these wavelengths over the same altitude range is significantly less than that for 355 nm and the signals are much more sensitive to the heterogeneity of particulate loading. Another reason is that the molecular backscatter component, which stabilizes the solution at 355 nm, at 1064 nm is almost hundred times less as compared to that at 355 nm. In the clear atmospheres under investigation, the Kano-Hamilton multiangle method is most applicable for short wavelength lidars (especially 355 nm).

It follows from our experimental data that the Kano-Hamilton multiangle method may work properly when the total vertical optical depth over the measured altitude range is not less than ~ 0.1. In this case, the derived vertical profiles of the optical depth at 355 nm mostly satisfy the condition of monotonically increasing profiles, with a zero value when extrapolated to the ground level. In certain cases, potentially good values for optical depth can be found for the 532 nm channel for ranges of a few hundred meters. Due to the noise, the retrieved profiles are not exactly monotonically increasing and therefore further smoothing is necessary to obtain acceptable measurement accuracy. The optical depth extracted from the signals at the wavelength 1064 nm was smaller than 0.1 and generally did not satisfy the condition of monotonically increasing profiles, with a zero value when extrapolated to the ground level. The a posteriori analysis of the functions $\tau(0, h)$, $\exp[A^*(h)]$, and $q(h)$

allows one to estimate the atmospheric conditions and decide if the existing atmospheric conditions are relevant enough to apply the multiangle approach and extract both vertical profiles of $\tau(0, h)$ and $\exp[A^*(h)]$, or if only the profile of $\exp[A^*(h)]$ might be used as the source of information on the searched atmosphere.

A method to calculate aerosol extinction coefficient from optical depth results, was tested on both simulated and experimental lidar data. A second method, to calculate aerosol backscatter coefficient from the intercept data, was tested on simulated lidar data. The later method needs a ground based measurement of the aerosol backscatter coefficient to determine the lidar constant.

References

Appendix I

Rayleigh scattering

Interaction of electromagnetic waves with particles is studied by means of Maxwell equations, which relate and describe the behavior of electric and magnetic fields (which are perpendicular on each other):

$$\nabla \bullet \boldsymbol{D} = 4\pi\rho \tag{A1.1}$$

$$\nabla \bullet \boldsymbol{B} = 0 \tag{A1.2}$$

$$\nabla \times \boldsymbol{H} = \frac{4\pi}{c}\boldsymbol{J} + \frac{1}{c}\frac{\partial \boldsymbol{D}}{\partial t} \tag{A1.3}$$

$$\nabla \times \boldsymbol{E} + \frac{1}{c}\frac{\partial \boldsymbol{B}}{\partial t} = 0 \tag{A1.4}$$

where ***E*** and ***H*** are the electric and magnetic fields, ***D*** and ***B*** are the electric displacement and magnetic induction, ρ is the density of charges, ***J*** is the electric current density, and c is the speed of light. The equation of continuity (charge conservation) is:

$$\frac{\partial \rho}{\partial t} + \nabla \bullet \boldsymbol{J} = 0 \tag{A1.5}$$

The relationships between these vectors are:

$$\begin{aligned} \boldsymbol{D} &= \varepsilon \boldsymbol{E} \\ \boldsymbol{B} &= \mu \boldsymbol{H} \\ \boldsymbol{J} &= \sigma \boldsymbol{E} \end{aligned} \tag{A1.6}$$

where ε is the electric permittivity, μ is the magnetic permeability and σ is the specific conductivity.

After some manipulations, the wave equation, in terms of scalar and vector potentials, is (see *Jackson*, 1975):

$$\nabla^2\Psi - \frac{1}{c^2}\frac{\partial^2\Psi}{\partial t^2} = -4\pi f(x,t) \tag{A1.7}$$

where Ψ and the source distribution $f(x,t)$ are either the scalar potential Φ and ρ, or vector potential A and J/c respectively. In terms of potentials, the following relationships are defined

$$B = \nabla \times A \tag{A1.8}$$

$$E + \frac{1}{c}\frac{\partial A}{\partial t} = -\nabla\Phi \tag{A1.9}$$

Equation A1.7 can be solved with Greens functions. Using Fourier transform (FT) for functions Ψ and f, we end up with a Helmholtz wave equation for $\Psi(x,\omega)$:

$$\left(\nabla^2 + k^2\right)\Psi(x,\omega) = -4\pi f(x,\omega) \tag{A1.10}$$

where $k = \omega/c$.

The corresponding Greens functions satisfy the inhomogeneous equation:

$$\left(\nabla^2 + k^2\right)G_k(x,x') = -4\pi\delta(x-x') \tag{A1.11}$$

If there are no boundary surfaces, then the Greens function can only depend on $R=|x-x'|$. In spherical coordinates, $G_k(R)$ satisfies:

$$\frac{1}{R}\frac{d^2}{dR^2}\left(RG_k\right) + k^2G_k = -4\pi\delta(\boldsymbol{R}) \tag{A1.12}$$

The solution for the homogeneous equation satisfied by G_k (everywhere but $R = 0$)

$$\frac{d^2}{dR^2}\left(RG_k\right) + k^2\left(RG_k\right) = 0 \tag{A1.13}$$

is

$$RG_k(R) = Ae^{ikR} + Be^{-ikR} \tag{A1.14}$$

For $R \to 0$, equation A1.12 reduces to a Poisson equation and in the limit $kR \ll 1$

$$\lim_{kR\to 0} G_k(R) = \frac{1}{R} \tag{A1.15}$$

The general solution for the Greens function is thus:

$$G_k(R) = A\frac{e^{ikR}}{R} + B\frac{e^{-ikR}}{R} \tag{A1.16}$$

with A + B = 0.

For outgoing wave, the Greens function is

$$G_k(R) = \frac{e^{ikR}}{R} \tag{A1.17}$$

The solutions for the vector potential A and scalar potential Φ become:

$$\boldsymbol{A(x)} = \frac{1}{c}\int J(\boldsymbol{x}')\frac{e^{ik|x-x'|}}{|\boldsymbol{x}-\boldsymbol{x}'|}d^3x' = \frac{e^{ikr}}{cr}\int J(\boldsymbol{x}')d^3x' \tag{A1.18}$$

$$\Phi\boldsymbol{(x)} = \int \rho(\boldsymbol{x}')\frac{e^{ik|x-x'|}}{|\boldsymbol{x}-\boldsymbol{x}'|}d^3x' = \frac{e^{ikr}}{r}\int \rho(\boldsymbol{x}')d^3x' \tag{A1.19}$$

then, the magnetic induction B is calculated using A1.8 and the electric field E outside the source is calculated using A1.9.

Consider charges and currents having a sinusoidal variation in time:

$$\begin{aligned} \rho(x,t) &= \rho(x)e^{-i\omega t} \\ J(x,t) &= J(x)e^{-i\omega t} \end{aligned} \tag{A1.20}$$

Then, by integrating by parts the current $J(x)$ becomes

$$\int \boldsymbol{J}d^3x' = -\int \boldsymbol{x}'(\nabla'\bullet\boldsymbol{J})d^3x' = -i\omega\int \boldsymbol{x}'\rho(\boldsymbol{x}')d^3x' \tag{A1.21}$$

from continuity (A1.5) we have $i\omega\rho = \nabla\bullet\mathbf{J}$.

Defining the electric dipole moment:

$$\boldsymbol{p} = \int \boldsymbol{x}'\rho(\boldsymbol{x}')d^3x' \tag{A1.22}$$

the vector potential A can be written as:

$$\boldsymbol{A}(\boldsymbol{x}) = -ik\boldsymbol{p}\frac{e^{ikr}}{r} \tag{A1.23}$$

The electric dipole field is defined with $\boldsymbol{E} = \frac{i}{k}\nabla\times\boldsymbol{B}$ and $\boldsymbol{B}=\nabla\times\boldsymbol{A}$. In the radiation zone (all terms with $1/r^{n}$, $n > 2$ will be negligible) we get:

$$\boldsymbol{B} = \nabla\times\boldsymbol{A} = k^2(\boldsymbol{n}\times\boldsymbol{p})\frac{\mathrm{e}^{\mathrm{ikr}}}{\mathrm{r}} \tag{A1.24}$$

$$\boldsymbol{E} = \frac{i}{k}\nabla\times\boldsymbol{B} = \boldsymbol{B}\times n = k^2(\boldsymbol{n}\times\boldsymbol{p})\times\boldsymbol{n}\frac{e^{ikr}}{r} = -k^2p\frac{\sin\gamma}{r}e^{ikr} \tag{A1.25}$$

where n is the normal in the radius direction, and γ is the direction of emitted radiation by dipole.

Consider unpolarized light with electric field E_0 isotropically distributed over directions orthogonal to the direction of propagation z, i.e. incident intensities are $I_{0x}=I_{0y}=I_0/2$ (Figure A1.1). After light interacts with a molecule (considered as a dipole), the scattered path makes an angle θ with z direction, in yz plane. The induced dipoles p_x and p_y radiate scattered waves. Radiated waves make an angle $\gamma_1 = \pi/2$ from p_x and an angle $\gamma_2 = \pi/2 - \theta$ from p_y. The corresponding electric fields of scattered radiation will be:

$$\boldsymbol{E}_{\boldsymbol{x}} = -k^2p_x\frac{e^{ikr}}{r} = -k^2E_{0x}\alpha\frac{e^{ikr}}{r} \tag{A1.26}$$

$$\boldsymbol{E}_{\boldsymbol{y}} = -k^2p_y\frac{\cos\theta e^{ikr}}{r} = -k^2E_{0y}\alpha\frac{\cos\theta e^{ikr}}{r} \tag{A1.27}$$

where $p = \alpha E_0$ is the induced dipole moment and α is the polarizability of the particle.

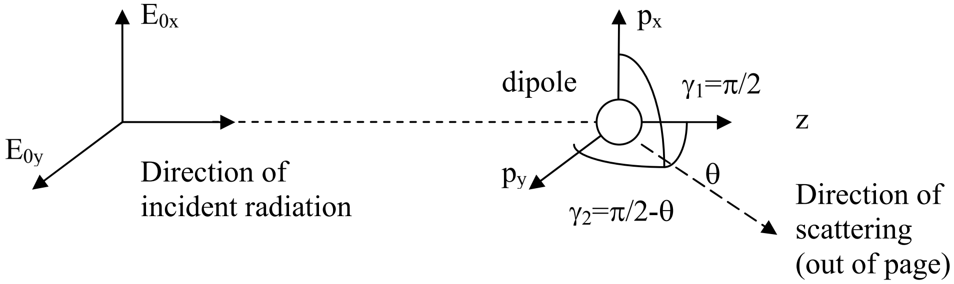

Figure A1.1. Unpolarized sunlight, with equal and independent fields E_{0x} and E_{0y} induce electric dipoles p_x and $p_{y;}$ the scattering path makes an angle θ with the z direction

The intensities of the incident and scattered fields (average of the Pointing vector) are:

$$I_0 = I_{0x} + I_{0y} = \frac{c}{8\pi}|E_0|^2, \quad I = I_x + I_y = \frac{c}{8\pi}|E|^2 \tag{A1.28}$$

such that we obtain:

$$I = I_0 k^4 \frac{\alpha^2}{r^2} \frac{1+\cos^2\theta}{2} \tag{A1.29}$$

In terms of λ, with k = 2π/λ

$$I = I_0 \frac{\alpha^2}{r^2} \frac{16\pi^4}{\lambda^4} \frac{1+\cos^2\theta}{2} = I_0 \frac{\alpha^2}{r^2} \frac{128\pi^5}{3\lambda^4} P(\theta) \tag{A1.30}$$

where P(θ) is the normalized phase function defined as:

$$P(\theta) = \frac{3}{16\pi}\left(1+\cos^2\theta\right) \tag{A1.31}$$

Figure A1.2 shows the shape of the molecular phase function (Rayleigh scattering) with maximum scattering in forward and backward directions.

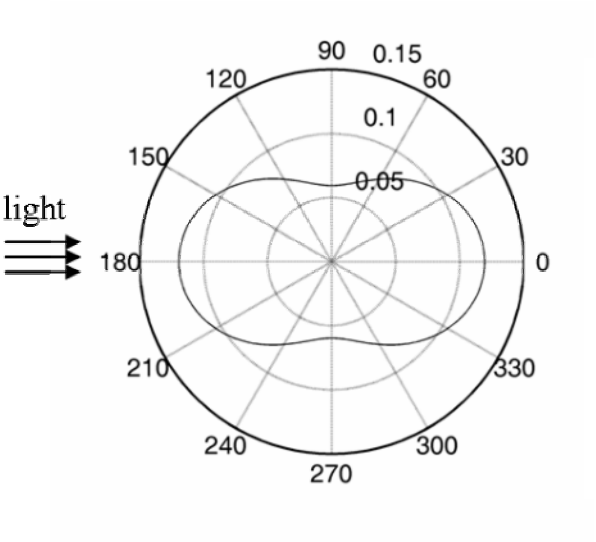

Figure A1.2. Phase function for Rayleigh scattering (equation A1.31). The incident light comes from the left. The maximum scattering occurs in forward (0^o) and backward (180^o) directions

The total energy scattered in all directions per unit time is given by the integral over the unit sphere in A1.29.

$$W = \int_0^1 \int_0^{2\pi} \int_0^{\pi} Ir^2 dr \sin\varphi d\theta d\varphi = \frac{8}{3}\pi k^4 \alpha^2 I_0 \tag{A1.32}$$

The scattering cross section is defined as the total scattered energy *W* over the incident intensity I_0.

$$C_{sca} = \frac{8}{3}\pi k^4 \alpha^2 = \frac{128\pi^5}{3\lambda^4}\alpha^2 \tag{A1.33}$$

Finally, the scattered intensity at distance *r* can be expressed as:

$$I = I_0 \frac{C_{sca}}{r^2} P(\theta) \tag{A1.34}$$

The scattering coefficient due to n_m molecules is:

$$\sigma_m = n_m C_{sca} = n_m \frac{128\pi^5}{3\lambda^4}\alpha^2 \tag{A1.35}$$

The polarizability α is related with the index of refraction *m* [$m = (\varepsilon_r)^{1/2}$] by the mean of the Lorentz – Lorenz formula (see, for example *Born and Wolf*, page 87):

$$\alpha = \frac{3}{4\pi n_m} \frac{m^2 - 1}{m^2 + 2} \tag{A1.36}$$

where n_m is the number of molecules per unit volume. For m close to 1, $m^2 - 1 \cong (m-1)^2 + 2m - 2 \cong 2(m-1)$ and $m^2 + 2 \cong 3$. The number of molecules can be found using the equation of state for the ideal gas: $P = n_m KT$. The final relation for the molecular scattering coefficient becomes:

$$\sigma_m = \frac{32\pi^3 \left(m-1\right)^2}{3\lambda^4} \frac{KT}{P} \tag{A1.37}$$

A depolarization factor δ is included to account for anisotropy of the molecules polarizability.

$$\sigma_m = \frac{32\pi^3 \left(m-1\right)^2}{3\lambda^4} \frac{KT}{P} \frac{6+3\delta}{6-7\delta} \tag{A1.38}$$

where $\delta = 0.035$ in case of air. The index of refraction for dry air (at standard P and T) is given by Edlen's formula (1966)

$$10^6 \left(m-1\right) = 83.4213 + \frac{24060.30}{130-\nu^2} + \frac{159.97}{38.9-\nu^2} \tag{A1.39}$$

To account for pressure and temperature dependence, equation A1.38 is written as:

$$\sigma_m = \frac{32\pi^3 \left(m-1\right)^2}{3\lambda^4} \frac{6+3\delta}{6-7\delta} \left(\frac{T_0}{P_0}\right)^2 \frac{KP}{T} \tag{A1.40}$$

The molecular backscatter, whose phase function is $P(\pi)=3/8\pi$, is:

$$b_m = \frac{3}{8\pi} \sigma_m \tag{A1.41}$$

Appendix II

Mie theory

To compute extinction, scattering, backscattering, and absorption coefficients of the particles, we need to know their extinction, scattering, backscattering and absorption efficiencies. These efficiencies are calculated solving the Maxwell equations, which describe the interaction of electromagnetic waves (plane waves) with particles. Mie theory assumes that the particles are homogeneous spheres. The radiation wavelength is comparable with the particle diameter. When the particle is a sphere, solutions to Maxwell equations are determined analytically. As previously said, the solutions of the Maxwell equations represent the scattered electromagnetic field within the particle (internal field) and outside the particle in the homogeneous medium in which the particle is embedded (external field). In our case, the medium is air, which is characterized by an index of refraction of about 1 such that, the relative index of refraction will equal the particle index of refraction.

In a medium free of charges (ρ and *J* are zero in equation A1.1 and A1.3), Maxwell equations (A1.1-A1.4) become:

$$\nabla \bullet \boldsymbol{D} = 0 \tag{A2.1}$$

$$\nabla \bullet \boldsymbol{B} = 0 \tag{A2.2}$$

$$\nabla \times \boldsymbol{H} = \frac{\varepsilon}{c}\frac{\partial \boldsymbol{E}}{\partial t} \tag{A2.3}$$

$$\nabla \times \boldsymbol{E} = -\frac{\mu}{c}\frac{\partial \boldsymbol{H}}{\partial t} \tag{A2.4}$$

where the relationships A1.6 were used.

Combining above equations, we obtain the vector wave equation for ***E*** and ***H***:

$$\Delta \boldsymbol{E} = \frac{\varepsilon\mu}{c^2}\frac{\partial^2 \boldsymbol{E}}{\partial t^2} \tag{A2.5}$$

$$\Delta \boldsymbol{H} = \frac{\varepsilon\mu}{c^2}\frac{\partial^2 \boldsymbol{H}}{\partial t^2} \tag{A2.6}$$

The velocity of wave propagation is:

$$v = \frac{c}{\sqrt{\varepsilon\mu}} \tag{A2.7}$$

For air, $\mu = 1$. The time evolution of $\boldsymbol{E}$ and $\boldsymbol{H}$ are ~ $\exp(-i\omega t)$ such that equation A2.5 and A2.6 can be written as:

$$\Delta \boldsymbol{E} + k^2 m^2 \boldsymbol{E} = 0 \tag{A2.8}$$

$$\Delta \boldsymbol{H} + k^2 m^2 \boldsymbol{H} = 0 \tag{A2.9}$$

where $k = \omega/c$ is the wave number and $m = \sqrt{\varepsilon\mu}$ is the refractive index. Consider that the incident radiation (plane wave) is linear polarized with the electric and magnetic components on x and y axes and the direction of propagation in the z axis (Figure A2.1). Each vector component will satisfy a scalar wave equation similar to A2.8 and A2.9 where instead of vectors $\boldsymbol{E}$ and $\boldsymbol{H}$ we will have spherical components E_r, E_θ, E_φ, H_r, H_θ, H_φ.

Equations A2.8 and A2.9 are rewritten in spherical coordinates. The solution will be a combination of spherical harmonics. The continuity of the tangential and perpendicular components of vectors $\boldsymbol{E}$ and $\boldsymbol{H}$ are the boundary conditions applied to the sphere surface. The incident wave (of amplitude 1) is described by:

$$\begin{aligned} \boldsymbol{E} &= \boldsymbol{i}e^{-ikz+i\omega t} \\ \boldsymbol{H} &= \boldsymbol{j}e^{-ikz+i\omega t} \end{aligned} \tag{A2.10}$$

where $\boldsymbol{i}$ and $\boldsymbol{j}$ are the unit vectors in x and y axes. Solution A2.10 can be written in terms of their components (scalar solutions), u and v:

$$u = e^{i\omega t}\cos\phi\sum_{n=1}^{\infty}\left(-i\right)^{n}\frac{2n+1}{n\left(n+1\right)}P_n^1\left(\cos\theta\right)j_n\left(kr\right) \quad \text{(A2.11)}$$

$$v = e^{i\omega t}\sin\phi\sum_{n=1}^{\infty}\left(-i\right)^{n}\frac{2n+1}{n\left(n+1\right)}P_n^1\left(\cos\theta\right)j_n\left(kr\right) \quad \text{(A2.12)}$$

where $P_n^1\left(\cos\theta\right)$ are associated Legendre polynomials and j_n are spherical Bessel functions (see for example *Stegun*, 1964 and *Antosiewicz*, 1964)

Outside the sphere, the scattered wave is:

$$u = e^{i\omega t}\cos\phi\sum_{n=1}^{\infty}-a_n\left(-i\right)^{n}\frac{2n+1}{n\left(n+1\right)}P_n^1\left(\cos\theta\right)h_n^{(2)}\left(kr\right) \quad \text{(A2.13)}$$

$$v = e^{i\omega t}\sin\phi\sum_{n=1}^{\infty}-b_n\left(-i\right)^{n}\frac{2n+1}{n\left(n+1\right)}P_n^1\left(\cos\theta\right)h_n^{(2)}\left(kr\right) \quad \text{(A2.14)}$$

where $h_n^{(2)}$ are spherical Bessel functions with an asymptotic behavior:

$$h_n^{(2)}\left(kr\right) \sim \frac{i^{n+1}}{kr}e^{-ikr} \quad \text{(A2.15)}$$

such that the conditions at infinity for *u* and *v* are satisfied.

Similar expressions are derived for the wave inside the sphere (internal field). From the boundary conditions, the coefficients a_n, b_n and two additional internal coefficients are determined. New notations are introduced using a combination of Bessel functions and their arguments *kr*. The expressions for the coefficients a_n and b_n are:

$$\begin{aligned} a_n &= \frac{\psi_n'\left(y\right)\psi_n\left(x\right) - m\psi_n\left(y\right)\psi_n'\left(x\right)}{\psi_n'\left(y\right)\zeta_n\left(x\right) - m\psi_n\left(y\right)\zeta_n'\left(x\right)} \\ b_n &= \frac{m\psi_n'\left(y\right)\psi_n\left(x\right) - \psi_n\left(y\right)\psi_n'\left(x\right)}{m\psi_n'\left(y\right)\zeta_n\left(x\right) - \psi_n\left(y\right)\zeta_n'\left(x\right)} \end{aligned} \quad \text{(A2.16)}$$

where $x = \frac{2\pi r}{\lambda}$ and $y = mx$; Ψ_n and ζ_n are defined as following:

$$\begin{aligned}\psi_n(z) &= zj_n(z)\\ \zeta_n(z) &= zh_n^{(2)}(z)\end{aligned} \tag{A2.17}$$

$j_n(z)$ and $h_n^{(2)}$ are spherical Bessel function of first and second kind (for more details see *Antosiewicz*, 1964).

In the far field, at large distances from the particle, the solutions of A2.13 and A2.14 for the scattered waves are:

$$u = -\frac{i}{kr} e^{-ikr+i\omega t} \cos\phi \sum_{n=1}^{\infty} a_n \frac{2n+1}{n(n+1)} P_n^1(\cos\theta) \tag{A2.18}$$

$$v = -\frac{i}{kr} e^{-ikr+i\omega t} \sin\phi \sum_{n=1}^{\infty} b_n \frac{2n+1}{n(n+1)} P_n^1(\cos\theta) \tag{A2.19}$$

The following functions, which depend on scattering angle, appear:

$$\begin{aligned}\pi_n(\cos\theta) &= \frac{1}{\sin\theta} P_n^1(\cos\theta)\\ \tau_n(\cos\theta) &= \frac{d}{d\theta} P_n^1(\cos\theta)\end{aligned} \tag{A2.20}$$

The resulting field components can be written at once as:

$$E_\theta = H_\varphi = -\frac{i}{kr} e^{-ikr+i\omega t} \cos\varphi S_2(\theta) \tag{A2.21}$$

$$-E_\varphi = H_\theta = -\frac{i}{kr} e^{-ikr+i\omega t} \sin\varphi S_1(\theta) \tag{A2.22}$$

where

$$S_1(\theta) = \sum_{n=1}^{\infty} \frac{2n+1}{n(n+1)} \left[a_n \pi_n(\cos\theta) + b_n \tau_n(\cos\theta) \right] \tag{A2.23}$$

$$S_2(\theta) = \sum_{n=1}^{\infty} \frac{2n+1}{n(n+1)} \left[b_n \pi_n(\cos\theta) + a_n \tau_n(\cos\theta) \right] \tag{A2.24}$$

$S_1(\theta)$ and $S_2(\theta)$ are the amplitude functions. If we decompose the incident electric field E into parallel and perpendicular components (Figure A2.1) we obtain:

$$\begin{aligned} E_{0r} &= \sin\varphi \\ E_{0l} &= \cos\varphi \end{aligned} \tag{A2.25}$$

The scattered wave components are:

$$\begin{aligned} E_r &= -E_\varphi \\ E_l &= E_\theta \end{aligned} \tag{A2.26}$$

We write the scattered wave components in a matrix form:

$$\begin{pmatrix} E_l \\ E_r \end{pmatrix} = \frac{e^{-ikr+i\omega t}}{ikr} \begin{pmatrix} S_2(\theta) & S_3(\theta) \\ S_4(\theta) & S_1(\theta) \end{pmatrix} \begin{pmatrix} E_{0l} \\ E_{0r} \end{pmatrix} \tag{A2.27}$$

where for sphere, $S_3(\theta) = S_4(\theta) = 0$.

The matrix of S_1, S_2, S_3, and S_4 is called amplitude scattering matrix.

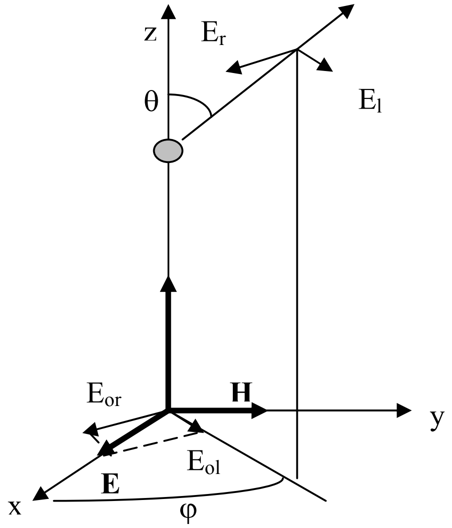

Figure A2.1 Decomposition of electric vector of incident and scattered waves

The intensities of incident and scattered fields are:

$$I_0 = \frac{c}{8\pi}\left|E_0\right|^2 = \frac{c}{8\pi} \tag{A2.28}$$

$$I = \frac{c}{8\pi}\left|E\right|^2 = \frac{c}{8\pi}\frac{F(\theta)}{(kr)^2} = \frac{F(\theta)}{(kr)^2} I_0 \tag{A2.29}$$

The extinction efficiency is computed from the amplitude function $S(\theta)$ with $\theta = 0$.

The amplitude functions S_1 and S_2 are then equal to:

$$S(0) = \frac{1}{2}\sum_{n=1}^{\infty}(2n+1)(a_n + b_n) \tag{A2.30}$$

and $F(\theta) = \mathrm{Re}[S(0)]$. The extinction cross section is

$$C_{ext} = \frac{4\pi r^2 I}{I_0} = \frac{4\pi}{k^2}\mathrm{Re}\left[S(0)\right] \tag{A2.31}$$

It follows that extinction efficiency ($Q_{ext} = C_{ext}/\pi r^2$) is

$$Q_{ext} = \frac{4}{x^2}\mathrm{Re}\left[S(0)\right] = \frac{2}{x^2}\sum_{n=1}^{\infty}(2n+1)\mathrm{Re}(a_n + b_n) \tag{A2.32}$$

For a scattered wave, the scattering cross section is

$$C_{sca} = \frac{1}{k^2}\int\int F(\theta,\varphi)\sin\theta d\theta d\varphi \tag{A2.33}$$

where

$$F(\theta,\varphi) = \left|S_2(\theta)\right|^2 \cos^2\varphi + \left|S_1(\theta)\right|^2 \sin^2\varphi \tag{A2.34}$$

The scattering efficiency has the final expression:

$$Q_{sca} = \frac{2}{x^2}\sum_{n=1}^{\infty}(2n+1)\left[\left|a_n\right|^2 + \left|b_n\right|^2\right] \tag{A2.35}$$

The absorption efficiency is the difference between extinction and scattering efficiency.

$$Q_{asb} = Q_{ext} - Q_{sca} \tag{A2.36}$$

The backscatter efficiency ($\theta = \pi$), for which

$$S_2(\pi) = -S_1(\pi) = \frac{1}{2}\sum_{n=1}^{\infty}(2n+1)(-1)^n(a_n - b_n) \tag{A2.37}$$

is

$$Q_{back} = \frac{1}{x^2}\left|\sum_{n=1}^{\infty}(2n+1)(-1)^n(a_n + b_n)\right|^2 \tag{A2.38}$$

Appendix III

Derivation of the lidar equation

The derivation described here follows *Measures* (1984).

The laser irradiance [rate of radiant energy (radiant power) incident per unit area upon a surface] [W/m^2] at range R is:

$$I(R) = \frac{E_L T(\lambda, R)}{\tau_L A_L(R)} \tag{A3.1}$$

where E_L is the pulse (rectangular shaped) energy, $T(\lambda, R)$ is the transmittance from the lidar to R, τ_L is the laser pulse duration and A_L the target area (depending on laser divergence, i.e. laser's solid angle); E/τ_L is the pulse power (radiant power)

More accurately, irradiance (and consequently radiance, volume backscatter, overlap function) also depends on the position, r, from the middle of the target to a certain point. Usually (as considered here) it is assumed that the laser pulse energy is uniform over the target area.

The target spectral radiance (the rate of radiant energy leaving at a point on the target surface per unit solid angle and unit projected area) [W/m^2 m sr] is proportional to the laser irradiance at R and backscatter coefficient:

$$J(\lambda, R) = \beta(\lambda, R) I(R) \tag{A3.2}$$

where

$$\beta(\lambda, R) = \sum_i N_i(R) \frac{d\sigma(\lambda)}{d\Omega}_i \tag{A3.3}$$

is the volume backscatter coefficient [1/m sr]; N_i is the number density of i^{th} species [1/m^3] and $\frac{d\sigma(\lambda)}{d\Omega}_i$ is the differential scattering cross section for the species i [m^2/sr].

The total signal power received by detector at $t = 2R/c$ is:

$$P(\lambda,t) = \int_{0}^{R=ct/2} dR \int_{\Delta\lambda_0} d\lambda \int J(\lambda,R) p(\lambda,R) dA(R) \qquad \text{(A3.4)}$$

where $p(\lambda, R)$ is the probability that the radiation emanated from range R will reach the detector and it contains:

$$p(\lambda,R) = \xi(\lambda) q(R) T(\lambda,R) \frac{A_0}{R^2} \qquad \text{(A3.5)}$$

where A_0/R^2 is the acceptance solid angle of the receiver optics, $T(\lambda, R)$ is atmospheric transmittance at wavelength λ over range R, $q(R)$ is the overlap function and $\xi(R)$ is the receiver's spectral transmission (accounts for lenses, filters, mirrors).

The range of wavelength integration extends over the lidar receiver's spectral window $\Delta\lambda_0$ centered about λ. Replacing A3.2 and A3.5 in A3.4 we obtain:

$$P(\lambda,t) = A_0 \int_{0}^{R=ct/2} \frac{dR}{R^2} \int_{\Delta\lambda_0} \xi(\lambda) d\lambda \int \beta(\lambda,R) T(\lambda,R) q(R) I(R) dA(R) \qquad \text{(A3.6)}$$

The observed radiation is a narrow band much smaller than $\Delta\lambda_0$ such that we can treat $\beta(\lambda, R)$ as a delta function. The medium is assumed to be homogeneous over the zone of the overlap such that equation A3.6 becomes:

$$P(\lambda,t) = A_0 \xi(\lambda) \int_{0}^{R=ct/2} \frac{dR}{R^2} \beta(\lambda,R) T(\lambda,R) \int q(R) I(R) dA(R) \qquad \text{(A3.7)}$$

If the lateral distribution of the laser pulse energy over the area A_L is uniform, then:

$$\int q(R) I(R) dA(R) = q(R) I(R) A_L(R) \qquad \text{(A3.8)}$$

and equation A3.7 becomes:

$$P(\lambda,t) = A_0 \xi(\lambda) \int_{0}^{R=ct/2} \frac{dR}{R^2} \beta(\lambda,R) T(\lambda,R) q(R) I(R) A_L(R) \qquad \text{(A3.9)}$$

For a rectangular shaped laser pulse, with duration τ_L, the limits of the integration extend from $c(t-\tau_L)/2$ to $ct/2$. The range dependent parameters can be considered constant over small interval of range integration. We obtain:

$$P(\lambda,t) = A_0\xi(\lambda)\beta(\lambda,R)T(\lambda,R)q(R)I(R)A_L(R)\frac{c\tau_L/2}{R^2} \quad \text{(A3.10)}$$

Radiative energy received by the detector during the interval $[t, t + \tau_d]$, where $t = 2R/c$ and τ_d is the detector sampling duration, is:

$$E(\lambda,R) = \int_{2R/c}^{2R/c+\tau_d} P(\lambda,t)dt \quad \text{(A3.11)}$$

$$E(\lambda,R) = A_0\xi(\lambda)\beta(\lambda,R)T(\lambda,R)q(R)I(R)\frac{A_L}{R^2}\frac{c\tau_L}{2}\tau_d \quad \text{(A3.12)}$$

Taking into account equation A3.1 we get:

$$E(\lambda,R) = E_L\xi(\lambda)\beta(\lambda,R)T^2(\lambda,R)q(R)\frac{A_0}{R^2}\frac{c\tau_d}{2} \quad \text{(A3.13)}$$

The transmittance $T(\lambda, R)$ is defined as:

$$T(\lambda,R) = e^{-\int_0^R \kappa(\lambda,r)dr} \quad \text{(A3.14)}$$

where $\kappa(\lambda, R)$ is the total extinction coefficient.

Finally, the lidar equation can be written

$$E(R) = \frac{\mathrm{C}}{R^2}\beta(R)e^{-2\int_0^R \kappa(r)dr} \quad \text{(A3.15)}$$

where the lidar constant C is defined as:

$$\mathrm{C} = E_L\xi(\lambda)q(R)A_0\frac{c\tau_d}{2} \quad \text{(A3.16)}$$

This kind of lidar equation is called the basic scattering lidar equation.

Appendix IV

Analytical solutions for lidar equation

The lidar equation, as presented in 5.1

$$P(r) = \frac{\mathrm{C}}{r^2}\beta(r)\exp\left(-2\int_0^r \kappa(r')dr'\right) \tag{A4.1}$$

has three unknowns: total backscatter coefficient $\beta(r)$, total extinction coefficient $\kappa(r)$ and lidar constant C. Since the $\beta_m(r)$ and $\kappa_m(r)$ are usually estimated either from balloon measurements or from US Standard Atmosphere, the unknowns are $\beta_p(r)$, $\kappa_p(r)$ and C. When backscatter to extinction ratio (or its inverse, the lidar ratio LR) is range independent (a = const, Π_p = const), it is possible to solve lidar equation analytically. The inversion of lidar equation can be done by solving for either $\beta_p(r)$ or $\kappa_p(r)$. The present derivation is made for particle extinction coefficient $\kappa_p(r)$. We define the ratio $a = \Pi_m/\Pi_p$ where Π_m ($3/8\pi$) is the molecular backscatter to extinction ratio $[\beta_m(r)/\kappa_m(r)]$ and Π_p is the particulate backscatter to extinction ratio or 1/LR $[\beta_p(r)/\kappa_p(r)]$. Equation (A4.1) is written as

$$\begin{aligned}
P(r)r^2 &= \mathrm{C}\left[\beta_m(r)+\beta_p(r)\right]e^{-2\int_0^r\left[\kappa_m(r')+\kappa_p(r')\right]dr'} = \\
&= \mathrm{C}\Pi_p\left[a\kappa_m(r)+\kappa_p(r)\right]e^{-2\int_0^r\left[\kappa_m(r')+\kappa_p(r')\right]dr'} = \\
&= \mathrm{C}\Pi_p\left[a\kappa_m(r)+\kappa_p(r)\right]e^{-2\int_0^r\left[a\kappa_m(r')+\kappa_p(r')-a\kappa_m(r')+\kappa_m(r')\right]dr'} = \\
&= \mathrm{C}\Pi_p\left[a\kappa_m(r)+\kappa_p(r)\right]e^{-2\int_0^r(1-a)\kappa_m(r')dr'}\,e^{-2\int_0^r\left[a\kappa_m(r')+\kappa_p(r')\right]dr'}
\end{aligned} \tag{A4.2}$$

With the notation

$$u(r) = a\kappa_m(r)+\kappa_p(r) \tag{A4.3}$$

the above equation becomes a Bernoulli type equation

$$P(r)r^2 e^{2\int_0^r (1-a)\kappa_m(r')dr'} = C\Pi_p u(r) e^{-2\int_0^r u(r')dr'} \tag{A4.4}$$

Integrating it from 0 to r:

$$\int_0^r P(r')r'^2 e^{2\int_0^{r'}(1-a)\kappa_m(r'')dr''}dr' = C\Pi_p \int_0^r u(r') e^{-2\int_0^{r'} u(r'')dr''}dr' =$$

$$= \frac{C\Pi_p}{2}\int_0^r \left(e^{-2\int_0^{r'} u(r'')dr''} \right)' dr' = \frac{C\Pi_p}{2} e^{-2\int_0^r u(r')dr'} \Bigg|_0^r = \frac{C\Pi_p}{2}\left(1 - e^{-2\int_0^r u(r')dr'}\right)$$

(A4.5)

From A4.5 we determine the exponential

$$e^{-2\int_0^r u(r')dr'} = 1 - \frac{2\int_0^r P(r')r'^2 e^{2\int_0^{r'}(1-a)\kappa_m(r'')dr''}dr'}{C\Pi_p} \tag{A4.6}$$

and plug it back into equation A4.4

$$P(r)r^2 e^{2\int_0^r (1-a)\kappa_m(r')dr'} =$$

$$= C\Pi_p\left[a\kappa_m(r)+\kappa_p(r)\right]\left[1 - \frac{2\int_0^r P(r')r'^2 e^{2\int_0^{r'}(1-a)\kappa_m(r'')dr''}dr'}{C\Pi_p}\right]$$

Then the particle extinction coefficient $\kappa_p(r)$ is determined

$$\kappa_p(r) = \frac{P(r)r^2 e^{2\int_0^r (1-a)\kappa_m(r')dr'}}{C\Pi_p - 2\int_0^r P(r')r'^2 e^{2\int_0^{r'}(1-a)\kappa_m(r'')dr''} dr'} - a\kappa_m(r) \qquad \text{(A4.7)}$$

Next, the constant $C\Pi_p$ has to be determined from the boundary condition. If we know $\kappa_p(r)$ at some range r_m ($0 < r_0 < r_m < r$) then from equation A4.7 for $r = r_m$ we determine $C\Pi_p$.

$$C\Pi_p = 2\int_0^{r_m} P(r')r'^2 e^{2\int_0^{r'}(1-a)\kappa_m(r'')dr''} dr' + \frac{P(r_m)r_m^2 e^{2\int_0^{r_m}(1-a)\kappa_m(r')dr'}}{\kappa_p(r_m) + a\kappa_m(r_m)} \qquad \text{(A4.8)}$$

Then replace A4.8 in equation A4.7 and we obtain the general formula

$$\kappa_p(r) = \frac{P(r)r^2 e^{2(1-a)\int_{r_m}^{r} \kappa_m(r')dr'}}{\frac{P(r_\mathrm{m})r_\mathrm{m}^2}{\kappa_p(r_\mathrm{m}) + a\kappa_m(r_\mathrm{m})} - 2\int_{r_m}^{r} P(r')r'^2 e^{2(1-a)\int_{r_m}^{r'} \kappa_m(r'')dr''} dr'} - a\kappa_m(r) \qquad \text{(A4.9)}$$

When $r_m = r_{max}$, such that $r_0 < r < r_{max}$, we obtain the far-end solution

$$\kappa_p(r) = \frac{P(r)r^2 e^{-2(1-a)\int_{r}^{r_{max}} \kappa_m(r')dr'}}{\frac{P(r_{max})r_{max}^2}{\kappa_p(r_{max}) + a\kappa_m(r_{max})} + 2\int_{r}^{r_{max}} P(r')r'^2 e^{-2(1-a)\int_{r'}^{r_{max}} \kappa_m(r'')dr''} dr'} - a\kappa_m(r)$$

(A4.10)

When $r_m = r_0$ such that $r_0 < r < r_{max}$,, we get the near-end solution

$$\kappa_p(r) = \frac{P(r)r^2 e^{2(1-a)\int_{r_0}^{r} \kappa_m(r')dr'}}{\dfrac{P(r_0)r_0^2}{\kappa_p(r_0)+a\kappa_m(r_0)} - 2\int_{r_0}^{r} P(r')r'^2 e^{2(1-a)\int_{r_0}^{r'} \kappa_m(r'')dr''} dr'} - a\kappa_m(r) \quad \text{(A4.11)}$$

The near-end solution is unstable due to the singularity when the denominator can be zero.

The optical depth solution uses optical depth measured over the entire measurements range as a boundary condition. Let us write equation A4.4 as

$$P(r)r^2 e^{2(1-a)\int_{r_0}^{r} \kappa_m(r')dr'} = \mathrm{C}\Pi_p T_o^2 u(r) e^{-2\int_{r_0}^{r} u(r')dr'} \qquad \text{(A4.12)}$$

where T_0^2 is two way transmittance from the ground to r_0.

$$T_o^2 = e^{-2\int_0^{r_0}\left[\kappa_m(r')+\kappa_p(r')\right]dr'} \qquad \text{(A4.13)}$$

Integrating equation A4.12 from r_0 to r

$$\int_{r_0}^{r} P(r')r'^2 e^{2(1-a)\int_{r_0}^{r'} \kappa_m(r'')dr''} dr' = \mathrm{C}\Pi_p T_o^2 \int_{r_0}^{r} u(r') e^{-2\int_{r_0}^{r'} u(r'')dr''} dr' =$$
$$= \frac{\mathrm{C}\Pi_p T_o^2}{2}\left(1 - e^{-2\int_{r_0}^{r} u(r')dr'}\right)$$

we get the exponential

$$e^{-2\int_{r_0}^{r} u(r')dr'} = 1 - \frac{2}{\mathrm{C}\Pi_p T_0^2}\int_{r_0}^{r} P(r')r'^2 e^{2(1-a)\int_{r_0}^{r'} \kappa_m(r'')dr''} dr' \qquad \text{(A4.14)}$$

Integrating equation A4.12 from r_0 to r_{max}

$$\int_{r_0}^{r_{max}} P(r')r'^2 e^{2(1-a)\int_{r_0}^{r'} \kappa_m(r'')dr''} dr' = C\Pi_p T_o^2 \int_{r_0}^{r_{max}} u(r') e^{-2\int_{r_0}^{r'} u(r'')dr''} dr' =$$

$$= \frac{C\Pi_p T_o^2}{2}\left(1 - e^{-2\int_{r_0}^{r_{max}} u(r')dr'}\right)$$

we get $C\Pi_p T_0^2$

$$C\Pi_p T_o^2 = \frac{2\int_{r_0}^{r_{max}} P(r')r'^2 e^{2(1-a)\int_{r_0}^{r'} \kappa_m(r'')dr''} dr'}{1 - e^{-2\int_{r_0}^{r_{max}} u(r')dr'}} \tag{A4.14}$$

By plugging equations A4.13 and A4.14 into equation A4.12 and we obtain the expression for particle extinction coefficient $\kappa_p(r)$

$$\kappa_p(r) = \frac{0.5P(r)r^2 e^{2(1-a)\int_{r_0}^{r} \kappa_m(r')dr'}}{\dfrac{\int_{r_0}^{r_{max}} P(r')r'^2 e^{2(1-a)\int_{r_0}^{r'} \kappa_m(r'')dr''} dr'}{1 - e^{-2\int_{r_0}^{r_{max}} \left[a\kappa_m(r') + \kappa_p(r')\right]dr'}} - \int_{r_0}^{r} P(r')r'^2 e^{2(1-a)\int_{r_0}^{r'} \kappa_m(r'')dr''} dr'} - a\kappa_m(r)$$

or

$$\kappa_p(r) = \frac{0.5P(r)r^2 e^{2(1-a)\int_{r_0}^{r} \kappa_m(r')dr'}}{\dfrac{\int_{r_0}^{r_{max}} P(r')r'^2 e^{2(1-a)\int_{r_0}^{r'} \kappa_m(r'')dr''} dr'}{1 - V_{max}^2} - \int_{r_0}^{r} P(r')r'^2 e^{2(1-a)\int_{r_0}^{r'} \kappa_m(r'')dr''} dr'} - a\kappa_m(r)$$

(A4.15)

where V_{max}^2 is the effective transmittance over the range $[r_0, r_{max}]$

$$V_{max}^2 = e^{-2\int_{r_0}^{r_{max}} \left[a\kappa_m(r')+\kappa_p(r')\right]dr'} \tag{A4.16}$$

Since initially the total atmospheric aerosol optical depth is used (provided by a ground based or satellite based sun photometer), the next step is a normalization of the extinction coefficient. Then, a second iterative solution for extinction coefficient is determined. The iterative process repeats until convergence is reached.

Appendix V

Multiangle methods

The first condition comes from the assumption of a homogeneous horizontally stratified atmosphere is (see Figure A5.1):

$$\beta(h,\varphi_1)=\beta(h,\varphi_2)=\ldots=\beta(h,\varphi_N)=const. \tag{A5.1}$$

The optical depth along a slant path is:

$$\tau(h,\varphi_j)=\int_0^{r_j}\kappa_t(r')dr'=\frac{1}{\sin\varphi_j}\int_0^{h}\kappa_t(h')dh' \tag{A5.2}$$

or
$$\tau(h,\varphi_j)=\frac{1}{\sin\varphi_j}h\overline{\kappa_t}(h) \tag{A5.3}$$

where $\tau(h,\varphi_j)=\tau(r_j)$ is the optical depth along a slant path and κ_t is extinction coefficient; it follows that:

$$\tau(h,\varphi_1)\sin\varphi_1=\tau(h,\varphi_2)\sin\varphi_2=\ldots=\tau(h,\varphi_N)\sin\varphi_N=const. \tag{A5.4}$$

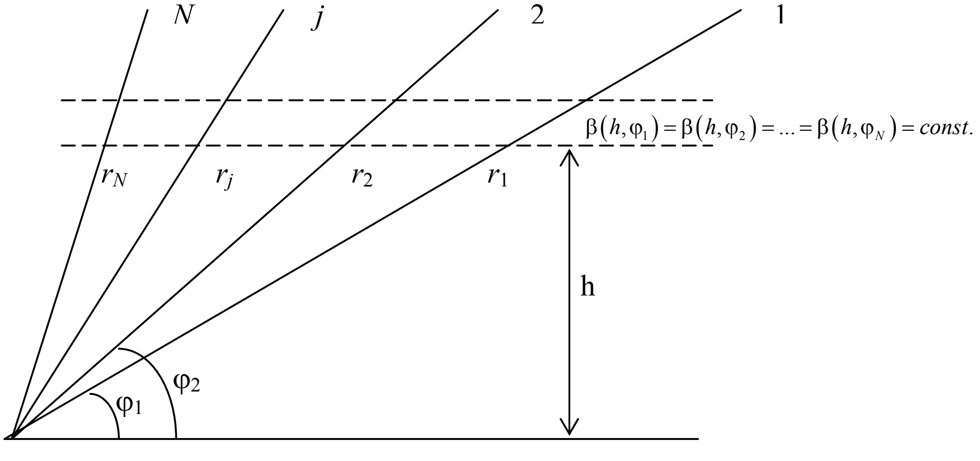

Figure A5.1. Schematic of multiangle measurements

$$\overline{\kappa_t}\left(h,\varphi_j\right)=\frac{\int_0^{r_j}\kappa_t\left(r'\right)dr'}{r_j}=\frac{\sin\varphi_j}{h}\int_0^{r_j}\kappa_t\left(r'\right)dr'=\frac{\sin\varphi_j}{h}\frac{h}{\sin\varphi_j}\overline{\kappa_t}\left(h\right)=\overline{\kappa_t}\left(h\right) \quad \text{(A5.5)}$$

such that

$$\overline{\kappa_t}\left(h,\varphi_1\right)=\overline{\kappa_t}\left(h,\varphi_2\right)=\ldots=\overline{\kappa_t}\left(h,\varphi_N\right)=\overline{\kappa_t}\left(h\right)=const. \quad \text{(A5.6)}$$

Consider two lidar measurements in the slant paths under elevation angles φ_1 and φ_2 (two angle method):

$$P\left(h,\varphi_1\right)=C\beta_t\left(h\right)\frac{\sin^2\varphi_1}{h^2}e^{-\frac{2h}{\sin\varphi_1}\overline{\kappa_t}(h)} \quad \text{(A5.7)}$$

$$P\left(h,\varphi_2\right)=C\beta_t\left(h\right)\frac{\sin^2\varphi_2}{h^2}e^{-\frac{2h}{\sin\varphi_2}\overline{\kappa_t}(h)} \quad \text{(A5.8)}$$

Combining the above two equations (take the logarithm and then subtract A5.7 from A5.8) the mean extinction coefficient is found:

$$\overline{\kappa_t}\left(h\right)=\frac{1}{2h}\frac{\ln\left(\frac{P\left(h,\varphi_2\right)\sin^2\varphi_1}{P\left(h,\varphi_1\right)\sin^2\varphi_2}\right)}{\left(\frac{1}{\sin\varphi_1}-\frac{1}{\sin\varphi_2}\right)} \quad \text{(A5.9)}$$

Appendix VI

Background subtraction and SNR estimation

In the measurement procedure, the first step is to calculate the mean lidar signal for each elevation angle. This is followed by a denoising (wavelets db10, level 2) in the case of JHU lidar. Then, the background is subtracted from the mean lidar signal for each elevation angle. The procedure for background subtraction is shown below using the data set of FSL lidar, channel 355 nm, from April 6, sequence 2. First we calculate a mean lidar signal $<P(r)>$ over 300 bins (1800 m) and then calculate the minimum $\min[<P(r)>]$. The range corresponding to this minimum is used to determine the linear fit which further is extrapolated to $r = 0$. For the JHU lidar data (noisier), 600 bins were used (3600 m range). Figure A6.1 shows an example of background subtraction for a lidar signal at elevation 5^o from April 6, sequence 2. Figure A6.1 (a) presents the signal $P(r)$, the background $\mathrm{BGR}(r)$ and the signal with background subtraction $P(r)$ - $\mathrm{BGR}(r)$.

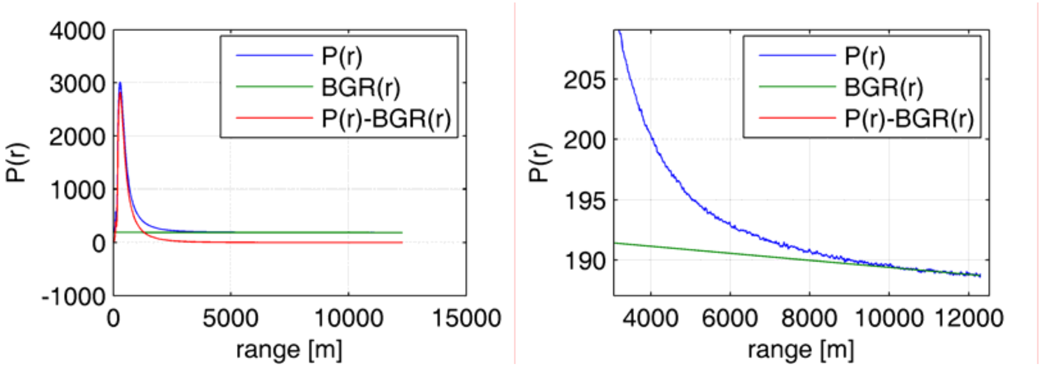

(a) (b)

Figure A6.1. Example background subtraction, FSL lidar, channel 355 nm, April 6, sequence 2, elevation 6^o; (b) is a zoom of (a)

A linear fit over the last 300 bins (from 10488 m to 12288 m) is determined and then extrapolated to $r = 0$ (green line).

Another issue is the estimation of the good (positive) signal $P(r)$. The option used in our calculation was as follows: the linear fit and its 99.9 % confidence intervals (residuals) were determined. The last good signal $P(r)$ is determined where $P(r)$ equals the upper confidence interval of the background linear fit (BGR + residual). Visualization is given in Figure A6.2 [where (b) is a zoom of (a)]. The black curves along the background linear fit (green line) represent the 99.9 % confidence intervals.

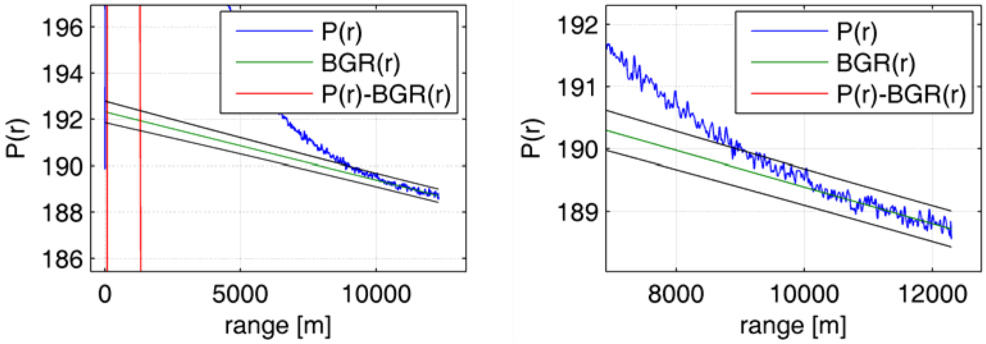

(a) (b)

Figure A6.2. Background linear fit and the 99.9 % confidence intervals; FSL lidar, channel 355 nm, April 6, sequence 2, elevation 6^o; (b) is a zoom of (a)

From figure A6.2 (b) we can see that the signal equals the upper confidence interval around 9000 m. At this point we consider that SNR = 1. In further statements we will refer at good lidar signal as at the signal for which SNR ≥ 1.

Note that the main assumption in such a fit is that the errors in the signals are normal distributed. This might not be true in the case where in addition to the random errors we have also some low frequency noise in the signal.

Figure A6.3 shows the final lidar signal after background subtraction. As mentioned before, the good *P*(*r*) lasts until ~ 9000 m.

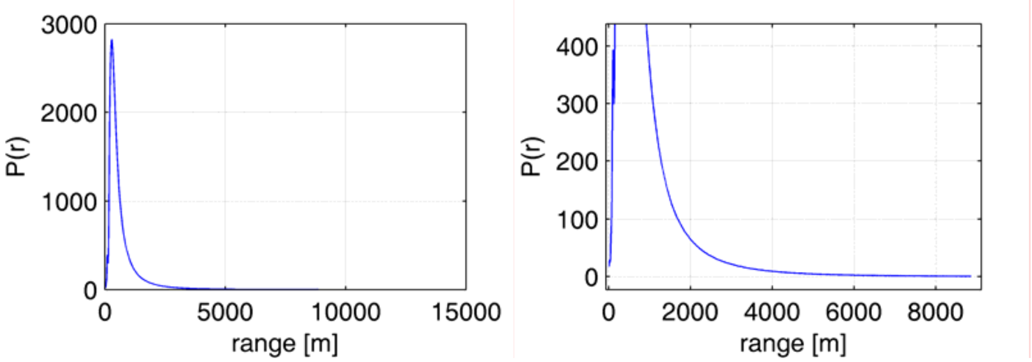

(a) (b)

Figure A6.3. Lidar signal after background subtraction, FSL lidar, channel 355 nm, April 6, sequence 2, elevation 6^o; (b) represents a zoom of (a)

In case of the occurrence of any nonhomogeneity in the far field of the lidar signal *P*(*r*), a manual selection of the range over which the linear fit is determined is chosen. Below is an example from the same day, lidar and sequence but for elevation angle 58^o.

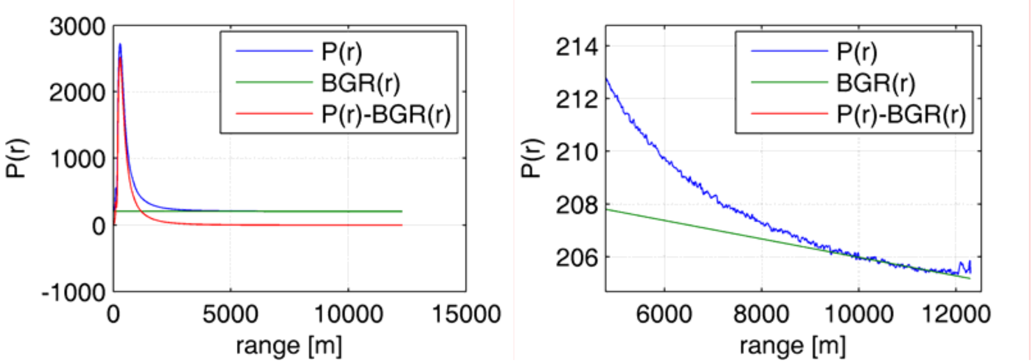

(a) (b)

Figure A6.4. Example of background subtraction in case of heterogeneity in the lidar signal, FSL lidar, channel 355 nm, April 6, sequence 2, elevation 58^o; (b) is a zoom of (a)

As can be seen in figure A6.4 (b), heterogeneity (cloud) in the lidar signal occurs at the end of the measurement range (12 km). In this case, the chosen range for determining the linear fit for the background subtraction is from 9900 m to 11700 m. The 99.9 % confidence intervals are shown in figure A6.5.

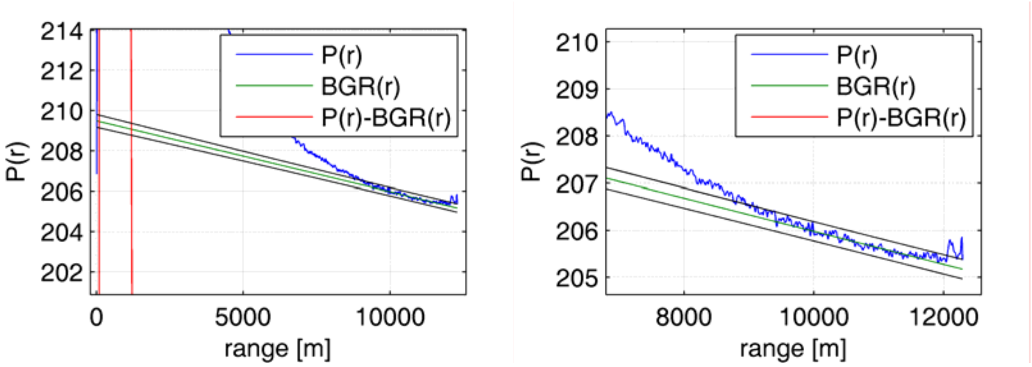

(a) (b)

Figure A6.5. Background linear fit and the 99.9 % confidence intervals, FSL lidar, channel 355 nm, April 6, sequence 2, elevation 58°

The lidar signal after background subtraction is shown in figure A6.6.

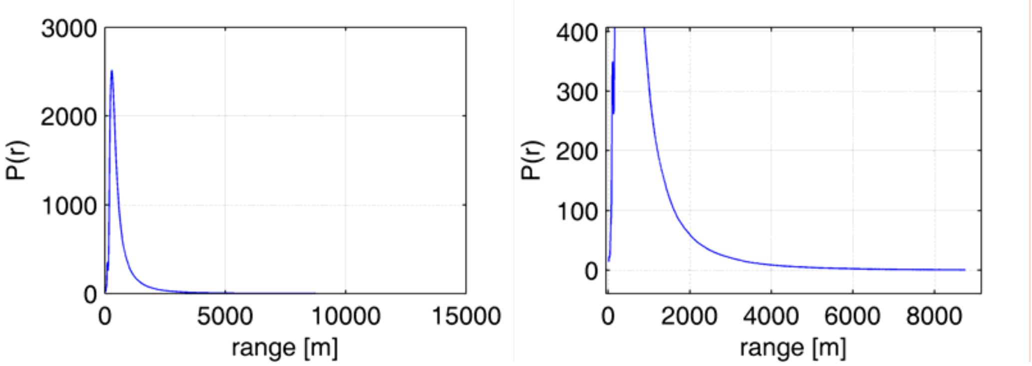

(a) (b)

Figure A6.6. Lidar signal after background subtraction, FSL lidar, channel 355 nm, April 6, sequence 2, elevation 58°; (b) represents a zoom of (a)

Appendix VII

Multiangle methods improved measurement procedure

The measurement procedure (as mentioned in section 4.4.2.) is given below with necessary details. An example of the measurement procedure is given for the data set of FSL lidar, channel 355 nm, from April 6, sequence 2 for r_{max} = 7000 m. The same procedure applies for all r_{max}.

1. First step is to calculate the mean lidar signal for each elevation angle. This means an average over 50 azimuthal angles. Each line of sight (LOS) is itself an average over 30 shots. As the laser frequency was 15 Hz, this means an average time of 2 s for each LOS and around 100 s for all azimuthal angles. In the case of JHU lidar, the mean signal is denoised (wavelets db10, level 2).
2. The background subtraction of the mean lidar signal for each elevation angle is calculated and subtracted(see Appendix 5); original lidar signal $P(r)$, background signal and final lidar signal (after background subtraction) are shown in Figure A7.1 upper plot. All the signals corresponding to all 14 elevation angles are shown so it is almost impossible to distinguish between different signals corresponding to different angles according to the legend. The lines almost constant around 200 bins represent the background. The criterion of SNR = 1 restrict the signals up to ~ 9000 m. The middle and the lower plots show the range corrected signal $P(r)r^2$ and the natural logarithm of the range corrected signal $\ln[P(r)r^2]$.
3. The lidar signal $P(r)$, range corrected signal $P(r)r^2$ and its logarithms are represented as function of h (where $h = r\sin\varphi$) (Figure A7.2)
4. We define $y_j(h)$ and x_j (see section 4.2) as $y_j=\ln[P_j(h)(h/\sin\varphi_j)^2]$ and $x_j = 1/\sin \varphi_j$ and we want to establish a relationship similar to equation 4.3

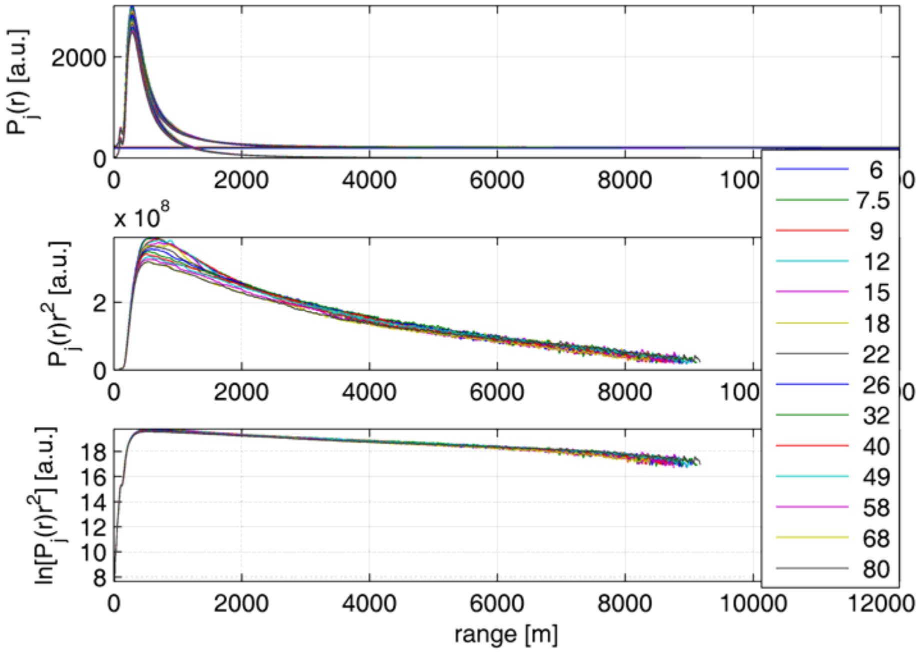

Figure A7.1. Lidar signal $P(r)$ (upper plot), range corrected signal $P(r)r^2$ (middle plot) and logarithm of range corrected signal $\ln[P(r)r^2]$ (lower plot) versus range for FSL lidar, 355 channel, April 6, sequence 2, r_{max} = 7000 m.

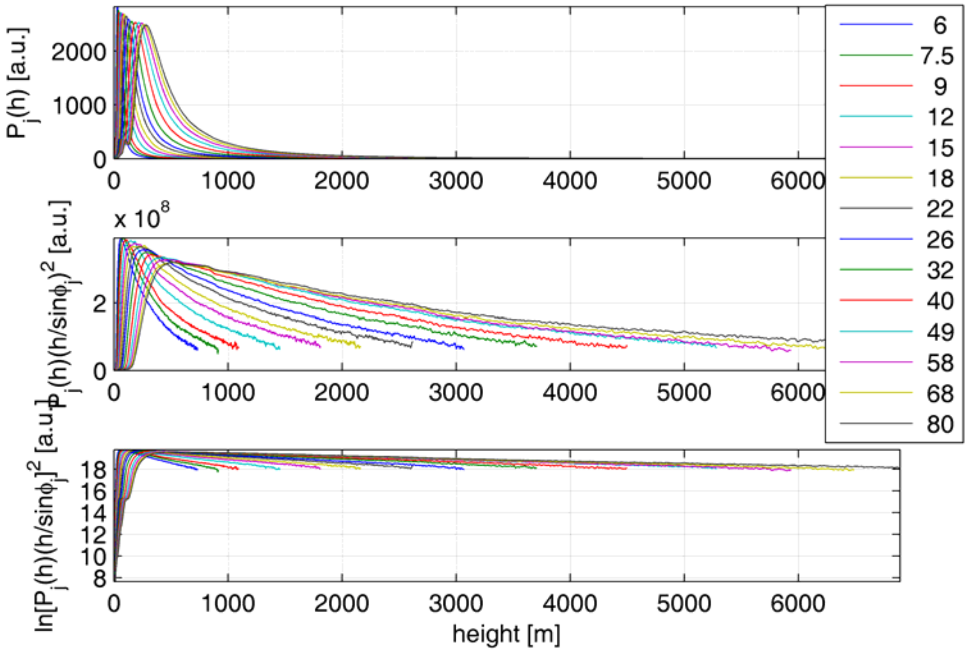

Figure A7.2. Same as figure A7.1 but versus height

$$y_j(h) = A^*(h) - 2\tau(0,h)x_j \tag{A7.1}$$

where the intercept is

$$A^*(h) = \ln[C\beta(h)] \tag{A7.2}$$

There are few criteria used to eliminate the “bad” points from initial $y_j(h)$. Criterion 1, restrict $y_j(h)$ to an upper limit determined by r_{max} i.e. until $h_{max,j} = r_{max}\sin\varphi_j$. For example, the signal along LOS at elevation 6° lasts until $h_{max,1} = 732$ m and the signal along LOS at elevation 80° lasts until $h_{max,14} = 6894$ m. Criterion 2 eliminates the points that are situated in the region of incomplete overlap. Initially, we do not have an estimate of the overlap function therefore we can not determine exactly where the complete overlap starts. We assume that complete overlap begins 100 m after the maximum of $\ln[P(r)r^2]$, which, in terms of height represents $100\sin\varphi_j$ m after the maximum of $y_j(h)$. Criterion 3, additionally restricts the range of $y_j(h)$ by eliminating possible points that can reside before of $\max[y_j(h)]$ as described in section 4.2 and illustrated in figures 4.5 and 4.6. The last criterion, 4, imposes the condition of minimum points available for regression at the end of the interval. As specified in section 4.4.2, in the case of 14 elevation angles, we chose $n_{min} = 6$. In this particular case ($r_{max} = 7000$ m) criterion 4 restricts the $y_j(h)$ up to around 3700 m (Figure A7.3).

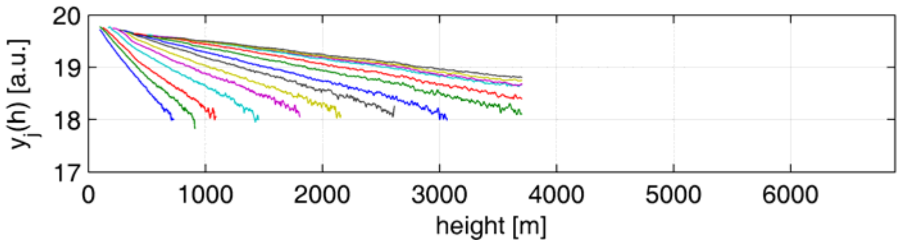

Figure A7.3. Selected range for $y_j(h)$ after the four criteria applied to eliminate the “bad” points, FSL lidar, 355 channel, April 6, sequence 2, r_{max} = 7000 m.

Elsewhere, the minimum points needed for regression was 2. Finally, the selected range of $y_j(h)$ covers the height interval from h_{min} = 96.58 m to h_{max} = 3704 m.

5. Once the selected range for $y_j(h)$ is established we go further and calculate the Hamilton coefficients, optical depth $\tau(0, h)$, and the intercept $A^*(h)$. In figure A7.3, for each height h we plot $y_j(h)$ versus x_j, which theoretically is a straight line whose slope gives us the optical depth and the intercept gives us $A^*(h)$. Figure A7.4 shows two example of the $y_j(x_j)$ for h = 316.72 m (a) and for h =3139 m (b). The optical depth $\tau(0, h)$ and intercept $A^*(h)$ calculated for all heights between h_{min} and h_{max} are shown in Figure A7.5. On the upper plot, the molecular optical depth is shown as well.

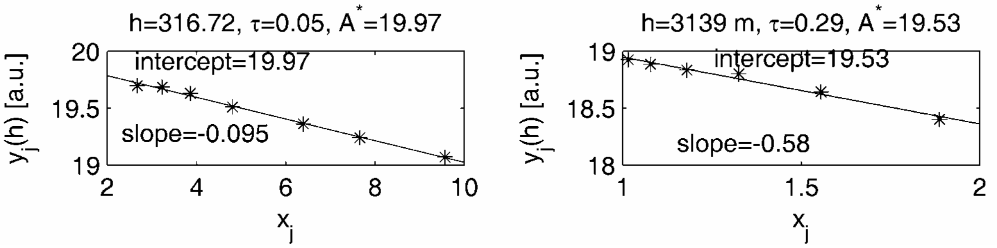

Figure A7.4. Examples of $y_j(x_j)$ regression for h = 316.72 m (a) and for h = 3139 m (b).

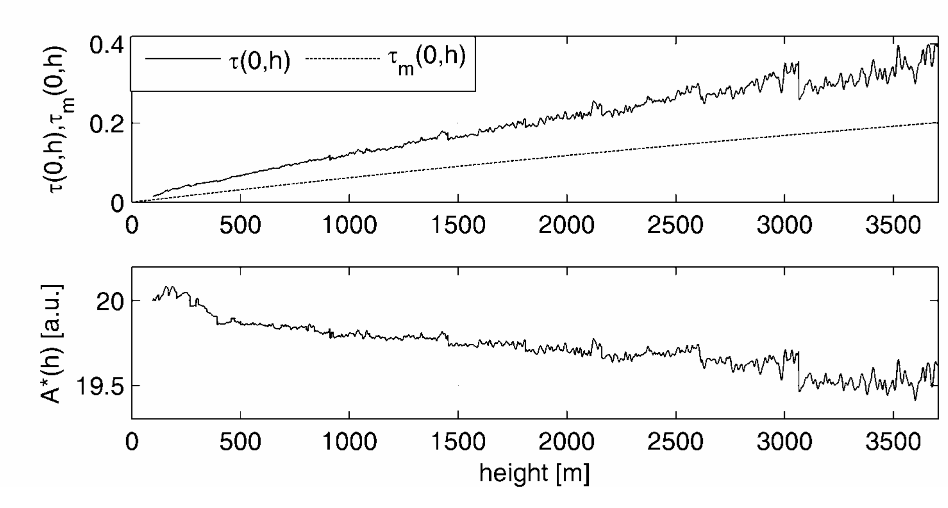

Figure A7.5. Total optical depth $\tau(0, h)$, molecular optical depth $\tau_m(0, h)$ and intercept $A^*(h)$ as determined for selected range of $y_j(h)$ (figure A7.3)

6. Synthetic signal $Z_j^*(h)$ is computed according to equation 4.8. Next, the overlap is calculated according to equation 4.9. Figure A7.6 shows the individual overlaps versus height (upper plot) and versus range (lower plot). Figure A7.7 presents the mean overlap versus range. The STD and relative STD (defined as ratio of STD over mean) are also shown.

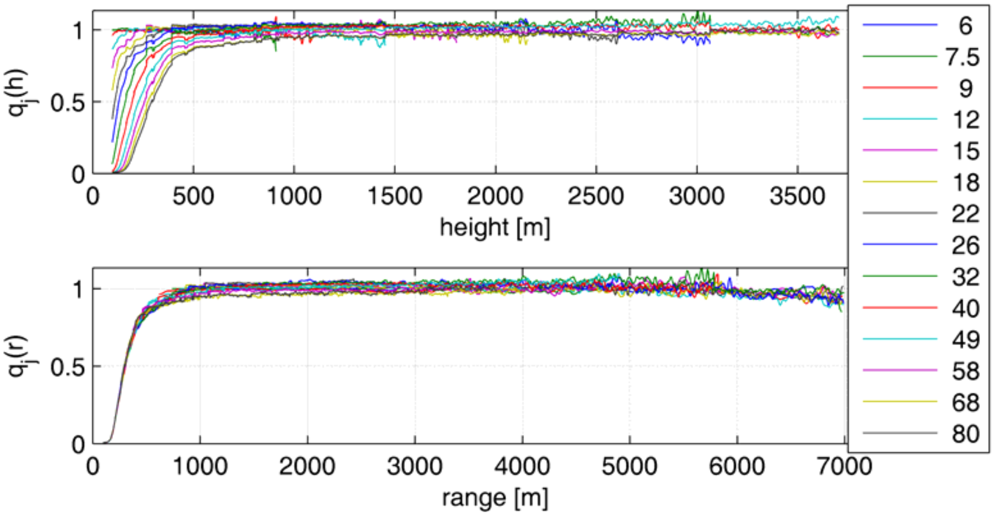

Figure A7.6. Individual overlaps versus height (upper plot) and versus range (lower plot)

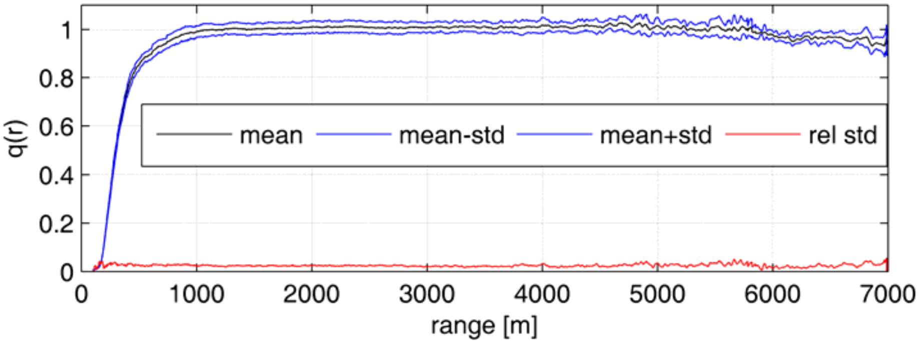

Figure A7.7. Mean overlap versus range (black line), standard deviation (blue lines) and relative standard deviation (red).

In this particular case, we observe that a good estimate of the mean overlap lasts until ~ 6000 m. Deviation from unity is shown for larger heights and comments about this are made in sections 4.2, 4.4 and 4.5. The complete overlap starts around 1000 m.

7. For statistical significance, the steps 1 - 6 are repeated for all $r_{max} = 2000 : 500 : 7000$ m. The mean optical depth $\tau(0, h)$, $A^*(h)$ and overlap are determined.

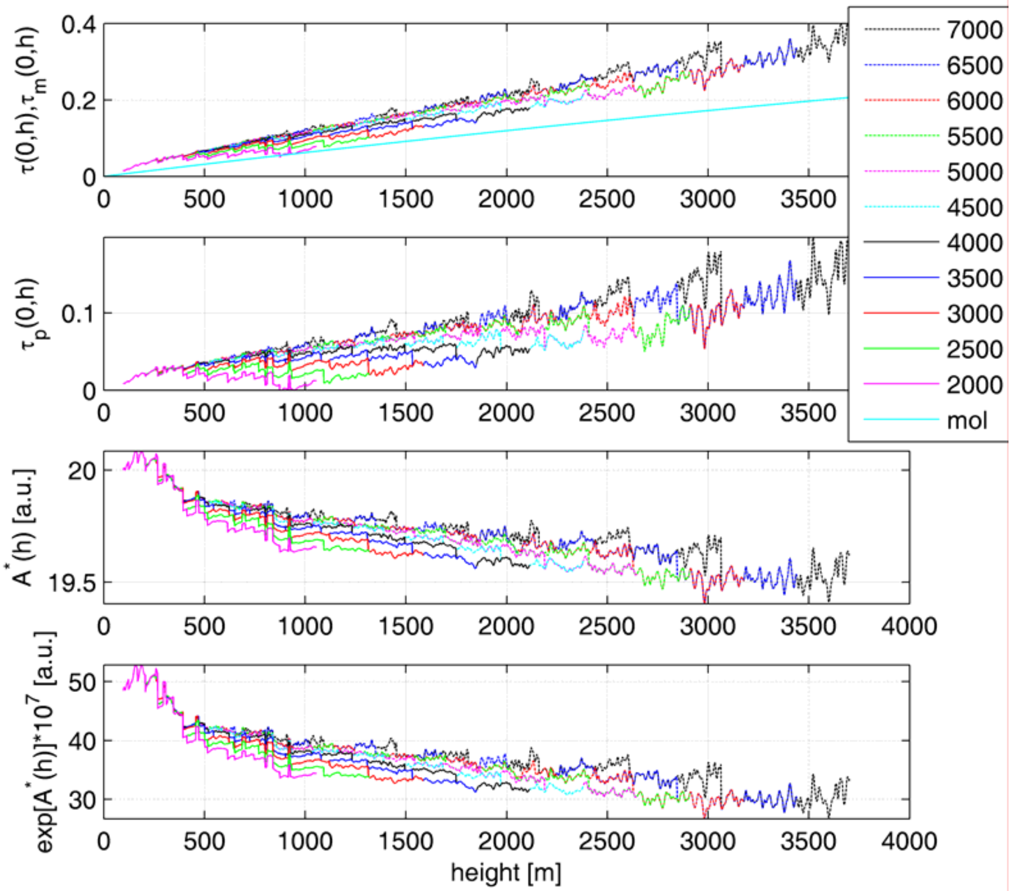

Figure A7.8. Individual total optical depth $\tau(0, h)$ (upper plot), particulate optical depth (second plot), intercept $A^*(h)$ (third plot) and exponential of intercept $\exp[A^*(h)]$ corresponding to each r_{max} (from 2000 m to 7000 m).

Figure A7.8 shows the individual (corresponding to each r_{max}) total optical depth $\tau(0, h)$, particulate optical depth $\tau_p(0, h)$, intercept $A^*(h)$ as well as exponential of the intercept $\exp[A^*(h)]$.

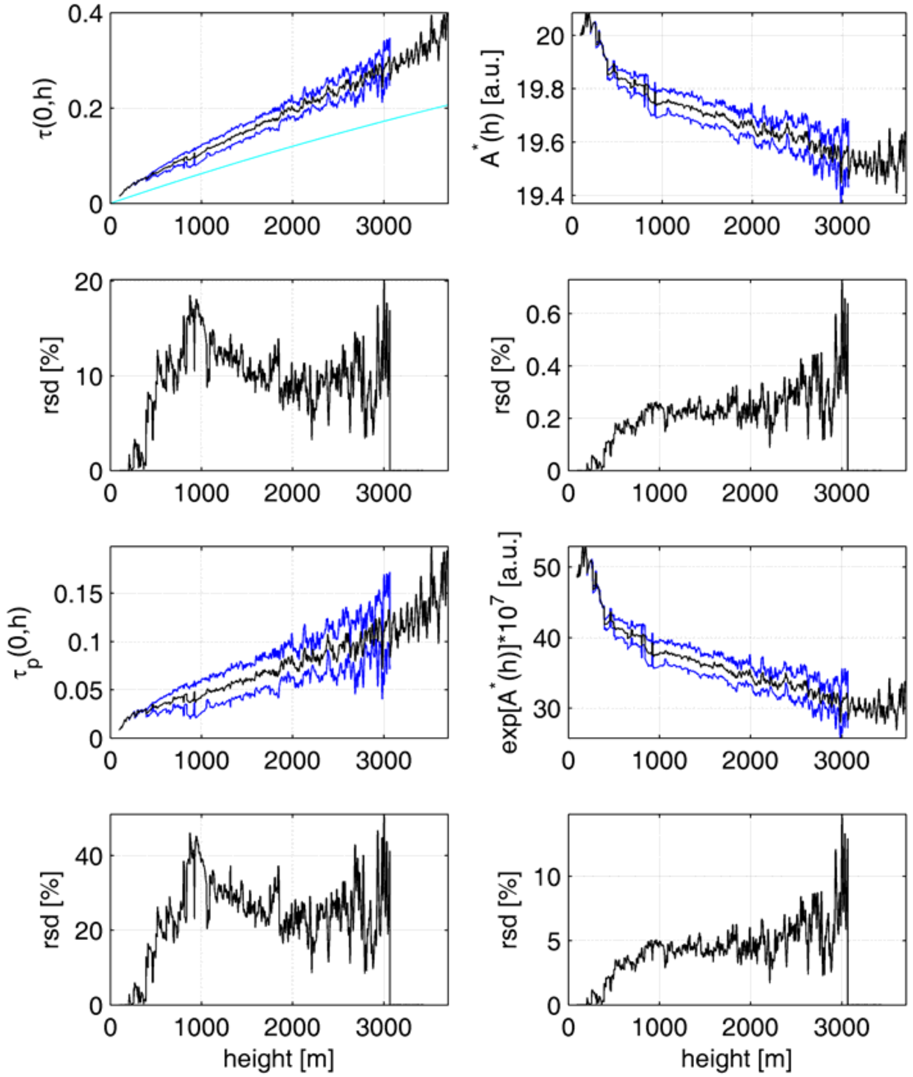

Figure A7.9. Mean total optical depth $\tau(0, h)$, particulate optical depth $\tau_p(0, h)$, intercept $A^*(h)$ and exponent of intercept $\exp[A^*(h)]$ along with their STD (blue curves), relative STD (second and lower plots). The cyan curve on upper left plot represents the molecular optical depth $\tau_m(0, h)$

The mean total optical depth, intercept and exponential of the intercept along with their STD (blue curves) and relative STD are shown in figure A7.9.

Finally, individual overlaps are shown in figure A7.10, upper plot, while the mean overlap is show in the lower plot. On each plot, the relative STD is also shown (less then 10 %). On the second plot, STD is also displayed.

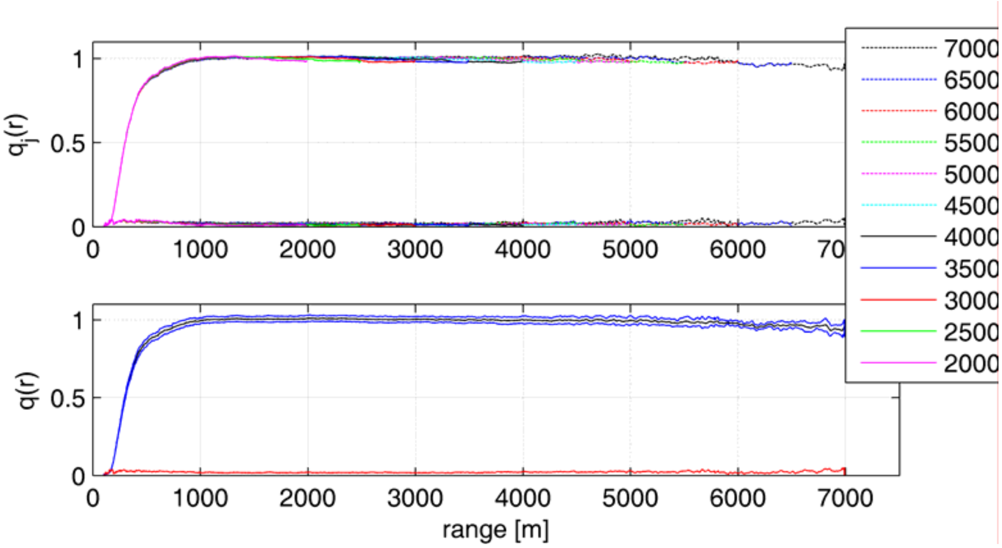

Figure A7.10. Individual overlaps (upper plot) and the mean overlap (lower plot). On both plots, the relative STD are shown. On the lower plot, STD is also shown (blue curves).

Appendix VIII

Notations of the main variables and parameters

In general, the Greek letters denote variables and they are not written in the italic mode. The other variables, denoted by Latin letters, are usually written in italic mode. The following variables and parameters are discussed in chapters 1 - 5.

Π_p – particles (aerosols) backscatter to extinction ratio [sr^{-1}]

Π_m – molecules backscatter to extinction ratio ($3/8\pi$) [sr^{-1}]

ΔN – particles number density in the particles diameter range $\Delta\log(d)$ [cm^{-3}]

$\alpha_p(\mathrm{r})$ – particles absorption coefficient [km^{-1}]

$\beta_t(\mathrm{r})$ – total backscatter coefficient, where $\beta_t(\mathrm{r}) = \beta_p(\mathrm{r}) + \beta_m(\mathrm{r})$ [$\mathrm{km}^{-1}\mathrm{sr}^{-1}$]

$\beta_p(\mathrm{r})$ – particles backscatter coefficient [$\mathrm{km}^{-1}\mathrm{sr}^{-1}$]

$\beta_m(\mathrm{r})$ – molecules backscatter coefficient [$\mathrm{km}^{-1}\mathrm{sr}^{-1}$]

δ – depolarization factor

φ – elevation angle [degrees]

$\kappa_t(\mathrm{r})$ – total extinction coefficient, where $\kappa_t(\mathrm{r}) = \kappa_p(\mathrm{r}) + \kappa_m(\mathrm{r})$ [km^{-1}]

$\kappa_p(\mathrm{r})$ – particles extinction coefficient [km^{-1}]

$\kappa_m(\mathrm{r})$ – molecules extinction coefficient [km^{-1}]

λ – wavelength [μm] or [nm]

ρ – density [kg m^{-3}]

$\sigma_m(\mathrm{r})$ – molecules scattering coefficient [km^{-1}]

$\sigma_p(\mathrm{r})$ – particles scattering coefficient [km^{-1}]

τ – optical depth

A – particle/molecule geometric cross section area [m^2]

A_t – telescope receiving are [m^2]

$A^*(h)$ – Hamilton constant (intercept) [a.u]

ABL – atmospheric boundary layer

APD – avalanche photodiode

APS – Aerodynamic Particle Sizer

AOD – aerosol optical depth

B – background of the lidar signal [a.u]

BGR – background

BL – boundary layer

C – lidar constant [a.u]

DIAL – differential absorption lidar

FSL – Fire Science Laboratory

FT – free troposphere

IR - infrared

JHU – Johns Hopkins University

K – Boltzmann constant ($1.38*10^{-23}$ J/K)

LOS – line of sight

LR – lidar ratio (aerosol extinction to backscatter ratio) [sr]

$M(V,\rho)$ – mass concentration [μg cm^{-3}]

ML – mixing (mixed) layer

MS – multiple scattering

NIR – near infrared

OAM – one angle method

OD – optical depth

$P(r)$ – lidar backscatter signal [a.u.]

PBL – planetary boundary layer

PM2.5 - particulate matter with diameter less or equal than 2.5 μm

PMT – photomultiplier tube

PSD – particles size distribution

Q_{ext}, Q_{sca}, Q_{back} – extinction, scattering and backscattering efficiencies

RCS – range corrected signal, where RCS = $P(r)r^2$ [a.u.]

RL – residual layer

SMPS – Scanning Mobility Particle Sizer

SNR – signal to noise ratio

STD – standard deviation

T – temperature [K]

– transmittance

TEOM – Tapered Element Oscillating Microbalance

UV – ultraviolet

V – volume [m^3]

V_{max}^2 – "effective" transmittance

VIS – visible

X_j – mass fraction

$Z(h)$ – lidar synthetic signal [a.u.]

a – the ratio Π_p/Π_m

c – speed of light [3*10^8 ms^{-1}]

d – particle or molecule diameter [μm]

f_i – volume fraction

h – height [m]

m – index of refraction, where $m = n - \mathrm{i}k$, with n and k the real and imaginary parts

n_m – number of molecules

n_p – number of particles

$n(r)$ – number density [cm^{-3}cm^{-3}]

p, P – pressure [atm]

q(r) – lidar overlap function

r – particle or molecule radius [μm]

– lidar range [m]

r_0 – beginning of the complete overlap [m]

r_{max} – maximum range for good lidar signals [m]

x – size parameter, where $x = 2\pi r/\lambda$

x_j – $1/\sin(\varphi_j)$

y_j – natural logarithm of RCS versus height [a.u.]

Note that when calibrated, $P(r)$ is in units of energy [J] or in units of power [W]. Consequently, if $P(r)$ is in J, then $P(r)r^2$ will be in Jm^2, C in J sr m^3 and so on.

Bibliography:

1. Ackermann, J., P. Völger, and M. Wiegner, Significance of multiple scattering from tropospheric aerosols for ground-based backscatter, *Appl. Opt., 38*(24), 5195-5201, 1999
2. Adam, M., M. Pahlow, V. A. Kovalev, J. M. Ondov, I. Balin ,V. Simeonov, H. van den Bergh, and M. B. Parlange, Determination of the Vertical Extinction Coefficient Profile in the Atmospheric Boundary Layer and the Free Troposphere, EGS-AGU meeting, A-06763, Nice, 2003
3. Adam, M., M. Pahlow, V. A. Kovalev, J. M. Ondov, M. B. Parlange, N. Nair, Aerosol optical characterization by nephelometer and lidar: the Baltimore Supersite experiment during the Canadian forest fire smoke intrusion, *J. Geophys. Res., 109*(D16S02), doi10.1029/2003JD004047, 2004
4. Adam, M., J. M. Ondov, and M. B. Parlange, Determination of aerosol extinction coefficient profiles from elastic backscatter lidar at 1064 nm using the near-end solution. Uncertainties arising from estimation of the boundary conditions, Proceedings of the Twenty-Second International Laser Radar Conference (ILRC22), 479-482, G. Pappalardo and A. Amodeo editors, 2004
5. Adam, M., V. A. Kovalev, C. Wold, J. Newton, M. B. Parlange and W. M. Hao, Practical application of the Kano-Hamilton multiangle inversion method in clear atmospheres. II. Experimental results, Submitted to *Appl. Opt.*, 2005
6. http://aeronet.gsfc.nasa.gov/
7. Althausen, D., D. Müller, A. Ansmann, U. Wandinger, H. Hube, E. Clauder, and S. Zörner, Scanning 6-wavelength 11-channel aerosol lidar, *J. Atmos. Oceanic Technol.*, 17, 1469-1482, 2000

8. Antosiewicz, H. A., Bessel functions of fractional order, *Handbook of mathematical functions with formulas, graphs, and mathematical tables,* edited by M. Abramowitz M. and I. A. Stegun, Dover Publications, Inc., New York, 1964
9. Barnaba, F. and G. P. Gobbi, Lidar estimation of tropospheric aerosol extinction, surface area and volume: Maritime and desert-dust cases, *J. Geophys. Res., 106*(D3), 3005-3018, 2001
10. Bohren, C. F., D. R. Huffman, *Absorption and Scattering of Light by Small Particles,* Wiley Science Paperback Series*,* John Wiley & Sons, Inc., 1983
11. Born, M., W. Wolf, *Principles of Optics*, Pergamon Press, 1965
12. Bristow, M., Suppression of afterpulsing in photomultipliers by gating the photocathode, *Appl. Opt. 41*, 4975-4987, 2002
13. Carrico, C. M., M. H. Bergin, J. Xu, K. Baumann, H. Maring, Urban aerosol radiative properties: Measurements during the 1999 Atlanta Supersite Experiment, J. Geophys. Res., 108(D7)8422, doi:10.1029/2001JD001222, 2003
14. Charlson, R. J., Atmospheric Visibility Related to Aerosol Mass Concentration, *Environ. Sci. Technol., 3*(10)*,* 913-918, 1969
15. Charlson, R. J., S. E. Schwartz, J. M. Hales, R. D. Cess, J. A. Coakley, J. E. Hansen, and D. J. Hofmann, Aerosols and global warming response, *Science, 256 (5057)*, 598-599, 1992
16. Chen, L. W., J. C. Chow, B. G. Doddridge, R. R. Dickerson, W. F. Ryan, and P. K. Mueller, Analysis of a summertime PM2.5 and Haze episode in the mid-Atlantic region, Air & Waste Manage. Assoc., 53, 946-956, 2003
17. Claes, M., K. Gysels, R. van Grieken and R. M. Harrison, Inorganic composition of atmospheric aerosols, *Atmospheric Particles*, edited by R. M. Harrison and R. van Grieken, 543-596, John Wiley & Sons, 1998

18. Collis, R.T. H., Lidar: a new atmospheric probe, *Q. J. R. Meteorol. Soc*., 92, 220-230, 1966
19. Collis, R. T. H., and P. B. Russell, Lidar measurement of particles and gases by elastic backscattering and differential absorption, *Laser monitoring of the atmosphere,* edited by E. D. Hinkley, 71-152, Springler-Verlag Berlin Heidelberg New York, 1976
20. Dalzell, W. H., and A. F. Sarofim, Optical constants of soot and their application to heat-flux calculations, *J. Heat Transfer, 91*, 100-104, 1969
21. Dho, S. W., Y. J. Park, and H. J. Kong, Experimental determination of the geometrical form factor in the lidar equation for inhomogeneous atmosphere, *Appl. Opt. 36*, 6009-6010, 1997
22. Dubovik, O., Holben. B., Eck T. F., Smirnov A., Kaufman Y. J., King M. D., Tanre D., Slutsker I., Variability of absorption and optical properties of key aerosol types observed in worldwide locations, *J. Atm. Sci*., 59(3), 590-608, 2002
23. Edlen, K., The refractive index of air, *Metrologia* 2: 12, 1966
24. Elterman, L., Vertical Attenuation Model with eight surface Meteorological Ranges 2 to 13 kilometers, *AFCRL_70_0200, Environmental Research Papers, no 318,* 1970
25. Ferrare, R. A., S. H. Melfi, D. N. Whiteman, K. D. Evans, and R. Leifer, Raman lidar measurements of aerosol extinction and backscattering 1. Methods and comparisons, *J. Geophys. Res., 103*(D16), 19,663-19,672, 1998
26. Ferrare, R. A., S. H. Melfi, D. N. Whiteman, K. D. Evans, M. Poellot, and Y. J. Kaufman, Raman lidar measurements of aerosol extinction and backscattering 2. Derivations of aerosol real refractive index, single-scattering albedo, and

humidification factor using Raman lidar and aircraft size distribution measurements, *J. Geophys. Res., 103*(D16), 19,673-19,689, 1998

27. Fernald, F.G., Analysis of atmospheric lidar observations: some comments, *Appl. Opt., 23*(5), 652-653, 1984
28. Flamant, C.,J. Pelon, P. Chazette, V. Trouillet, P. K. Quinn, R. Frouin, D. Bruneau, J. F. Leon, T. S. Bates, J. Johnson and J. Livingston, Airborne lidar measurements of aerosol spatial distribution and optical properties over the Atlantic Ocean during a European pollution outbreak of ACE-2, *Tellus*, 52B, 662-677, 2000
29. Garratt, J. R., *The atmospheric boundary layer*, Cambridge University Press, 1992
30. Gobbi, G. P., F. Barnaba, M. Blumthaler, G. Labow, J. R. Herman, Observed effects of particles Nonsphericity on the retrieval of marine and desert dust aerosol optical depth by lidar, *Atmos. Res., 61,* 1-14, 2002
31. Gobbi, G. P., F. Barnaba, R. van Dingenen, J. P. Putaud, M. Mircea, and M. C. Facchini, Lidar and in situ observations of continental and Saharan aerosol: closure analysis of particles optical and physical properties, *Atmos. Chem. Phys. Discuss.*, 3, 445-477, 2003
32. Goody, R. M., Y. L. Yung, *Atmospheric Radiation Theoretical Basis*, Oxford University Press, 1989
33. Hamilton, P. M., Lidar measurement of backscatter and attenuation of atmospheric aerosol, *Atmos. Environ.* 3, 221-223, 1969
34. Hand, J.L., and S. Kreidenweis, A new method for retrieving particle refractive index and effective density from aerosol size distribution data, *Aerosol. Sci. and Technol.* 36, 1012-1026, 2002

35. Hasan, H., and T. G. Dzubay, Apportioning light extinction coefficients to chemical species in atmospheric aerosol, *Atmos. Environ.* 17(8), 1573-1581, 1983
36. Hobbs, P. V., Aerosol-cloud interactions, *Aerosol-cloud-climate interactions,* edited by P. V. Hobbs, 33-69, Academic Press, Inc, 1993
37. Hobbs P.V., and M. P. McCormick, editors, *Aerosols and climate,* A. Deepak Publishing, 1988
38. Hoff, R. M., H. A. Wiebe, L. Guise-Bagley, Lidar, nephelometer, and in situ aerosol experiments in southern Ontario, *J. Geophys. Res., 101*(D14), 19199-19209, 1996
39. Horvath, H., Influence of atmospheric aerosols upon the global radiation balance, *Atmospheric particles,* edited by R. M. Harrison and R. van Grieken, 543-596, John Wiley & Sons, 1998
40. Houghton, J.T., Y. Ding, D. J. Griggs, M. Noguer, P.J. van der Linden, X. Dai, K. Maskell, and C.A. Johnson editors*, Climate change 2001: the scientific basis: contribution of working group I to the third assessment report of the intergovernmental panel on climate change,* Cambridge University Press, Cambridge, UK. 2001
41. Hulbert, E. O., Optics of atmospheric haze, *J. Opt. Soc. Am., 31*(7), 467-476, 1941
42. van de Hulst, H. C., *Light scattering by small particles,* Dover Publications, Inc. New York, 1981
43. Jackson, J. D., *Classical electrodynamics*, John Willey & Sons, 1975
44. Jaenicke, R., Atmospheric aerosol size distribution, *Atmospheric Particles*, edited by R. M. Harrison and R. van Grieken, 543-596, John Wiley & Sons, 1998

45. Kano, M., On the determination of backscattered and extinction coefficient of the atmosphere by using laser radar, *Papers Meteorol. and Geophys. 19*, 121-129, 1968

46. Klett, J.D., Lidar inversion with variable backscatter/extinction ratios, *Appl. Opt., 24*(11), 1638-1643, 1985

47. Kovalev, V. A, H. Moosmüller, Distortion of particulate extinction profiles measured with lidar in a two-component atmosphere*, Appl. Opt., 33*(27), 6499-6507, 1994

48. Kovalev, V. A., C. Wold, J. Newton, and Wei Min Hao, Combination of one-directional and multiangle data processing techniques to reduce uncertainty in the elastic lidar measurement data, Proceedings of SPIE 5575 *Laser Radar Techniques for Atmospheric Sensing*, 82-90, Upendra N. Singh, editor, 2004

49. Kovalev, V.A., Sensitivity of the lidar solution to errors of the aerosol backscatter-to-extinction ratio: influence of a monotonic change in the aerosol extinction coefficient, *Appl. Opt., 34*(18), 3457-3462, 1995

50. Kovalev, V. A., Analytical differentiation of the differential-absorption-lidar data distorted by noise, *Appl. Opt. 41*, 1156-1162 , 2002

51. Kovalev, V. A., Stable Near-end solution of the Lidar equation for clear atmosphere*, Appl. Opt., 42*(3), *585-591*, 2003

52. Kovalev, V. A., Distortions of the extinction coefficient profile caused by systematic errors in lidar data, *Appl. Opt. 43*, 3191-3198, 2004

53. V. A. Kovalev and M. Adam, "Practical application of the Kano-Hamilton multiangle inversion method in clear atmospheres. I. Measurement and data inversion methodology," (Submitted to Applied Optics, 2005)

54. Kovalev V. A. and W. E. Eichinger, *Elastic lidar. Theory, practice, and analysis methods*, WILEY-INTERSCIENCE, Wiley & Sons Inc., 295-304, 2004
55. Kovalev V. A. and M. Adam, Practical application of the Kano-Hamilton multiangle inversion method in clear atmospheres. I. Measurement and data inversion methodology, Submitted to *Appl, Opt.*, 2005
56. Kunz G. J. and G. Leeuw, Inversion of lidar signals with the slope method, *Appl. Opt. 32*, 3249-3256, 1993
57. LaRocca, A. J., and Turner, R.E., Atmospheric Transmittance and Radiance: Methods of Calculation, Rpt. No. 107600-10-T, Environmental Research Institute of Michigan, Ann Arbor, MI, June 1975
58. Lee, H. S., G. K. Schwemmer, C. L. Korb, M. Dombrowski, and C. Prasad Gated photomultiplier response characterization for DIAL measurements, *Appl. Opt. 29*, 3303-3315, 1990
59. Marenco, F., V. Santacesaria, A. F. Bais, D. Balis, A. di Sarra, A. Papayannis, and C. Zerefos, Optical properties of tropospheric aerosols determined by lidar and spectrophotometric measurements (Photochemical Activity and Solar Ultraviolet Radiation campaign), *Appl. Opt*., 36 (27), 6875-6886, 1997
60. Measures, R. M., *Laser remote sensing; Fundamentals and applications*, John Wiley & Sons, 1984
61. www.mathworks.com, MATLAB701 Wavelet toolbox
62. G. Strang, T. Nguyen, "*Wavelets and filter banks*", Wellesley-Cambridge Press (1996),
63. Mayor, S. D., and E. W. Eloranta, Two-dimensional vector wind fields from volume imaging lidar data, *J. Appl. Meteorol. 40*, 1331-1346, 2001

64. Mishchenko, M. I., Calculation of the amplitude matrix for a nonspherical particle in a fixed orientation, *Appl.Opt., 39* (6): 1026-1031, 2000
65. Mishchenko, M. I., L. D. Travis, and A. Macke, T-matrix method and its applications, *Light scattering by nonspherical particles*, edited by Mishcenko, M. I., J. W. Hovenier and L. D. Travis, Academic Press, San Diego, 2000
66. Müller, D., U. Wandinger, D. Althausen, and M. Fiebig, Comprehensive particle characterization from three-wavelength Raman-lidar observations: case study, *Appl. Opt., 40*(27), 4863-4869, 2001
67. NASA, U.S. Standard Atmosphere Supplements, 1976, U.S. Government Printing Office, Washington, D.C., 1976
68. Ouimette, J. R., and R. C. Flagan, The extinction coefficient of multicomponent aerosols, *Atmos. Environ.* 16(10), 2405-2419, 1982
69. Pahlow, M., *Atmospheric boundary layer dynamics and inversion technologies to obtain extinction coefficient profiles in the atmosphere from elastic lidar*, Ph.D. thesis, JHU, Baltimore, 2002 (http://wwwlib.umi.com/dissertations/dlnow/3080740)
70. Pahlow, M., J. Kleissl, M. B. Parlange, J. Ondov, and D. Harrison, Atmospheric boundary layer structure as observed during a haze event due to forest fire smoke, *Boundary-Layer Meteorol.*, 114, 53-70, 2005
71. Pahlow, M., V. A. Kovalev, and M. B. Parlange, Calibration method for multiangle lidar measurements, *Appl. Opt., 43*(14), 2948-2956, 2004
72. Redemann, J., R. P. Turco, R. F. Pueschel, E. V. Browell, and W. B. Grant, Comparison of aerosol measurements by lidar and in situ methods in the Pacific basin troposphere, *Advances in atmospheric remote sensing with lidar,* selected

papers of the 18th ILRC, A. Ansmann, R. Neuber, P. Rairoux and U. Wandinger editors, Springer, 1996

73. Redemann, J., R.P. Turco, K.N. Liou, P.B. Russell, R.W. Bergstrom, B. Schmid, J.M. Livingston, P.V. Hobbs, W.S. Hartley, S. Ismail, R.A Ferrare, E.V. Browell, *Retrieving the Vertical Structure of the Effective Aerosol Complex Index of Refraction From a Combination of Aerosol In Situ and Remote Sensing Measurements During TARFOX* (accepted for publication at J. of Geophys. Res. 2003) (http://geo.arc.nasa.gov/sgg/tarfox/whatnew/SpecialSection/JGRspecsec2_ppr1.html)
74. Rocadenbosch, F., A. Comeron, and L. Albiol, Statistics of the slope-method estimator, *Appl. Opt. 39*, 6049-6057, 2000
75. Rocadenbosch, F., A. Comeron, and D. Pineda, Assessment of lidar inversion errors for homogeneous atmospheres, *Appl. Opt. 37*, 2199-2206, 1998
76. Rocadenbosch, F., M. Sicard, and A. Comeron, Automated variable-resolution algorithm for Raman extinction retrieval, Proceedings of the Twenty-Second International Laser Radar Conference (ILRC22), 467-470, G. Pappalardo and A. Amodeo editors, 2004
77. Rothermal J. and W. Jones, Ground-based measurements of atmospheric backscatter and absorption using coherent CO_2 lidar, *Appl. Opt. 24*, 3487-3496, 1985
78. Russel P. B. and J. M. Livingston, Slant-lidar aerosol extinction measurements and their relation to measured and calculated albedo changes, *J. Clim. Appl. Meteorol. 23*, 1204-1221, 1984
79. Salby, M. L., *Fundamentals of Atmospheric Physics*, Academic Press, 1996

80. Sasano, Y., H. Shimizu, N. Takeuchi, and M. Okuda, Geometrical form factor in the laser radar equation: an experimental determination, *Appl. Opt. 18*, 3908-3910, 1979
81. Sasano, Y., and E. V. Browell, Light scattering characteristics of various aerosol types derived from multiple wavelength lidar observations, *Appl. Opt., 28*(9), 1670-1679, 1989
82. Sasano, Y., Tropospheric Aerosol Extinction Coefficient Properties Derived from Scanning Lidar Measurements over Tsukiba, Japan, from 1990 to 1993, *Appl. Opt. 35*, 4941-4952, 1996
83. Sassen K. and G. C. Dodd, Lidar crossover function and misalignment effects, *Appl. Opt. 21*, 3162-3165, 1982
84. Sassen, K., M. K. Griffin and G. C. Dodd, Optical Scattering and Microphysical Properties of Subvisual Cirrus Clouds, and Climatic Implications, *J. Appl. Meteorol., 28*, 91-98, 1989
85. Sassen, K., B. S. Cho, Subvisual-thin Cirrus Lidar Dataset for Satellite Verification and Climatological Research, *J. Appl. Meteorol., 31,* 1275-1285, 1992
86. Seinfeld, J. H., and S. N. Pandis, *Atmospheric chemistry and physics; from air pollution to climate change*, John Willey & Sons, 1998
87. Sicard, M., P. Chazette, J. Pelon, J. G. Won, and S. C. Yoon, Variational Method for the Retrieval of the Optical Thickness and the Backscatter Coefficient from Multiangle Lidar Profiles, *Appl. Opt. 41*, 493-502, 2002
88. V. Simeonov, G. Larcheveque, P. Quaglia, H. van den Bergh, and B. Calpini, Influence of the photomultiplier tube spatial uniformity on lidar signals, *Appl. Opt. 38*, 5186-5190, 1999.

89. Sloane, C. S., Effect of composition on aerosol light scattering efficiencies, *Atmos. Environ*., 20(5), 1025-1037, 1986
90. Smith, K. C., and C. R. Shadix, The elusive history of m=1.57-0.56i for the refractive index of soot, *Combust. flame, 107,* 314-320, 1996
91. Spinhirne, J. D. , J. A. Reagan, and B. M. Herman, Vertical distribution of aerosol extinction cross section and interference of aerosol imaginary index in the troposphere by lidar technique, *J. Appl. Meteorol. 19*, 426-438, 1980
92. Stegun, I. A., Legendre functions, *Handbook of mathematical functions with formulas, graphs, and mathematical tables,* edited by M. Abramowitz M. and I. A. Stegun, Dover Publications, Inc., New York, 1964
93. Stull, R. B., *An introduction to boundary layer meteorology*, Kluwer Academic Publishers, 1988
94. Takamura, T., Y. Sasano, and T. Hayasaka, Tropospheric Aerosol Optical Properties Derived from Lidar, Sun Photometer, and Optical Particle Counter Measurements, *Appl. Opt. 33*, 7132-7140, 1994
95. Tomine, K., C. Hirayama, K. Michimoto, and N. Takeuchi, Experimental determination of the crossover function in the laser radar equation for days with a light mist, *Appl. Opt. 28*, 2194-2195, 1989
96. Turpin, B., and H-J Lin, Species contributions to PM2.5 mass concentrations: revisiting common assumptions for estimating organic mass, *Aerosol Sci. and Technol*. 35, 602:610, 2001
97. Upendra, N. S., S. Ismail, and G. K. Schwemmer, editors, *Ninetheenth International Laser Radar Conference,* NASA/CP-1998-207671/PT2, 1998
98. Volkov, S. N. , B. V. Kaul, and D. I. Shelefontuk, Optimal method of linear regression in laser remote sensing, *Appl. Opt. 41*, 5078-5083, 2002

99. Warneck, P., *Chemistry of the natural atmosphere*, Academic Press, 1999

100. Weinman, J., Derivation of atmospheric extinction profiles and wind speed over the ocean from a satellite-borne lidar, *Appl. Opt., 27*(19), 3994-4001, 1988

101. Welton, E. J., K. J. Voss, P. K. Quinn, P. J. Flatau, K. Markowicz, J. R. Campbell, J. D. Spinhirne, H. R. Gordon, and J. E. Johnson, Measurements of aerosol vertical profiles and optical properties during INDOEX 1999 using micropulse lidars, J. Geophys. Res, 107, dio: 10.1029/2000JD000038, 2002

102. Whiteman, D. N., Application of statistical methods to the determination of slope in lidar data, *Appl. Opt. 15*, 3360-3369, 1999

103. Zhao, Y., Signal-induced fluorescence in photomultipliers in differential absorption lidar systems, *Appl. Opt. 38*, 4639-4648, 1999

104. Zuev, V. E., *Laser beams in the atmosphere*, Consultants bureau, New York, 1982

CURRICULUM VITAE

Born on January 6, 1968 in Tărtăşeşti, Romania

1988-1993: BS in Physics, University of Bucharest, Bucharest, Romania

1994-1996: MS in Water Resources Engineering, Technical University of Civil Engineering, Bucharest, Romania

2000-2005: MSE in Mechanical Engineering, Johns Hopkins University, Baltimore, USA

2000-2005: PhD in Environmental Engineering, Johns Hopkins University, Baltimore, USA